The Plasma Environment of Comet 67P/Churyumov-Gerasimenko

Von der Fakultät für Elektrotechnik, Informationstechnik, Physik
der Technischen Universität Carolo-Wilhelmina zu Braunschweig

zur Erlangung des Grades einer Doktorin
der Naturwissenschaften (Dr. rer. nat.)

genehmigte Dissertation
Kumulative Arbeit

von Charlotte Josefine Götz

aus Hamm

eingereicht am 21.01.2019

Disputation am 30.04.2019

1. Referent: Prof. Dr. Karl-Heinz Glaßmeier
2. Referent: Dr. Marina Galand, Reader

Druckjahr: 2019

Dissertation an der Technischen Universität Braunschweig,
Fakultät für Elektrotechnik, Informationstechnik, Physik

Teilergebnisse aus dieser Arbeit wurden mit Genehmigung der Fakultät für Elektrotechnik, Informationstechnik, Physik, vertreten durch den Mentor der Arbeit, in folgenden Beiträgen vorab veröffentlicht:

Publikationen

Erst-, Zweit-, und Drittautor Publikationen

- **Goetz, C.**, Koenders, C., Richter, I., Altwegg, K., Burch, J., Carr, C., Cupido, E., Eriksson, A., Güttler, C., Henri, P., Mokashi, P., Nemeth, Z., Nilsson, H., Rubin, M., Sierks, H., Tsurutani, B., Vallat, C., Volwerk, M., Glassmeier, K. H., 2016, First detection of a diamagnetic cavity at comet 67P/Churyumov-Gerasimenko, Astronomy & Astrophysics, 588, A24

- Koenders, C., Perschke, C., **Goetz, C.**, Richter, I., Motschmann, U., Glassmeier, K. H., 2016, Low-frequency waves at comet 67P/Churyumov-Gerasimenko. Observations compared to numerical simulations, Astronomy & Astrophysics, 594, A66

- Koenders, C., **Goetz, C.**, Richter, I., Motschmann, U., Glassmeier, K. H., 2016, Magnetic field pile-up and draping at intermediately active comets: results from comet 67P/Churyumov-Gerasimenko at 2.0 AU, Monthly Notices of the Royal Astronomical Society, 462, S235-S241

- Nemeth, Z., Burch, J., **Goetz, C.**, Goldstein, R., Henri, P., Koenders, C., Madanian, H., Mandt, K., Mokashi, P., Richter, I., Timar, A., Szego, K., 2016, Charged particle signatures of the diamagnetic cavity of comet 67P/Churyumov-Gerasimenko, Monthly Notices of the Royal Astronomical Society, 462, S415-S421

- Kolokolova, L., Koenders, C., **Goetz, C.**, Rosenbush, V., Kiselev, N., Hoang, T., Lazarian, A., 2016, Clues to cometary circular polarization from studying the magnetic field in the vicinity of the nucleus of comet 67P/Churyumov-Gerasimenko, Monthly Notices of the Royal Astronomical Society, 462, S422-S431

- **Goetz, C.**, Koenders, C., Hansen, K. C., Burch, J., Carr, C., Eriksson, A., Frühauff, D., Güttler, C., Henri, P., Nilsson, H., Richter, I., Rubin, M., Sierks, H., Tsurutani, B., Volwerk, M., Glassmeier, K. H., 2016, Structure and evolution of the diamagnetic cavity at comet 67P/Churyumov-Gerasimenko, Monthly Notices of the Royal Astronomical Society, 462, S459-S467

- Gunell, H., **Goetz, C.**, Eriksson, A., Nilsson, H., Simon Wedlund, C., Henri, P., Maggiolo, R., Hamrin, M., De Keyser, J., Rubin, M., Stenberg Wieser, G., Cessateur, G., Dhooghe, F., Gibbons, A., 2017, Plasma waves confined to the diamagnetic cavity of comet 67P/Churyumov-Gerasimenko, Monthly Notices of the Royal Astronomical Society, 469, S84-S92

- **Goetz, C.**, Volwerk, M., Richter, I., Glassmeier, K. H., 2017, Evolution of the magnetic field at comet 67P/Churyumov-Gerasimenko, Monthly Notices of the Royal Astronomical Society, 469, S268-S275

- Plaschke, F., **Goetz, C.**, Volwerk, M., Richter, I., Frühauff, D., Narita, Y., Glassmeier, K. H., Dougherty, M. K., 2017, Fluxgate magnetometer offset vector determination by the 3D mirror mode method, Monthly Notices of the Royal Astronomical Society, 469, S675-S684

- Volwerk, M., **Goetz, C.**, Richter, I., Delva, M., Ostaszewski, K., Schwingenschuh,K., Glassmeier, K. H., 2018, A tail like no other. The RPC-MAG view of Rosetta's tail excursion at comet 67P/Churyumov-Gerasimenko, Astronomy & Astrophysics, 614, A10

- Gunell, H., **Goetz, C.**, Wedlund, C. S., Lindkvist, J., Hamrin, M., Nilsson, H., LLera, K., Eriksson, A., Holmström, M., 2018, The infant bow shock: a new frontier at a weak activity comet, Astronomy & Astrophysics, 619, L2

- Plaschke, F., Karlsson, T., **Götz, C.**, Möstl, C., Richter, I., Volwerk, M., Eriksson, A., Behar, E., Goldstein, R., 2018, First observations of magnetic holes deep within the coma of a comet, Astronomy & Astrophysics, 618, A114

- **Goetz, C.**, Tsurutani, B. T., Henri, P., Volwerk, M., Behar, E., Edberg, N. J. T., Eriksson, A., Goldstein, R., Mokashi, P., Nilsson, N., Richter, I., Wellbrock, A., Glassmeier, K. H., 2018, Unusually high magnetic fields in the coma of 67P/Churyumov-Gerasimenko during its high-activity phase, Astronomy & Astrophysics, in press

Koautor Publikationen

- Richter, I., Koenders, C., Auster, H. -U., Frühauff, D., **Götz, C.**, Heinisch, P., Perschke, C., Motschmann, U., Stoll, B., Altwegg, K., Burch, J., Carr, C., Cupido, E., Eriksson, A., Henri, P., Goldstein, R., Lebreton, J. -P., Mokashi, P., Nemeth, Z., Nilsson, H., Rubin, M., Szegö, K., Tsurutani, B. T., Vallat, C., Volwerk, M., Glassmeier, K. H., 2015, Observation of a new type of low-frequency waves at comet 67P/Churyumov-Gerasimenko, Annales Geophysicae, 33, 1031–1036

- Richter, I., Auster, H.-U., Berghofer, G., Carr, C., Cupido, E., Fornaçon, K.-H., **Goetz, C.**, Heinisch, P., Koenders, C., Stoll, B., Tsurutani, B. T., Vallat, C., Volwerk, M., Glassmeier, K. H., 2016, Two-point observations of low-frequency waves at 67P/Churyumov-Gerasimenko during the descent of PHILAE: comparison of RPCMAG and ROMAP, Annales Geophysicae, 34, 609-622

- Volwerk, M., Richter, I., Tsurutani, B., **Götz, C.**, Altwegg, K., Broiles, T., Burch, J., Carr, C., Cupido, E., Delva, M., Dósa, M., Edberg, N. J. T., Eriksson, A., Henri, P., Koenders, C., Lebreton, J. -P., Mandt, K. E., Nilsson, H., Opitz, A., Rubin, M., Schwingenschuh, K., Stenberg Wieser, G., Szegö, K., Vallat, C., Vallieres, X., Glassmeier, K. H., 2016, Mass-loading, pile-up, and mirror-mode waves at comet 67P/Churyumov-Gerasimenko, Annales Geophysicae, 34, 1-15

- Mandt, K. E., Eriksson, A., Edberg, N. J. T., Koenders, C., Broiles, T., Fuselier, S. A., Henri, P., Nemeth, Z., Alho, M., Biver, N., Beth, A., Burch, J., Carr, C., Chae, K., Coates, A. J., Cupido, E., Galand, M., Glassmeier, K. H., **Goetz, C.**, Goldstein, R., Hansen, K. C., Haiducek, J., Kallio, E., Lebreton, J. -P., Luspay-Kuti, A., Mokashi, P., Nilsson, H., Opitz, A., Richter, I., Samara, M., Szego, K., Tzou, C. -Y., Volwerk, M., Simon Wedlund, C., Stenberg Wieser, G., 2016, RPC observation of the development and evolution of plasma interaction boundaries at 67P/Churyumov-Gerasimenko, Monthly Notices of the Royal Astronomical Society, 462, S9-S22

- Edberg, N. J. T., Alho, M., André, M., Andrews, D. J., Behar, E., Burch, J. L., Carr, C. M., Cupido, E., Engelhardt, I. A. D., Eriksson, A. I., Glassmeier, K. H., **Goetz, C.**, Goldstein, R., Henri, P., Johansson, F. L., Koenders, C., Mandt, K., Möstl, C., Nilsson, H., Odelstad, E., Richter, I., Simon Wedlund, C., Stenberg Wieser, G., Szego, K., Vigren, E., Volwerk, M., CME impact on comet 67P/Churyumov-Gerasimenko, 2016, Monthly Notices of the Royal Astronomical Society, 462, S45-S56

- Grün, E., Agarwal, J., Altobelli, N., Altwegg, K., Bentley, M. S., Biver, N., Della Corte, V., Edberg, N., Feldman, P. D., Galand, M., Geiger, B., **Götz, C.**, Grieger, B., Güttler, C., Henri, P., Hofstadter, M., Horanyi, M., Jehin, E., Krüger, H., Lee, S., Mannel, T., Morales, E., Mousis, O., Müller, M., Opitom, C., Rotundi, A., Schmied, R., Schmidt, F., Sierks, H., Snodgrass, C., Soja, R. H., Sommer, M., Srama, R., Tzou, C.-Y., Vincent, J.-B., Yanamandra-Fisher, P., A'Hearn, M. F., Erikson, A. I., Barbieri, C., Barucci, M. A., Bertaux, J.-L., Bertini, I., Burch, J., Colangeli, L., Cremonese, G., Da Deppo, V., Davidsson, B., Debei, S., De Cecco, M., Deller, J., Feaga, L. M., Ferrari, M., Fornasier, S., Fulle, M., Gicquel, A., Gillon, M., Green, S. F., Groussin, O., Gutiérrez, P. J., Hofmann, M., Hviid, S. F., Ip, W.-H., Ivanovski, S., Jorda, L., Keller, H. U., Knight, M. M., Knollenberg, J., Koschny, D., Kramm, J.-R., Kührt, E., Küppers, M., Lamy, P. L., Lara, L. M., Lazzarin, M., Lòpez-Moreno, J. J., Manfroid, J., Epifani, E. M., Marzari, F., Naletto, G., Oklay, N., Palumbo, P., Parker, J. W., Rickman, H., Rodrigo, R., Rodrìguez, J., Schindhelm, E., Shi, X., Sordini, R., Steffl, A. J., Stern, S. A., Thomas, N., Tubiana, C., Weaver, H. A., Weissman, P., Zakharov, V. V., Taylor, M. G. G. T., 2016, The 2016 Feb 19 outburst of comet 67P/CG: an ESA Rosetta multi-instrument study, Monthly Notices of the Royal Astronomical Society, 462, S220

- Behar, E., Lindkvist, J., Nilsson, H., Holmström, M., Stenberg-Wieser, G., Ramstad, R., **Götz, C.**, 2016, Mass-loading of the solar wind at 67P/Churyumov-Gerasimenko. Observations and modelling, Astronomy & Astrophysics, 596, A42

- Madanian, H., Cravens, T. E., Burch, J., Goldstein, R., Rubin, M., Nemeth, Z., **Goetz, C.**, Koenders, C., Altwegg, K., 2017, The Astronomical Journal, 153, 30

- Volwerk, M., Jones, G. H.;, Broiles, T., Burch, J., Carr, C., Coates, A. J., Cupido, E., Delva, M., Edberg, N. J. T., Eriksson, A., **Goetz, C.**, Goldstein, R., Henri, P., Madanian, H., Nilsson, H., Richter, I., Schwingenschuh, K., Stenberg Wieser, G.,

Glassmeier, K. H., 2017, Current sheets in comet 67P/Churyumov-Gerasimenko's coma, Journal of Geophysical Research: Space Physics, 122, 3308-3321

- Vigren, E.;, Andre, M., Edberg, N. J. T., Engelhardt, I. A. D., Eriksson, A. I., Galand, M., **Goetz, C.**, Henri, P., Heritier, K., Johansson, F. L., Nilsson, H., Odelstad, E., Rubin, M., Stenberg-Wieser, G., Tzou, C. -Y., Vallières, X., 2017, Effective ion speeds at ~200-250 km from comet 67P/Churyumov-Gerasimenko near perihelion, Monthly Notices of the Royal Astronomical Society, 469, S142-S148

- Nilsson, H., Stenberg Wieser, G., Behar, E., Gunell, H., Wieser, M., Galand, M., Simon Wedlund, C., Alho, M., **Goetz, C.**, Yamauchi, M., Henri, P., Odelstad, E., Vigren, E., 2017, Evolution of the ion environment of comet 67P during the Rosetta mission as seen by RPC-ICA, Monthly Notices of the Royal Astronomical Society, 469, S252-S261

- Henri, P., Vallières, X., Hajra, R., **Goetz, C.**, Richter, I., Glassmeier, K. H., Galand, M., Rubin, M., Eriksson, A. I., Nemeth, Z., Vigren, E., Beth, A., Burch, J. L., Carr, C., Nilsson, H., Tsurutani, B., Wattieaux, G., 2017, Diamagnetic region(s): structure of the unmagnetized plasma around Comet 67P/CG, Monthly Notices of the Royal Astronomical Society, 469, S372-S379

- Behar, E., Nilsson, H., Alho, M., **Goetz, C.**, Tsurutani, B., 2017, The birth and growth of a solar wind cavity around a comet - Rosetta observations, Monthly Notices of the Royal Astronomical Society, 469, S396-S403

- Stenberg Wieser, G., Odelstad, E., Wieser, M., Nilsson, H., **Goetz, C.**, Karlsson, T., Andre, M., Kalla, L., Eriksson, A. I., Nicolaou, G., Simon Wedlund, C., Richter, I., Gunell, H., 2017, Investigating short-time-scale variations in cometary ions around comet 67P, Monthly Notices of the Royal Astronomical Society, 469, S522-S534

- Timar, A., Nemeth, Z., Szego, K., Dosa, M., Opitz, A., Madanian, H., **Goetz, C.**, Richter, I., 2017, Modelling the size of the very dynamic diamagnetic cavity of comet 67P/Churyumov-Gerasimenko, Monthly Notices of the Royal Astronomical Society, 469, S723-S730

- Witasse, O., Sanchez-Cano, B., Mays, M. L., Kajdic, P., Opgenoorth, H., Elliott, H. A., Richardson, I. G., Zouganelis, I., Zender, J., Wimmer-Schweingruber, R. F., Turc, L., Taylor, M. G. G. T., Roussos, E., Rouillard, A., Richter, I., Richardson, J. D., Ramstad, R., Provan, G., Posner, A., Plaut, J. J., Odstrcil, D., Nilsson, H., Niemenen, P., Milan, S. E., Mandt, K., Lohf, H., Lester, M., Lebreton, J. -P., Kuulkers, E., Krupp, N., Koenders, C., James, M. K., Intzekara, D., Holmstrom, M., Hassler, D. M., Hall, B. E. S., Guo, J., Goldstein, R., **Goetz, C.**, Glassmeier, K. H., Genot, V., Evans, H., Espley, J., Edberg, N. J. T., Dougherty, M., Cowley, S. W. H., Burch, J., Behar, E., Barabash, S., Andrews, D. J., Altobelli, N., 2017, Interplanetary coronal mass ejection observed at STEREO-A, Mars, comet 67P/Churyumov-Gerasimenko, Saturn, and New Horizons en route to Pluto: Comparison of its Forbush decreases at 1.4, 3.1, and 9.9 AU, Journal of Geophysical Research: Space Physics, 122, 7865-7890

- Hajra, R., Henri, P., Vallieres, X., Galand, M., Héritier, K., Eriksson, A. I., Odelstad, E., Edberg, N. J. T., Burch, J. L., Broiles, T., Goldstein, R., Glassmeier, K. H., Richter, I., **Goetz, C.**, Tsurutani, B. T., Nilsson, H., Altwegg, K., Rubin, M., 2017, Impact of a cometary outburst on its ionosphere. Rosetta Plasma Consortium observations of the outburst exhibited by comet 67P/Churyumov-Gerasimenko on 19 February 2016, Astronomy & Astrophysics, 607, A34

- Hajra, R., Henri, P., Vallières, X., Moré, J., Gilet, N., Wattieaux, G., **Goetz, C.**, Richter, I., Tsurutani, B. T., Gunell, H., Nilsson, H., Eriksson, A. I., Nemeth, Z., Burch, J. L., Rubin, M., 2018, Dynamic unmagnetized plasma in the diamagnetic cavity around comet 67P/Churyumov-Gerasimenko, Monthly Notices of the Royal Astronomical Society, 475, 4140

- Madsen, B., Wedlund, C. S., Eriksson, A., **Goetz, C.**, Karlsson, T., Gunell, H., Spicher, A., Henri, P., Vallières, X., Miloch, W. J., 2018, Extremely Low-Frequency Waves Inside the Diamagnetic Cavity of Comet 67P/Churyumov-Gerasimenko, Geophysical Research Letters, 45, 3854

- Berčič, L., Behar, E., Nilsson, H., Nicolaou, G., Wieser, G. S., Wieser, M., **Goetz, C.**, 2018, Cometary ion dynamics observed in the close vicinity of comet 67P/Churyumov-Gerasimenko during the intermediate activity period, Astronomy & Astrophysics, 613, A57

- Engelhardt, I. A. D., Eriksson, A. I., Stenberg Wieser, G., **Goetz, C.**, Rubin, M., Henri, P., Nilsson, H., Odelstad, E., Hajra, R., Vallières, X., 2018, Plasma density structures at comet 67P/Churyumov-Gerasimenko, Monthly Notices of the Royal Astronomical Society, 477, 1296

- Behar, E., Nilsson, H., Henri, P., Berčič, L., Nicolaou, G., Stenberg Wieser, G., Wieser, M., Tabone, B., Saillenfest, M., **Goetz, C.**, 2018, The root of a comet tail: Rosetta ion observations at comet 67P/Churyumov-Gerasimenko, Astronomy & Astrophysics, 616, A21

- Nilsson, H., Gunell, H., Karlsson, T., Brenning, N., Henri, P., **Goetz, C.**, Eriksson, A. I., Behar, E., Wieser, G. S., Vallières, X., 2018, Size of a plasma cloud matters. The polarisation electric field of a small-scale comet ionosphere, Astronomy & Astrophysics, 616, A50

- Hajra, R., Henri, P., Myllys, M., Héritier, K. L., Galand, M., Wedlund, C. S., Breuillard, H., Behar, E., Edberg, N. J. T., **Goetz, C.**, Nilsson, H., Eriksson, A. I., Goldstein, R., Tsurutani, B. T., Moré, J., Vallières, X., Wattieaux, G., 2018, Cometary plasma response to interplanetary corotating interaction regions during 2016 June - September: a quantitative study by the Rosetta Plasma Consortium, Monthly Notices of the Royal Astronomical Society, 2064

Tagungsbeiträge

- Goetz, C., Der Singende Komet - Eine Statistik, IGEP Oberseminar, Braunschweig, 07/2015 (Vortrag)
- Goetz, C., et al., Polarisation Properties of Low-Frequency Waves in the Inner Coma of Comet 67P/Churyumov-Gerasi"-menko, EPSC 2015, Nantes, 09/2015 (Vortrag)
- Goetz, C., et al., Evidence of Inhomogeneous Coma Composition at 67P/Churyumov-Gerasimenko, AGU Fall Meeting 2015, San Francisco, 12/2015 (Poster)
- Goetz, C., et al., First Detection of a Diamagnetic Cavity at 67P/Churyumov-Gerasimenko, AGU Fall Meeting 2015, San Francisco, 12/2015 (Vortrag)
- Goetz, C., The diamagnetic cavity - What I know so far, RPC Team Meeting Uppsala, Uppsala, 02/2016 (Vortrag)
- Goetz, C., et al., Properties of the Diamagnetic Cavity at Comet 67P/Churyumov-Gerasimenko, ESLAB 2016, Leiden, 03/2016 (Vortrag)
- Goetz, C., et al., Magnetic Field on the Nightside of Comet 67P, RPC Team Meeting Frankfurt, Frankfurt, 05/2016 (Vortrag)
- Goetz, C., et al., Plasma on the Nightside of Comet 67P, Rosetta SWT, London, 06/2016 (Vortrag)
- Goetz, C., Komet am Schreibtisch, JDPG Braunschweig, Braunschweig, 06/2016 (Vortrag)
- Goetz, C., Update on the diamagnetic cavity, RPC Team Meeting London, London, 09/2016 (Vortrag)
- Goetz, C., Summary of diamagnetic cavity observations with RPC-MAG, University of Michigan Seminar, Ann Arbor, 09/2016 (eingeladener Vortrag)
- Goetz, C., A comet's life, End of Mission Press Conference, Darmstadt, 09/2016 (Vortrag)
- Goetz, C., et al., A review of the magnetic field at comets, Comets 2016, Toulouse, 11/2016 (Vortrag)
- Goetz, C., CIR impact on the cometary plasma environment, ICA Team Meeting, Kiruna, 01/2017 (Vortrag)
- Goetz, C., The singing comet and other stories, IWF Seminar, Kiruna, 01/2017 (eingeladener Vortrag)
- Goetz, C., CIR impact on the cometary plasma environment, IWF Seminar, Graz, 02/2017 (Vortrag)
- Goetz, C., What has Rosetta ever done for us?, Magnetometer Workshop Vilm, Rügen, 04/2017 (Vortrag)

- Goetz, C., Mysteries of the plasma environment, Magnetometer Workshop Vilm, Rügen, 04/2017 (Vortrag)
- Goetz, C., et al., Evolution of the magnetic field at comet 67P/Churyumov-Gerasimenko, RPC Team Meeting Orléans, Orléans, 05/2017 (Vortrag)
- Goetz, C., A Review of Diamagnetic Regions in the Solar System, AOGS 2017, Singapur, 08/2017 (eingeladener Vortrag)
- Goetz, C., et al., Evolution of the magnetic field at comet 67P/Churyumov-Gerasimenko, EPSC 2017, Riga, 09/2017 (Vortrag)
- Goetz, C., A comet's life: a magnetic perspective, IWF Seminar, Graz, 10/2017 (Vortrag)
- Goetz, C., Why is the magnetic field behaving weirdly?, RPC Team Meeting Madrid, Madrid, 11/2017 (Vortrag)
- Goetz, C., A review of the magnetic field at 67P, ISSI Meeting, Bern, 11/2017 (Vortrag)
- Goetz, C., et al., (Over-)Reaction of the Cometary Plasma to Extreme Solar Wind Conditions, AGU Fall Meeting 2017, New Orleans, 12/2017 (Vortrag)
- Goetz, C., An update on the diamagnetic cavity, RPC Team Meeting Kiruna, Kiruna, 03/2018 (Vortrag)
- Goetz, C., Exploring a comet's magnetic signature in the solar wind, LPC2E Seminar, Orléans, 04/2018 (eingeladener Vortrag)
- Goetz, C., Exploring a comet's magnetic signature in the solar wind, Rosetta SWT, Rhodos, 05/2018 (eingeladener Vortrag)
- Goetz, C., Neues von 67P/Churyumov-Gerasimenko, IGeP Oberseminar, Braunschweig, 06/2018 (Vortrag)
- Goetz, C., et al., Magnetic Field at comet 67P/Churyumov-Gerasimenko, COSPAR 2018, Pasadena, 07/2018 (Vortrag)
- Goetz, C., et al., The infant bow shock: a new frontier at a weak activity comet, Rosetta SWT, Interlaken, 11/2018 (Vortrag)

Contents

Kurzzusammenfassung

Wenn sich ein Komet der Sonne nähert, sublimiert das Oberflächeneis und breitet sich im Raum aus. Diese Neutralgasteilchen werden ionisiert und sind somit ein Hindernis für den Sonnenwind. Da die Kometengase vor allem aus Wasser und Kohlenstoffdioxid bestehen, sind diese Ionen schwerer als die Sonnenwindprotonen, weshalb der Beschleunigungsprozess der kometaren Ionen auch als Massenbeladung bezeichnet wird. Die Interaktion der beiden Plasmen hängt von der heliozentrischen Distanz ab, da mit abnehmendem Abstand zur Sonne die Dichte der Ionen zunimmt.

Die Raumsonde Rosetta hat den Kometen 67P/Tschurjumov-Gerasimenko während eines Periheliondurchgangs begleitet und das Plasma vermessen.

Drei Interaktionsmoden werden unterschieden: schwach-, mittel- und stark-ausgasende Phase. In der ersten Phase sind die Plasmadichten klein und das Magnetfeld wird von niederfrequenten Wellen dominiert. In der mittleren Phase enstehen erste dezidierte Regionen. Wenn die kometaren Ionen beschleunigt werden, verlangsamt sich der Sonnenwind und wird schlussendlich komplett aus der inneren Region verdrängt. Diese Sonnenwindkavität wird von einer jungen, asymmetrischen Bugstoßwelle begrenzt. Das Magnetfeld wird stärker mit abnehmender Sonnenwindgeschwindigkeit und beginnt sich um die innerste Region zu legen. Abschließend ist die Plasmaumgebung in der starken Phase stark verändert. Die Interaktionsregion ist mehrere tausend Kilometer groß und besitzt eine Bugstoßwelle, Magnetfeldaufstau und Magnetfeldverformung, sowie eine feldfreie diamagnetische Kavität.

Die Magnetfeldstärke am Kometen wird von dem dynamischen Druck im Sonnenwind bestimmt. Während Intervallen mit hohen Drücken kann das Magnetfeld um einen Faktor von bis zu sechs ansteigen.

Die diamagnetische Kavität am Kometen 67P/Tschurjumov-Gerasimenko ist viel dynamischer als erwartet, sodass sie von Rosetta vermessen werden konnte. Die Größe nimmt mit der Gasproduktionsrate zu, und mit dem anströhmenden Magnetfeld ab. Ein Modell, das die Ionen-Neutralgasreibung in der inneren Koma benutzt um den Magnetfelddruck auszugleichen, konnte nicht bestätigt werden, da Plasmaparameter zeigen, dass die Ionen nicht durch Kollisionen an das Neutralgas gebunden sind.

Abstract

When a comet approaches the Sun, surface ices sublimate and escape into space. When these neutrals are ionised they present an obstacle to the solar wind flow. As most comet's volatiles are water and carbon dioxide, these ions are much heavier than the protons in the solar wind, hence the process of accelerating and incorporating the cometary ions is called mass-loading. With decreasing heliocentric distance the density of cometary ions increases and thus the interaction of the two plasmas heavily depends on the heliocentric distance and activity of the comet.

The Rosetta spacecraft followed comet 67P/Churyumov-Gerasimenko for an entire perihelion passage observing the evolution of the cometary plasma.

Three interaction regimes are distinguished: the weakly, intermediately and strongly active stages. During the weak stage the plasma densities are low and the magnetic field is dominated by ultra-low-frequency waves. In the intermediately active stage, first boundaries start to emerge. As the cometary ions are accelerated, the solar wind is deflected and ultimately excluded from the inner regions of the interaction region. This solar wind cavity may be bounded by an infant bow shock that is highly asymmetric. The magnetic field magnitude increases with the increasing deceleration of the solar wind electrons and much more so along the stagnation streamline meaning that the magnetic field lines start to drape around the inner coma. Lastly, the strongly active comet has a plasma environment that is heavily modified. With a fully developed bow shock, magnetic field pile-up, draping and the formation of the field-free diamagnetic cavity, the cometary environment can extend several thousand kilometers from the nucleus.

The magnetic field magnitude at the comet is modulated by the solar wind dynamic pressure. During solar wind events with high dynamic pressure the magnetic field increases up to a factor of six.

The diamagnetic cavity at 67P/Churyumov-Gerasimenko is much more dynamic than expected, so much so that its extent was large enough to be measurable by Rosetta. A close investigation of the measurements shows that the diamagnetic cavity expands with gas production rate and contracts with higher upstream magnetic field. A model using the ion-neutral friction in the inner coma to balance the magnetic pressure at the boundary of this region cannot be applied for this comet, as plasma parameters indicate that the ions are not collisionally coupled to the neutrals.

1 Comets and the Rosetta Mission

Comets have inspired humanity for thousands of years, first seen by eye from Earth and in recent years explored in-situ by spacecraft. In ancient times, they were viewed as omens from the gods and believed to alter the course of history (see Fig. 1.1). We now know that comets are small bodies with impressive dust and plasma tails that can be millions of kilometers long and visible by observers several AU away. The age of space plasma physics was launched by the discovery that the plasma tail of comets was always directed anti-sunward, which led first Biermann (1951, 1952) and later Alfvén (1957) to introduce the idea of the solar wind as a flow of charged particles and magnetic field expanding from the Sun. The perihelion passage of Halley's comet in 1986 inspired multiple space agencies to send spacecraft to the comet and investigate its properties and the shape and form of the plasma surrounding it and preliminary artificial comet experiments were conducted in the Earth's magnetosphere. The findings from those missions were supplemented by ground observations and visits to other comets in the decade following the apparition of Halley's comet. But without a doubt the most influential source of knowledge of comets and their plasma stems from the European Space Agency's Rosetta mission, an ambitious project to follow comet 67P/Churyumov-Gerasimenko along its orbit through an entire perihelion passage and observe the changes of the comet itself and the cometary plasma and its interaction with the solar wind. The new discoveries following this mission are a cornerstone of cometary research and will inspire investigations for years to come.

This work will address new findings based on measurements by the plasma instruments

Figure 1.1.: "Comet coin" minted by Augustus shortly after Julius Cesar's death. The Julian comet, one of the brightest comets in ancient times, is depicted on the back of the coin. It was seen by the people as a sign of Cesar's soul ascending to the heavens. Its apparition during the games that Augustus held in honor of Cesar was seen as a good omen and ultimately sealed the fate of Markus Antonius and led to the ascension of Augustus to emperor (Gurval 1997).

onboard Rosetta and relate them to established models and theories. It aims to give a summary of the structure of the plasma in general and the magnetic field in particular and give a concise view of processes in the coma.

1.1. Comets

1.1.1. Comet populations and the nucleus

According to the Encyclopedia Britannica, a comet is "a small body orbiting the Sun with a substantial fraction of its composition made up of volatile ices. When a comet comes close to the Sun, the ices sublimate (go directly from the solid to the gas phase) and form, along with entrained dust particles, a bright outflowing atmosphere around the comet nucleus known as a coma."[1] The gases and dust escape the nucleus and form a coma and a bright tail, the existence of which is usually used to distinguish a comet from non-active asteroids. The cometary tail is three-fold: a dust tail, a dust trail and a plasma tail, that point into different directions, depending on the orbit of the comet. This originally gave comets their name; the greek word "$\kappa o \mu \eta \tau \eta \varsigma$" translates as long-haired, and describes the long, bright tails that were observable by eye and fascinated people long before a comet had ever been visited. Although comets were historically often regarded as harbingers of doom, they do not pose any thread to Earth and its inhabitants. The dust trail of comets is responsible for yearly meteor showers like the perseids, but the fear of cometary gases reaching toxic concentrations in the atmosphere was unfounded.

In general, comets are separated into groups according to their origin: comets orbiting in the ecliptic usually originate in the Kuiper belt (a region outside Neptune's orbit that is confined to the ecliptic), main-belt comets in the asteroid belt and comets from the Oort cloud typically have high eccentricities (Dones et al. 2015). The most visited comets are those from the Kuiper belt, simply because they tend to have periodic orbits and come close to the Sun and Earth. These types of comets are divided into sub-categories that can be quantified by the Tisserand parameter with regard to a certain planet. As the Tisserand parameter is a measure of how much a body is affected by another body, Jupiter with its large mass plays the most important role here. Jupiter family comets have been captured by Jupiter at some point in their history and are now on orbits coupled to Jupiter's (Coates and Jones 2009). This usually implies orbital periods below 20 years and low inclinations of the orbit. In contrast to that, Halley-type comets usually have orbital periods between 20 and 200 years, inclinations as high as 90°, and their orbits can either be pro- or retrograde (Duncan 2008). Long-period comets have orbital periods above 200 years and can have any orbital configuration, as they often originate from the Oort cloud, which is not confined to the ecliptic.

The nucleus of a comet is a mixture of dust and ices, that is often non-spherical and even bi-lobal (see Fig. 1.2) and up to a few hundred kilometers in diameter. Local features such as cliffs, hills, craters, and pits dominate the pictures of nuclei. The ice on the surface and in the subsurface is mostly H_2O- and CO_2-ice in a mixture with silicates and organics (Levasseur-Regourd et al. 2018). The most abundant elements are carbon, nitrogen, sodium, silicon and oxygen, which are well known to be the constituents of rocky

[1] https://www.britannica.com/science/comet-astronomy

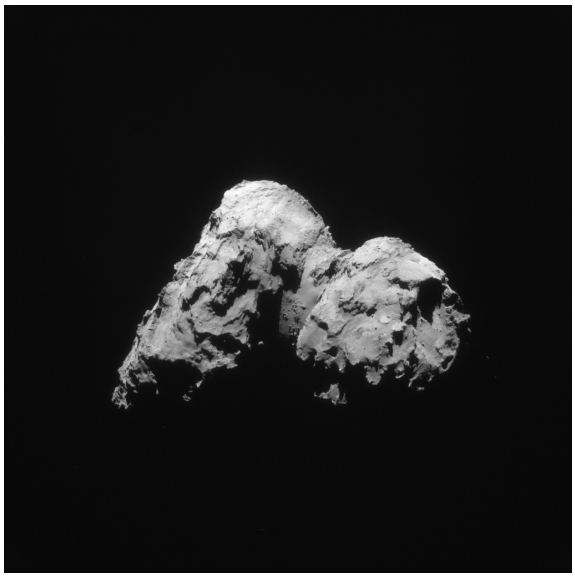

Figure 1.2.: The nucleus of comet 67P/Churyumov-Gerasimenko as observed by the Rosetta spacecraft on January 17, 2016. Due to its rubber-duck-shape the smaller lobe (right) is often referred to as the head, whereas the larger lobe is called the body of the nucleus (Copyright: ESA/Rosetta/NavCam).

materials in the solar system like asteroids and the moon. Consequently the albedo of comets is typically very low (< 0.1). Although the dust to ice ratio and the dust to gas ratio are still under debate, it is nowadays commonly understood that comets are mostly made of dust, making them icy-dustballs instead of the previously thought dusty-snowballs (Fulle et al. 2017). The nucleus itself is homogeneous and does not have any large cavities or inhomogeneities in the subsurface and all visited comets are non-magnetized (Auster et al. 2015, Pätzold et al. 2016).

The composition and structure of comets are especially interesting for solar system formation theories. Comets are too small to compress due to their own gravity, and Aluminium-26 heating does not contribute to the metamorphism of the rocks and ices that constitute the nucleus. They spend most of their lifetime far away from the Sun, so that insolation does not affect the nucleus, making them the most unaltered leftovers from the early solar system (Davidsson et al. 2016, Blum et al. 2017).

The detection of fluffy dust aggregates, i.e. aggregates with extremely high porosities, indicates that comets are formed through low-velocity accretion of sub-micrometer particles. The slow growth produces fractal aggregates that are compacted by collisions until a size limit is reached around 1 mm. Consequently other mechanisms like the streaming instability (Johansen et al. 2007) and subsequent gravitational collapse, or collisional coagulation (Davidsson et al. 2016) are needed for further growth.

The formation mechanism also has implications for cometary activity. The mixing of ice and dust on the surface and in the sub-surface of the comet dictate the amount and geometry of the outgassing. The three major sources of outgassing are jets, outbursts and diffuse outgassing, illustrated in Fig. 1.3. Surface changes contribute to activity, e. g. a collapsing cliff has been identified as a source of a major outburst of cometary materials (Pajola et al. 2017). Active regions on the comet feed daily reoccurring jets of

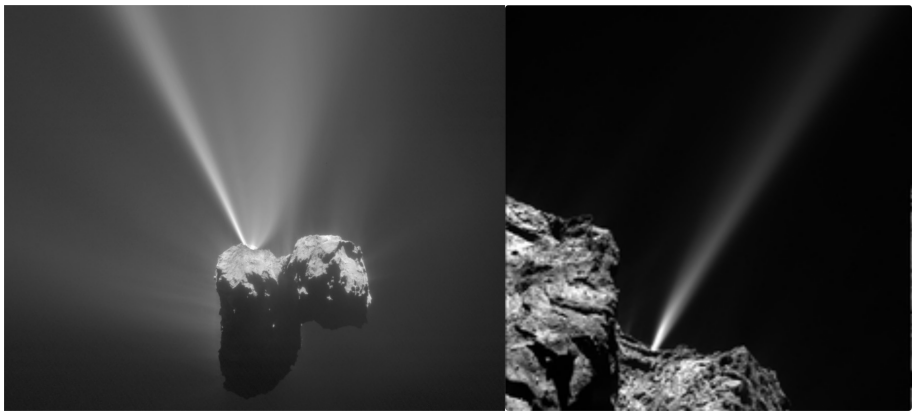

Figure 1.3.: The three kinds of outgassing illustrated in two events imaged by Rosetta. The bright feature in the left panel is a jet that reoccurred during 67P's perihelion, with diffuse outgassing seen as brighter coma features around the entire nucleus. The right hand panel shows an outburst on July 29, 2015 (Copyright: ESA/Rosetta/MPS for OSIRIS Team MPS/UPD/LAM/IAA/SSO/INTA/UPM/DASP/IDA).

cometary materials, while most of the gas is released over the entirety of the illuminated area (Kramer et al. 2015).

1.1.2. Cometary spacecraft missions

To this day eight comets have been visited by six spacecraft. Deep Impact visited comet 9P/Tempel 1 and deployed an impactor that created a small crater on the comet. Observations of the impact, the ejecta cloud and the crater were used to determine the composition of the upper layer of dust (Nagdimunov et al. 2014). The Stardust spacecraft also passed 9P/Tempel 1 and observed that the crater had substantially altered the surface features. It was also speculated that due to dust coverage the crater shrunk to a third of its original size during one perihelion passage (Schultz et al. 2013). After Deep Space 1 completed its primary mission, the characterization of an asteroid, it was rerouted to comet 19P/Borelly. It passed the comet with a minimum distance of 2171 km (Richter et al. 2011). The camera onboard acquired detailed images of the nucleus and found that it was the shape of a bowling pin with many different terrains on the surface. The camera also caught several dust jets, which are stationary structures of enhanced dust density in the coma (Soderblom et al. 2002).

In addition to their flybys of comet 1P/Halley (1P) the International Cometary Explorer (ICE) and Giotto flew by comet 21P/Giacobini-Zinner and 26P/Grigg-Skjellerup respectively (e. g. Neubauer et al. 1986, 1993)

Stardust's original target was 81P/Wild 2, where it collected samples from the comet's dust and gas coma. The extended mission of Deep Impact allowed for it to visit comet 103P/Hartley as well as observe comet ISON from afar. The former of which is a hyperactive comet, meaning that the percentage of the surface that is active is far greater than the usual values below 10% (A'Hearn et al. 2011). All of the observed nuclei have pronounced bi-lobate shapes (Harker et al. 2018). The missions Deep Impact and Stardust especially contribute to our understanding of the formation of cometary nuclei and their properties by gaining insight into the composition of the nucleus.

The spacecraft that visited comet 1P/Halley and 67P/Churyumov-Gerasimenko (67P) are described in the following, as they provide the most information on the plasma interaction, which is the subject of this work. The Rosetta mission and comet 67P shall then be described in more detail in section 1.2.

The Halley Armada

The expected reappearance of comet Halley in 1986 inspired many different space agencies to send spacecraft to investigate. In the years 1985 and 1986 a total of seven spacecraft performed flybys of the comet and its tail, assisted by a multitude of ground based observations. Due to the comet's retrograde orbit, the flyby speeds of the spacecraft were very high ($\sim$ 70 km/s) and the flybys were all conducted in March 1986, when the orbit of 1P crossed the Earth's orbit (Reinhard 1986). Vega I and Vega II were russian spacecraft originally targeted for Venus that were redirected to 1P after their successful Venus mission. They carried instruments to determine composition and thermal properties of the nucleus as well as the dust in the coma (Sagdeev et al. 1986). Pioneer Venus Orbiter (PVO) observed comet Halley remotely from its orbit around Venus taking Lyman-α images of the hydrogen coma (Smyth et al. 1991). The ICE was repurposed from the International Sun-Earth Explorer (ISEE) mission and transited not only Halley but also comet 21P/Giacobini-Zinner's tail (Tsurutani and Smith 1986, Cowley 1987). Pioneer 7 was launched in 1966 and was designed to measure the solar wind in a heliocentric orbit near 1 AU and came within $\sim 1 \times 10^6$ km of comet 1P.

Suisei was a Japanese mission that flew by Halley with a distance of 150000 km that was optimized with data from a previous spacecraft, Sakigake, which passed the comet with 7×10^6 km distance, but provided information that helped constrain Suisei's trajectory. Sakigake was designed to investigate the solar wind in front of the comet, whereas Suisei also had instrumentation for photometry of the comet (Hirao and Itoh 1987).

By far the most successful mission was ESA's Giotto (Reinhard 1987), which reached a closest approach distance of 600 km and was the first spacecraft to take a detailed visible light picture of the nucleus of a comet. The instruments onboard allowed for measurements of the composition of the dust and gas in the coma, as well as the nucleus and detailed studies of the plasma (including the magnetic field) in the coma. However, a dust impact rendered the cameras inoperational early in the flyby and the charged particle instruments for the protons also stopped working before closest approach.

1.2. The Rosetta mission

1.2.1. The spacecraft

The Rosetta mission (Glassmeier et al. 2007a) consists of two spacecraft: the Rosetta orbiter (Rosetta) and the lander Philae, it is a European Space Agency (ESA) cornerstone mission in the Horizon 2000 program and has contributions from the National Aeronautics and Space Administration (NASA). The spacecraft was launched in 2004 from the European spaceport in Kourou. From there it performed flybys at Earth (2005, 2007, 2009) and Mars (2007) to gain the required velocity to rendezvous with the comet. In 2008 the spacecraft performed a flyby at asteroid 2867 Steins and in 2010 it passed asteroid

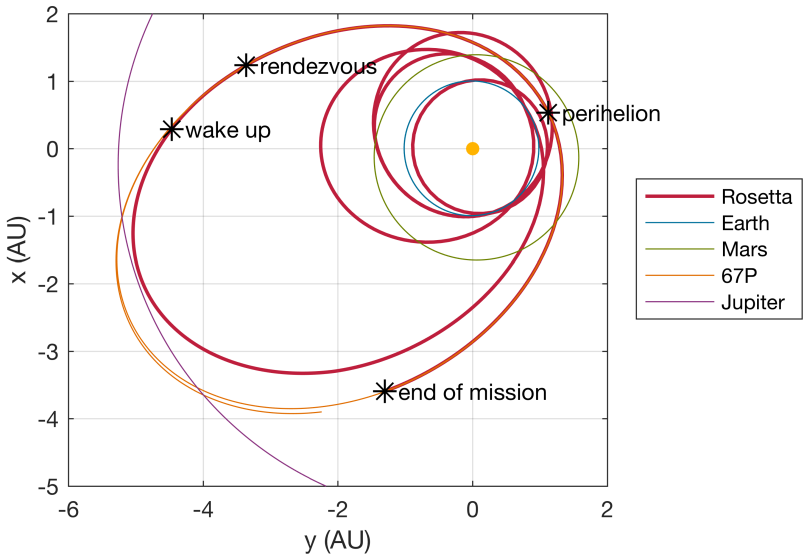

Figure 1.4.: Trajectory of the Rosetta spacecraft and comet 67P in the solar system. The trajectory shows the timespan from launch on March 2, 2004 to the end of mission on September 30, 2016. The orbits of Earth, Mars and Jupiter are shown for reference.

21 Lutetia. In 2011 it was required to put the spacecraft into hibernation to conserve energy, as the power output of the solar array was not sufficient to operate the spacecraft. An internal alarm clock was set to reactivate the spacecraft on January 20, 2014, when it was successfully reactivated for the main mission phase. After periods of commissioning and instrument testing, Rosetta rendezvoused with comet 67P on August 6, 2014 with distances of below 100 km to the nucleus. Rosetta's journey from launch to the end of mission is shown in Fig. 1.4.

Although only detected in 1969 by astronomers Klim Ivanovich Churyumov and Svetlana Ivanovna Gerasimenko, 67P is by far the best explored comet, because the Rosetta mission orbiter spent over two years observing it and the Rosetta mission lander Philae made measurements on the surface. Comet 67P was selected as the target for the Rosetta mission after a change of the launch window meant that the original target comet 46P/Wirtanen had to be abandoned (Glassmeier et al. 2007a).

67P is a Jupiter family comet with an orbital period of 6.45 years, perihelion of 1.24 AU, and aphelion of 5.68 AU. Its orbit is prograde with an inclination of 7° (European Space Agency 2018). The strange "duck" shape (see Fig. 1.2) is a result of a slow collision of two smaller cometesimals, that circled each other until they eventually stuck together (Massironi et al. 2015). With a mass of $\sim 10^{10}$ kg and a density of 533 kg/m^3 the porosity of the nucleus is around 75% (Pätzold et al. 2016).

The gas production rate varies from 1×10^{25} molecules/s to around 5×10^{28} molecules/s depending on the intensity of the insolation. As the nucleus is cratered and consists of many cliffs and shaded regions, the neutral density above the two hemispheres also varies significantly (Hansen et al. 2016). For a more detailed description see section 2.2.

The original mission design foresaw an end of mission on December 31, 2015, but with a fully functioning spacecraft, the mission was extended to September 30, 2016. This was in line with the science goals to study the evolution of the comet, not only on its

inbound journey around the Sun, but also on its outbound leg and increased the dataset significantly.

The trajectory of the spacecraft during the active mission was dictated by the comet's low gravitational field as well as the dust concentration in the coma. During the early mission phases, it was crucial to get as close as possible, so that images of the surface could be taken at high resolution. These images were then used to select a landing site for the lander Philae.

On November 12, 2014, the lander was deployed and slowly descended to the surface while Rosetta continued to orbit the comet and served as relay station for the lander data. Despite three separate mechanisms to anchor the lander to the surface, it bounced off and continued to tumble above the surface, before finally coming to rest in a dark crevice (Heinisch et al. 2017). There, the instruments on Philae performed as many measurements as possible before the primary battery was drained and all contact with the lander was lost on November 15, 2014.

After lander delivery Rosetta began its primary science phase, studying the comet and its surroundings in detail. All instruments and their science goals are listed in Tab. 1.1 and their location on the spacecraft body is shown in Fig. 1.5. With this instrument suite and supportive ground based observations, Rosetta was capable to fulfill its main scientific objective, "to investigate the origin of our solar system by studying the origin of comets" (Glassmeier et al. 2007a). In general, three main topics were investigated by the instruments:

1. nucleus properties and processes: CONSERT, COSIMA, MIRO, OSIRIS, RSI, VIRTIS

2. dust and gases in the coma: ALICE, GIADA, MIDAS, OSIRIS, ROSINA, VIRTIS, ground based observations

3. plasma: RPC, ROSINA, ALICE, ground based observations

Although all investigations are fascinating, only the third topic, plasma, will be discussed in this work. Therefore, the reader is referred to review articles on the two other topics, for example Boehnhardt et al. (2017) for Philae science, Snodgrass et al. (2017) for ground based observations, Altwegg (2018) for gas composition, Blum et al. (2017) for nucleus formation, and Mannel et al. (2016) for dust.

The instruments' requirements paired with the nucleus' gravity and dust environment dictated the distance of the spacecraft to the comet. Since the gravitation is not large enough to keep the spacecraft on conventional elliptical orbits (Pätzold et al. 2016), the trajectory is highly irregular, with triangular orbits and escape trajectories connected by orbit correction maneuvers. In addition, Rosetta navigates by sight, i. e. the spacecraft has two star trackers that capture pictures of the stellar background and compares them to internally stored star maps as well as a navigational camera for orientation with regards to the nucleus.

An overview of the spacecraft-nucleus distance is shown in Fig. 1.6. Mission milestones are marked and the comet-Sun distance R is also shown for reference. The trajectory usually followed an "as close as possible" approach, meaning the distance was minimal without endangering the spacecraft. Dangers include pointing errors due to gas drag and

Instrument	Scientific Goals	Publication
ALICE	Perform far-ultraviolet spectroscopy to determine the production rates of gases and spatial structure of the neutral coma.	Stern et al. (2007)
CONSERT	Study the deep interior of the cometary nucleus using radio waves.	Kofman et al. (2007)
COSIMA	Collect cometary dust and examine its composition using a time-of-flight mass spectrometer.	Kissel et al. (2007)
GIADA	Study the mass, size and momentum of dust grains in the dust coma.	Colangeli et al. (2007)
MIDAS	Collect cometary dust and study its structure using an atomic force microscope.	Riedler et al. (2007)
MIRO	Millimeter-submillimeter spectrometer instrument to study the thermal properties of the nucleus.	Gulkis et al. (2007)
OSIRIS	Image the nucleus to determine shape, rotation and surface features.	Keller et al. (2007)
ROSINA	In-situ measurement of the gaseous environment and its isotopic composition.	Balsiger et al. (2007)
RPC	Investigate the plasma environment of the comet.	Carr et al. (2007)
- ICA	Study the ion distribution function for ions of different masses.	Nilsson et al. (2007)
- IES	Examine the ion and electron energy and angle distribution.	Burch et al. (2007)
- LAP	Measure plasma parameters like density and electron temperature as well as the spacecraft potential.	Eriksson et al. (2007)
- MAG	Measure the magnetic field of the cometary plasma.	Glassmeier et al. (2007b)
- MIP	Study the electron density and temperature of the cometary plasma.	Trotignon et al. (2007)
RSI	Study the mass, bulk density and gravitational field of the nucleus.	Pätzold et al. (2007)
VIRTIS	Examine the composition of the coma and nucleus using micrometer imaging spectroscopy.	Coradini et al. (2007)

Table 1.1.: Overview of all Rosetta instruments and their scientific goals. For more details, see the given publication.

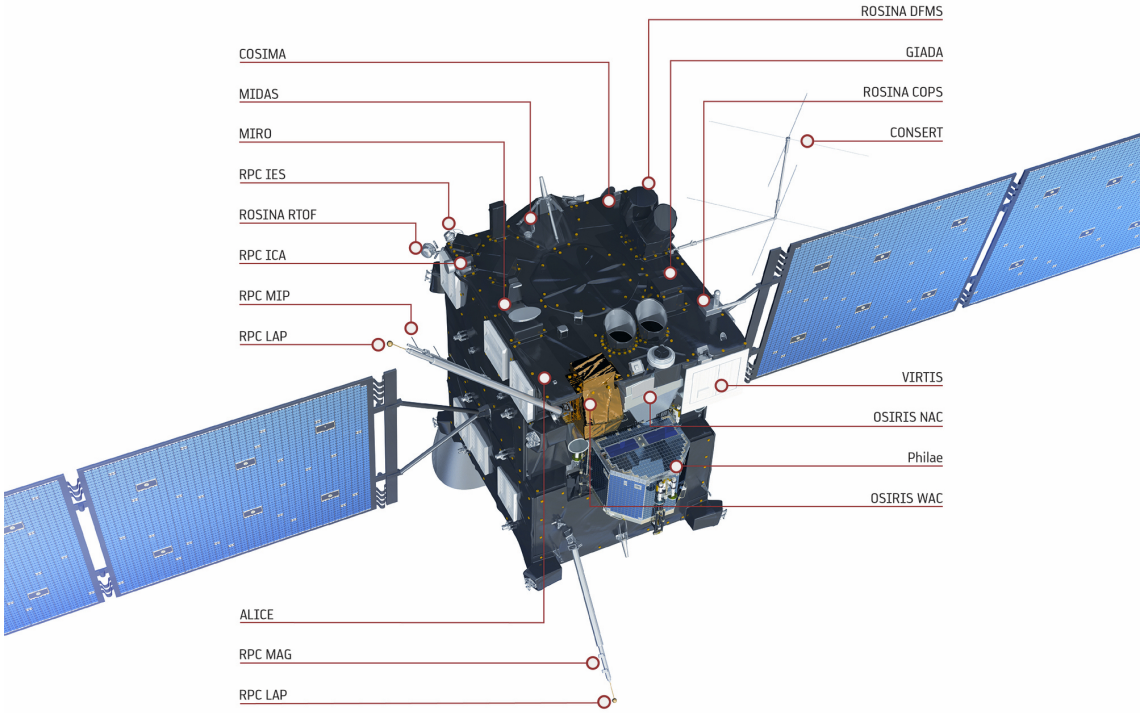

Figure 1.5.: The Rosetta spacecraft with scientific instruments marked by their abbreviations (Copyright: ESA/ATG medialab).

gravitational uncertainties as well as false star detections in the star tracker. An example for these dangers was the close flyby on March 28, 2015, where the dust background below 30 km height generated too many false star detections in the star tracker and prompted the spacecraft to go into "safe mode". In this mode all instruments are shut off, the spacecraft moved to 400 km distance and oriented the high gain antenna toward the last known position of the Earth. After this, the distances were increased to prevent a reoccurence of this potentially fatal event. Thus, the distance of Rosetta to the nucleus actually increased as the comet approached the Sun and produced more gas and dust.

Other scheduled maneuvers include the dayside and nightside excursions, two periods of time where Rosetta explored the far coma, once in Sun direction and once towards the comet's tail.

1.2.2. The Rosetta Plasma Consortium

To fulfill the mission objective regarding plasma investigations at a comet, Rosetta is equipped with five instruments that measure the plasma properties. Together with the Plasma Interface Unit (PIU), they form the Rosetta Plasma Consortium (RPC). Their location on the spacecraft is shown in Fig. 1.5, except for the PIU, which is located inside the spacecraft. As these instruments are the main source of data for this work, their capabilities and shortcomings are discussed in the following section.

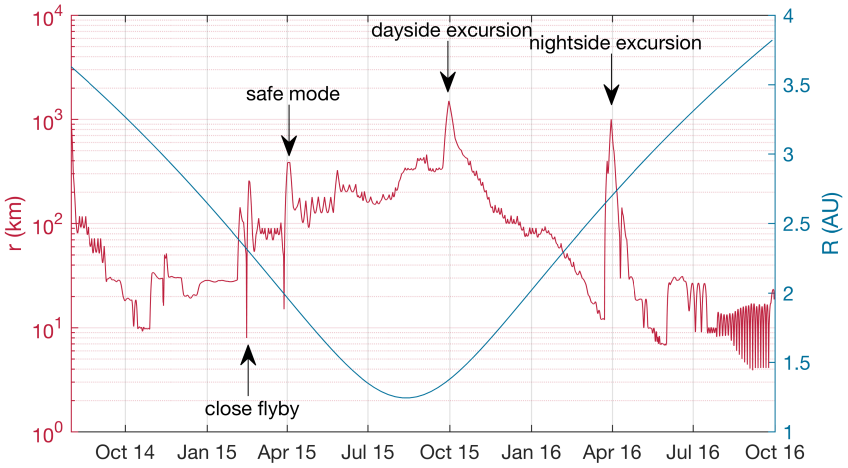

Figure 1.6.: Cometocentric distance of the Rosetta spacecraft (red) during the cometary phase of the mission and radial distance of 67P to the Sun (blue). Significant events during the mission are indicated by arrows.

Plasma Interface Unit (PIU)

The PIU is designed to facilitate the transmission of data and commands between Rosetta and the five RPC instruments (Carr et al. 2007). All commands for RPC go through the unit and are checked and validated there before being sent to the instruments. In return, the PIU collects all RPC science and housekeeping packages and sends them to the central Data Management System. A special provision is also made for the magnetometer data, which is filtered and packaged by the PIU instead of the magnetometer electronics themselves. The PIU also provides the power supply and management for all five RPC instruments, for more details see Carr et al. (2007).

Ion Composition Analyzer (ICA)

The Ion Composition Analyzer can measure the 3D energy distribution of ions with mass resolution (Nilsson et al. 2007). The field of view is 360° by 90° and the energy range is between 25 eV/q and 40 keV/q. In addition ICA has the capability to separate the mass of the incoming ions, which enables it to distinguish between protons, alpha particles, and heavy ions such as water and carbon dioxyde ions. Although a full sweep of the field of view and energy range takes 192 s, the instrument can also be operated in modes that have a higher time resolution with reductions in either angular or energy resolution. For example, the high-time resolution mode has a sampling time of 4 s, but the field of view is reduced to 360° by 5° and the energy range is only 0.3 eV/q to 82 eV/q. For more details see Stenberg Wieser et al. (2017) and Nilsson et al. (2007).

Ion and Electron Sensor (IES)

Complementary to ICA, the Ion and Electron Sensor (IES) can measure 3D energy distributions of ions, with an added electron sensor for 3D distributions of electrons. It has an energy range of 1 eV to 18 keV and a field of view of 360° by 90° for both electrons and

ions. Compared to ICA, the field of view is shifted and thus covers a different part of the sky, with some blockage by the spacecraft body and the high gain antenna (Clark et al. 2015). A full sweep of all energies and angles takes 128 s. For details see Burch et al. (2007).

Langmuir Probe (LAP)

The Langmuir Probe (LAP) on Rosetta consists of two metal spheres at the end of the two instrument booms. Depending on the mode, it can measure plasma density, electron temperature, plasma velocity, electric field variations, spacecraft potential and solar EUV flux (Eriksson et al. 2007). The two Langmuir probes are mounted on two booms, with spacecraft distances of 2.24 m and 1.64 m and a probe-probe separation of 5 m. This separation becomes important when measuring the drift velocity, as larger separations increase the measurement range. Due to high electron temperatures and densities at the comet, the spacecraft itself is charged and thus immersed in a spacecraft electric potential. This can be measured by LAP, but it also complicates the analysis of the data as a change in spacecraft potential also affects the current that can be collected by the Langmuir probe. For more details see Eriksson et al. (2007), Odelstad et al. (2015) and Odelstad et al. (2018).

Magnetometer (MAG)

The magnetometer (MAG) consists of two sensors that are mounted on one of the LAP booms, that measure the magnetic field vector at the comet (Glassmeier et al. 2007b). The two units are separated by 15 cm. The outboard magnetometer (OB) is located 1.5 m from the spacecraft. Both OB and the inboard sensor (IB) have the same configuration. The measurement range is ±16000 nT for each component and the maximal sampling frequency is 20 Hz for both sensors. MAG is usually run in either normal or burst mode, in normal mode OB has a sampling frequency of 20 Hz and IB of 1 Hz, in burst mode OB has a sampling frequency of 1 Hz and IB of $1/32$ Hz. The lower sampling frequencies are achieved by filtering and resampling the 20 Hz measurements, which is done by the PIU, before forwarding the data for transmission to the ground station. For more details see section 1.3.

Mutual Impedance Probe (MIP)

The Mutual Impedance Probe (MIP) uses a set of electrodes mounted on a boom to determine the electron density and temperature (Trotignon et al. 2007). As MIP uses the resonance of the plasma frequency, the measurement range changes with the Debye length of the plasma. If the plasma frequency is within the measurement frequency range, the time resolution is 2.5 s. MIP has two major modes: Short Debye Length (SDL) and Long Debye Length (LDL). The measurement range for LDL is larger, because it uses the far LAP sensor as a transmitter. However, for low Debye lengths SDL is preferred. For more details see Trotignon et al. (2007).

Cross-validation

Several of the RPC instruments measure the same properties and may be compared for cross-validation and cross-calibration. Additionally, the spacecraft potential that is measured by LAP is an important correctional factor in IES and ICA spectra. The spacecraft potential is the result of electric charges accumulating on the spacecraft, which can accelerate or decelerate the particles that are measured by IES and ICA, thus creating a shift in the measured energy and count rates proportional to the spacecraft potential. Knowledge of the spacecraft potential is therefore essential for the analysis of the energy spectra.

The electron temperatures and densities that are measured by LAP and MIP can also be cross-calibrated. This allows for more accurate (MIP) but higher time resolution (LAP) measurements. Also, LAP measurements can be used to access densities below the MIP threshold. However, some assumptions for the plasma still need to be made to correctly interpret the measurements.

ROSINA-COPS

Although not a part of RPC the Cometary Pressure Sensor (COPS), that is part of the ROSINA instrument suite, shall be discussed briefly. It can measure the neutral gas pressure and number density at the spacecraft location and thus provides important parameters for the plasma investigations (Balsiger et al. 2007). The measurement range is between 4×10^{-11} mbar and 10^{-5} mbar with a temporal resolution of 10 s. It should also be noted that high energy electrons interfere with the pressure measurements and increase the noise. For more details see Balsiger et al. (2007).

1.3. Calibrating the magnetic field data

The correct interpretation of magnetic field observations made by RPC-MAG requires that the offset of the measurements is determined within a few nanotesla. If the offset is not determined correctly, it will result in incorrect field magnitudes and directions and will make the data unusable.

Measuring the magnetic field in a plasma requires that the magnetometer is removed from any spacecraft source that produces a magnetic field, be it a constant background field from a permanent magnet or a spacecraft-current-induced field. Most of the time this is accomplished by attaching the sensor to a boom that points away from the spacecraft body. For some missions this boom is a couple of meters long, but for Rosetta only a 1.5 m-boom was possible. Thus there remains a significant contribution to the measured field from the spacecraft itself and its payload. Especially the thrusters and reaction wheels contribute significantly to the time varying background spacecraft field (Glassmeier et al. 2007b). Another source of error in the measurements is a temperature dependent response function of the sensor. The measurement can be described by:

$$\vec{B}_{meas} = \vec{B} + \vec{O_{sc}}(t) + \vec{O}_{sensor}(T). \tag{1.1}$$

The terms on the right hand side are the actual physical field, the time-dependent offset from the spacecraft and the temperature dependent offset of the sensor. This equation

assumes that any misalignment or sensitivity factors have been applied already. The offsets should already be determined on ground before and after integration of the sensor on the spacecraft, however, depending on the quality of the sensor, in-flight calibration also plays an important role.

There are several methods that have been previously used to determine the offsets of three-axis magnetometers:

1. Spin plane offset: if the spacecraft is spinning with a stable frequency at a fixed axis, the magnetic field offset in the two directions that lie in the spin plane is easily determined by minimizing the spin tone.

2. Hedgecock method: Alfvénic fluctuations in the solar wind have a well defined propagation direction that should on average be aligned with the magnetic field direction. Using a minimum variance analysis to determine the propagation direction of the wave gives the direction of the magnetic field vector and therefore an offset in that direction (Hedgecock 1975, Leinweber et al. 2008).

3. Mirror mode method: Highly compressive waves such as mirror modes usually have propagation directions that are orthogonal to the magnetic field direction. Thus, the maximum variance direction should be aligned with the magnetic field direction (Plaschke et al. 2017).

4. Cross-calibration: Using other instruments to determine the offset provides a wide variety of methods. For example, a second (scalar) magnetometer may be used to provide field values. Alternatively, information on plasma frequencies that depend on the magnetic field may be used to reconstruct the offset. This information may come from the magnetic field measurements themselves or other plasma instruments on the spacecraft.

5. Known field: if the spacecraft is crossing a region where the magnetic field value is known with reasonable accuracy, the remaining measured field may be attributed to the offset and can be used to retrieve it.

All methods are simplified when applied to spinning spacecraft, because only one component (the spin axis component) needs to be calibrated.

In the case of Rosetta, offset determination is very difficult, because only very few of the listed methods are applicable. Method 1 does not work as such, because Rosetta is three-axis stabilized, however a modified version can be used whenever the spacecraft is performing large angular slews. One example of this are grand circle scans that are done to provide the ALICE instrument with a wider field of view. However, the method is extremely limited, because the scans need to be as fast as possible and as large as possible to make sure that the offset is determined correctly. Method 2 requires that the spacecraft is measuring the magnetic field in the solar wind and detecting alfvénic fluctuations which is not the case here, as Rosetta is always in the plasma region at the comet that is modified by the presence of cometary ions. Method 3 is applicable and has been used to determine the offset (Plaschke et al. 2017), however this method needs long time intervals to achieve the necessary accuracy. In the mentioned publication a good result was only obtained using three days of data to determine one offset and therefore it is not able to describe the

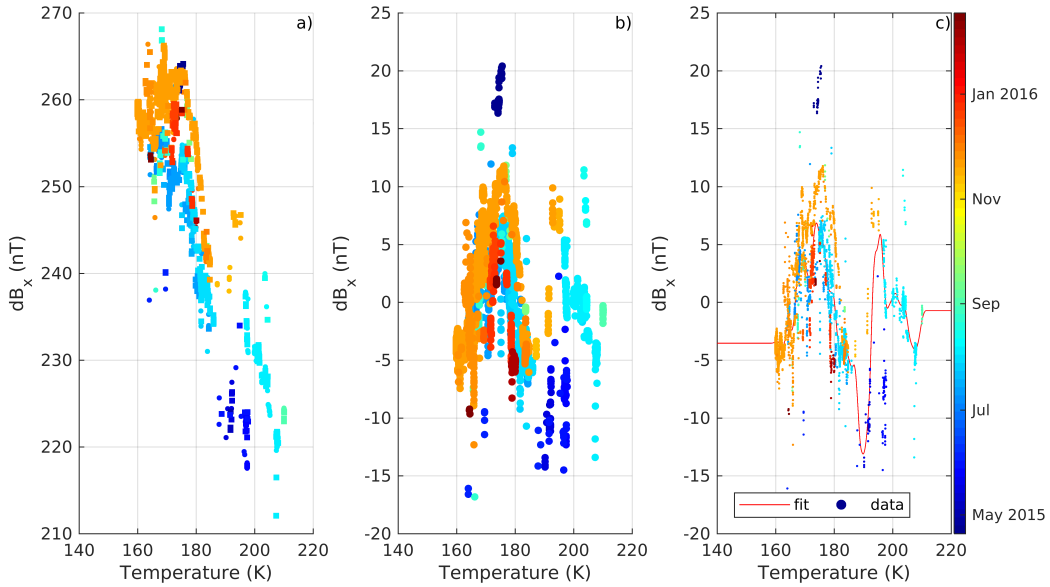

Figure 1.7.: Three stages of the magnetic field offset inside the diamagnetic cavity. All plots show the remaining field in the diamagnetic cavity as a function of sensor temperature and time (color coded) for the IB x-component. The left panel shows the initial situation before any offset correction. In the middle panel the first step of the calibration has been applied, and the remaining field is closer to zero. The right panel shows the interpolation of the remaining field as described in step two of the calibration procedure. Note the different scale of the y-axis in panel a).

short-time changes in e. g. temperature. Method 4 requires that other instruments provide information on the magnetic field magnitude, however Rosetta does not carry a scalar magnetometer and so far no suitable plasma fluctuations have been found to compare to other plasma instruments.

Therefore only method 5 remains. Fortunately, the spacecraft was located in the diamagnetic cavity for more than 15 hours in total over a span of eleven months. From observations and modeling it has been determined that the magnetic field inside the diamagnetic cavity is very close to zero, probably below 2 nT (see section 3). Therefore all components of the field should be close to zero in the diamagnetic cavity, and if they are not, the remaining field is the offset $\vec{O}_{sc}(t) + \vec{O}_{sensor}(T)$.

For the calibration, the residual field components inside the diamagnetic cavity were calculated. For every 32 s interval in the diamagnetic cavity one value was computed, because temperature values are only logged every 32 s. Fig. 1.7 shows the residual field of the x-component measured by the IB sensor over temperature for three stages during the calibration process. The process consists of a stage-wise improvement of the offset:

1. The offset depends on temperature and time, therefore the first step is to find a linear fit function in both time and temperature: $O = at + bT + c$, where a, b, and c are constants. This method takes into account a long term offset drift, under the assumption that the temperature dependence is also linear. As shown in Fig. 1.7, panels a) and b), this procedure already improves the residual field substantially.

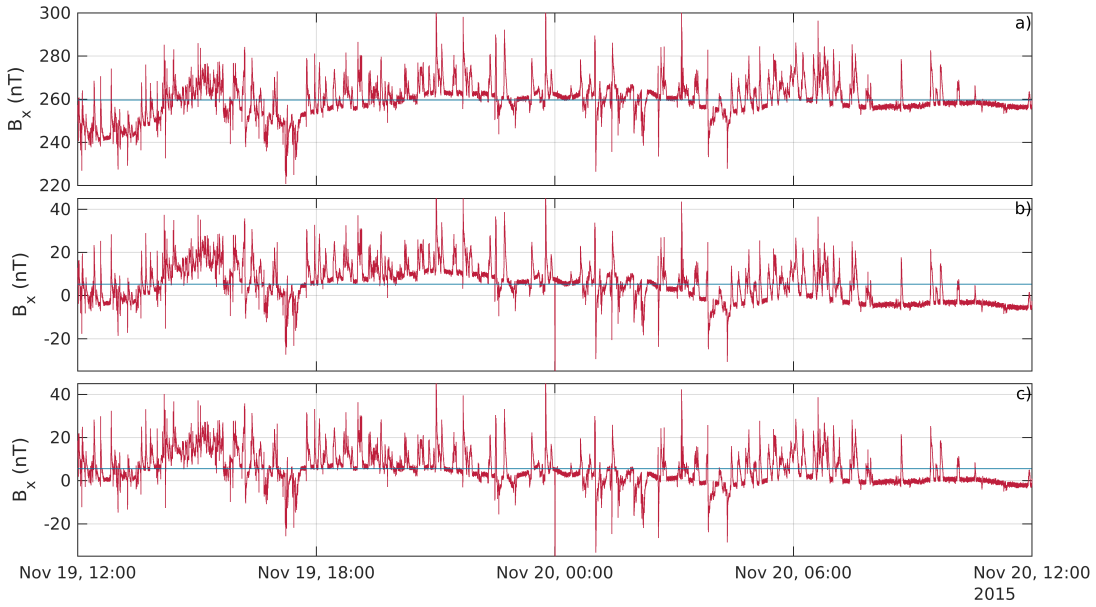

Figure 1.8.: Example interval showing the step-by-step improvement of the data. Shown is the IB x-component of the magnetic field for a 24h interval in November 2015 in red and the average field in blue.

Also note that the spread in time is reduced after this first step (panel b)). A further treatment of the time dependence does not improve the result, as the temperature dependent offset dominates. Thus, the $\vec{O}_{sc}(t)$ is only modeled with the linear model.

2. As shown in Fig. 1.7, panel b), $\vec{O}_{sensor}(T)$ is highly non-linear and does not appear to follow any simple or closed functional form. Therefore the method that is chosen here is a step-wise interpolation. For this, all residual fields in a temperature bin are averaged and the average value is interpolated. The resulting function is shown in red in Fig. 1.7, panel c). Only bins with a sufficient number of values are taken into account. Outside of the temperature range the fit is chosen to be constant with the value of the last known point. This fit constitutes the last step of the calibration and improves the temperature dependent part of the offset.

The main drawback of this method is that the offset can only be calculated in a certain temperature range. Outside of this range the functional form of the calibration curve may be entirely different and cannot be extrapolated.

Fig. 1.8 shows the step-by-step improvement of the data, from the raw data (panel a)) to the finished product (panel c)). Although some drift of the offset remains, the measurements inside the cavity (visible as almost horizontal lines between magnetic field increases) are now much more stable and closer to 0 nT. For further validation, the residual field for all diamagnetic cavity detections is binned to get a histogram of the remaining offset. This is shown in Fig. 1.9 for all data points in the diamagnetic cavity. The red bars show the original offset, with the mean removed for visibility, and the blue bars show the remaining offset after calibration. The mean offset is now below 0.2 nT for each component with a standard deviation below 2 nT for the y- and z-component and below 3 nT for the

x-component. This figure shows the validity of the calibration procedure and also gives a measure of the error of the magnetic field measurements in the standard deviation. The calibration as described above was used in a variety of scientific publications, for example in Goetz et al. (2017) and Goetz et al. (2016a).

To improve the calibration, this method is supplemented by solar wind measurements. The magnetic field in the solar wind should, on time scales of one solar rotation, also be close to zero (e.g. Tsurutani et al. 1990) as Rosetta is far from the Sun, especially at large distances to the Sun. This information can be used in a similar way as the residual field in the diamagnetic cavity. And lastly, whenever large spacecraft slews happen, they can also be used for calibration and validation of the data. The entire process is implemented in a data processing pipeline that produces the archive-ready magnetometer measurements.

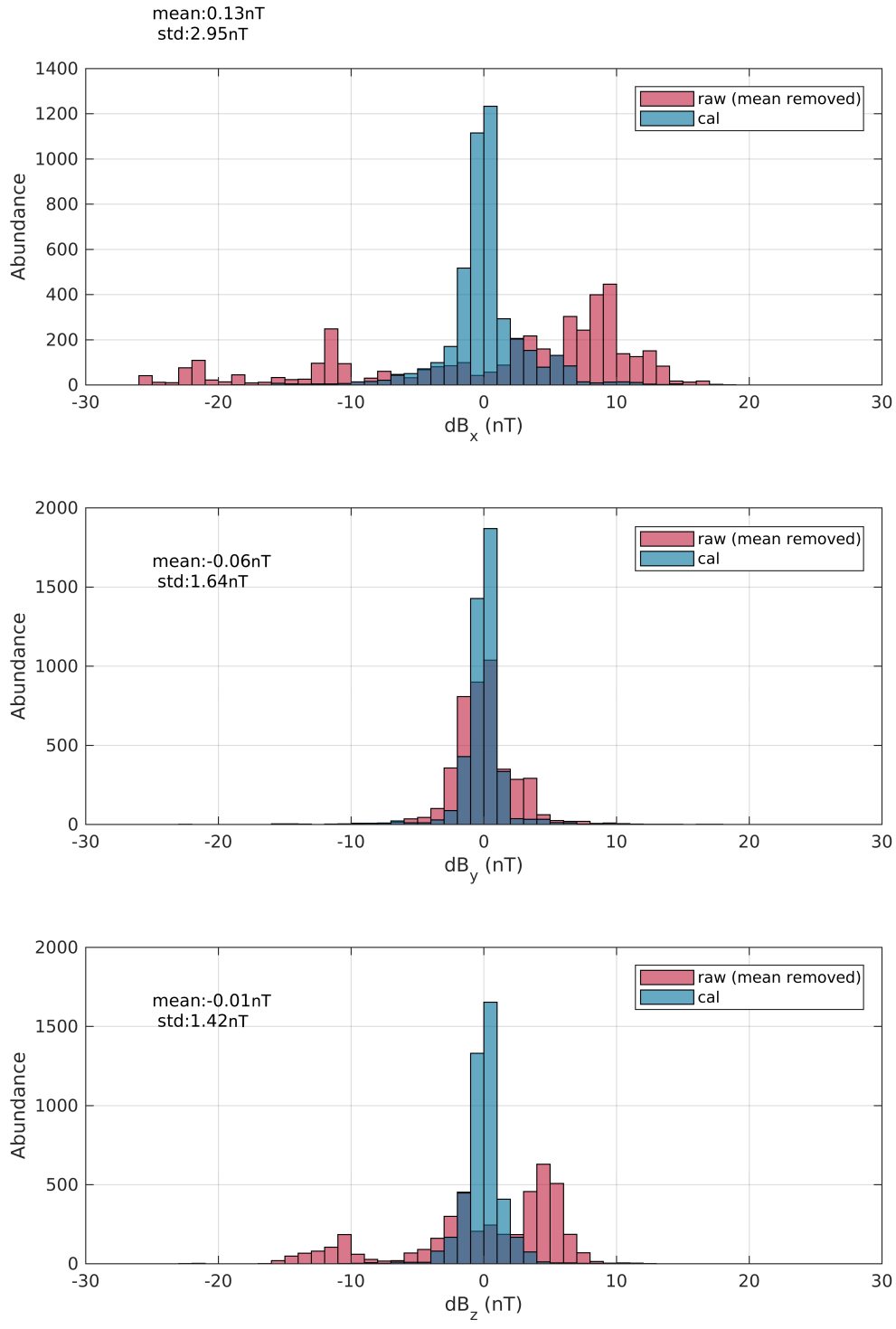

Figure 1.9.: Residual field components inside the diamagnetic cavity for the raw data and the calibrated data for each individual component of the field. The temporal resolution of the offset vector is 32 s. The mean and standard deviation of the calibrated data are also given in the panels.

2 Cometary Plasma Physics

2.1. Plasma Physics

2.1.1. From single particles to the fluid description

A plasma is a mixture of positively and negatively charged particles and neutral gas and may carry an external magnetic field. The plasma satisfies the criterion of quasi-neutrality, meaning that on frequency scales below the plasma frequency ω_p and on spatial scales above the Debye length λ_D there exists no charge separation. The Debye length and plasma frequency of singly charged particles are defined as:

$$\lambda_D = \sqrt{\frac{\epsilon_0 k_B T_k}{n_k q^2}} \tag{2.1}$$

and

$$\omega_p = \sqrt{\frac{q^2 n_k}{m_k \epsilon_0}}, \tag{2.2}$$

where ϵ_0 is the dielectric constant, k_B is the Boltzmann constant and q is the elementary charge. The temperature T, mass m and number density n depend on the species k of the particle. As a result there are different length scales for ions and electrons.

The description of the motion of the particles in the plasma is a fundamental problem that, at first glance, is easily done, but becomes difficult after further considerations. The motion of a single particle in the plasma is described by its equation of motion:

$$\vec{F} = m\vec{a} = q\left(\vec{E} + \vec{v} \times \vec{B}\right) + \vec{F}_s. \tag{2.3}$$

Here $\vec{a} = \frac{d\vec{v}}{dt}$ is the acceleration of the particle, $\vec{E}$ and $\vec{B}$ are the external electric and magnetic fields and $\vec{F}_s$ are additional forces (e. g. collisions, electric forces exerted by other particles). This equation describes how the velocity $\vec{v}$ of the particle changes with time and it has to be solved for all particles in the plasma at the same time, because each particle influences all other particles. The variation of the fields is given by the Maxwell's

equations:

$$\nabla \cdot \vec{B} = 0 \tag{2.4}$$

$$\nabla \cdot \vec{E} = \frac{\rho_c}{\epsilon_0} \tag{2.5}$$

$$\nabla \times \vec{B} = \mu_0 \vec{j} + \mu_0 \epsilon_0 \frac{\partial \vec{E}}{\partial t} \tag{2.6}$$

$$\nabla \times \vec{E} = -\frac{\partial \vec{B}}{\partial t} \tag{2.7}$$

where the current density $\vec{j}$ and the charge density ρ_c depend on each of the single particles. This results in a coupled system of differential equations. Typical laboratory plasmas have particle numbers well above Avogadro's number (6×10^{23} particles). This means that even for rarefied plasmas the number of particles is so large that it is not feasible to solve this system of equations. Therefore, other descriptions of the plasma are better suited for the high number of particles. In the kinetic description of a plasma the probability distribution function (pdf) $f(\vec{x}, \vec{v}, t)$ is used to describe the state of all particles in a plasma. Their functional form and evolution over time is described by the Boltzmann equation (Baumjohann and Treumann 1997). Alternatively, one can impose a functional form on the pdf The one that is most commonly used is the Maxwell-Boltzmann distribution, because it describes the velocity distribution of particles in an ideal gas in spherical symmetry:

$$f(v) = 4\pi \left(\frac{m}{2\pi k_B T} \right)^{3/2} v^2 \exp\left(-\frac{m v^2}{2 k_B T} \right). \tag{2.8}$$

An even simpler approach uses the moments of the distribution function as a way to approximate the pdf. The mth moment for species k is defined as:

$$M_k^m(\vec{x}, t) = \int f_k(\vec{x}, \vec{v}, t)\, \vec{v}^{\,m} d^3 v \tag{2.9}$$

and then the plasma density, bulk velocity and pressure tensor are the first three moments of a given pdf. The plasma parameter Γ can be used as an indicator of the quasineutrality of a plasma, for

$$\Gamma = \frac{3}{4\pi n_k \lambda_D} \ll 1 \tag{2.10}$$

the plasma is called quasineutral.

By integrating the Vlasov equation (weighted by $\vec{v}^n$) over the velocity space and assuming no sources or losses, it is possible to derive equations for the conservation of mass, momentum and energy for a plasma. For the zeroth order moment, the Vlasov equation is integrated over the entire velocity space, giving the conservation of mass or simply the continuity equation for species k:

$$\frac{\partial n_k}{\partial t} + \nabla \cdot (n_k \vec{u_k}) = 0 \tag{2.11}$$

where $\vec{u_k}$ is the bulk velocity of the species k. The first order moment gives the conservation of momentum, called the momentum equation:

$$\frac{\partial \left(n_k \vec{u_k}\right)}{\partial t} + \nabla \cdot \left(n_k \vec{u_k} \circ \vec{u_k}\right) + \frac{1}{m_k} \nabla \cdot \underline{\underline{P_k}} - \frac{q_k n_k}{m_k} \left(\vec{E} + \vec{u_s} \times \vec{B}\right) = 0 \tag{2.12}$$

where $\underline{\underline{P_k}}$ is the pressure tensor of species k and $\circ$ denotes the dyadic product of two vectors. The second order moment will then give the energy density conservation equation:

$$\frac{\partial}{\partial t} \left(\frac{m_k n_k \vec{u_k}^2 + 2\varepsilon_k}{2} \right) + \nabla \cdot \left(\left(\frac{1}{2} m_k n_k \vec{u_k}^2 + \varepsilon_k + \underline{\underline{P_k}} \right) \vec{u_k} + \vec{q_k} \right) - q_k n_k \vec{u_k} \vec{E} = 0 \tag{2.13}$$

where ε_k is the internal energy of the plasma. The system is not closed, one equation always depends on moments of higher order. In addition, all species have to be considered, because all species contribute to the fields via the Maxwell equations. This system can also be further complicated by source terms for each of the conservation laws, as is the case for the plasma at comets. A common way to close the system is to use an adiabatic equation of state and an isotropic pressure instead of the energy density equation:

$$\frac{p}{(n_k m_k)^\gamma} = const. \tag{2.14}$$

where γ is the adiabatic index.

These equations are used for a multi-fluid approach to the plasma, most commonly when electrons and ions contribute to the effects or if there is more than one species involved. However, the simplest and most useful approach in terms of understanding the general behaviour of a flowing plasma is magnetohydrodynamics (MHD). Here, the number of fluids is reduced to one and the difference in density flux of the electrons (index e) and ions (index i) is expressed as a current:

$$\vec{j} = e(n_i \vec{u_i} - n_e \vec{u_e}) \tag{2.15}$$

and with $m_e \ll m_i$ it follows that the bulk velocity $\vec{u} \approx \vec{u_i}$ and the mass density $\rho \approx m_i n_i$. Then the set of MHD equations becomes:

$$\frac{\partial \rho}{\partial t} + \nabla \cdot (\rho \vec{u}) = 0 \tag{2.16}$$

$$\frac{\partial}{\partial t} (\rho \vec{u}) + \nabla \cdot (\rho \vec{u} \circ \vec{u}) + \nabla \underline{\underline{P}} - \vec{j} \times \vec{B} = 0 \tag{2.17}$$

$$\frac{p}{\rho^\gamma} = const. \tag{2.18}$$

which is closed by the Maxwell equations. The hydrodynamic equations can then simply be derived by neglecting the electric and magnetic fields. The MHD equations are only valid for low frequencies and large spatial scales, at a comet they are mostly only applicable at high gas production rates, when the gyroradius of the heavy ions becomes smaller than typical scales in the plasma (Huang et al. 2016b).

For interpretation of the scale of the terms in the momentum equation, the $\vec{j} \times \vec{B}$ term is often expanded with the help of Ampère's law:

$$\vec{j} \times \vec{B} = -\nabla \left(\frac{\vec{B}^2}{2\mu_0} \right) + \nabla \cdot \frac{\vec{B}\vec{B}}{\mu_0}. \tag{2.19}$$

This format proves very useful in interpreting the processes in a plasma, because the two terms on the right hand side are the magnetic pressure gradient and the magnetic tension, two concepts that have clear analogues in everyday life. The magnetic tension describes the effect of magnetic field line curvature, analogous to a rubber band that is stretched and the magnetic pressure is most easily described by the density of field lines, analogous to the density of particles in a gas.

Another useful concept in this area is the frozen-in theorem which is valid for high to infinite conductivity. In essence it states that the magnetic flux through the surface enclosing a certain plasma volume is conserved. For the derivation of this theorem it is opportune to use the induction law and the general Ohm's law of MHD combined:

$$\frac{\partial \vec{B}}{\partial t} = \nabla \times \left(\vec{u} \times \vec{B} - \frac{\vec{j} \times \vec{B} - \nabla \cdot \underline{\underline{P_e}}}{ne} - \frac{m_e}{ne^2} \frac{\partial \vec{j}}{\partial t} - \eta \vec{j} \right). \tag{2.20}$$

Under the assumptions of zero resistivity η, stationarity and negligible electron pressure gradient only the first and second (Hall) term remain. In the simplest cases (ideal MHD) with weak fields the Hall term can be neglected as well and with Faraday's law the electric field becomes:

$$\vec{E} = -\vec{u} \times \vec{B}. \tag{2.21}$$

This is a commonly used relation in the solar wind. In that case, the solar wind ions and electrons are not affected by an electric field, because their velocity is zero with respect to the interplanetary magnetic field, but any ion or electron with a velocity different from the solar wind velocity will feel an electric field.

In reality, the Hall term cannot be neglected as easily, but it can be shown that at least the electrons are frozen into the field. This is a useful concept in cometary plasma physics, where the large ion gyroradius means that the Hall term becomes important.

2.1.2. Single particle motion

For test particle pictures it is advantageous to describe the motion of a single charged particle in electric and magnetic fields. For this purpose Eq. (2.3) is used without the additional force term $\vec{F}_s$. The change in position of the particle is then computed via $\frac{d\vec{x}}{dt} = \vec{v}$, making it a coupled system of differential equations. Without loss of generality the coordinate system can be chosen such that $\vec{B} = B_0 \vec{e}_z$, where $\vec{e}_z$ is the unit vector along the z-axis of a right-handed cartesian coordinate system. Then the general solution to Eq. (2.3) is:

$$\vec{v}(t) = \begin{pmatrix} (1 - \cos(\omega_g t)) \frac{E_y}{B_0} + v_{0x} \cos(\omega_g t) - \left(v_{0y} + \frac{E_x}{B_0} \right) \sin(\omega_g t) \\ \left(\frac{E_y}{B_0} - v_{0x} \right) \sin(\omega_g t) - v_{0y} \cos(\omega_g t) + \frac{E_x}{B_0} (\cos(\omega_g t) - 1) \\ \frac{q}{m} E_z t + v_{0z} \end{pmatrix} \tag{2.22}$$

where $\vec{v_0} = (v_{0x}, v_{0y}, v_{0z})$ is the initial velocity of the particle at $t = 0$ and the index x, y, z denotes the three components of the electric field. The angular frequency ω_g is called the gyro frequency and is defined as:

$$\omega_g = \frac{|qB_0|}{m}. \tag{2.23}$$

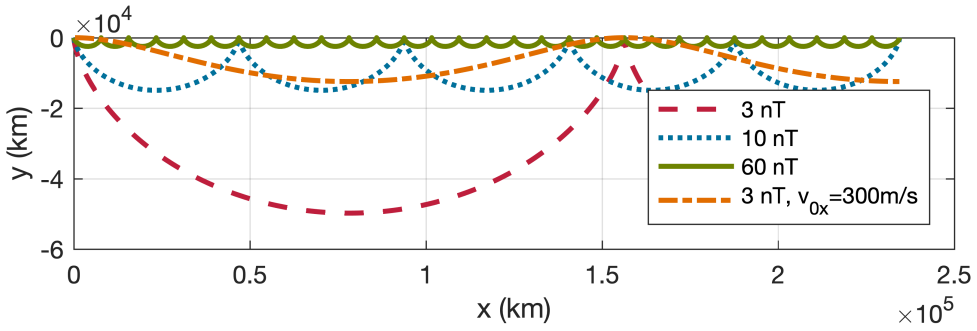

Figure 2.1.: Single particle trajectories for given magnetic fields. The electric field was assumed to be only in y-direction with a value calculated by $E = -B \cdot 4 \times 10^5$m/s and the particle was assumed to be a H_2O^+ ion. In the first three cases the initial velocity of the particle is zero in all directions, the last case has a non-zero velocity in x-direction.

There are two cases of interest here: for $\vec{E} = 0$ the solution becomes a simple gyration of the particle around the field line, with angular frequency ω_g and gyro radius $r_g = \frac{v_\perp}{\omega_g}$:

$$\vec{x}(t) = \begin{pmatrix} r_g \sin(\omega_g t) + r_g \cos(\omega_g t) - r_g + x_0 \\ r_g \cos(\omega_g t) - r_g \sin(\omega_g t) - r_g + y_0 \\ v_{0z} t + z_0 \end{pmatrix}. \tag{2.24}$$

The second case of interest is for $\vec{E} \nparallel \vec{B}_0$, when a drift arises, the $\vec{E} \times \vec{B}$ drift, that adds to the velocity component that is perpendicular to $\vec{B}_0$. Fig. 2.1 shows examples of the trajectory of a particle in such a case. The particle follows a cycloidal trajectory, meaning that averaged over a gyro period it is moving with the drift velocity of

$$\vec{v_D} = \frac{\vec{E} \times \vec{B}_0}{|\vec{B}_0|^2}. \tag{2.25}$$

For $\vec{E} \parallel \vec{B}_0$ the drift velocity is zero.

The above solution is an example of a generalized drift in a magnetized plasma with an additional force $\vec{F}$, in this case the electric force. Other forces that are commonly present in a plasma include gravitational forces, curvature forces and gradient forces. The general drift equation for a force field independent of position and time then becomes:

$$\vec{v_D} = \frac{\vec{F} \times \vec{B}_0}{q|\vec{B}_0|^2}, \tag{2.26}$$

note that only the $\vec{E} \times \vec{B}$ drift is independent of the charge of the particles in question, meaning that charge separation is a result of all other forces.

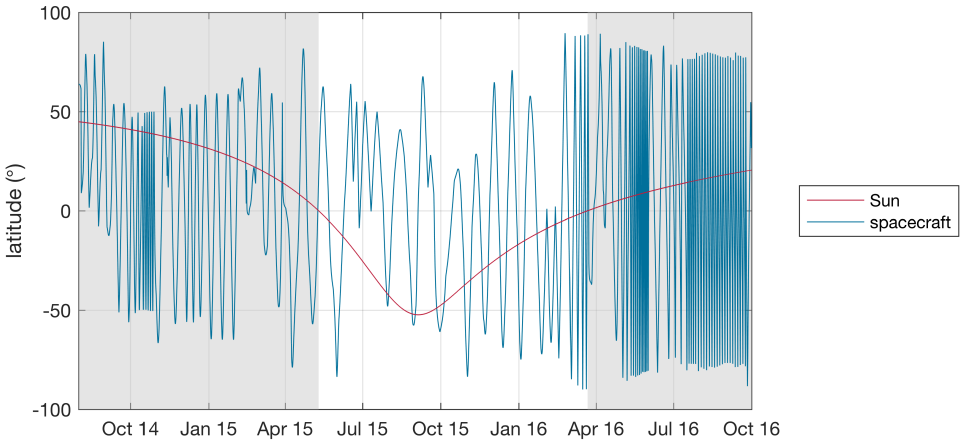

Figure 2.2.: Latitude of the Sun and the Rosetta spacecraft in a nucleus fixed system for August 2014 to October 2016. The northern summer is marked in grey.

2.2. Comet 67P

2.2.1. From neutrals to ions

The cometary plasma environment is mainly determined by the amount of neutral gas and the intensity of the solar EUV radiation in the coma. As the comet approaches the Sun, the insolation heats the surface and interior of the nucleus and causes the ices to sublimate into space. Due to the low gravitation of the comet, the gases and any loose dust escape the nucleus and flow radially outward with velocities of $u_n = 0.5 - 1$ km/s (Hansen et al. 2016). The neutral density profile n_n with regard to distance to the comet r may be described by (Haser 1957):

$$n(r) = \frac{Q}{4\pi r^2 u_n} exp\left(-\frac{\nu_p(r - r_n)}{u_n}\right) \tag{2.27}$$

where Q is the global outgassing rate, i. e. the number of molecules that leave the comet per second. r_n is the size of the nucleus, which can be neglected for sufficiently large r and ν_p is the photoionisation frequency. The exponential term accounts for the loss of neutrals due to ionisation, which is negligible over the regions probed by Rosetta ($r < 100$s km of the nucleus). This model does not account for the inhomogeneities of the comet, as it assumes a spherical coma and nucleus. Hansen et al. (2016) and Gasc et al. (2017) showed that the outgassing profile is highly asymmetric as a result of the comet's shape and the fact that most of the energy for sublimation is added on the sunward side. Simulations showed that the latter is most important, as an illumination driven model producing higher densities on the sunward side significantly altered the plasma environment, while the addition of a realisticly shaped nucleus did not improve accuracy significantly (Huang et al. 2016b). For the neutral gas density, it is also advantageous to describe it in connection with the seasons of the comet, as they affect not only the intensity of the outgassing, but also the composition of the outflowing gas (Hansen et al. 2016). During the beginning of the Rosetta mission it was northern summer, which means that the subsolar point was at positive latitudes in the nucleus fixed system (see Fig. 2.2). Although northern summer

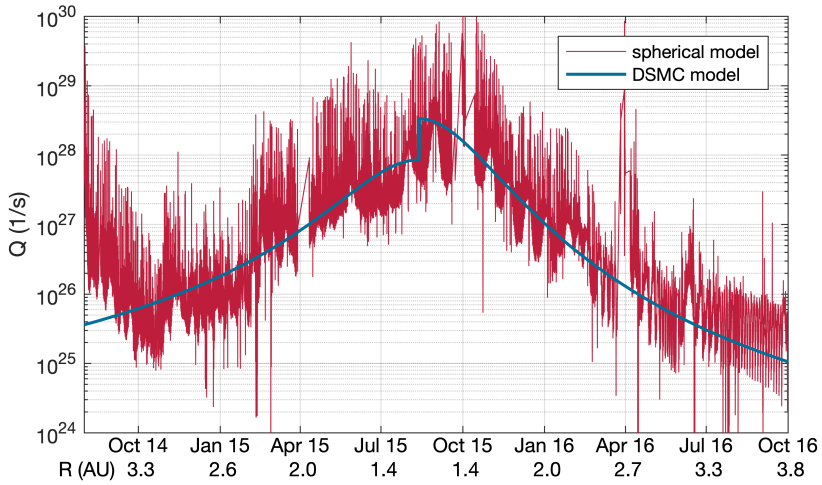

Figure 2.3.: Estimates of the gas production rate of 67P from two different models. The spherical model is from Haser (1957) using measured data from ROSINA as input and a fixed outgassing velocity of 500 m/s. The large variations in the second model are a result of the non-spherical and heterogeneous nucleus and solar illumination thereof. These effects are taken into account in the DSMC model. The curve shown here is the empirical model from Hansen et al. (2016)

.

is much longer than southern summer (negative latitudes), the integrated activity on the southern hemisphere is higher because the southern summer coincides with perihelion and the southern hemisphere contains more CO_2 ices, which are more volatile than water (Hoang et al. 2017).

The neutral gas can be ionized by several different processes and ions and electrons may also recombine. In general the continuity equation in spherical coordinates with loss terms L and source terms S needs to be solved for all ion species:

$$\frac{1}{r^2}\frac{d}{dr}\left(n_i(r)u_i r^2\right) = S - L \tag{2.28}$$

where $n_i(r)$ and u_i are the ion number density profile and the ion expansion velocity for species i. The dominant source term at a comet close to perihelion is photoionisation (Galand et al. 2016, Heritier et al. 2018). In its simplest form (without taking absorption of the photons into account) this process can be described as:

$$S_{ph} = \nu_p n_n = \frac{\nu_p Q}{4\pi r^2 u_n} \tag{2.29}$$

where the left hand side made use of Eq. (2.27) for the neutral gas profile (without the exponential) and S_{ph} is the source density. The photoionisation rate ν_p is heavily dependent on the distance to the Sun R, because the intensity of the solar radiation falls off as $1/R^2$, and on the wavelength of the impinging photon. In the case of comets this means that the photoionisation rate is highest at perihelion and lowest at aphelion. Note that the attenuation of the solar flux due to the dust coma is not taken into account, this would influence the ionisation rate in the inner coma (where the optical thickness is greatest)

most (Johansson et al. 2017). If all other contributions to the continuity equation are neglected, the ion density profile can simply be calculated by integration and is given by:

$$n_i(r) = \frac{\nu_p Q}{4\pi u_n u_i} \frac{r - r_n}{r^2}. \tag{2.30}$$

Another common simplification is to assume that the ion velocity is equal to the neutral velocity, i. e. that the ions are not accelerated by external forces after being ionised. This description is best suited to comets with low outgassing rates and at large heliocentric distances, where transport is important and the losses through chemical processes happen on very large timescales and do not contribute (Galand et al. 2016).

A second source term is electron impact ionisation, this term is more difficult to describe accurately as the electron impact ionisation rate ν_e is heavily dependent on the electron mean energy, which in itself cannot be described by a simple radial profile, because electron heating can occur on small spatial scales (e. g. in a shock). Thus it is not possible to find a simple ion density profile. However, Galand et al. (2016) found that electron impact ionisation can contribute significantly to the electron density, especially over the less active hemisphere of the comet. Simulations also indicate that electron impact ionisation is effective around the bow shock, because of the thermalization of electrons at the shock (Simon Wedlund et al. 2017). This also increases the bow shock distance significantly due to additional mass-loading.

A third source term is added for charge exchange collisions of doubly charged helium from the solar wind with neutral water. This mechanism was used by Simon Wedlund et al. (2016) to infer the gas production rate. However, including this process in the continuity equation is also non-trivial, because the source density depends on the column density of the helium ions, which is variable with solar wind conditions.

The most important loss term at a comet is dissociative recombination. In this process an ion and electron recombine and form a new neutral, which subsequently dissociates. The loss rate is dependent on the ion density and the electron density, which means that as a loss term, dissociative recombination may be described by:

$$L_{dr} = \alpha n_i^2 \tag{2.31}$$

assuming charge neutrality and defining α as the recombination coefficient. With this it is possible to describe the system in photochemical equilibrium, i. e. the case where photoionisation and recombination are balanced out and transport of the ions is neglected. Eq. (2.28) then becomes

$$0 = S_{ph} - L_{dr} = \frac{\nu_p Q}{4\pi r^2 u_n} - \alpha n_i^2 \tag{2.32}$$

and simply solving for n_i without taking photoabsorption into account gives the ion profile:

$$n_i(r) = \sqrt{\frac{\nu_p Q}{4\pi\alpha u_n}} \frac{1}{r}. \tag{2.33}$$

For comets with high outgassing rates like 1P, the coma is in photochemical equilibrium, whereas the transport dominated coma is found at comets with low outgassing rates. Also

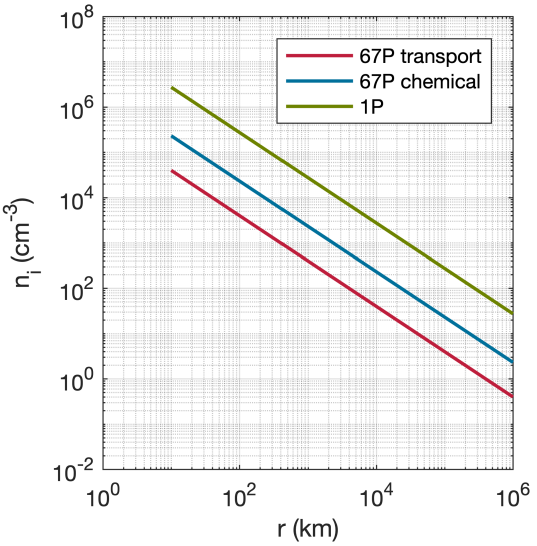

	1P	67P
Q (1/s)	7×10^{29}	10^{28}
ν_p (1/s)	10^{-6}	5×10^{-7}
u_n (km/s)	1	1
α (m^3/s)	7.4×10^{-14}	7.4×10^{-14}

Figure 2.4.: Comparison of the neutral gas profiles at comets 1P and 67P without taking photoabsorption into account. The input parameters are given in the table on the right. For 1P the model in photochemical equilibrium was chosen, whereas the profile at comet 67P is shown for both the pure transport (no chemical losses) and the photochemical equilibrium cases.

note that in both cases the ion density falls off as $1/r$ but the factor is very different, especially with respect to the dependence on the gas production rate Q. Fig. 2.4 shows the two different ion density profiles for perihelion conditions at comet 1P and 67P. For a more detailed discussion of the ionospheric dynamics and a solution of the full continuity equation including attenuation see Beth et al. (2018).

2.2.2. Collisions and electron cooling

The new ions and electrons at a comet may undergo collisions with neutrals and other charged particles, which can change their temperature or momentum. There are several collision mechanisms that are important in the coma. One mechanism is the creation of H_3O^+ ions from H_2O^+ and water collisions. It has been shown, that for high gas production rate comets, this reaction is very effective making H_3O^+ the dominant ion most of the time(Gan and Cravens 1990), whereas the collisions are less likely at low gas production rate comets like 67P. There the H_3O^+ to H_2O^+ ratio is variable and has not been explained yet (Beth et al. 2016).

The effectiveness of this ion neutral reaction also has implications for the ion velocities in the coma. The simplest model for the plasma at a comet assumes that ions and neutral gas are collisionally coupled and therefore have similar speeds: $u_n \approx u_i$ (e.g. Coates and Jones 2009). More detailed measurements at comet 67P have revealed that this might not be the case, the velocity of the expanding ions can be larger than the neutral gas velocity, which indicates an additional acceleration process and inefficient collisional coupling of ions and neutrals (Vigren et al. 2017, Vigren and Eriksson 2017, Odelstad et al. 2018).

Newly created electrons (either by photoionisation or by electron-impact ionisation)

typically have temperatures around $T_e \approx 10\,\mathrm{eV}$. However it has been speculated even early on in cometary science, that electron cooling through collisions with neutrals is significant, especially in the densest part of the coma (Gan and Cravens 1990). Several different electron populations are expected: cold ($T_e < 1\,\mathrm{eV}$), warm ($1\,\mathrm{eV} < T_e < 15\,\mathrm{eV}$), and hot ($T_e > 15\,\mathrm{eV}$) electrons, with the warm and hot electrons usually originating either in the solar wind or from ionisation. Eriksson et al. (2017) and Odelstad et al. (2018) showed that the cold electrons are dominant only in the innermost region of a comet, and even there warm electrons can always be observed. Engelhardt et al. (2018) showed that the electron temperature during the Rosetta mission was bifurcated with one maximum at 10 eV and a second maximum at 0.1 eV. This was interpreted as a photoelectron population and a cold population. The cold electron population is thought to be the result of electron-neutral collisions, as it occurs only close to the electron exobase or electron collisionopause. The collisionopause is the radius in a spherically expanding neutral coma that is equal to the mean free path of a charged particle (Mandt et al. 2016):

$$L_k = \sigma_{nk} n_n r^2 \tag{2.34}$$

with $k = i, e$ for ions or electrons and σ_{nk} as the collisional crosssection of the species k with the neutral gas. It has been shown that the electron collisionopause is an ordering parameter for many phenomena at a high activity comet (Henri et al. 2017), which will be discussed in chapter 3. A warm electron population alone is not an indication of a plasma without collisions, because additional heating mechanisms have been suggested, primarily by wave-particle interactions (Broiles et al. 2016, Karlsson et al. 2017).

The last significant source term for water ions at the comet is charge exchange. Here, a neutral water molecule collides with an ion and loses an electron to become a positively charged ion. In the coma the most important charge exchange partners are solar wind protons and doubly and singly charged alpha particles. Consequently, the charge exchange rates depend on the energy and density of the neutrals and the ions (Simon Wedlund et al. 2017). Another charge exchange process is the ion-neutral friction. Here, a water ion exchanges an electron with a neutral water molecule. This mechanism does not contribute to the charge density, but it does change the momentum balance in the plasma, if the neutral particle and the ion have different momenta.

2.3. Comets in the solar wind

2.3.1. The solar wind

The solar wind is a stream of charged particles carrying a magnetic field that emanates from the Sun's corona and expands into the solar system. In fact comets were integral to the detection of the solar wind in the 1950s, as the behaviour of the plasma tail of comets could not be explained. Instead of following the comet's motion, they always pointed away from the Sun, leading Biermann (1951) to speculate that a flow of particles and magnetic field was responsible for accelerating the cometary ions radially outward. Parker (1958) calculated the expansion velocities and densities in the corona and the solar system with simple hydrodynamic equations. Although this does not account for the magnetic field, the approximation has been shown to be sufficient for many uses. The solution of the

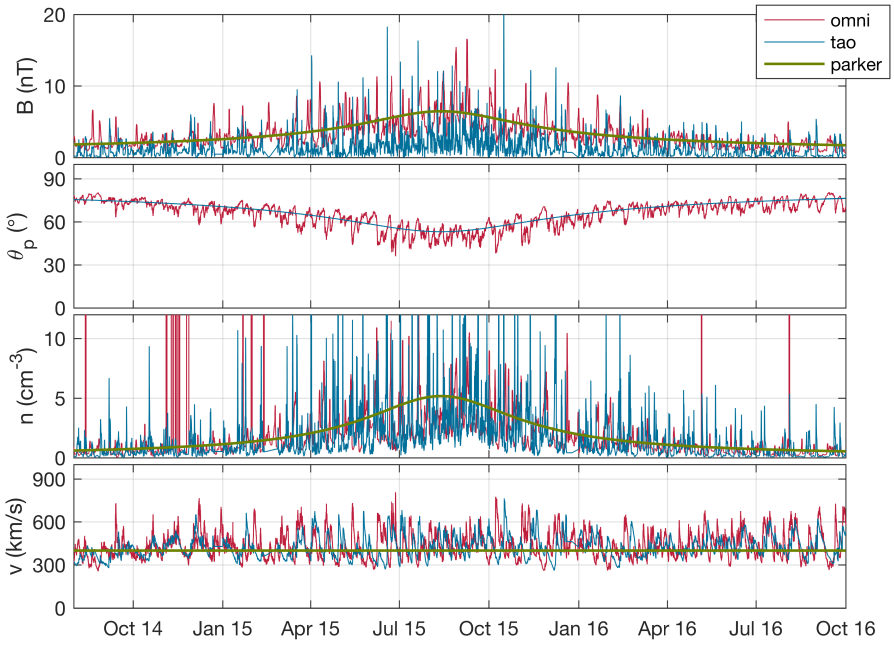

Figure 2.5.: Solar wind predictions at 67P during the Rosetta mission. The Parker model uses average values at Earth for solar wind propagation to 67P, the OMNImodel uses real time solar wind data at Earth as extracted from NASA/GSFC's OMNI data set through OMNIWeb for the propagation. Both use the simple Parker model to extrapolate from Earth to 67P. The Tao model is taken from Tao et al. (2005)

.

hydrodynamic continuity, momentum and energy equations show that the solar wind is accelerated and compressed until it reaches Mach one, a point that is usually located at a few solar radii. After this the flow becomes supersonic and expands further. Eventually, for large heliocentric distances R, the velocity asymptotically approaches the solar wind velocity in the heliosphere v_{sw}. The density of the particles n_{sw} decreases with $1/(4\pi R^2)$ as the particle flux through an ever increasing spherical shell will remain constant.

Simple additions to this model can be used to account for the magnetic field, which is usually called the interplanetary magnetic field (IMF). Here, it is assumed that the foot point of the field line is fixed on the Sun and that the magnetic field, governed by the frozen-in concept, moves outward with solar wind velocity. This model is called the Parker model or Parker spiral for the picture of spiraling field lines in the solar system. For most applications it is sufficient to consider the radial and azimuthal components, as the elevation component will be close to zero in the ecliptic plane. Simple geometrical considerations and Gauss's law give the radial and azimuthal components (B_r and B_ϕ) for the magnetic field:

$$B_r = B_0 \frac{R_0^2}{R^2} \tag{2.35}$$

$$B_\phi = - B_0 \frac{R_0^2\, \omega_s}{v_{sw}\, R} \tag{2.36}$$

where B_0 is the magnetic field at point R_0 and ω_s the angular frequency of the Sun at the

foot point of the field line. With that the so called Parker angle θ_p is defined as

$$\tan\left(\theta_p\right) = -\frac{B_\phi}{B_r}, \tag{2.37}$$

thus it approaches 90° for large solar distances, usually far above 3 AU. At Earth, θ_p is usually around 45° and the IMF has magnitudes around 6 nT. The average density is $\sim 8\,\mathrm{cm}^{-3}$ and the solar wind velocity is around 350 – 450 km/s. Due to different polarities of the magnetic field of the Sun, the Parker spiral usually has 3 – 4 segments with opposite IMF polarity.

Propagation models are used extensively to predict solar wind parameters for planetary exploration. The Parker model is the simplest approach, but lacks accuracy, thus other models have been developed. The Tao et al. (2005) model and the MSWiM model (Zieger and Hansen 2008) are examples of a simple 1D MHD model for the solar wind, that inherently includes the magnetic field in the propagation. More sophisticated models are ENLIL (Odstrcil 2003) and SUSANOO (Shiota et al. 2014), both 3D MHD models that can also include transient structures like interplanetary coronal mass ejections (ICMEs). However, all of these models still have significant uncertainties and have to be used carefully.

Fig. 2.5 shows the different predictions for the IMF magnitude and Parker angle, as well as the velocity and density of the solar wind at 67P for the entirety of the Rosetta mission.

2.3.2. Mass-loading

The main problem in understanding the solar wind-coma interaction is the incorporation of the cometary ions into the solar wind flow. The nucleus itself is small compared to the scale sizes in the solar wind, meaning that the ion cloud is the obstacle that the solar wind encounters. Biermann et al. (1967) were the first to describe this situation with a hydrodynamic 1D model.

For an analytical solution, the conservation equations are solved with the solar wind fluid moving along the axis from infinity towards an outgassing comet at the origin of the coordinate system. Biermann et al. (1967) showed that the comet can be described by the addition of a non-zero mass-source term in the mass continuity equation only, and that all other source terms (in the momentum, number density, and energy equations) can be neglected. The mass source is described by using Eq. (2.27) without the exponential term:

$$M_s = m_i S_i = m_i \nu_p n_n = \frac{m \nu_p Q}{4\pi u_n r^2}. \tag{2.38}$$

This combined with Eq. (2.16)-(2.18) yield a term for the flow velocity (Biermann et al. 1967):

$$\frac{u_x}{u_\infty} = \frac{\gamma - 1}{\gamma}\left(1 \pm \sqrt{1 - \frac{\gamma^2 - 1}{\gamma^2}\frac{\rho u_x}{\rho_\infty u_{x\infty}}}\right)^{-1} \tag{2.39}$$

where the index ∞ denotes the values at infinity, i. e. in the solar wind very far upstream of the comet. This equation becomes complex if

$$\frac{\rho u_x}{\rho_\infty u_{x\infty}} > \Phi_{crit} = \frac{\gamma^2}{\gamma^2 - 1} \tag{2.40}$$

which is also referred to as the critical mass flux ratio. In essence the solar wind can only accommodate a certain amount of mass flux, and if this amount is exceeded a shock has to form to allow for more mass-loading. Thus the equation can also be used to approximate the distance of the bow shock to the nucleus. However, Koenders et al. (2013) show that this is only an approximation and that the distance of the bow shock also depends on the gyro radius of the cometary ions. This is due to the approximation in the Biermann model that the cometary ions are at rest and do not get accelerated (which would be a source term in the momentum equation) and the non-existence of a magnetic field. Simon Wedlund et al. (2017) have also shown that the bow shock moves much farther from the comet if additional ionisation mechanisms are implemented, especially electron impact ionisation increases the bow shock distance significantly as the higher electron temperature behind the bow shock results in a larger ionisation rate and higher mass-loading. However, sometimes it is advantageous to approximate the bow shock distance in its simplest form. Galeev et al. (1985) found an analytical expression for the bow shock distance R_{BS}:

$$R_{BS} = \frac{m\nu Q}{4\pi u_n \rho_\infty u_\infty (\Phi_{crit} - 1)}. \tag{2.41}$$

Behind the shock, the analytical approximation breaks down and additional terms have to be included in the conservation equations. The Galeev et al. (1985) model takes into account the $\vec{j} \times \vec{B}$ term and the velocity distribution of the cometary ions in the solar wind as well as additional charge exchange cooling of the ions. It was shown by Goetz et al. (2017) that this simple model is sufficient to describe the measurements at comet 67P, because the uncertainties in the input variables are far greater than the model uncertainties.

Although the Rosetta mission does not include a solar wind monitor, it is still possible to relate some solar wind changes to the magnetic field changes at the comet. Goetz et al. (2017) showed that the magnetic field magnitude was modulated by the solar rotation period, indicating that indeed the strength of the magnetic field is related to the dynamic pressure in the solar wind, which shows periodic enhancements as well. In contrast to that the power of the low frequency waves at the comet is modulated by the cometary rotation period. This in turn implies that the wave activity at the comet depends on the amount of mass that is added to the solar wind flow.

In reality, the theory of mass-loading is more complicated and not easily described by a fully analytical model. However, parts of the process can be described more easily by an ion kinetic approach. There, the solar wind and cometary ion distribution function can be described by a ring-beam distribution, which follows from the $\vec{E} \times \vec{B}$-drift of the cometary ions. Fig. 2.6 shows the ring distribution that is expected upstream of a high-activity comet. As the neutral gas expands, some ions are produced very far upstream of the cometary bow shock and start to gyrate around the magnetic field lines and drift along the solar wind direction. The full ring distribution is achieved if cometary ions are produced over a length scale that is larger than the cometary ion gyroradius. If the cometary ions are produced on smaller scales, the ring distribution is only partially filled (Fig. 2.6) and the description of the subsequent processes goes beyond analytical models. This mechanism is only efficient for large angles between the solar wind velocity and the magnetic field.

This ring-beam distribution is unstable and starts to collapse first in pitch angle and then in energy (Johnstone et al. 1991) and the generation of pick-up waves that are close to the ion-cyclotron frequency is a good indicator for the presence of a full ring-beam

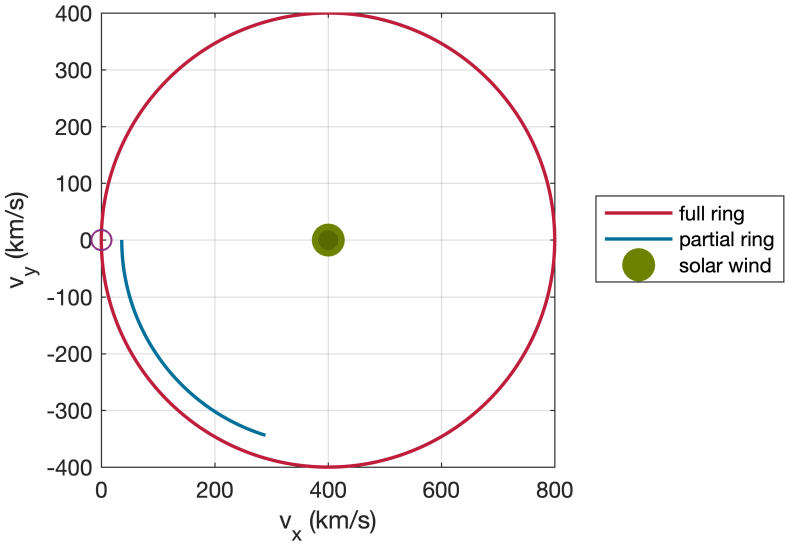

Figure 2.6.: The velocity distribution functions for the case with $B = 3\,\mathrm{nT}$ from Fig. 2.1. The two-tone of the solar wind distribution indicates the Maxwellian shape and the partial ring distribution is shifted inwards for visibility. The small circle at the origin is the injection point of the cometary ions.

distribution. In fact, the pitch-angle scattering produces a bispherical shell that is centered on the positive and negative Alfvén velocity in a solar wind reference frame (Galeev and Sagdeev 1988) and the energy scattering collapses this shell to a Maxwellian distribution that has roughly the same bulk velocity as the solar wind. Then the cometary ions are fully incorporated into the solar wind flow.

The full ring distribution was observed upstream of the bow shock of 1P (Coates et al. 1989) with partially filled shells closer to the bow shock. At the lower activity comet Grigg-Skjellerup the ring distribution had not yet collapsed, because the length scales over which ions are produced are simply smaller and the ions have not had enough time to pitch-angle scatter (Coates et al. 1993).

At comet 67P the ring-beam distribution was only expected for the months around perihelion and at large distances from the comet. This region was not visited by Rosetta and thus no measurements were made. It should be noted though, that the pick-up waves were expected also at lower gas production rates, but never observed (Glassmeier 2017), indicating that the low gas production rate of 67P is not sufficient to fill the full ring distribution.

Instead, at 67P all cometary ions are simply following the first part of the cyloidal motion that arises from the $\vec{E} \times \vec{B}$ force (Behar et al. 2016). This causes the cometary ions to flow across the field lines, constituting a cross-field current that was speculated to be the source of the low-frequency waves that were observed in the first months of the Rosetta mission (Richter et al. 2015).

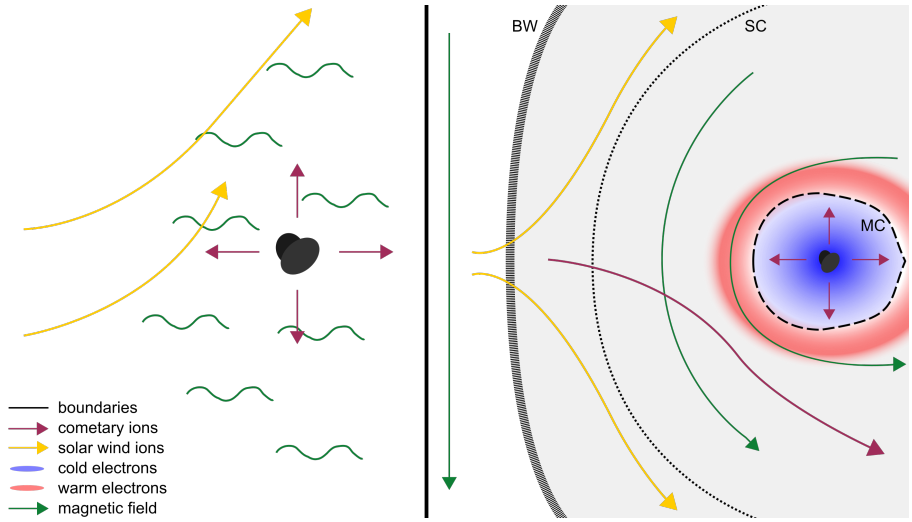

Figure 2.7.: Overview of the plasma environment of a comet for two different stages in cometary activity, the weakly active comet (left) and the strongly active comet (right). Known boundaries are labeled: bow wave (BW), solar wind cavity (SC) and diamagnetic cavity (MC) and the cometosheath is marked in grey. The plane shown is the one that contains the magnetic field (in vertical direction) and the solar wind flow velocity (in horizontal direction).

2.3.3. The stages of a comet's life

For the understanding of the plasma around a comet it is advantageous to consider three different stages in a comet's development depending on the outgassing rate and solar wind input. The three stages have very different scale sizes and distinct regions are formed (Nilsson et al. 2017, Goetz et al. 2017). Only the most active stage has been observed at multiple comets, the intermediate and weak stages are recent additions due to the Rosetta mission. Fig. 2 in A.3 shows an overview of the magnetic field magnitude measured during the Rosetta mission as well as its variance in a sliding ten-minute interval and the power spectra for the same intervals. The magnetic field magnitude increases with gas production rate, but the variance of the field is a much better indicator of the cometary activity. The two most extreme stages of the comet's life (weakly and strongly active) are illustrated in Fig. 2.7.

Weakly active comet

For gas production rates lower than $10^{26}\,\mathrm{s}^{-1}$ the ion density at a comet is not sufficient to produce the classical bow shock or diamagnetic cavity from the Biermann model. At that stage the solar wind dynamic pressure is typically also very low, because the comet will be far away from the Sun. In a solar wind reference frame the newborn cometary ions have a velocity of $-v_{sw}$ and start to gyrate around the magnetic field lines of the solar wind. The gyro frequency (Eq. (2.23)) and radius of a water ion (H_2O^+) in a 2 nT field with a velocity of $-v_{sw} = -400\,\mathrm{km/s}$ are

$$\omega_g = 0.013\,\mathrm{s}^{-1} \tag{2.42}$$

$$r_g = 30000\,\mathrm{km} \tag{2.43}$$

assuming that the solar wind velocity is perpendicular to the magnetic field. Therefore the ion gyroradius is much larger than the nucleus and a fluid description of the plasma no longer applies here. However, the electron gyroradius is much smaller (by a factor of $\sim$ 1800). This fact is exploited in hybrid simulations, where the ions are described as particles, but the electrons are treated as fluid. This has the advantage of faster simulations compared with particle-in-cell schemes, but neglects electron and charge separation effects. Notable examples of this include Koenders et al. (2013, 2015) and Simon Wedlund et al. (2017). In recent years, fully kinetic simulations where ions and electrons are treated as particles have also become possible, but are limited to cases where collisions in the plasma can be neglected (Deca et al. 2017). This is usually the case at weakly active comets, where the neutral and ion densities are too low for collisions to be important.

At a low activity comet the plasma density is correlated to the neutral gas density, at 67P the plasma and neutral densities both followed a $\sim$ 6 hour periodicity, owing to the presence of two active regions on a rotating nucleus (with a rotation period of $\sim$ 12 hours Heritier et al. 2018) . The effects of solar illumination could also be detected, by the nominally higher plasma densities above the summer hemisphere, although there are exceptions to this due to electron-impact ionisation (Galand et al. 2016). The density profile follows the predicted $1/r$-law, but there are significant variations around the average (Edberg et al. 2015, Odelstad et al. 2015). There are periods where the cometary pickup ions follow the solar wind convective electric field, but that is not always the case (Behar et al. 2016). Typical ion densities were between $< 10\,\mathrm{cm}^{-3}$ and $100\,\mathrm{cm}^{-3}$ with magnetic field magnitudes of 1 nT to 10 nT (Edberg et al. 2015, Goetz et al. 2017, Hajra et al. 2018).

Although the comet's environment at this stage does not have any distinguishable regions, there are still features of interest at this point. The magnetic field is dominated by ultra low frequency waves, often termed "the singing comet waves" (Richter et al. 2015, 2016, Koenders et al. 2016b) and the cometary ions are moving perpendicular to the magnetic field and solar wind velocity (Behar et al. 2016). It was also found that solar wind events such as corotating interaction regions (CIRs) and magnetic holes can penetrate easily and almost unchanged into the innermost cometary regions (Edberg et al. 2016b, Plaschke et al. 2018). No magnetic field draping can be observed at this activity level (see Fig. 5 in Goetz et al. 2017).

For comet 67P this stage corresponds to the months before January 2015 and after March 2016.

Intermediately active comet

The intermediate stage ranges from gas production rates around $10^{26}\,\mathrm{s}^{-1}$ to $5 \times 10^{27}\,\mathrm{s}^{-1}$. Now the gyroradius becomes smaller as the IMF increases, with typical values of $\sim$ 20000 km and smaller. Whereas in the weaker stage, the solar wind velocity was only marginally decreased, the solar wind ions in this stage are deflected and decelerated significantly, in some cases up to 180° (Behar et al. 2017). Close to the comet, the solar wind ions might even be expelled entirely and a solar wind cavity forms. This cavity is asymmetrical and bounded by an infant bow shock (Gunell et al. 2018). This boundary has been identified as a caustic by Behar et al. (2017), but this description is insufficient to describe the thermalisation of the electrons that has been observed to coincide with the solar wind ion cavity boundary (Gunell et al. 2018). Thus a shock gives a more accurate

picture of the situation.

The singing comet waves are diminished and the magnetic field starts to drape around the nucleus at close distances and the power spectral density is increased compared to the previous stage (Goetz et al. 2017, Fig. 5). As the solar wind that carries the field is deflected, the draping was even observed to be in an entirely unexpected plane perpendicular to the Sun-comet line (Koenders et al. 2016a).

At this point an ion collisionopause might have been observed at 67P as a sudden change in plasma properties (Mandt et al. 2016), however at least some of the events in that publication are misidentified CIR impacts (Hajra et al. 2018) and others are similar to the infant bow shock signatures (Gunell et al. 2018), casting doubt on the detection of this region.

For comet 67P this stage corresponds to the months between January and May 2015 and between December 2015 and March 2016, however due to large variations in gas production rate the distinction to the other two stages is not very clear.

Strongly active comet

Finally, comets with gas production rates above 5×10^{27} s^{-1} are considered strongly active. At this point, the fluid picture applies for most of the coma, because the pile-up in the magnetic field causes the ion gyroradius to decrease below the scales of most structures.

The bow shock is now fully developed and ion-cyclotron waves can be observed upstream of the shock, as it was done at 1P during the Giotto flyby (Neubauer et al. 1986). Due to the small gyroradius the ring distribution of the ions in velocity space is complete and in the case of 1P, the ring distribution has changed to a shell in velocity space. This is due to pitch-angle scattering of the ions (Coates and Jones 2009). The solar wind is deflected and decelerated upstream of the solar wind cavity which extends at least 1500 km from the nucleus of 67P (Edberg et al. 2016a). At 1P it was not possible to detect this region with certainty due to instrument failure, however the cometopause at Halley is similar to this feature. There, the density of protons decreases significantly, whereas the density of water ions increases (Gringauz et al. 1986). At 1P, a mystery boundary was also identified, however this could not be verified at 67P (Mandt et al. 2016). The magnetic pile-up boundary at 1P is a region where the magnetic field magnitude and draping suddenly increase. This boundary could not be observed at 67P, which is not surprising, since the observations of this region were made outside the solar wind cavity and the Rosetta orbiter did not leave the solar wind cavity at all during the strongly active stage. At this stage it is also possible to detect lower-hybrid waves (Karlsson et al. 2017), which are known to occur at plasma gradients, and can contribute to electron heating in such plasmas.

In the innermost regions of interaction, the warm electrons from photoionization dominate and cooling seems to not play a significant role, due to low neutral densities. Cold electrons can mostly be found inside the diamagnetic cavity, which is fully developed by now (see section 3).

Examples of this interaction regime are comets 1P/Halley and 67P at perihelion and to a lesser degree Borelly, Giacobini-Zinner and Grigg-Skjellerup.

2.3.4. Transient events at a comet

Transient events are characterized by short durations up to a couple of hours in an otherwise quasistable cometary environment. Two sources can be distinguished: those of cometary origin and those of solar wind origin.

For the first group only outbursts are known to influence the plasma. The diurnal variations of the diffuse outgassing and of jets are reoccuring and thus do not qualify as transients. Only one cometary outburst has been studied so far, because most outbursts observed by Rosetta's cameras occur in the plane that is perpendicular to the line of sight of the camera, which means that the direction of the outburst is 90° from the comet-spacecraft line. These outbursts do not impact the neutral density at the spacecraft (Vincent et al. 2016). However, two outbursts are known to have originated near the subspacecraft point on the nucleus, one on February 19, 2016 and one on July 3, 2016 (Grün et al. 2016, Agarwal et al. 2017). The first event was studied by Hajra et al. (2017) in more detail as regards the plasma response. They found that the overall plasma density increased just after the outburst was observed. At the same time the suprathermal electrons are suppressed, as well as the low frequency wave activity in the magnetic field. The last observation is in direct contradiction to the finding by Goetz et al. (2017), who show that higher neutral gas densities usually lead to higher wave activity in the magnetic field. A possible explanation for this could be that the low-frequency waves have a different generation mechanism than other cometary plasma waves and thus react differently to parameter changes. At that point in the mission, Rosetta was outside of the solar wind ion cavity, but for the duration of the outburst and the subsequent relaxation, the solar wind ions were expelled from the inner coma again. In addition to that a lower ion velocity suggests that the ion-neutral coupling is more efficient during the outburst due to high neutral densities.

The two main transients in the solar wind are CIRs and ICMEs (Smith and Wolfe 1976, Tsurutani et al. 1988). The impact of both has been studied for several different activity levels. CIRs are characterized mainly by higher solar wind velocity, magnetic field and density and originate from active regions on the Sun from where they expand into the solar system. Edberg et al. (2016b) studied four CIR impacts for heliocentric distances larger than 2.7 AU. They found that the plasma density as well as the suprathermal electron flux and the cometary ion flux increased by at least a factor of 2 and the magnetic field magnitude was observed to increase by a similar factor. However, the reaction of the cometary plasma environment to such an event varied from event to event, with one possibly causing a tail disconnection, i.e. a discontinuity in the column density of the comet's tail. However, this could not be confirmed, as remote observations were not available and Rosetta was orbiting too close to the nucleus to detect such an event. Hajra et al. (2018) also studied the reaction of the plasma to CIR impacts more quantitatively with a focus on the outbound leg of the comet's journey around the Sun. They showed that the increase in cometary ion density after the CIR impact was due to additional electron impact ionisation.

Two ICME impacts have been studied at 67P. The first one was observed during the dayside excursion at a heliocentric distance of 1.4 AU. At that time Rosetta was comparatively far away from the comet (800 km) and thus not in the inner coma anymore. The dayside excursion showed that the magnetic field strength in the 1500 km around the nucleus did

not change significantly (Goetz et al. 2017), but also illustrated again that the plasma density decreases with distance. The spacecraft did not leave the solar wind cavity at all during the excursion, indicating that the interaction region at the comet is much larger than expected (e.g. Koenders et al. 2013). The ICME caused a significant compression of the plasma itself, with densities increasing by a factor of 10 and the magnetic field magnitude also increasing by a factor of 2.5. The magnetic field as well as the electron flux after the initial impact exhibit a high amount of variation. During this event, the solar wind ion cavity was also compressed to below spacecraft altitude and a highly deflected and decelerated solar wind population could be observed by RPC-ICA (Edberg et al. 2016a). The detection of flux rope structures in the disturbed plasma after the ICME impact led the authors to speculate about reconnection in the inner coma, however no further evidence was found of this. An increase of the suprathermal electron flux in congruence with the magnetic field increase indicates that at least part of the electron population was subject to adiabatic heating. This event was also studied with the ALICE instrument, an ultraviolet spectrograph (Noonan et al. 2018). They found a significant increase of the UV emissions in the inner coma during the interval that was identified in the Edberg et al. (2016a) publication. This was attributed to an increase in the electron impact ionisation that causes an enhancement of ion density in the inner coma. This fits well with the enhancement in the suprathermal electron flux measured in-situ by RPC-IES. However, they could not make any prediction as to the extension of the diamagnetic cavity before or after the ICME impact.

A second study by (Goetz et al. 2018) confirmed much of the above. For this study, an ICME impact was found at a similar heliocentric distance, but at a much lower cometocentric distance of 170 km. Consequently the plasma densities in the quiet time before the impact were much higher than for the event during the dayside excursion with values around $1000\,\mathrm{cm}^{-3}$ and temperatures around 3 eV to 8 eV. Thus, the initial conditions are very different for this event. The impact of the solar wind event then increased the density to $3000\,\mathrm{cm}^{-3}$ to $7000\,\mathrm{cm}^{-3}$ and the magnetic field reached record breaking values of 300 nT (Goetz et al. 2018, Fig. 1). The plasma experienced a violent increase in electron and cometary ion fluxes as well as electron temperature. However, the interaction was not uniform, the plasma experienced at least two different states after the onset, which alternated when the magnetic field cone angle changed significantly. This was attributed to effects of magnetic connectivity, which means that the spacecraft is connected magnetically to different parts of the coma, with different plasma properties. However, an alternating structure in the solar wind could not be ruled out as the trigger for this kind of behaviour. For this event no solar wind protons were observed in the inner coma, an observation that is easily explained by the smaller distance of the spacecraft to the nucleus. Simple models showed that the bow shock was still very far from the spacecraft position even for extremely high solar wind dynamic pressures. No flux ropes could be observed, putting into doubt the previous explanation of reconnection in the inner coma causing these structures.

It should be noted that the origin of this signature is here identified as ICME-triggered, but in the publication it was also speculated that the ICME could have interacted with a CIR while encountering the comet. This coincidence of the two events is one way to explain the unusual features in the observations. The existence of a Forbush decrease (Cane 2000, Goetz et al. 2018, Fig. 3) preceding the event is indicative of an ICME,

necessitating that the ICME is the dominant component of the solar wind event.

3 The Diamagnetic Cavity

It was speculated very early that the peculiar situation of the induced cometosphere would produce a region around the nucleus that could not be reached by the solar wind, if the gas production rate was sufficiently high. As a consequence, the magnetic field that is carried along with the solar wind cannot reach this region either, and with cometary nuclei having no magnetic field of their own, a completely field free region is formed. This chapter concerns the structure and formation of that region. It should be noted at this point that the boundary layer surrounding that region has different names in literature. Although it is often referred to as a contact surface or ionopause, here it is called the diamagnetic cavity boundary, for reasons that will become clear in the following.

	AMPTE	1P	67P
R (AU)	1	0.9	1.24
Q (1/s)	10^{25}	7×10^{29}	10^{28}
ν_p (1/s)	0.036	10^{-6}	5×10^{-7}
u_n (km/s)	1.35	1	1
α (m^3/s)	10^{-18}	7.4×10^{-14}	-
B_0 (nT)	130	60	40
k_{in} (m^3/s)	1.2×10^{-15}	1.1×10^{-15}	1.1×10^{-15}
n_i (cm^{-3})	500	1000	1000
ω_{gi} (1/s)	0.1	0.3	0.2
ω_{ge} (1/s)	22800	10680	7040
l_ν (km)	38	1×10^6	2×10^6
v_A (km/s)	11	9.5	6.3

Table 3.1.: Relevant length and time scales and their input parameters for the AMPTE release experiments as well as for comet 67P and comet 1P at Giotto. Scales are calculated for the inner coma. All parameters at real comets are based on water, whereas the AMPTE experiment uses barium ions. All values are taken from Luehr et al. (1986), Valenzuela et al. (1986), Cravens (1987), Sauer and Baumgaertel (1987) and Hansen et al. (2016).

3.1. The diamagnetic cavity before Rosetta

Biermann et al. (1967) and Galeev et al. (1985) realized that their fluid model of the cometary plasma had a particular consequence, namely that the flow would stagnate at some distance r_c in front of the comet, if the mass loading exceeds a certain threshold. As a consequence of this, they speculated that there might be a region without a magnetic field at cometocentric distances smaller than r_c. However, even if the flow stagnates, there could still be diffusion of the magnetic field into the inner region. It was then speculated that the dynamic pressure of the outflowing cometary ions would limit this diffusion and maintain the diamagnetic cavity.

In preparation for the Giotto mission to comet 1P, an experiment was designed to investigate not only the diamagnetic cavity, but the entire interaction of a comet with a plasma flow. This Active Magnetospheric Particle Tracer Experiment (AMPTE) consisted of two spacecraft, the Ion Release Module (IRM) and the United Kingdom Satellite (UKS). The ion release module was build to release small cans of pressurized gas, either Barium or Lithium, into the solar wind or magnetospheric plasma at Earth (Valenzuela et al. 1986). Both satellites then monitored the magnetic field and plasma parameters. For the sake of comparability, only the experiments in the solar wind are considered here, as they are closest to a real comet in parameter space. For the releases in the magnetosphere, the dynamic pressure of the plasma flow was much smaller and thus does not represent the real comet accurately.

The two Barium releases in the solar wind are described in detail in Valenzuela et al. (1986), Haerendel et al. (1986), Rodgers et al. (1986) and Luehr et al. (1986). A Lithium release experiment is described in Sauer and Baumgaertel (1987). Besides the remote observations of a comet head and tail, they also observed the magnetic field draping and the formation of a field free region. To compare this artificial comet with a real comet, it is advantageous to investigate the length and time scales for both cases, which are listed in Tab. 3.1. The table gives estimates for comet 67P at perihelion and comet 1P during the Giotto flyby, as well as the AMPTE Barium experiments in December 1984. From the table, one can see that most parameters are very similar between the comets and the artificial comet. Although the gas production rate is lower for the latter, the extremely high ionisation rate of Barium combined with the seven times higher mass (137 amu instead of 18 − 19 amu) give very similar values of the cometary ion density n_i in the inner coma. The table also lists the values for the ionisation length scale

$$l_\nu = \frac{u_n}{\nu_p} \tag{3.1}$$

which gives the distance that, statistically, a neutral molecule can travel before it is ionised. These values are extremely different for the artificial comet, with values around 40 km instead of millions of km in the case of a real comet. Stallmann (2018) found that this results in an extremely compressed cometosheath, which is shrunk to almost non-existence. This is due to the fact that the mass-loading region scales with l_ν because the cometary ions in the solar wind upstream of the comet (and its bow shock) are newborn from neutrals that can move far from the nucleus before being ionised. For the artificial comet, almost all neutrals are ionised behind the bow shock and upstream mass-loading is negligible. For the formation of a diamagnetic cavity, this behaviour will be less consequential, because

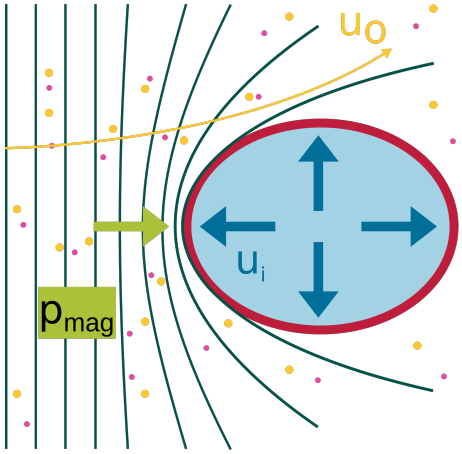

Figure 3.1.: Sketch of the pressure balance at the diamagnetic cavity boundary in the plane that contains the magnetic field and upstream flow. Magnetic field lines are indicated in dark green and electrons and ions are pink and yellow. The yellow arrow shows the bulk velocity of the plasma around the diamagnetic cavity which is indicated in blue. The velocity of the plasma inside the diamagnetic cavity is shown in dark blue. The magnetic pressure (light green) should be balanced by another pressure at the boundary (red).

the flow near the diamagnetic cavity has stagnated already and it is unimportant for the model how this stagnation was achieved. Thus, the diamagnetic cavity at a comet should be comparable to that of the artificial Barium comet.

The assumption for all models is that the solar wind fluid with its magnetic field has already reached a stagnation point x_s, which means that $\vec{u}_{sw}(x_s) = 0$. Thus all dynamic pressure from the solar wind has been converted into magnetic pressure:

$$\frac{B^2}{2\mu_0} = \rho_{sw}\vec{u}_{sw}^2 \tag{3.2}$$

where the solar wind values are taken in the undisturbed solar wind. This equality is a direct result of the 1D fluid approach to the mass-loading problem and it has been verified for several comets (Richter et al. 2011). For the artificial comet, this equality does not seem to be satisfied, as the dynamic pressure is approximately the same in the solar wind, but the magnetic field in the pile-up region is more than twice as high as expected from the pressure equality. Haerendel et al. (1986) use another estimation of the magnetic field in the pile-up region, in which the compression ratio B_0/B_∞ is equal to the alfvénic Mach number in the solar wind. This is in good agreement with the AMPTE-UKS measurements, but does not agree with measurements at comets 1P or 67P. Haerendel et al. (1986) derived this relationship by calculating the behavior of a flux tube that encounters the comet and drapes around the cometosphere, from which a diamagnetic cavity distance is then also derived. This distance is much lower than observed at comet 1P and does not predict a cavity at all for a gas production rate below $2 \times 10^{28}\,\mathrm{s}^{-1}$, which also does not agree with observations at 67P (Goetz et al. 2016a). Therefore the model seems to be doubtful at the least.

This discrepancy warrants further investigations of the magnetic field profile during the AMPTE Barium releases. Fig. 3.2 shows the measurements of the IRM magnetometer

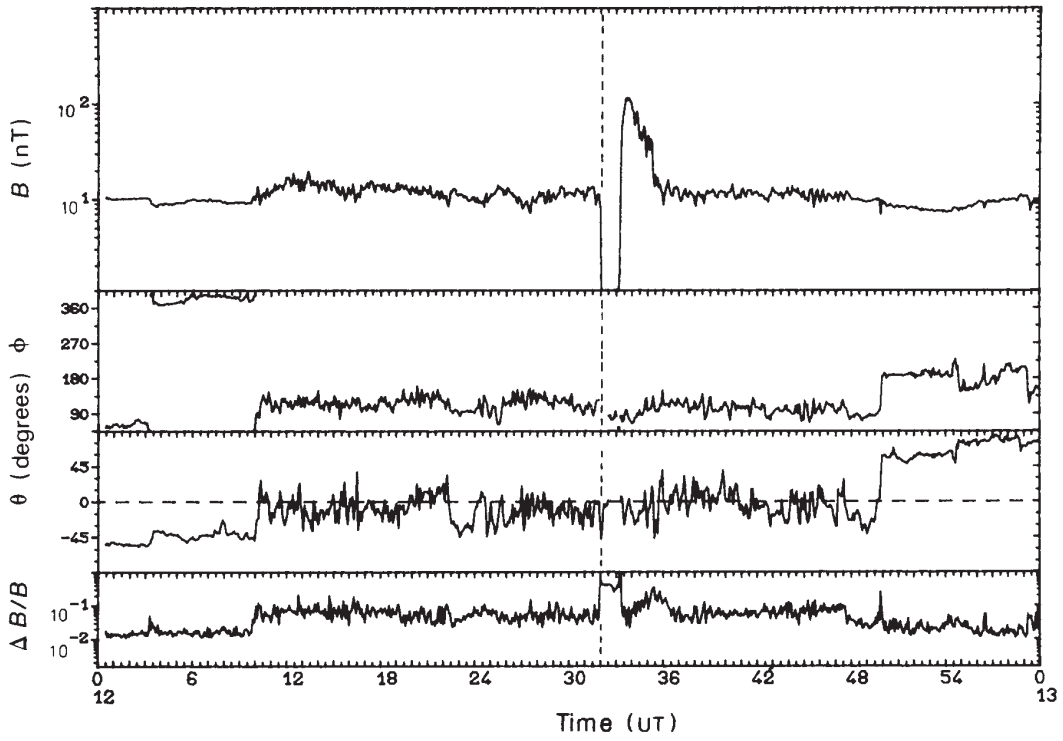

Figure 3.2.: Magnetic field measurements from AMPTE-IRM during a Barium release, with elevation θ and azimuth Φ given in Geocentric solar ecliptic coordinates. The last panel shows the variability of the field. The release time is indicated by the vertical dashed line. Adapted from Luehr et al. (1986). Reprinted with permission from the publishers.

during the AMPTE Barium release in December 1984. The field before the release is indicative of the spacecraft being in the foreshock region of the magnetosphere at Earth. Then, after the Barium release the magnetic field decreases to zero for about a minute before increasing again to a maximum of around 100 nT. In total the magnetic field signatures of the artificial comet last for about 4 min. Thus the high field in the magnetic pile-up region is not actually the field in the stationary pile-up region in front of a diamagnetic cavity at a comet, but the moving field in the high density region that overtakes the diamagnetic cavity as the Barium cloud is moving downstream with the plasma. This could explain the discrepancy.

Regarding diamagnetic cavity formation, Haerendel et al. (1986) find that the dynamic pressure of the expanding ion cloud is sufficient to prevent the magnetic field from entering the densest part of the ion cloud. Thus a pressure balance exists at the interface between dynamic pressure and magnetic pressure (see Fig. 3.1). However, Valenzuela et al. (1986) and Luehr et al. (1988) showed that the thermal pressure of the new electrons could also be sufficient to balance the magnetic pressure. Numerical simulations by Sauer and Baumgaertel (1987) showed that the dynamic pressure was the more favorable of the two mechanisms. A more detailed study was not conducted and the data quality seems to be insufficient at this point to exclude any of the two mechanisms.

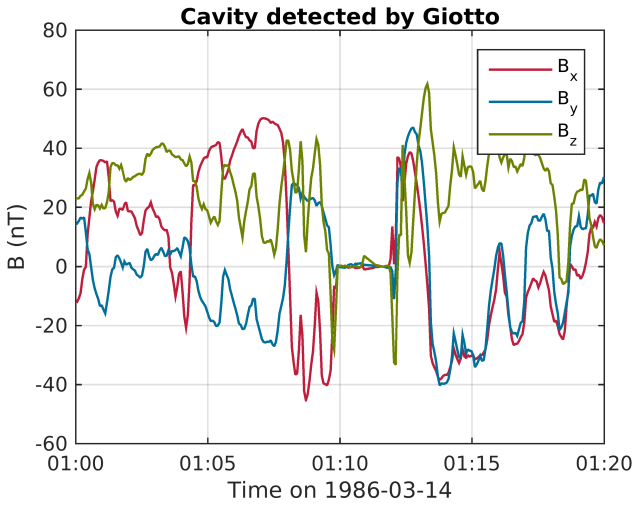

Figure 3.3.: Magnetometer measurements during Giotto's flyby at comet 1P. Only the innermost part of the flyby is shown, so that the zero field measurements in the diamagnetic cavity are clearly seen. Datasets of the Giotto MAG instrument have been downloaded from the ESA Planetary Science Archive (http://archives.esac.esa.int/psa).

Giotto's results

Of all spacecraft that visited comets prior to the Rosetta mission, only Giotto was able to traverse and investigate the diamagnetic cavity, because all other spacecraft passed the comet at too large distances, whereas Giotto's closest approach was ~ 600 km (Reinhard 1986). Neubauer et al. (1986) were the first to present the magnetometer measurements in Halley's coma, which for the most part agreed well with expectations. They identified signatures of a bow shock, a pile-up region and the diamagnetic cavity as well as low-frequency wave activity associated with a gyrotropic cometary ion distribution. In general the position of the regions also agreed well with predictions from models like the ones presented in Biermann et al. (1967) or Galeev et al. (1985). The magnetic field measurements in the inner coma of comet 1P are shown in Fig. 3.3. The diamagnetic cavity is clearly visible as a period of low field magnitude and fluctuation. The magnetic field in the pile-up region, just outside the cavity, has a magnitude of ~ 65 nT, which is in good agreement with the models as well (Goetz et al. 2017).

After Giotto's measurements at comet 1P, it became clear that the dynamic pressure of the expanding ions was not sufficient for the formation of a completely field free region. This was mainly due to the discovery that the cometary ion density and velocity did not change at the boundary, meaning that the dynamic pressure on each side was similar. This warranted an overhaul of the theory regarding the diamagnetic cavity formation and the plasma in that region.

The most commonly acknowledged explanation for the formation of the diamagnetic cavity at 1P is the one presented in Cravens (1986) and Cravens (1987). Based on plasma parameters determined by Giotto, they propose that the ion-neutral drag is the most significant term in the momentum equation, which then becomes:

$$\left(\vec{j} \times \vec{B}\right)_r = n_i m_i k_{in} n_n \left(\vec{u_i} - \vec{u_n}\right)_r \tag{3.3}$$

where $m_n = m_i$ is assumed. As stated in section 2.1, the left-hand-side of that equation can be expanded into the magnetic pressure and magnetic tension:

$$\left(\frac{(\vec{B}\cdot\nabla)\vec{B}}{\mu_0}\right)_r - \frac{\partial}{\partial r}\frac{B^2}{2\mu_0} = n_i m_i k_{in} n_n (\vec{u_i} - \vec{u_n})_r \tag{3.4}$$

where the r indicates that only the radial component is used. This is one of the simplifications made by the model, which uses only a radial outflow from the comet and is strictly speaking only valid on the stagnation streamline. Another assumption here is that the incoming plasma in the inner coma is already at rest, thus all dynamic pressure has been converted into magnetic pressure. The magnetic tension is then shown to be negligible. This is easily done by considering the curvature radius R_{curv} of the magnetic field lines, which must be slightly larger than the radius of the diamagnetic cavity itself, because the field lines drape around this cavity. The radius of the diamagnetic cavity at 1P was determined to be $\sim 5000\,\mathrm{km}$, which gives an estimate of the magnetic tension:

$$\left(\frac{(\vec{B}\cdot\nabla)\vec{B}}{\mu_0}\right)_r \approx \frac{B^2}{\mu_0 R_{curv}} = 6\times10^{-4}\mathrm{nPa/km} \tag{3.5}$$

The estimate for the magnetic pressure is then

$$\frac{\partial}{\partial r}\frac{B^2}{2\mu_0} \approx \frac{B^2}{2\mu_0 l} = 6\times10^{-2}\mathrm{nPa/km} \tag{3.6}$$

which is two orders of magnitude larger than the magnetic tension. Here $l = 25\,\mathrm{km}$ was used as the thickness of the transition region (Koenders et al. 2015, Goetz et al. 2016a). Therefore, the momentum equation can be simplified to contain only the magnetic pressure and ion-neutral drag. Next, the Cravens model assumes that the plasma inside the diamagnetic cavity is in photochemical equilibrium. The ion velocity inside the diamagnetic cavity then equals the neutral velocity, because a newly created ion is born with $u_i = u_n$ and then removed before they can be accelerated. Close to the boundary, the cometary ion velocity is assumed to be zero, because the flow should stagnate at the boundary. Thus the ion profile from Eq. 2.33 may be used for the ion density. Eq. 2.27 can be used for the neutral density profile, where the exponential term may be neglected because r is small. Then Eq. 3.4 becomes:

$$-\frac{\partial}{\partial r}\frac{B^2}{2\mu_0} = -m_i k_{in}\left(\frac{Q}{4\pi}\right)^{\frac{3}{2}}\sqrt{\frac{\nu_p}{\alpha u_n}}\frac{1}{r^3} \tag{3.7}$$

which can be integrated from infinity to any r' outside of the diamagnetic cavity boundary r_c:

$$B(r')^2 = B_0^2 - \mu_0 m_i k_{in}\left(\frac{Q}{4\pi}\right)^{\frac{3}{2}}\sqrt{\frac{\nu_p}{\alpha u_n}}\frac{1}{(r')^2} \tag{3.8}$$

where B_0 is the magnitude of the field in the pile-up region (i. e. at infinity). Then the diamagnetic cavity distance is the radius at which $B = 0\,\mathrm{nT}$:

$$r_c^2 = \frac{\mu_0 m_i k_{in}}{B_0^2}\left(\frac{Q}{4\pi}\right)^{\frac{3}{2}}\sqrt{\frac{\nu_p}{\alpha u_n}}. \tag{3.9}$$

Thus the diamagnetic cavity contracts when the field in the pile-up region is high (more magnetic pressure) and it expands if the gas production rate or the ion-neutral friction coefficient increase. With typical values at comet 1P r_c = 5000 km which agrees well with measurements (Neubauer et al. 1986). Fig. 3.6 shows the magnetic field profile at the diamagnetic cavity for this case.

In the following years, no other feasible model emerged, and the ion-neutral friction was thought to be crucial for the generation mechanism of the diamagnetic cavity.

Neubauer (1987) then tried to model the shape of the diamagnetic cavity. They determined the boundary normal upon entry and exit and fit a displaced sphere to the position and boundary normal. Because this sphere had a very large displacement in y- and z-directions, they also found that the diamagnetic cavity could be described by a nucleus centered sphere with small ripples in the boundary, both cases are illustrated in Fig. 3.4. After this, Ershkovich and Mendis (1986) and Ershkovich and Flammer (1988) investigated the stability of the boundary and found that it was probably unstable to the Kelvin-Helmholtz and flute instabilities. This was later also shown to be the case in 3D MHD simulations (Rubin et al. 2012), thus making the rippled diamagnetic cavity a likely scenario.

At this point, it remains to be discussed if the diamagnetic cavity boundary can also be called an ionopause or contact surface. Neubauer (1988) argued that it is an ionopause and not a contact surface, because the magnetic field shows that it is a tangential discontinuity and not a contact discontinuity. It is also analogous to the magnetopause at Earth, which separates the solar wind driven part of the plasma from the inner sources driven part of the plasma. As will be shown in the next section, this boundary may not even be a true ionopause because it can be extremely porous, with electrons and ions simply traversing the boundary. However, since the absence of the field inside the boundary is a common feature in any case, here it will be referred to as the diamagnetic cavity boundary.

3.2. Rosetta's discoveries

After the spacecraft entered a safe mode in March 2015 caused by star tracker malfunction due to high dust densities in the coma, the cometocentric distance of Rosetta was raised significantly to avoid permanently losing or damaging the spacecraft. Consequently, the diamagnetic cavity, which was projected to extend only up until 50 km (Koenders et al. 2015), was thought to be out of reach. Goetz et al. (2016b) then reported that short intervals could be found in the magnetic field data which displayed a remarkably quiet and constant magnetic field (see Fig. 1 in A.1). Although a magnetic field magnitude of a few nT remained in the measurements, it was concluded that the signature was indicative of the diamagnetic cavity and that the remaining field was simply due to spacecraft disturbance fields. Since the event was found at much larger than predicted distance of 170 km, the authors speculated that the diamagnetic cavity might be a highly dynamic structure. This was supported by the fact that the event was intermittent and of relatively short duration (25 min). As the Rosetta spacecraft was moving slowly with respect to the plasma and nucleus ($\sim$ 1 m/s), the diamagnetic cavity boundary was determined to be moving over the spacecraft. Another possibility for this behaviour was raised by Huang et al. (2016a), who presented simulations where the electron pressure had been artificially increased in

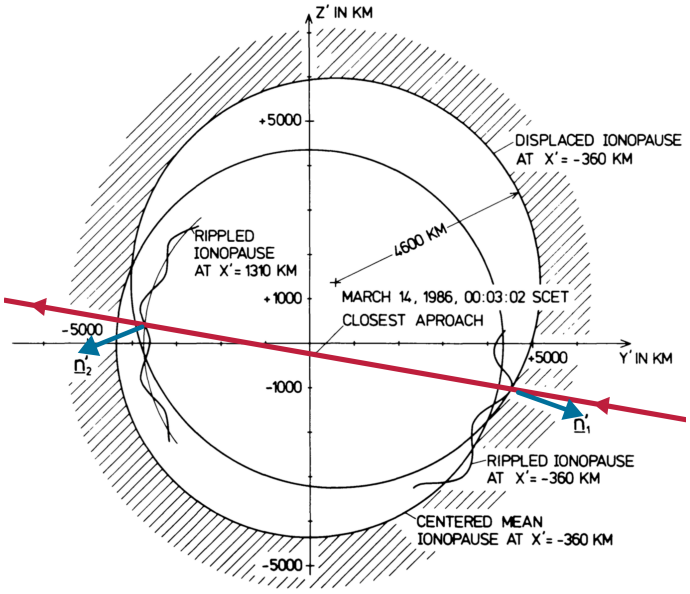

Figure 3.4.: Sketch of the diamagnetic cavity at comet 1P. The red line indicates the Giotto trajectory and the blue arrows show the orientation of the boundary normal, derived from a minimum variance analysis. Adapted from Neubauer (1987). Reprinted with permission from the publishers.

a certain region. This also created a magnetic field free region. This possibility was then later discarded in Goetz et al. (2016a), as the regularity of the events and gas production rate dependence indicated that the diamagnetic cavity was indeed a global structure. It was also shown by Goetz et al. (2016a) that a small, outgassing boulder of cometary origin passing close to the spacecraft could not provide enough additional ions to create a diamagnetic cavity of the observed duration. Thus it was concluded that an instability of the boundary was the cause of the unexpected size of the diamagnetic cavity, which was corroborated by an estimation of the stability criterion for the Kelvin-Helmholtz instability, which showed that it could very well be satisfied for the diamagnetic cavity boundary. Goetz et al. (2016b) were also the first to note that the diamagnetic cavity at 67P was surrounded by large amplitude, asymmetric fluctuation which were later investigated by Stenberg Wieser et al. (2017) and Engelhardt et al. (2018).

After this initial report, a follow-up study was published (Goetz et al. 2016a) in which it was shown that Rosetta had actually crossed into the diamagnetic cavity more than 600 times, with dwell times ranging from only seconds up to 40 min. These crossings occurred for gas production rates larger than $6 \times 10^{26} \mathrm{s}^{-1}$ and heliocentric distances below 2.4 AU. Therefore a more detailed study could be performed and it was found that, in general, as gas production increased, so did the extension of the diamagnetic cavity. Some events were detected in clusters, while other events were singular. Examples of the two types of detections are given in Fig. 1 in A.2. All crossings had a similar appearance in the magnetic field observation: after a prolonged decrease of the magnitude follows an interval with close to zero field, whereas the subsequent increase tends to be much sharper (see Fig. 1 and 2 in A.2). This asymmetry is similar to the large amplitude variations surrounding the cavity, which tend to have a sharp increase in magnitude and a long decay

timescale. Additionally, Goetz et al. (2016a) find that the diamagnetic cavity radius can be described as a function of gas production rate, indeed with a simple power law. It was then shown that all diamagnetic cavities that were observed after Spring equinox (May 2015) could be described by a $Q^{0.6}$-law, where Q was empirically obtained from the Hansen et al. (2016) model. The diamagnetic cavity observations before that time were unusual in the sense that they were large outliers in the fit, thus they were not considered. At that point it was not clear why these events were so different.

The left panel in Fig. 3.5 shows a very different exponent for the power law fit, because the estimate of the gas production rate was determined from in-situ ROSINA-COPS measurements. The figure shows all events, and the difference between the events before equinox and after equinox is greatly diminished. With this it becomes clear that the empirical model for the gas production rate greatly underestimates the actual measured gas production rate around spring equinox and the measured-density-derived gas production rate is a much better predictor for r_c than the empirical model. The right hand side of Fig. 3.5 attempts to take into account the magnitude of the magnetic field in the pile up region as well as the gas production rate. It is assumed that $r_c \propto B_o^{-1}$ in accordance with the Cravens model. This assumption seems justified, as a higher magnetic pressure should decrease the size of the diamagnetic cavity. The goodness of the power law fit is then slightly improved, but still below a significance threshold of 0.7. The magnetic field was determined as the mean field in the hour before and after the event, with the exclusion of other cavity events. No further conclusion can be drawn from this, except that the interplay of gas production rate, magnetic field magnitude and diamagnetic cavity size is still too poorly understood for a more sophisticated model.

Contrary to the Cravens model, the gas production rate then did not follow a 3/4-law with respect to the diamagnetic cavity radius r_c. This was a first indication that this model may not be applicable at 67P. It should be noted here that Timar et al. (2017) used the Cravens model to predict the diamagnetic cavity radius and found some agreement with the measurements. Their assumption was that the large amplitude waves outside of the diamagnetic cavity were evidence of Rosetta moving along the increasing flank of the magnetic field profile of the Cravens model and thus the peak values would represent the field magnitude in the pile-up region. This is not corroborated by further analyses. In revisiting the Cravens model, it is found that the assumption of photochemical equilibrium is not supported by observations and models at 67P. For example, Vigren et al. (2017) and Odelstad et al. (2018) find that the ion velocity close to the diamagnetic cavity boundary is $1-4$ km/s and thus larger than the neutral gas expansion velocity and certainly larger than the zero velocity that is assumed in the Cravens model. Additionally, as shown in section 2.2, the transport term cannot be ignored in the inner coma of 67P, and the recombination term only plays a role near perihelion (Beth et al. 2018). This means that the ion profile used in the Cravens model is not applicable at 67P and the profile from Eq. 2.30 has to be used. This gives a different expression for the magnetic field profile:

$$(B(r'))^2 = B_0^2 - \frac{\mu_0 Q^2 m_i \nu_p k_{in}}{16\pi^2 u_n^2 r'^2}. \tag{3.10}$$

It should be noted that this model is not self-consistent, as it uses $u_i = u_n$ which is not true when the transport term is non-negligible. Fig. 3.6 shows a comparison of the magnetic field model at 67P from the Cravens model, either with the recombination dominated or

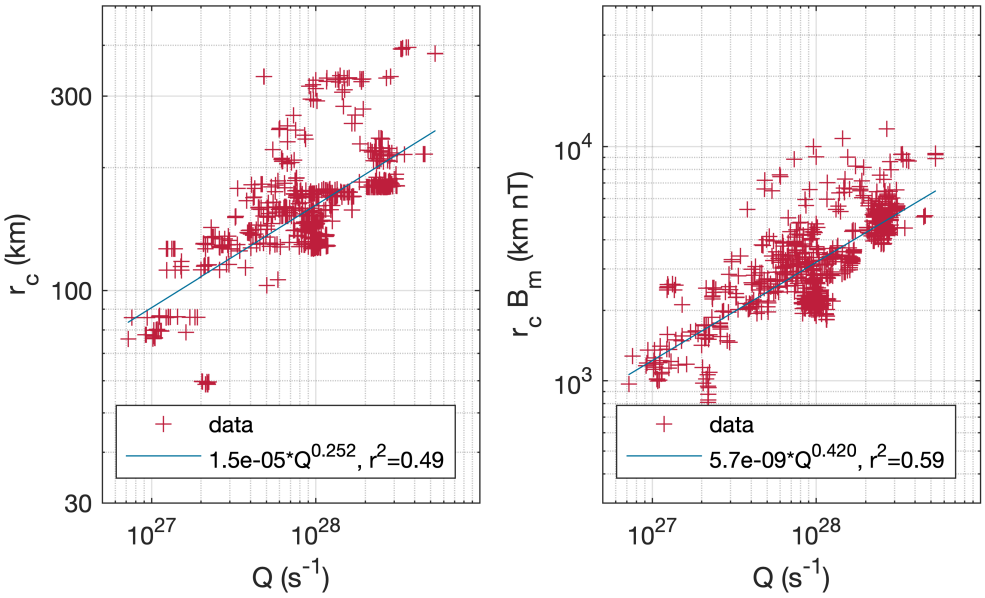

Figure 3.5.: Diamagnetic cavity distance and diamagnetic cavity distance modified by the magnetic field over gas production rate. The data (red) was fitted with a linear least squares fit in logarithmic scaling (blue), the fit parameters are given in the legend. The local gas production rate was derived from the ROSINA in-situ total number density measurements using a Haser model type outgassing with a neutral velocity u_n = 1 km/s.

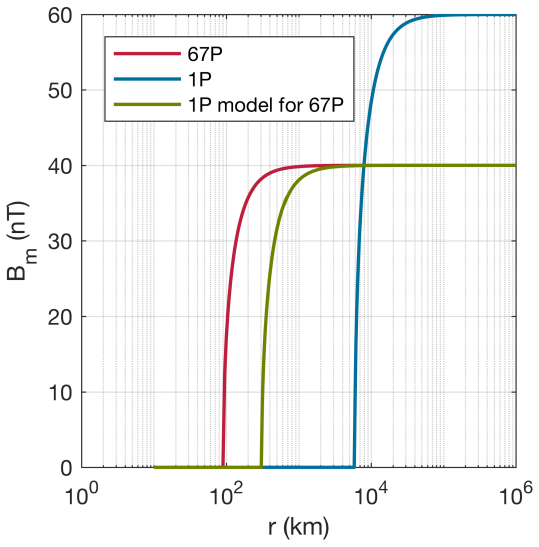

	1P	67P
Q (1/s)	7×10^{29}	10^{28}
ν_p (1/s)	10^{-6}	5×10^{-7}
u_n (km/s)	1	1
α (m^3/s)	7.4×10^{-14}	-
B_0 (nT)	60	40
k_{in} (m^3/s)	1.1×10^{-15}	1.1×10^{-15}

Figure 3.6.: Comparison of the magnetic field profile as determined by the Cravens model at 1P (photochemical equilibrium) and 67P (transport only, no chemical loss) and the 1P model for 67P parameters (photochemical equilibrium). The two cases for 67P are the same as in Fig. 2.4. The table on the right lists the input parameters for the models.

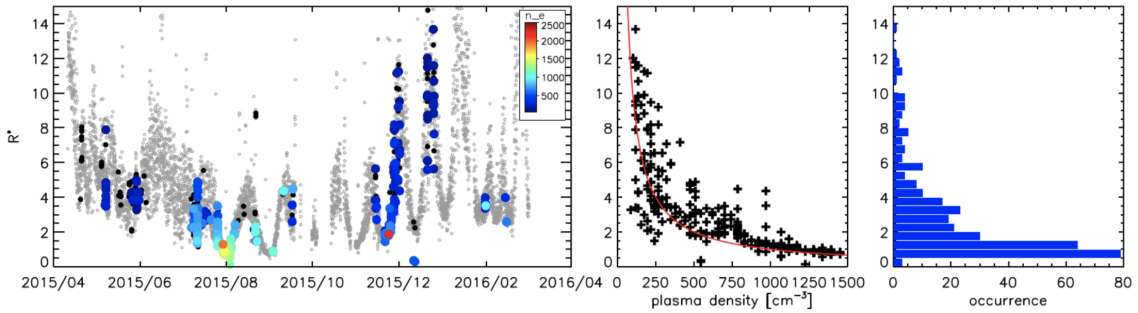

Figure 3.7.: Distance of the diamagnetic cavity boundary with regards to the electron neutral collisionopause over time, and density. The value R^* represents r_c/L_e, and the right panel gives the summed occurrence rate of the diamagnetic cavity detection with regards to R^*. Adapted from Fig. 5 in Henri et al. (2017). Reprinted with permission from the publishers.

with the transport dominated ion profile. Although the general shape of the function is the same, the distance r_c which appears as the intersection of the function with the x-axis, is significantly different. The more realistic model predicts $r_c = 100\,\mathrm{km}$ whereas the other (Halley-type) model predicts 2.5 times that distance. In reality, the ion profile will be a mixture of the two extremes presented here, thus the most realistic magnitude profile will then lie below the two cases shown here. It should be noted at this point that the model used here still uses the ion-neutral friction term in the momentum equation, but as Odelstad et al. (2018) showed the ion velocity at 67P is actually larger than the neutral velocity, which changes the sign of the ion-neutral friction term in the momentum equation. Then the force will not be outward but inward and cannot prevent the magnetic field from entering the innermost coma. The high ion velocities are compelling evidence against the ion-neutral friction force as the opponent of the magnetic pressure. Indeed, Odelstad et al. (2018) find that the measured ion velocity close to the diamagnetic cavity boundary is not affected by changes in the in-situ neutral density at all. If the ion-neutral coupling were effective in decelerating the ions, there should be an anti-correlation between the two quantities. This adds to the case against the ion-neutral friction as an important term in the momentum equation.

Multiple investigations have since shed new light on the situation in and around the diamagnetic cavity. Henri et al. (2017) found that the plasma density in the diamagnetic cavity was much less disturbed than outside and that the density outside was higher than inside. An important result of that study was that the diamagnetic cavity boundary distance could be related to the electron-neutral collisionopause as defined by Eq. 2.34. Fig. 3.7 shows the relative distance of the cavity boundary crossings at Rosetta over time and electron density. For the calculations of the collisionopause in-situ measurements by ROSINA-COPS and RPC-MIP electron densities were used. It was also found that the clustered events were preferentially found very close to the electron collisionopause, whereas singular events were mostly detected further outside of that region. It was also found that the asymmetric wave structures visible in the magnetic field in the inner coma, just outside the diamagnetic cavity, was accompanied by large amplitude variation in the electron density as well as the ion spectra, with fluxes and energies increasing in phase with the magnetic field (Henri et al. 2017, Stenberg Wieser et al. 2017).

Nemeth et al. (2016) and Madanian et al. (2017) investigated the electron spectra close to the diamagnetic cavity boundary. They found in particular that the fluxes of electron populations between 60 eV and 100 eV and between 150 eV and 250 eV are decreased inside the diamagnetic cavity. This is explained by shielding of the solar wind electrons at the cavity boundary. This absence of parts of the suprathermal electron population is contradictive of the magnetic field dropout thesis presented in Huang et al. (2016a), as those simulations required a sudden increase in the suprathermal electron population inside the field-free region.

In addition to a decrease in electrons, the plasma in the diamagnetic cavity is sometimes dominated by high density "blobs" of plasma (Hajra et al. 2017). These have a remarkable similarity to the asymmetric wave structures outside of the cavity in a sense that their profile is also steepened and the duration is similar. The compression ratio of the unmagnetized density enhancement is slightly lower than that of the magnetized one. They estimate the scale of these structures to be larger than the diamagnetic cavity itself, thus the entire region is filled with the high density plasma. The propagation direction of the density enhancements is thought to be cometward, i.e. from the boundary toward the comet. This implies that the asymmetric waves propagate toward the boundary (from outside) and are sometimes transmitted through the boundary, although the exact nature of this transmission is not elaborated on.

The plasma inside the diamagnetic cavity shows signs of a mix of a cold and a warm electron population, whereas the warm population dominates outside (Gilet et al. 2017, Eriksson et al. 2017, Odelstad et al. 2018). As the diamagnetic cavity was mostly detected close to, but outside of, the electron collisionopause, this indicates that the electrons are cooled only closer to the comet and then move outward to be detected by the spacecraft.

To better understand the region in the diamagnetic cavity several studies have investigated the plasma wave activity in that region. For example, Madsen et al. (2018) found that the electric field fluctuations in the diamagnetic cavity were suppressed compared to the magnetized plasma. Gunell et al. (2017) found ion acoustic waves in the cavity with frequencies around 200 Hz. As these waves do not occur outside of the cavity, they propose that the wave generation mechanism is related to a strong current close to the boundary layer. This current could form as a consequence of the highly unstable boundary, where boundary currents may be closed through a small part of the diamagnetic cavity itself. This finding agrees with Goetz et al. (2016a,b) and Henri et al. (2017), who also found evidence of a highly dynamic and unstable boundary. They suggest that this is due to an instability like the Kelvin-Helmholtz instability. Simulations for comet 1P (Rubin et al. 2012) and measurements at the same comet (Neubauer 1987) also suggest that the boundary is unstable, making this a very likely scenario.

The plasma flow pattern in and around the diamagnetic cavity is still unclear. The main obstacle for measurements of the flow direction of the ions is the very negative spacecraft potential. It has been shown that slow ions can be deflected by the spacecraft potential, which means that directional information is lost as they hit a detector (Masunaga et al. in preparation). However, spacecraft wake effects indicate that the bulk plasma flow (inferred from the electrons) is directed radially outward (Odelstad et al. 2018). The high density "blobs" of plasma are an exception to this, as they are shown to propagate inward from the diamagnetic cavity boundary, whereas usually the plasma outside of the cavity flows tailward (Masunaga et al. in preparation).

The preceding discussions show that the plasma around the cavity boundary is still poorly understood. Fig. 3.8 is an attempt to illustrate the conditions in that region. The left panel shows the situation during normal conditions: the magnetic field strength and the plasma density are lower inside the cavity and the plasma is expanding radially outward. The cold electrons are produced close to the nucleus and expand outward into a warm plasma. There are pronounced compressional magnetic field waves outside of the cavity and the field is draped around it. Solar wind electrons gyrate along the magnetic field lines and cannot enter the magnetic field free region, which is non-spherical and has an irregular surface. The plane perpendicular to the magnetic field is not shown, but it is reasonable to assume that the magnetic field is draped as well with a velocity component perpendicular to the field line and the surface normal. This enables the field to flow around the diamagnetic cavity. In the right panel, the magnetic field is still zero in the innermost region, but the density is enhanced. This is the case during one of the high density events in the cavity (Hajra et al. 2017). In this case, the bulk velocity of the ions is tailward and electrons are warm. The high density "blob" fills the entire cavity region, and the plasma somehow penetrates the magnetic cavity boundary without carrying the magnetic field. It is not clear yet which mechanism could cause this behaviour. The spacecraft is depicted at the terminator of the nucleus, which was by far the most common configuration of measurement. Note that this illustration makes no claim as to the pressure balance or lack thereof, but the dynamics of the ions and electrons indicate that the ion-neutral friction is not significant at comet 67P.

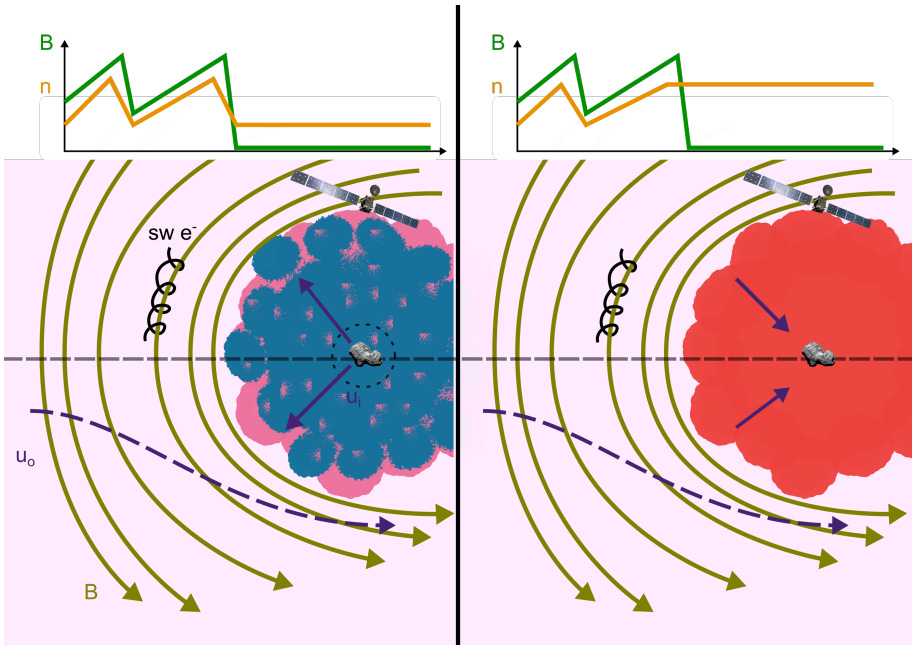

Figure 3.8.: Sketch of the plasma in and around the diamagnetic cavity at 67P in the crosssection that contains the draped magnetic field lines (green). The flow of the plasma inside (u_i) and outside (u_o) is shown in purple and an exemplary solar wind electron trajectory near the cavity is shown in black. The light pink background indicates the existence of warm electrons everywhere in the inner coma. The diamagnetic cavity is colored according to the electron temperature and density in that region (blue: cold, pink: warm, red: warm, dense) and the electron collisionopause is shown as a black dotted circle. The line plot on top shows the magnetic field and density values along the grey dashed line. The situation in the left panel is the most common one: a mix of cold and warm electrons below the collisionopause and predominantly warm electrons outside of it. The right panel shows the situation during a high density "blob" with reversed flow direction and warmer electrons (Credit: ESA/ATG medialab and ESA/Rosetta/MPS for OSIRIS Team MPS/UPD/LAM/IAA/SSO/INTA/UPM/DASP/IDA).

4 Summary

The ESA Rosetta mission has greatly enhanced our knowledge of comets during its operation from 2014 to 2016. Observations of comet 67P/Churyumov-Gerasimenko and its surroundings were made during an entire perihelion passage and enable the study of the evolution of a comet for the first time. Although the contributions to fields like solar system formation and origin of comets were significant, this work is focused on how the plasma at the comet is affected by the solar wind flow. As the gas leaving the comet is ionised the solar wind is slowed down by the additional mass from the heavy cometary water ions and, depending on the gas production rate, different regions may form. For simplicity, three stages of interaction have been identified:

- weakly active with gas production rates below $10^{26}\mathrm{s}^{-1}$,
- intermediately active with gas production rates between $10^{26}\mathrm{s}^{-1}$ and $5 \times 10^{27}\mathrm{s}^{-1}$,
- strongly active with gas production rates above $5 \times 10^{27}\mathrm{s}^{-1}$.

During the weakly active stage, the solar wind is only marginally slowed and magnetic field waves (singing comet waves) occur. This changes in the intermediately active stage, where boundaries in the plasma environment start to form, e.g. the solar wind cavity. This region is free of solar wind ions and bounded by an infant bow shock. At this point the magnetic field starts to show signs of draping, albeit in an unexpected plane. And lastly, the strongly active stage at 67P is most comparable to previously visited comets, especially 1P/Halley, with the presence of magnetic field draping, cold electrons and a diamagnetic cavity.

In general the magnetic field magnitude is mostly modulated by the solar wind dynamic pressure, whereas the power spectral density is governed by the rotation of the nucleus. This simple picture may be disturbed by the appearance of transient events like outbursts and interplanetary coronal mass ejections, which modify the plasma and compress the interaction region. Outbursts are by far the less influential of the two events. When an interplanetary coronal mass ejection encounters the cometary plasma, the magnetic field magnitude may increase by a factor of six. With the presence of high energy electrons, the ionisation rate due to electron impact ionisation is increased dramatically. This also causes a higher plasma density that surpasses that of compressed plasma. The specific response of the plasma to the solar wind event depends on the gas production rate, with events during perihelion causing a more pronounced signature in the plasma.

Rosetta has passed into the diamagnetic cavity over 600 times, thereby confirming the existence of such a region as well as the dynamic nature of its boundary. The diamagnetic cavity was found to be much larger than expected from simulations and simple models. It

is clear from measurements that the cavity expands with gas production rate and contracts with higher upstream magnetic field magnitudes, but this relation is not well defined indicating that other factors also play a role. The in-situ gas production rate is a better predictor for the diamagnetic cavity size than an empirical model of the gas production rate. Measurements of the diamagnetic cavity boundary normal indicate that the variability of the gas production rate and large amplitude instabilities of the boundary are the reason for the larger than predicted size. Clusters of events are usually found close to the electron collisionopause. Low electron temperatures and high ion velocities indicate that the electrons are collisionally coupled to the neutrals in the innermost region of the coma (far inside the diamagnetic cavity), whereas the ions are not.

Comparing the formation mechanisms of the diamagnetic cavity at 67P and 1P reveals that the ion-neutral friction model favored until recently is not applicable at 67P. Arguments against this model include higher than expected ion velocities, smaller amounts of cold electrons and a different ion profile. The occasional presence of high density anti-sunward flowing plasma in the cavity has shown that the boundary can be permeable. This does not apply to solar wind electrons which are found exclusively outside of the diamagnetic cavity. Table 4.1 summarizes the main questions that were unclear before Rosetta's encounter with 67P and can now be answered.

Although the measurements made by the instruments onboard Rosetta have greatly enhanced our knowledge of comets, many open questions remain and new questions have emerged. Many unexplored measurements remain that can contribute to answering these questions, but the accuracy of the measurements is a key factor in future investigations. The calibration of the magnetic field measurements has greatly enhanced the quality of the data which can now be used for more in depth investigations. The same goes for the plasma instruments, where additional calibration has improved accuracy and cross-calibration and cross-validation has improved data quality. In the future these new datasets will give a more complete picture of the plasma in the coma.

Key open questions pertaining to the stages of interaction are: how are plasma regions influenced by changing upstream solar wind conditions? Are there regions that are transient? How entangled are the different stages of the interaction?

In terms of transient events, it is not yet understood if they can trigger cometary tail disonnections and how this affects the plasma in the upstream region of the comet.

The diamagnetic cavity formation mechanism is not yet understood and a model that can accurately describe the diamagnetic cavity at both 67P and at 1P has not been found. The situation is complicated by the sparseness of low energy velocity measurements. Other questions for this topic include: How does the high density plasma pass through the diamagnetic cavity boundary? What is the flow pattern of the different ion and electron populations near the boundary? Is there a point at which the upstream flow stagnates?

Further investigations using the data collected by Rosetta will answer some of these questions, but for a more detailed analysis a new cometary plasma mission is necessary. This mission should include at least two spacecraft for simultaneous measurements of the solar wind and the cometary plasma. Only then can the plasma regions that are fixed at the comet be disentangled from transient events. And only then can the input conditions for the interaction model be constrained while measurements are being made downstream in the flow.

Are there different interaction regimes?	Three regimes are distinguished based on gas production rate. The features in the plasma environment are unique for each regime.
Is the diamagnetic cavity boundary stable?	The diamagnetic cavity boundary is highly unstable, the size varies on the scale of seconds and there are indications that instabilities propagate along the boundary.
What determines the size of the diamagnetic cavity?	The diamagnetic cavity expands with gas production rate. A clear dependence of the size on the magnetic field in the pile-up region could not be found.
How efficient is ion-neutral friction?	High ion velocities show that ion-neutral friction is not efficient even in the innermost, densest part of the coma.
What is the significance of large ion gyro radii?	The cometary ion distribution is clearly non-gyrotropic, and ions constituting a cross-field current may trigger low-frequency wave activity.
What drives the magnetic field?	The magnetic field magnitude is driven by solar wind input conditions, the magnetic field variability is driven by gas production rate.
What is the impact of an interplanetary coronal mass ejection on the plasma at a comet?	The magnetic field magnitude and variability increases as well as the density and temperature of the plasma. Additional electron impact ionisation increases the density above the purely compressed values.

Table 4.1.: Open questions before the Rosetta mission and their answers based on results thereof.

Bibliography

Agarwal, J., Della Corte, V., Feldman, P. D., Geiger, B., Merouane, S., Bertini, I., Bodewits, D., Fornasier, S., Grün, E., Hasselmann, P., Hilchenbach, M., Höfner, S., Ivanovski, S., Kolokolova, L., Pajola, M., Rotundi, A., Sierks, H., Steffl, A. J., Thomas, N., A'Hearn, M. F., Barbieri, C., Barucci, M. A., Bertaux, J. L., Boudreault, S., Cremonese, G., Da Deppo, V., Davidsson, B., Debei, S., De Cecco, M., Deller, J. F., Feaga, L. M., Fischer, H., Fulle, M., Gicquel, A., Groussin, O., Güttler, C., Gutiérrez, P. J., Hofmann, M., Hornung, K., Hviid, S. F., Ip, W. H., Jorda, L., Keller, H. U., Kissel, J., Knollenberg, J., Koch, A., Koschny, D., Kramm, J. R., Kührt, E., Küppers, M., Lamy, P. L., Langevin, Y., Lara, L. M., Lazzarin, M., Lin, Z. Y., Lopez Moreno, J. J., Lowry, S. C., Marzari, F., Mottola, S., Naletto, G., Oklay, N., Parker, J. W., Rodrigo, R., Rynö, J., Shi, X., Stenzel, O., Tubiana, C., Vincent, J. B., Weaver, H. A., Zaprudin, B., 2017, Evidence of sub-surface energy storage in comet 67P from the outburst of 2016 July 03, Monthly Notices of the Royal Astronomical Society, 469, s606–s625

A'Hearn, M. F., Belton, M. J. S., Delamere, W. A., Feaga, L. M., Hampton, D., Kissel, J., Klaasen, K. P., McFadden, L. A., Meech, K. J., Melosh, H. J., Schultz, P. H., Sunshine, J. M., Thomas, P. C., Veverka, J., Wellnitz, D. D., Yeomans, D. K., Besse, S., Bodewits, D., Bowling, T. J., Carcich, B. T., Collins, S. M., Farnham, T. L., Groussin, O., Hermalyn, B., Kelley, M. S., Kelley, M. S., Li, J.-Y., Lindler, D. J., Lisse, C. M., McLaughlin, S. A., Merlin, F., Protopapa, S., Richardson, J. E., Williams, J. L., 2011, EPOXI at Comet Hartley 2, Science, 332, 1396

Alfvén, H., 1957, On the theory of comet tails, Tellus, 9

Altwegg, K., 2018, Chemical highlights from the Rosetta mission, in IAU Symposium, (Eds.) M. Cunningham, T. Millar, Y. Aikawa, vol. 332, pp. 153–162

Auster, H.-U., Apathy, I., Berghofer, G., Fornacon, K.-H., Remizov, A., Carr, C., Güttler, C., Haerendel, G., Heinisch, P., Hercik, D., Hilchenbach, M., Kührt, E., Magnes, W., Motschmann, U., Richter, I., Russell, C. T., Przyklenk, A., Schwingenschuh, K., Sierks, H., Glassmeier, K.-H., 2015, The nonmagnetic nucleus of comet 67P/Churyumov-Gerasimenko, Science, 349, 015 102

Balsiger, H., Altwegg, K., Bochsler, P., Eberhardt, P., Fischer, J., Graf, S., Jäckel, A., Kopp, E., Langer, U., Mildner, M., Müller, J., Riesen, T., Rubin, M., Scherer, S., Wurz, P., Wüthrich, S., Arijs, E., Delanoye, S., de Keyser, J., Neefs, E., Nevejans, D., Rème, H., Aoustin, C., Mazelle, C., Médale, J.-L., Sauvaud, J. A., Berthelier, J.-J., Bertaux, J.-L., Duvet, L., Illiano, J.-M., Fuselier, S. A., Ghielmetti, A. G., Magoncelli, T., Shelley, E. G., Korth, A., Heerlein, K., Lauche, H., Livi, S., Loose, A., Mall, U., Wilken, B., Gliem, F., Fiethe, B., Gombosi, T. I., Block, B., Carignan, G. R., Fisk, L. A., Waite,

J. H., Young, D. T., Wollnik, H., 2007, Rosina Rosetta Orbiter Spectrometer for Ion and Neutral Analysis, Space Science Reviews, 128, 745–801

Baumjohann, W., Treumann, R., 1997, Basic Space Plasma Physics, Imperial College Press, ISBN 9781860940798

Behar, E., Nilsson, H., Wieser, G. S., Nemeth, Z., Broiles, T. W., Richter, I., 2016, Mass loading at 67P/Churyumov-Gerasimenko: A case study, Geophysical Research Letters, 43, 1411–1418

Behar, E., Nilsson, H., Alho, M., Goetz, C., Tsurutani, B., 2017, The birth and growth of a solar wind cavity around a comet - Rosetta observations, Monthly Notices of the Royal Astronomical Society, 469, S396–S403

Beth, A., Altwegg, K., Balsiger, H., Berthelier, J. J., Calmonte, U., Combi, M. R., De Keyser, J., Dhooghe, F., Fiethe, B., Fuselier, S. A., Galand, M., Gasc, S., Gombosi, T. I., Hansen, K. C., Hässig, M., Héritier, K. L., Kopp, E., Le Roy, L., Mandt, K. E., Peroy, S., Rubin, M., Sémon, T., Tzou, C. Y., Vigren, E., 2016, First in-situ detection of the cometary ammonium ion NH_4$^+$ (protonated ammonia NH_3) in the coma of 67P/C-G near perihelion, Monthly Notices of the Royal Astronomical Society, 462, S562–S572

Beth, A., Galand, M., Heritier, K., 2018, Comparative study of photo-produced ionosphere in the close environment of comets, Astronomy & Astrophysics, accepted

Biermann, L., 1951, Kometenschweife und solare Korpuskularstrahlung, Zeitschrift fur Astrophysik, 29, 274

Biermann, L., 1952, Physical Processes in Comet Tails and their Relation to Solar Activity, in Liege International Astrophysical Colloquia, (Ed.) P. Swings, vol. 4 of Liege International Astrophysical Colloquia, pp. 251–262

Biermann, L., Brosowski, B., Schmidt, H. U., 1967, The interactions of the solar wind with a comet, Solar Physics, 1, 254–284

Blum, J., Gundlach, B., Krause, M., Fulle, M., Johansen, A., Agarwal, J., von Borstel, I., Shi, X., Hu, X., Bentley, M. S., Capaccioni, F., Colangeli, L., Della Corte, V., Fougere, N., Green, S. F., Ivanovski, S., Mannel, T., Merouane, S., Migliorini, A., Rotundi, A., Schmied, R., Snodgrass, C., 2017, Evidence for the formation of comet 67P/Churyumov-Gerasimenko through gravitational collapse of a bound clump of pebbles, Monthly Notices of the Royal Astronomical Society, 469, S755–S773

Boehnhardt, H., Bibring, J.-P., Apathy, I., Auster, H. U., Ercoli Finzi, A., Goesmann, F., Klingelhöfer, G., Knapmeyer, M., Kofman, W., Krüger, H., Mottola, S., Schmidt, W., Seidensticker, K., Spohn, T., Wright, I., 2017, The Philae lander mission and science overview, Philosophical Transactions of the Royal Society of London Series A, 375, 20160248

Broiles, T. W., Burch, J. L., Chae, K., Clark, G., Cravens, T. E., Eriksson, A., Fuselier, S. A., Frahm, R. A., Gasc, S., Goldstein, R., Henri, P., Koenders, C., Livadiotis, G., Mandt, K. E., Mokashi, P., Nemeth, Z., Odelstad, E., Rubin, M., Samara, M., 2016,

Statistical analysis of suprathermal electron drivers at 67P/Churyumov- Gerasimenko, Monthly Notices of the Royal Astronomical Society, 462, S312–S322

Burch, J. L., Goldstein, R., Cravens, T. E., Gibson, W. C., Lundin, R. N., Pollock, C. J., Winningham, J. D., Young, D. T., 2007, RPC-IES: The Ion and Electron Sensor of the Rosetta Plasma Consortium, Space Science Reviews, 128, 697–712

Cane, H. V., 2000, Coronal Mass Ejections and Forbush Decreases, Space Science Reviews, 93, 55–77

Carr, C., Cupido, E., Lee, C. G. Y., Balogh, A., Beek, T., Burch, J. L., Dunford, C. N., Eriksson, A. I., Gill, R., Glassmeier, K. H., Goldstein, R., Lagoutte, D., Lundin, R., Lundin, K., Lybekk, B., Michau, J. L., Musmann, G., Nilsson, H., Pollock, C., Richter, I., Trotignon, J. G., 2007, RPC: The Rosetta Plasma Consortium, Space Science Reviews, 128, 629–647

Clark, G., Broiles, T. W., Burch, J. L., Collinson, G. A., Cravens, T., Frahm, R. A., Goldstein, J., Goldstein, R., Mandt, K., Mokashi, P., Samara, M., Pollock, C. J., 2015, Suprathermal electron environment of comet 67P/Churyumov-Gerasimenko: Observations from the Rosetta Ion and Electron Sensor, Astronomy & Astrophysics, 583, A24

Coates, A. J., Jones, G. H., 2009, Plasma environment of Jupiter family comets, Planetary Space Science, 57, 1175–1191

Coates, A. J., Johnstone, A. D., Wilken, B., Jockers, K., Glassmeier, K. H., 1989, Velocity space diffusion of pickup ions from the water group at Comet Halley, Journal of Geophysical Research, 94, 9983–9993

Coates, A. J., Johnstone, A. D., Wilken, B., Neubauer, F. M., 1993, Velocity space diffusion and nongyrotropy of pickup water group ions at comet Grigg-Skjellerup, Journal of Geophysical Research, 98, 20 985–20 994

Colangeli, L., Lopez-Moreno, J. J., Palumbo, P., Rodriguez, J., Cosi, M., Della Corte, V., Esposito, F., Fulle, M., Herranz, M., Jeronimo, J. M., Lopez-Jimenez, A., Epifani, E. M., Morales, R., Moreno, F., Palomba, E., Rotundi, A., 2007, The Grain Impact Analyser and Dust Accumulator (GIADA) Experiment for the Rosetta Mission: Design, Performances and First Results, Space Science Reviews, 128, 803–821

Coradini, A., Capaccioni, F., Drossart, P., Arnold, G., Ammannito, E., Angrilli, F., Barucci, A., Bellucci, G., Benkhoff, J., Bianchini, G., Bibring, J. P., Blecka, M., Bockelee-Morvan, D., Capria, M. T., Carlson, R., Carsenty, U., Cerroni, P., Colangeli, L., Combes, M., Combi, M., Crovisier, J., De Sanctis, M. C., Encrenaz, E. T., Erard, S., Federico, C., Filacchione, G., Fink, U., Fonti, S., Formisano, V., Ip, W. H., Jaumann, R., Kuehrt, E., Langevin, Y., Magni, G., McCord, T., Mennella, V., Mottola, S., Neukum, G., Palumbo, P., Piccioni, G., Rauer, H., Saggin, B., Schmitt, B., Tiphene, D., Tozzi, G., 2007, Virtis: An Imaging Spectrometer for the Rosetta Mission, Space Science Reviews, 128, 529–559

Cowley, S. W. H., 1987, ICE Observations of Comet Giacobini-Zinner, Philosophical Transactions of the Royal Society of London Series A, 323, 405–420

Cravens, T. E., 1986, The Physics of the Cometary Contact Surface, in ESLAB Symposium on the Exploration of Halley's Comet, (Eds.) B. Battrick, E. J. Rolfe, R. Reinhard, vol. 250, p. 241

Cravens, T. E., 1987, Theory and observations of cometary ionospheres, Advances in Space Research, 7, 147–158

Davidsson, B. J. R., Sierks, H., Güttler, C., Marzari, F., Pajola, M., Rickman, H., A'Hearn, M. F., Auger, A. T., El-Maarry, M. R., Fornasier, S., Gutiérrez, P. J., Keller, H. U., Massironi, M., Snodgrass, C., Vincent, J. B., Barbieri, C., Lamy, P. L., Rodrigo, R., Koschny, D., Barucci, M. A., Bertaux, J. L., Bertini, I., Cremonese, G., Da Deppo, V., Debei, S., De Cecco, M., Feller, C., Fulle, M., Groussin, O., Hviid, S. F., Höfner, S., Ip, W. H., Jorda, L., Knollenberg, J., Kovacs, G., Kramm, J. R., Kührt, E., Küppers, M., La Forgia, F., Lara, L. M., Lazzarin, M., Lopez Moreno, J. J., Moissl-Fraund, R., Mottola, S., Naletto, G., Oklay, N., Thomas, N., Tubiana, C., 2016, The primordial nucleus of comet 67P/Churyumov-Gerasimenko, Astronomy & Astrophysics, 592, A63

Deca, J., Divin, A., Henri, P., Eriksson, A., Markidis, S., Olshevsky, V., Horányi, M., 2017, Electron and Ion Dynamics of the Solar Wind Interaction with a Weakly Outgassing Comet, Physical Review Letters, 118, 205101

Dones, L., Brasser, R., Kaib, N., Rickman, H., 2015, Origin and Evolution of the Cometary Reservoirs, Space Science Reviews, 197, 191–269

Duncan, M. J., 2008, Dynamical origin of comets and their reservoirs, Space Science Reviews, 138, 109–126, ISSN 1572-9672

Edberg, N. J. T., Eriksson, A. I., Odelstad, E., Henri, P., Lebreton, J.-P., Gasc, S., Rubin, M., André, M., Gill, R., Johansson, E. P. G., Johansson, F., Vigren, E., Wahlund, J. E., Carr, C. M., Cupido, E., Glassmeier, K.-H., Goldstein, R., Koenders, C., Mandt, K., Nemeth, Z., Nilsson, H., Richter, I., Wieser, G. S., Szego, K., Volwerk, M., 2015, Spatial distribution of low-energy plasma around comet 67P/CG from Rosetta measurements, Geophysical Research Letters, 42, 4263–4269, 1608.06745

Edberg, N. J. T., Alho, M., André, M., Andrews, D. J., Behar, E., Burch, J. L., Carr, C. M., Cupido, E., Engelhardt, I. A. D., Eriksson, A. I., Glassmeier, K.-H., Goetz, C., Goldstein, R., Henri, P., Johansson, F. L., Koenders, C., Mandt, K., Möstl, C., Nilsson, H., Odelstad, E., Richter, I., Simon Wedlund, C., Stenberg Wieser, G., Szego, K., Vigren, E., Volwerk, M., 2016a, CME impact on comet 67P/Churyumov-Gerasimenko, Monthly Notices of the Royal Astronomical Society, 462, S45–S56

Edberg, N. J. T., Eriksson, A. I., Odelstad, E., Vigren, E., Andrews, D. J., Johansson, F., Burch, J. L., Carr, C. M., Cupido, E., Glassmeier, K.-H., Goldstein, R., Halekas, J. S., Henri, P., Koenders, C., Mandt, K., Mokashi, P., Nemeth, Z., Nilsson, H., Ramstad, R., Richter, I., Wieser, G. S., 2016b, Solar wind interaction with comet 67P: Impacts of corotating interaction regions, Journal of Geophysical Research (Space Physics), 121, 949–965

Engelhardt, I. A. D., Eriksson, A. I., Vigren, E., Valliéres, X., Rubin, M., Gilet, N., Henri, P., 2018, Cold electrons at comet 67P/Churyumov-Gerasimenko, Astronomy & Astrophysics, 616, A51

Eriksson, A. I., Boström, R., Gill, R., Åhlén, L., Jansson, S.-E., Wahlund, J.-E., André, M., Mälkki, A., Holtet, J. A., Lybekk, B., Pedersen, A., Blomberg, L. G., 2007, RPC-LAP: The Rosetta Langmuir Probe Instrument, Space Science Reviews, 128, 729–744

Eriksson, A. I., Engelhardt, I. A. D., André, M., Boström, R., Edberg, N. J. T., Johansson, F. L., Odelstad, E., Vigren, E., Wahlund, J. E., Henri, P., Lebreton, J. P., Miloch, W. J., Paulsson, J. J. P., Simon Wedlund, C., Yang, L., Karlsson, T., Jarvinen, R., Broiles, T., Mandt, K., Carr, C. M., Galand, M., Nilsson, H., Norberg, C., 2017, Cold and warm electrons at comet 67P/Churyumov-Gerasimenko, Astronomy & Astrophysics, 605, A15

Ershkovich, A. I., Flammer, K. R., 1988, Nonlinear stability of the dayside cometary ionopause, Astrophysical Journal, 328, 967–973

Ershkovich, A. I., Mendis, D. A., 1986, Effects of the interaction between plasma and neutrals on the stability of the cometary ionopause, Astrophysical Journal, 302, 849–852

European Space Agency, 2018, Rosetta's Target: Comet 67P/Churyumov-Gerasimenko, http://sci.esa.int/rosetta/14615-comet-67p/, accessed 4-October-2018

Fulle, M., Della Corte, V., Rotundi, A., Green, S. F., Accolla, M., Colangeli, L., Ferrari, M., Ivanovski, S., Sordini, R., Zakharov, V., 2017, The dust-to-ices ratio in comets and Kuiper belt objects, Monthly Notices of the Royal Astronomical Society, 469, S45–S49

Galand, M., Héritier, K. L., Odelstad, E., Henri, P., Broiles, T. W., Allen, A. J., Altwegg, K., Beth, A., Burch, J. L., Carr, C. M., Cupido, E., Eriksson, A. I., Glassmeier, K. H., Johansson, F. L., Lebreton, J. P., Mandt, K. E., Nilsson, H., Richter, I., Rubin, M., Sagnières, L. B. M., Schwartz, S. J., Sémon, T., Tzou, C. Y., Vallières, X., Vigren, E., Wurz, P., 2016, Ionospheric plasma of comet 67P probed by Rosetta at 3 au from the Sun, Monthly Notices of the Royal Astronomical Society, 462, S331–S351

Galeev, A. A., Sagdeev, R. Z., 1988, Alfvén waves in a space plasma and its role in the solar wind interaction with comets, Astrophysics & Space Science, 144, 427–438

Galeev, A. A., Cravens, T. E., Gombosi, T. I., 1985, Solar wind stagnation near comets, ApJ, 289, 807–819

Gan, L., Cravens, T. E., 1990, Electron energetics in the inner coma of Comet Halley, Journal of Geophysical Research, 95, 6285–6303

Gasc, S., Altwegg, K., Balsiger, H., Berthelier, J.-J., Bieler, A., Calmonte, U., Fiethe, B., Fuselier, S., Galli, A., Gombosi, T., Hoang, M., De Keyser, J., Korth, A., Le Roy, L., Mall, U., Rème, H., Rubin, M., Sémon, T., Tzou, C.-Y., Waite, J. H., Wurz, P., 2017, Change of outgassing pattern of 67P/Churyumov-Gerasimenko during the March 2016 equinox as seen by ROSINA, Monthly Notices of the Royal Astronomical Society, 469, S108–S117

Gilet, N., Henri, P., Wattieaux, G., Cilibrasi, M., Béghin, C., 2017, Electrostatic Potential Radiated by a Pulsating Charge in a Two-Electron Temperature Plasma, Radio Science, 52, 1432–1448

Glassmeier, K.-H., 2017, Interaction of the solar wind with comets: A rosetta perspective, Philosophical Transactions of the Royal Astronomical Society A, 375, 20160 256

Glassmeier, K.-H., Boehnhardt, H., Koschny, D., Kührt, E., Richter, I., 2007a, The Rosetta Mission: Flying Towards the Origin of the Solar System, Space Science Reviews, 128, 1–21

Glassmeier, K.-H., Richter, I., Diedrich, A., Musmann, G., Auster, U., Motschmann, U., Balogh, A., Carr, C., Cupido, E., Coates, A., Rother, M., Schwingenschuh, K., Szegö, K., Tsurutani, B., 2007b, RPC-MAG The Fluxgate Magnetometer in the ROSETTA Plasma Consortium, Space Science Reviews, 128, 649–670

Goetz, C., Koenders, C., Hansen, K. C., Burch, J., Carr, C., Eriksson, A., Frühauff, D., Güttler, C., Henri, P., Nilsson, H., Richter, I., Rubin, M., Sierks, H., Tsurutani, B., Volwerk, M., Glassmeier, K. H., 2016a, Structure and evolution of the diamagnetic cavity at comet 67P/Churyumov-Gerasimenko, Monthly Notices of the Royal Astronomical Society, 462, S459–S467

Goetz, C., Koenders, C., Richter, I., Altwegg, K., Burch, J., Carr, C., Cupido, E., Eriksson, A., Güttler, C., Henri, P., Mokashi, P., Nemeth, Z., Nilsson, H., Rubin, M., Sierks, H., Tsurutani, B., Vallat, C., Volwerk, M., Glassmeier, K.-H., 2016b, First detection of a diamagnetic cavity at comet 67P/Churyumov-Gerasimenko, Astronomy & Astrophysics, 588, A24

Goetz, C., Volwerk, M., Richter, I., Glassmeier, K.-H., 2017, Evolution of the magnetic field at comet 67P/Churyumov-Gerasimenko, Monthly Notices of the Royal Astronomical Society, 469, S268–S275

Goetz, C., Tsurutani, B. T., Henri, P., Volwerk, M., Behar, E., Edberg, N. J. T., Eriksson, A., Goldstein, R., Mokashi, P., Nilsson, H., Richter, I., Wellbrock, A., Glassmeier, K. H., 2018, Unusually high magnetic fields in the coma of 67P/Churyumov-Gerasimenko during its high-activity phase, Astronomy & Astrophysics

Gringauz, K. I., Gombosi, T. I., Tátrallyay, M., Verigin, M. I., Remizov, A. P., Richter, A. K., Apáthy, I., Szemerey, I., Dyachkov, A. V., Balakina, O. V., Nagy, A. F., 1986, Detection of a new "chemical" boundary at comet Halley, Geophysical Research Letters, 13, 613–616

Grün, E., Agarwal, J., Altobelli, N., Altwegg, K., Bentley, M. S., Biver, N., Della Corte, V., Edberg, N., Feldman, P. D., Galand, M., Geiger, B., Götz, C., Grieger, B., Güttler, C., Henri, P., Hofstadter, M., Horanyi, M., Jehin, E., Krüger, H., Lee, S., Mannel, T., Morales, E., Mousis, O., Müller, M., Opitom, C., Rotundi, A., Schmied, R., Schmidt, F., Sierks, H., Snodgrass, C., Soja, R. H., Sommer, M., Srama, R., Tzou, C. Y., Vincent, J. B., Yanamandra-Fisher, P., A'Hearn, M. F., Erikson, A. I., Barbieri, C., Barucci, M. A., Bertaux, J. L., Bertini, I., Burch, J., Colangeli, L., Cremonese, G., Da Deppo,

V., Davidsson, B., Debei, S., De Cecco, M., Deller, J., Feaga, L. M., Ferrari, M., Fornasier, S., Fulle, M., Gicquel, A., Gillon, M., Green, S. F., Groussin, O., Gutiérrez, P. J., Hofmann, M., Hviid, S. F., Ip, W. H., Ivanovski, S., Jorda, L., Keller, H. U., Knight, M. M., Knollenberg, J., Koschny, D., Kramm, J. R., Kührt, E., Küppers, M., Lamy, P. L., Lara, L. M., Lazzarin, M., Lò pez-Moreno, J. J., Manfroid, J., Epifani, E. M., Marzari, F., Naletto, G., Oklay, N., Palumbo, P., Parker, J. W., Rickman, H., Rodrigo, R., Rodrìguez, J., Schindhelm, E., Shi, X., Sordini, R., Steffl, A. J., Stern, S. A., Thomas, N., Tubiana, C., Weaver, H. A., Weissman, P., Zakharov, V. V., Taylor, M. G. G. T., 2016, The 2016 Feb 19 outburst of comet 67P/CG: an ESA Rosetta multi-instrument study, Monthly Notices of the Royal Astronomical Society, 462, S220–S234

Gulkis, S., Frerking, M., Crovisier, J., Beaudin, G., Hartogh, P., Encrenaz, P., Koch, T., Kahn, C., Salinas, Y., Nowicki, R., Irigoyen, R., Janssen, M., Stek, P., Hofstadter, M., Allen, M., Backus, C., Kamp, L., Jarchow, C., Steinmetz, E., Deschamps, A., Krieg, J., Gheudin, M., Bockelée-Morvan, D., Biver, N., Encrenaz, T., Despois, D., Ip, W., Lellouch, E., Mann, I., Muhleman, D., Rauer, H., Schloerb, P., Spilker, T., 2007, MIRO: Microwave Instrument for Rosetta Orbiter, Space Science Reviews, 128, 561–597

Gunell, H., Goetz, C., Eriksson, A., Nilsson, H., Simon Wedlund, C., Henri, P., Maggiolo, R., Hamrin, M., De Keyser, J., Rubin, M., Stenberg Wieser, G., Cessateur, G., Dhooghe, F., Gibbons, A., 2017, Plasma waves confined to the diamagnetic cavity of comet 67P/Churyumov- Gerasimenko, Monthly Notices of the Royal Astronomical Society, 469, S84–S92

Gunell, H., Goetz, C., Wedlund, C. S., Lindkvist, J., Hamrin, M., Nilsson, H., Llera, K., Eriksson, A., Holmström, M., 2018, The infant bow shock: a new frontier at a weak activity comet, Astronomy & Astrophysics, 619, L2

Gurval, R. A., 1997, Caesar's comet: The politics and poetics of an augustan myth, Memoirs of the American Academy in Rome, 42, 39–71, ISSN 00656801

Haerendel, G., Paschmann, G., Baumjohann, W., Carlson, C. W., 1986, Dynamics of the AMPTE artificial comet, Nature, 320, 720–723

Hajra, R., Henri, P., Vallières, X., Galand, M., Héritier, K., Eriksson, A. I., Odelstad, E., Edberg, N. J. T., Burch, J. L., Broiles, T., Goldstein, R., Glassmeier, K. H., Richter, I., Goetz, C., Tsurutani, B. T., Nilsson, H., Altwegg, K., Rubin, M., 2017, Impact of a cometary outburst on its ionosphere. Rosetta Plasma Consortium observations of the outburst exhibited by comet 67P /Churyumov-Gerasimenko on 19 February 2016, Astronomy & Astrophysics, 607, A34

Hajra, R., Henri, P., Myllys, M., Héritier, K. L., Galand, M., Wedlund, C. S., Breuillard, H., Behar, E., Edberg, N. J. T., Goetz, C., Nilsson, H., Eriksson, A. I., Goldstein, R., Tsurutani, B. T., Moré, J., Vallières, X., Wattieaux, G., 2018, Cometary plasma response to interplanetary corotating interaction regions during 2016 June-September: a quantitative study by the Rosetta Plasma Consortium, Monthly Notices of the Royal Astronomical Society, 480, 4544–4556

Hansen, K. C., Altwegg, K., Berthelier, J.-J., Bieler, A., Biver, N., Bockelée-Morvan, D., Calmonte, U., Capaccioni, F., Combi, M. R., de Keyser, J., Fiethe, B., Fougere, N., Fuselier, S. A., Gasc, S., Gombosi, T. I., Huang, Z., Le Roy, L., Lee, S., Nilsson, H., Rubin, M., Shou, Y., Snodgrass, C., Tenishev, V., Toth, G., Tzou, C.-Y., Wedlund, C. S., Rosina Team, 2016, Evolution of water production of 67P/Churyumov-Gerasimenko: An empirical model and a multi-instrument study, Monthly Notices of the Royal Astronomical Society, 462, S491–S506

Harker, D. E., Woodward, C. E., Kelley, M. S. P., Wooden, D. H., 2018, Hyperactivity and Dust Composition of Comet 103P/Hartley 2 During the EPOXI Encounter, AJ, 155, 199

Haser, L., 1957, Distribution d'intensité dans la tête d'une comète, Bulletin de la Societe Royale des Sciences de Liege, 43, 740–750

Hedgecock, P. C., 1975, Measurements of the Interplanetary Magnetic Field in Relation to the Modulation of Cosmic Rays, Solar Physics, 42, 497–527

Heinisch, P., Auster, H.-U., Plettemeier, D., Kofman, W., Herique, A., Statz, C., Hahnel, R., Rogez, Y., Richter, I., Hilchenbach, M., Jurado, E., Garmier, R., Martin, T., Finke, F., Güttler, C., Sierks, H., Glassmeier, K.-H., 2017, Reconstruction of the flight and attitude of Rosetta's lander Philae, Acta Astronautica, 140, 509–516

Henri, P., Vallières, X., Hajra, R., Goetz, C., Richter, I., Glassmeier, K.-H., Galand, M., Rubin, M., Eriksson, A. I., Nemeth, Z., Vigren, E., Beth, A., Burch, J. L., Carr, C., Nilsson, H., Tsurutani, B., Wattieaux, G., 2017, Diamagnetic region(s): structure of the unmagnetized plasma around Comet 67P/CG, Monthly Notices of the Royal Astronomical Society, 469, S372–S379

Heritier, K. L., Galand, M., Henri, P., Johansson, F. L., Beth, A., Eriksson, A. I., Vallières, X., Altwegg, K., Burch, J. L., Carr, C., Ducrot, E., Hajra, R., Rubin, M., 2018, Plasma source and loss at comet 67P during the Rosetta mission, Astronomy & Astrophysics, 618, A77

Hirao, K., Itoh, T., 1987, The Sakigake / Suisei Encounter with Comet p/ Halley, Astronomy & Astrophysics, 187, 39

Hoang, M., Altwegg, K., Balsiger, H., Beth, A., Bieler, A., Calmonte, U., Combi, M. R., De Keyser, J., Fiethe, B., Fougere, N., Fuselier, S. A., Galli, A., Garnier, P., Gasc, S., Gombosi, T., Hansen, K. C., Jäckel, A., Korth, A., Lasue, J., Le Roy, L., Mall, U., Rème, H., Rubin, M., Sémon, T., Toublanc, D., Tzou, C. Y., Waite, J. H., Wurz, P., 2017, The heterogeneous coma of comet 67P/Churyumov-Gerasimenko as seen by ROSINA: H_2O, CO_2, and CO from September 2014 to February 2016, Astronomy & Astrophysics, 600, A77

Huang, Z., Tóth, G., Gombosi, T. I., Bieler, A., Combi, M. R., Hansen, K. C., Jia, X., Fougere, N., Shou, Y., Cravens, T. E., Tenishev, V., Altwegg, K., Rubin, M., 2016a, A possible mechanism for the formation of magnetic field dropouts in the coma of 67P/Churyumov-Gerasimenko, Monthly Notices of the Royal Astronomical Society, 462, S468–S475

Huang, Z., Tóth, G., Gombosi, T. I., Jia, X., Rubin, M., Fougere, N., Tenishev, V., Combi, M. R., Bieler, A., Hansen, K. C., Shou, Y., Altwegg, K., 2016b, Four-fluid MHD simulations of the plasma and neutral gas environment of comet 67P/Churyumov-Gerasimenko near perihelion, Journal of Geophysical Research (Space Physics), 121, 4247–4268

Johansen, A., Oishi, J. S., Mac Low, M.-M., Klahr, H., Henning, T., Youdin, A., 2007, Rapid planetesimal formation in turbulent circumstellar disks, Nature, 448, 1022–1025, 0708.3890

Johansson, F. L., Odelstad, E., Paulsson, J. J. P., Harang, S. S., Eriksson, A. I., Mannel, T., Vigren, E., Edberg, N. J. T., Miloch, W. J., Simon Wedlund, C., Thiemann, E., Eparvier, F., Andersson, L., 2017, Rosetta photoelectron emission and solar ultraviolet flux at comet 67P, Monthly Notices of the Royal Astronomical Society, 469, S626–S635, 1709.03874

Johnstone, A. D., Huddleston, D. E., Coates, A. J., 1991, The spectrum and energy density of solar wind turbulence of cometary origin, Washington DC American Geophysical Union Geophysical Monograph Series, 61, 259–271

Karlsson, T., Eriksson, A. I., Odelstad, E., André, M., Dickeli, G., Kullen, A., Lindqvist, P. A., Nilsson, H., Richter, I., 2017, Rosetta measurements of lower hybrid frequency range electric field oscillations in the plasma environment of comet 67P, Geophysical Research Letters, 44, 1641–1651

Keller, H. U., Barbieri, C., Lamy, P., Rickman, H., Rodrigo, R., Wenzel, K.-P., Sierks, H., A'Hearn, M. F., Angrilli, F., Angulo, M., Bailey, M. E., Barthol, P., Barucci, M. A., Bertaux, J.-L., Bianchini, G., Boit, J.-L., Brown, V., Burns, J. A., Büttner, I., Castro, J. M., Cremonese, G., Curdt, W., da Deppo, V., Debei, S., de Cecco, M., Dohlen, K., Fornasier, S., Fulle, M., Germerott, D., Gliem, F., Guizzo, G. P., Hviid, S. F., Ip, W.-H., Jorda, L., Koschny, D., Kramm, J. R., Kührt, E., Küppers, M., Lara, L. M., Llebaria, A., López, A., López-Jimenez, A., López-Moreno, J., Meller, R., Michalik, H., Michelena, M. D., Müller, R., Naletto, G., Origné, A., Parzianello, G., Pertile, M., Quintana, C., Ragazzoni, R., Ramous, P., Reiche, K.-U., Reina, M., Rodríguez, J., Rousset, G., Sabau, L., Sanz, A., Sivan, J.-P., Stöckner, K., Tabero, J., Telljohann, U., Thomas, N., Timon, V., Tomasch, G., Wittrock, T., Zaccariotto, M., 2007, OSIRIS The Scientific Camera System Onboard Rosetta, Space Science Reviews, 128, 433–506

Kissel, J., Altwegg, K., Clark, B. C., Colangeli, L., Cottin, H., Czempiel, S., Eibl, J., Engrand, C., Fehringer, H. M., Feuerbacher, B., Fomenkova, M., Glasmachers, A., Greenberg, J. M., Grün, E., Haerendel, G., Henkel, H., Hilchenbach, M., von Hoerner, H., Höfner, H., Hornung, K., Jessberger, E. K., Koch, A., Krüger, H., Langevin, Y., Parigger, P., Raulin, F., Rüdenauer, F., Rynö, J., Schmid, E. R., Schulz, R., Silén, J., Steiger, W., Stephan, T., Thirkell, L., Thomas, R., Torkar, K., Utterback, N. G., Varmuza, K., Wanczek, K. P., Werther, W., Zscheeg, H., 2007, Cosima High Resolution Time-of-Flight Secondary Ion Mass Spectrometer for the Analysis of Cometary Dust Particles onboard Rosetta, Space Science Reviews, 128, 823–867

Koenders, C., Glassmeier, K.-H., Richter, I., Motschmann, U., Rubin, M., 2013, Revisiting cometary bow shock positions, Planetary and Space Science, 87, 85–95

Koenders, C., Glassmeier, K.-H., Richter, I., Ranocha, H., Motschmann, U., 2015, Dynamical features and spatial structures of the plasma interaction region of 67P/Churyumov-Gerasimenko and the solar wind, Planetary Space Science, 105, 101–116

Koenders, C., Goetz, C., Richter, I., Motschmann, U., Glassmeier, K.-H., 2016a, Magnetic field pile-up and draping at intermediately active comets: results from comet 67P/Churyumov-Gerasimenko at 2.0 AU, Monthly Notices of the Royal Astronomical Society, 462, S235–S241

Koenders, C., Perschke, C., Goetz, C., Richter, I., Motschmann, U., Glassmeier, K. H., 2016b, Low-frequency waves at comet 67P/Churyumov-Gerasimenko. Observations compared to numerical simulations, Astronomy & Astrophysics, 594, A66

Kofman, W., Herique, A., Goutail, J.-P., Hagfors, T., Williams, I. P., Nielsen, E., Barriot, J.-P., Barbin, Y., Elachi, C., Edenhofer, P., Levasseur-Regourd, A.-C., Plettemeier, D., Picardi, G., Seu, R., Svedhem, V., 2007, The Comet Nucleus Sounding Experiment by Radiowave Transmission (CONSERT): A Short Description of the Instrument and of the Commissioning Stages, Space Science Reviews, 128, 413–432

Kramer, T., Noack, M., Baum, D., Hege, H.-C., Heller, E. J., 2015, Dust and gas emission from cometary nuclei: the case of comet 67P /Churyumov-Gerasimenko, ArXiv e-prints, arXiv:1505.08041, 1505.08041

Leinweber, H. K., Russell, C. T., Torkar, K., Zhang, T. L., Angelopoulos, V., 2008, An advanced approach to finding magnetometer zero levels in the interplanetary magnetic field, Measurement Science and Technology, 19, 055104

Levasseur-Regourd, A.-C., Agarwal, J., Cottin, H., Engrand, C., Flynn, G., Fulle, M., Gombosi, T., Langevin, Y., Lasue, J., Mannel, T., Merouane, S., Poch, O., Thomas, N., Westphal, A., 2018, Cometary Dust, Space Science Reviews, 214, 64

Luehr, H., Kloecker, N., Southwood, D. J., Dunlop, M. W., Mier-Jedrzejowicz, W. A. C., Rijnbeek, R. P., Six, M., Haeusler, B., Acuna, M., 1986, In situ magnetic field observations of the AMPTE artificial comet, Nature, 320, 708–711

Luehr, H., Kloecker, N., Acuna, M. H., 1988, The diamagnetic effect during AMPTE's tail releases - Initial results, Advances in Space Research, 8, 11–14

Madanian, H., Cravens, T. E., Burch, J., Goldstein, R., Rubin, M., Nemeth, Z., Goetz, C., Koenders, C., Altwegg, K., 2017, Plasma Environment around Comet 67P/Churyumov-Gerasimenko at Perihelion: Model Comparison with Rosetta Data, AJ, 153, 30

Madsen, B., Wedlund, C. S., Eriksson, A., Goetz, C., Karlsson, T., Gunell, H., Spicher, A., Henri, P., Vallières, X., Miloch, W. J., 2018, Extremely Low-Frequency Waves Inside the Diamagnetic Cavity of Comet 67P /Churyumov-Gerasimenko, Geophysical Research Letters, 45, 3854–3864

Mandt, K. E., Eriksson, A., Edberg, N. J. T., Koenders, C., Broiles, T., Fuselier, S. A., Henri, P., Nemeth, Z., Alho, M., Biver, N., Beth, A., Burch, J., Carr, C., Chae, K., Coates, A. J., Cupido, E., Galand, M., Glassmeier, K.-H., Goetz, C., Goldstein, R., Hansen, K. C., Haiducek, J., Kallio, E., Lebreton, J.-P., Luspay-Kuti, A., Mokashi, P., Nilsson, H., Opitz, A., Richter, I., Samara, M., Szego, K., Tzou, C.-Y., Volwerk, M., Simon Wedlund, C., Stenberg Wieser, G., 2016, RPC observation of the development and evolution of plasma interaction boundaries at 67P/Churyumov-Gerasimenko, Monthly Notices of the Royal Astronomical Society, 462, S9–S22

Mannel, T., Bentley, M. S., Schmied, R., Jeszenszky, H., Levasseur-Regourd, A. C., Romstedt, J., Torkar, K., 2016, Fractal cometary dust - a window into the early Solar system, Monthly Notices of the Royal Astronomical Society, 462, S304–S311

Massironi, M., Simioni, E., Marzari, F., Cremonese, G., Giacomini, L., Pajola, M., Jorda, L., Naletto, G., Lowry, S., El-Maarry, M. R., Preusker, F., Scholten, F., Sierks, H., Barbieri, C., Lamy, P., Rodrigo, R., Koschny, D., Rickman, H., Keller, H. U., A'Hearn, M. F., Agarwal, J., Auger, A.-T., Barucci, M. A., Bertaux, J.-L., Bertini, I., Besse, S., Bodewits, D., Capanna, C., da Deppo, V., Davidsson, B., Debei, S., de Cecco, M., Ferri, F., Fornasier, S., Fulle, M., Gaskell, R., Groussin, O., Gutiérrez, P. J., Güttler, C., Hviid, S. F., Ip, W.-H., Knollenberg, J., Kovacs, G., Kramm, R., Kührt, E., Küppers, M., La Forgia, F., Lara, L. M., Lazzarin, M., Lin, Z.-Y., Lopez Moreno, J. J., Magrin, S., Michalik, H., Mottola, S., Oklay, N., Pommerol, A., Thomas, N., Tubiana, C., Vincent, J.-B., 2015, Two independent and primitive envelopes of the bilobate nucleus of comet 67P, Nature, 526, 402–405

Masunaga, K., Nilsson, H., Goetz, C., in preparation, Ion velocity near the diamagnetic cavity, Astronomy & Astrophysics

Nagdimunov, L., Kolokolova, L., Wolff, M., A'Hearn, M. F., Farnham, T. L., 2014, Properties of comet 9P/Tempel 1 dust immediately following excavation by deep impact, Planetary and Space Science, 100, 73–78, 1406.3308

Nemeth, Z., Burch, J., Goetz, C., Goldstein, R., Henri, P., Koenders, C., Madanian, H., Mandt, K., Mokashi, P., Richter, I., Timar, A., Szego, K., 2016, Charged particle signatures of the diamagnetic cavity of comet 67P/Churyumov-Gerasimenko, Monthly Notices of the Royal Astronomical Society, 462, S415–S421

Neubauer, F. M., 1987, Giotto magnetic-field results on the boundaries of the pile-up region and the magnetic cavity, Astronomy & Astrophysics, 187, 73–79

Neubauer, F. M., 1988, The ionopause transition and boundary layers at Comet Halley from Giotto magnetic field observations, Journal of Geophysical Research, 93, 7272–7281

Neubauer, F. M., Glassmeier, K. H., Pohl, M., Raeder, J., Acuna, M. H., Burlaga, L. F., Ness, N. F., Musmann, G., Mariani, F., Wallis, M. K., Ungstrup, E., Schmidt, H. U., 1986, First results from the Giotto magnetometer experiment at comet Halley, Nature, 321, 352–355

Neubauer, F. M., Glassmeier, K.-H., Coates, A. J., Johnstone, A. D., 1993, Low-frequency electromagnetic plasma waves at comet P/Grigg-Skjellerup analysis and interpretation, Journal of Geophysical Research, 98, 20 937–20 954

Nilsson, H., Lundin, R., Lundin, K., Barabash, S., Borg, H., Norberg, O., Fedorov, A., Sauvaud, J.-A., Koskinen, H., Kallio, E., Riihelä, P., Burch, J. L., 2007, RPC-ICA: The Ion Composition Analyzer of the Rosetta Plasma Consortium, Space Science Reviews, 128, 671–695

Nilsson, H., Wieser, G. S., Behar, E., Gunell, H., Wieser, M., Galand, M., Simon Wedlund, C., Alho, M., Goetz, C., Yamauchi, M., Henri, P., Odelstad, E., Vigren, E., 2017, Evolution of the ion environment of comet 67P during the Rosetta mission as seen by RPC-ICA, Monthly Notices of the Royal Astronomical Society, 469, S252–S261

Noonan, J. W., Stern, S. A., Feldman, P. D., Broiles, T., Wedlund, C. S., Edberg, N. J. T., Schindhelm, E., Parker, J. W., Keeney, B. A., Vervack, Ronald J., J., Steffl, A. J., Knight, M. M., Weaver, H. A., Feaga, L. M., A'Hearn, M., Bertaux, J.-L., 2018, Ultraviolet Observations of Coronal Mass Ejection Impact on Comet 67P /Churyumov-Gerasimenko by Rosetta Alice, AJ, 156, 16

Odelstad, E., Eriksson, A. I., Edberg, N. J. T., Johansson, F., Vigren, E., André, M., Tzou, C. Y., Carr, C., Cupido, E., 2015, Evolution of the plasma environment of comet 67P from spacecraft potential measurements by the Rosetta Langmuir probe instrument, Geophysical Research Letters, 42, 10,126–10,134

Odelstad, E., Eriksson, A. I., Johansson, F. L., Vigren, E., Henri, P., Gilet, N., Heritier, K. L., Vallières, X., Rubin, M., André, M., 2018, Ion velocity and electron temperature inside and around the diamagnetic cavity of comet 67P, ArXiv e-prints, arXiv:1808.03581, 1808.03581

Odstrcil, D., 2003, Modeling 3-D solar wind structure, Advances in Space Research, 32, 497–506

Pajola, M., Höfner, S., Vincent, J. B., Oklay, N., Scholten, F., Preusker, F., Mottola, S., Naletto, G., Fornasier, S., Lowry, S., Feller, C., Hasselmann, P. H., Güttler, C., Tubiana, C., Sierks, H., Barbieri, C., Lamy, P., Rodrigo, R., Koschny, D., Rickman, H., Keller, H. U., Agarwal, J., A'Hearn, M. F., Barucci, M. A., Bertaux, J. L., Bertini, I., Besse, S., Boudreault, S., Cremonese, G., da Deppo, V., Davidsson, B., Debei, S., de Cecco, M., Deller, J., Deshapriya, J. D. P., El-Maarry, M. R., Ferrari, S., Ferri, F., Fulle, M., Groussin, O., Gutierrez, P., Hofmann, M., Hviid, S. F., Ip, W. H., Jorda, L., Knollenberg, J., Kovacs, G., Kramm, J. R., Kührt, E., Küppers, M., Lara, L. M., Lin, Z. Y., Lazzarin, M., Lucchetti, A., Lopez Moreno, J. J., Marzari, F., Massironi, M., Michalik, H., Penasa, L., Pommerol, A., Simioni, E., Thomas, N., Toth, I., Baratti, E., 2017, The pristine interior of comet 67P revealed by the combined Aswan outburst and cliff collapse, Nature Astronomy, 1, 0092

Parker, E. N., 1958, Dynamics of the Interplanetary Gas and Magnetic Fields., ApJ, 128, 664

Pätzold, M., Häusler, B., Aksnes, K., Anderson, J. D., Asmar, S. W., Barriot, J.-P., Bird, M. K., Boehnhardt, H., Eidel, W., Grün, E., Ip, W. H., Marouf, E., Morley, T., Neubauer, F. M., Rickman, H., Thomas, N., Tsurutani, B. T., Wallis, M. K., Wickramasinghe, N. C., Mysen, E., Olson, O., Remus, S., Tellmann, S., Andert, T., Carone, L., Fels, M., Stanzel, C., Audenrieth-Kersten, I., Gahr, A., Müller, A.-L., Stupar, D., Walter, C., 2007, Rosetta Radio Science Investigations (RSI), Space Science Reviews, 128, 599–627

Pätzold, M., Andert, T., Hahn, M., Asmar, S. W., Barriot, J. P., Bird, M. K., Häusler, B., Peter, K., Tellmann, S., Grün, E., Weissman, P. R., Sierks, H., Jorda, L., Gaskell, R., Preusker, F., Scholten, F., 2016, A homogeneous nucleus for comet 67P/Churyumov-Gerasimenko from its gravity field, Nature, 530, 63–65

Plaschke, F., Goetz, C., Volwerk, M., Richter, I., Frühauff, D., Narita, Y., Glassmeier, K.-H., Dougherty, M. K., 2017, Fluxgate magnetometer offset vector determination by the 3D mirror mode method, Monthly Notices of the Royal Astronomical Society, 469, S675–S684

Plaschke, F., Karlsson, T., Götz, C., Möstl, C., Richter, I., Volwerk, M., Eriksson, A., Behar, E., Goldstein, R., 2018, First observations of magnetic holes deep within the coma of a comet, Astronomy & Astrophysics, 618, A114

Reinhard, R., 1986, The Giotto encounter with comet Halley, Nature, 321, 313–318

Reinhard, R., 1987, The Giotto mission to Comet Halley, Journal of Physics E Scientific Instruments, 20, 700–712

Richter, I., Koenders, C., Glassmeier, K. H., Tsurutani, B. T., Goldstein, R., 2011, Deep Space 1 at comet 19P/Borrelly: Magnetic field and plasma observations, Planetary Space Science, 59, 691–698

Richter, I., Koenders, C., Auster, H.-U., Frühauff, D., Götz, C., Heinisch, P., Perschke, C., Motschmann, U., Stoll, B., Altwegg, K., Burch, J., Carr, C., Cupido, E., Eriksson, A., Henri, P., Goldstein, R., Lebreton, J.-P., Mokashi, P., Nemeth, Z., Nilsson, H., Rubin, M., Szegö, K., Tsurutani, B. T., Vallat, C., Volwerk, M., Glassmeier, K.-H., 2015, Observation of a new type of low-frequency waves at comet 67P/Churyumov-Gerasimenko, Annales Geophysicae, 33, 1031–1036, 1505.06068

Richter, I., Auster, H.-U., Berghofer, G., Carr, C., Cupido, E., Fornaçon, K.-H., Goetz, C., Heinisch, P., Koenders, C., Stoll, B., Tsurutani, B. T., Vallat, C., Volwerk, M., Glassmeier, K.-H., 2016, Two-point observations of low-frequency waves at 67P/Churyumov-Gerasimenko during the descent of PHILAE: comparison of RPCMAG and ROMAP, Annales Geophysicae, 34, 609–622

Riedler, W., Torkar, K., Jeszenszky, H., Romstedt, J., Alleyne, H. S. C., Arends, H., Barth, W., Biezen, J. V. D., Butler, B., Ehrenfreund, P., Fehringer, M., Fremuth, G., Gavira, J., Havnes, O., Jessberger, E. K., Kassing, R., Klöck, W., Koeberl, C., Levasseur-Regourd, A. C., Maurette, M., Rüdenauer, F., Schmidt, R., Stangl, G., Steller, M., Weber, I., 2007, MIDAS The Micro-Imaging Dust Analysis System for the Rosetta Mission, Space Science Reviews, 128, 869–904

Rodgers, D. J., Coates, A. J., Johnstone, A. D., Smith, M. F., Bryant, D. A., 1986, UKS plasma measurements near the AMPTE artificial comet, Nature, 320, 712–716

Rubin, M., Hansen, K. C., Combi, M. R., Daldorff, L. K. S., Gombosi, T. I., Tenishev, V. M., 2012, Kelvin-Helmholtz instabilities at the magnetic cavity boundary of comet 67P/Churyumov-Gerasimenko, Journal of Geophysical Research (Space Physics), 117, A06227

Sagdeev, R. Z., Blamont, J., Galeev, A. A., Moroz, V. I., Shapiro, V. D., Shevchenko, V. I., Szegó, K., 1986, Vega spacecraft encounters with comet Halley, Nature, 321, 259–262

Sauer, K., Baumgaertel, K., 1987, Magnetic cavity formation at comet Halley and at the AMPTE Li release., in Diversity and Similarity of Comets, (Eds.) E. J. Rolfe, B. Battrick, M. Ackerman, M. Scherer, R. Reinhard, vol. 278, pp. 113–118

Schultz, P. H., Hermalyn, B., Veverka, J., 2013, The Deep Impact crater on 9P/Tempel-1 from Stardust-NExT, Icarus, 222, 502–515

Shiota, D., Kataoka, R., Miyoshi, Y., Hara, T., Tao, C., Masunaga, K., Futaana, Y., Terada, N., 2014, Inner heliosphere MHD modeling system applicable to space weather forecasting for the other planets, Space Weather, 12, 187–204

Simon Wedlund, C., Kallio, E., Alho, M., Nilsson, H., Stenberg Wieser, G., Gunell, H., Behar, E., Pusa, J., Gronoff, G., 2016, The atmosphere of comet 67P/Churyumov-Gerasimenko diagnosed by charge- exchanged solar wind alpha particles, Astronomy & Astrophysics, 587, A154

Simon Wedlund, C., Alho, M., Gronoff, G., Kallio, E., Gunell, H., Nilsson, H., Lindkvist, J., Behar, E., Stenberg Wieser, G., Miloch, W. J., 2017, Hybrid modelling of cometary plasma environments. I. Impact of photoionisation, charge exchange, and electron ionisation on bow shock and cometopause at 67P/Churyumov-Gerasimenko, Astronomy & Astrophysics, 604, A73

Smith, E. J., Wolfe, J. H., 1976, Observations of interaction regions and corotating shocks between one and five AU: Pioneers 10 and 11, Geophysical Research Letters, 3, 137–140

Smyth, W. H., Combi, M. R., Stewart, A. I. F., 1991, Analysis of the Pioneer-Venus Lyman-α Image of the Hydrogen Coma of Comet P/Halley, Science, 253, 1008–1010

Snodgrass, C., A'Hearn, M. F., Aceituno, F., Afanasiev, V., Bagnulo, S., Bauer, J., Bergond, G., Besse, S., Biver, N., Bodewits, D., Boehnhardt, H., Bonev, B. P., Borisov, G., Carry, B., Casanova, V., Cochran, A., Conn, B. C., Davidsson, B., Davies, J. K., de León, J., de Mooij, E., de Val-Borro, M., Delacruz, M., DiSanti, M. A., Drew, J. E., Duffard, R., Edberg, N. J. T., Faggi, S., Feaga, L., Fitzsimmons, A., Fujiwara, H., Gibb, E. L., Gillon, M., Green, S. F., Guijarro, A., Guilbert-Lepoutre, A., Gutiérrez, P. J., Hadamcik, E., Hainaut, O., Haque, S., Hedrosa, R., Hines, D., Hopp, U., Hoyo, F., Hutsemékers, D., Hyland, M., Ivanova, O., Jehin, E., Jones, G. H., Keane, J. V., Kelley, M. S. P., Kiselev, N., Kleyna, J., Kluge, M., Knight, M. M., Kokotanekova, R., Koschny, D., Kramer, E. A., López-Moreno, J. J., Lacerda, P., Lara, L. M., Lasue,

J., Lehto, H. J., Levasseur-Regourd, A. C., Licandro, J., Lin, Z. Y., Lister, T., Lowry, S. C., Mainzer, A., Manfroid, J., Marchant, J., McKay, A. J., McNeill, A., Meech, K. J., Micheli, M., Mohammed, I., Monguió, M., Moreno, F., Muñoz, O., Mumma, M. J., Nikolov, P., Opitom, C., Ortiz, J. L., Paganini, L., Pajuelo, M., Pozuelos, F. J., Protopapa, S., Pursimo, T., Rajkumar, B., Ramanjooloo, Y., Ramos, E., Ries, C., Riffeser, A., Rosenbush, V., Rousselot, P., Ryan, E. L., Santos-Sanz, P., Schleicher, D. G., Schmidt, M., Schulz, R., Sen, A. K., Somero, A., Sota, A., Stinson, A., Sunshine, J. M., Thompson, A., Tozzi, G. P., Tubiana, C., Villanueva, G. L., Wang, X., Wooden, D. H., Yagi, M., Yang, B., Zaprudin, B., Zegmott, T. J., 2017, The 67P/Churyumov-Gerasimenko observation campaign in support of the Rosetta mission, Philosophical Transactions of the Royal Society of London Series A, 375, 20160249

Soderblom, L. A., Becker, T. L., Bennett, G., Boice, D. C., Britt, D. T., Brown, R. H., Buratti, B. J., Isbell, C., Giese, B., Hare, T., Hicks, M. D., Howington-Kraus, E., Kirk, R. L., Lee, M., Nelson, R. M., Oberst, J., Owen, T. C., Rayman, M. D., Sandel, B. R., Stern, S. A., Thomas, N., Yelle, R. V., 2002, Observations of Comet 19P/Borrelly by the Miniature Integrated Camera and Spectrometer Aboard Deep Space 1, Science, 296, 1087–1091

Stallmann, N., 2018, Simulation eines künstlichen Kometen, Bachelor Thesis, TU Braunschweig

Stenberg Wieser, G., Odelstad, E., Wieser, M., Nilsson, H., Goetz, C., Karlsson, T., André, M., Kalla, L., Eriksson, A. I., Nicolaou, G., Simon Wedlund, C., Richter, I., Gunell, H., 2017, Investigating short-time-scale variations in cometary ions around comet 67P, Monthly Notices of the Royal Astronomical Society, 469, S522–S534

Stern, S. A., Slater, D. C., Scherrer, J., Stone, J., Versteeg, M., A'Hearn, M. F., Bertaux, J. L., Feldman, P. D., Festou, M. C., Parker, J. W., Siegmund, O. H. W., 2007, Alice: The Rosetta Ultraviolet Imaging Spectrograph, Space Science Reviews, 128, 507–527, astro-ph/0603585

Tao, C., Kataoka, R., Fukunishi, H., Takahashi, Y., Yokoyama, T., 2005, Magnetic field variations in the Jovian magnetotail induced by solar wind dynamic pressure enhancements, Journal of Geophysical Research (Space Physics), 110, A11208

Timar, A., Nemeth, Z., Szego, K., Dosa, M., Opitz, A., Madanian, H., Goetz, C., Richter, I., 2017, Modelling the size of the very dynamic diamagnetic cavity of comet 67P/Churyumov-Gerasimenko, Monthly Notices of the Royal Astronomical Society, 469, S723–S730

Trotignon, J. G., Michau, J. L., Lagoutte, D., Chabassière, M., Chalumeau, G., Colin, F., Décréau, P. M. E., Geiswiller, J., Gille, P., Grard, R., Hachemi, T., Hamelin, M., Eriksson, A., Laakso, H., Lebreton, J. P., Mazelle, C., Randriamboarison, O., Schmidt, W., Smit, A., Telljohann, U., Zamora, P., 2007, RPC-MIP: the Mutual Impedance Probe of the Rosetta Plasma Consortium, Space Science Reviews, 128, 713–728

Tsurutani, B. T., Smith, E. J., 1986, Hydromagnetic waves and instabilities associated with cometary ion pickup - ICE observations, Geophysical Research Letters, 13, 263–266

Tsurutani, B. T., Gonzalez, W. D., Tang, F., Akasofu, S. I., Smith, E. J., 1988, Origin of interplanetary southward magnetic fields responsible for major magnetic storms near solar maximum (1978-1979), Journal of Geophysical Research, 93, 8519–8531

Tsurutani, B. T., Gould, T., Goldstein, B. E., Gonzalez, W. D., Sugiura, M., 1990, Interplanetary Alfvén waves and auroral (substorm) activity: IMP 8, Journal of Geophysical Research, 95, 2241–2252

Valenzuela, A., Haerendel, G., Föppl, H., Melzner, F., Neuss, H., Rieger, E., Stöcker, J., Bauer, O., Höfner, H., Loidl, J., 1986, The AMPTE artificial comet experiments, Nature, 320, 700–703

Vigren, E., Eriksson, A. I., 2017, A 1D Model of Radial Ion Motion Interrupted by Ion-Neutral Interactions in a Cometary Coma, AJ, 153, 150

Vigren, E., André, M., Edberg, N. J. T., Engelhardt, I. A. D., Eriksson, A. I., Galand, M., Goetz, C., Henri, P., Heritier, K., Johansson, F. L., Nilsson, H., Odelstad, E., Rubin, M., Stenberg-Wieser, G., Tzou, C. Y., Valliéres, X., 2017, Effective ion speeds at 200-250 km from comet 67P/Churyumov-Gerasimenko near perihelion, Monthly Notices of the Royal Astronomical Society, 469, S142–S148

Vincent, J. B., A'Hearn, M. F., Lin, Z. Y., El- Maarry, M. R., Pajola, M., Sierks, H., Barbieri, C., Lamy, P. L., Rodrigo, R., Koschny, D., Rickman, H., Keller, H. U., Agarwal, J., Barucci, M. A., Bertaux, J. L., Bertini, I., Besse, S., Bodewits, D., Cremonese, G., Da Deppo, V., Davidsson, B., Debei, S., De Cecco, M., Deller, J., Fornasier, S., Fulle, M., Gicquel, A., Groussin, O., Gutiérrez, P. J., Gutiérrez-Marquez, P., Güttler, C., Höfner, S., Hofmann, M., Hviid, S. F., Ip, W. H., Jorda, L., Knollenberg, J., Kovacs, G., Kramm, J. R., Kührt, E., Küppers, M., Lara, L. M., Lazzarin, M., Lopez Moreno, J. J., Marzari, F., Massironi, M., Mottola, S., Naletto, G., Oklay, N., Preusker, F., Scholten, F., Shi, X., Thomas, N., Toth, I., Tubiana, C., 2016, Summer fireworks on comet 67P, Monthly Notices of the Royal Astronomical Society, 462, S184–S194

Zieger, B., Hansen, K. C., 2008, Statistical validation of a solar wind propagation model from 1 to 10 AU, Journal of Geophysical Research (Space Physics), 113, A08 107

A Appendix

A.1. Paper I: First detection of a diamagnetic cavity at comet 67P/Churyumov-Gerasimenko

Authors: C. Goetz, C. Koenders, I. Richter, K. Altwegg, J. Burch, C. Carr, E. Cupido, A. Eriksson, C. Güttler, P. Henri, P. Mokashi, Z. Nemeth, H. Nilsson, M. Rubin, H. Sierks, B. Tsurutani, C. Vallat, M. Volwerk, K.-H. Glassmeier

Bibliographic Information: Astronomy & Astrophysics, 588, A24, doi: 10.1051/0004-6361/201527728

Year: 2016

Citations: 49 (The SAO/NASA Astrophysics Data System, December 2018)

A&A 588, A24 (2016)
DOI: 10.1051/0004-6361/201527728
© ESO 2016

Astronomy & Astrophysics

First detection of a diamagnetic cavity at comet 67P/Churyumov-Gerasimenko

C. Goetz[1], C. Koenders[1], I. Richter[1], K. Altwegg[2], J. Burch[3], C. Carr[4], E. Cupido[4], A. Eriksson[5], C. Güttler[6], P. Henri[7], P. Mokashi[3], Z. Nemeth[8], H. Nilsson[9], M. Rubin[2], H. Sierks[6], B. Tsurutani[10], C. Vallat[11], M. Volwerk[12], and K.-H. Glassmeier[1]

[1] Institut für Geophysik und extraterrestrische Physik, TU Braunschweig, Mendelssohnstr. 3, 38106 Braunschweig, Germany
e-mail: c.goetz@tu-bs.de
[2] Physikalisches Institut, University of Bern, Sidlerstrasse 5, 3012 Bern, Switzerland
[3] Southwest Research Institute, PO Drawer 28510, San Antonio, TX 78228-0510, USA
[4] Space and Atmospheric Physics Group, Imperial College London, Exhibition Road, London SW7 2AZ, UK
[5] Swedish Institute of Space Physics, Angström Laboratory, Lägerhyddsvägen 1, 75105 Uppsala, Sweden
[6] Max-Planck-Institut für Sonnensystemforschung, Justus-von-Liebig-Weg 3, 37077 Göttingen, Germany
[7] Laboratoire de Physique et Chimie de l'Environnement et de l'Espace, UMR 7328 CNRS, Université d'Orléans, 45100 Orléans, France
[8] Wigner Research Centre for Physics, Konkoly Thege Miklós út 29-33, 1121 Budapest, Hungary
[9] Swedish Institute of Space Physics, PO Box 812, 981 28 Kiruna, Sweden
[10] Jet Propulsion Laboratory, California Institute of Technology, 4800 Oak Grove Drive, Pasadena, CA 91109, USA
[11] European Space Astronomy Centre, 28691 Villanueva de la Canada, Madrid, Spain
[12] Space Research Institute, Austrian Academy of Sciences, Schmiedlstr. 6, 8042 Graz, Austria

Received 10 November 2015 / Accepted 4 February 2016

ABSTRACT

Context. The Rosetta magnetometer RPC-MAG has been exploring the plasma environment of comet 67P/Churyumov-Gerasimenko since August 2014. The first months were dominated by low-frequency waves which evolved into more complex features. However, at the end of July 2015, close to perihelion, the magnetometer detected a region that did not contain any magnetic field at all.
Aims. These signatures match the appearance of a diamagnetic cavity as was observed at comet 1P/Halley in 1986. The cavity here is more extended than previously predicted by models and features unusual magnetic field configurations, which need to be explained.
Methods. The onboard magnetometer data were analyzed in detail and used to estimate the outgassing rate. A minimum variance analysis was used to determine boundary normals.
Results. Our analysis of the data acquired by the Rosetta Plasma Consortium instrumentation confirms the existence of a diamagnetic cavity. The size is larger than predicted by simulations, however. One possible explanation are instabilities that are propagating along the cavity boundary and possibly a low magnetic pressure in the solar wind. This conclusion is supported by a change in sign of the Sun-pointing component of the magnetic field. Evidence also indicates that the cavity boundary is moving with variable velocities ranging from 230−500 m/s.

Key words. comets: individual: 67P/Churyumov-Gerasimenko – plasmas – magnetic fields – methods: data analysis

1. Introduction

The existence of a boundary region between the mass-loaded solar wind and the cometary plasma was first hypothesized by Biermann et al. (1967), who demonstrated with a semi-analytical approach that the solar wind is slowed and redirected when approaching a comet with significant outgassing rates. The incorporation or mass-loading of the heavy cometary ions into the solar wind also leads to the formation of a bow shock on the sunward side of the comet (Szegö et al. 2000; Koenders et al. 2013), then after passing this shock, the solar wind decelerates further and, on the Sun-comet line, eventually stops at the contact surface. Although this purely hydrodynamical approach did not include a treatment of the magnetic field, it was still possible to infer that this so-called contact surface would also affect the interplanetary magnetic field. In a first, simplified model we assume that the magnetic field is frozen into the solar wind flow, and as it decelerates, so does the field, leading to a significant increase in strength. This pile-up then abruptly stops at the contact surface where the magnetic field strength drops to zero because the comet does not have a magnetic field of its own (Auster et al. 2015). This region has been named the "diamagnetic cavity" and is bounded on the outside by an ion composition boundary that the solar wind ions cannot penetrate. This is the cometary ionopause.

The existence of a diamagnetic cavity could not be proven until the *Giotto* flyby at comet 1P/Halley in 1986. Neubauer et al. (1986) and Neubauer (1988) presented magnetometer data in which a field-free region was detected at a distance of 4760 km inbound and 3840 km outbound. This distance was greater than expected for a simple balance between magnetic pressure upstream and dynamic pressure downstream of the boundary. This led Cravens (1987) and Ip & Axford (1987) to the conclusion that the cavity must be sustained by an ion-neutral friction force.

A&A 588, A24 (2016)

The corresponding equation shows the balance of the magnetic pressure and the ion-neutral drag:

$$-\frac{\partial}{\partial r}\left(\frac{B^2}{2\mu_0}\right) = n_i m_i \nu_{in}\,(u_i - u_n)\,, \quad (1)$$

where B is the magnetic field on the solar wind side, r is the radial distance and n_i, m_i and u_i are number density, mass, and velocity of the cometary ions. ν_{in} is the ion-neutral collision coefficient and u_n the neutral gas velocity. Hence, the cavity standoff distance is balanced on one side by the incoming magnetic field and on the other side by the outgassing parameters of the comet. For simple approximations, the ion velocity u_i is often assumed to be zero because the cometary ions and solar wind ions both reach a stagnation point at the cavity boundary. This equation can be used to estimate the distance of the cavity depending on the parameters.

Additionally, Ershkovich & Mendis (1986) found that the boundary region is susceptible to both Kelvin-Helmholtz and Rayleigh-Taylor instabilities, although the latter requires a very high gravitational force. Later, the evolution of these unstable modes was investigated by Ershkovich & Flammer (1988) with the conclusion that these modes can indeed convect downstream and reach high amplitudes especially in the case of a weakly outgassing comet (e.g., 21P/Giacobini-Zinner).

Almost three decades after the *Giotto* flyby at comet 1P/Halley, the Rosetta mission has now afforded a new opportunity to study a cometary plasma environment in situ. The Rosetta spacecraft (Glassmeier et al. 2007a) was launched in 2004 and arrived at comet 67P/Churyumov-Gerasimenko (67P) in August 2014. Since its arrival Rosetta scientists have studied the plasma environment of this comet while it approached the Sun and its activity increased. New findings include the detection of low-frequency magnetic field waves (Richter et al. 2015) and heavy ion and solar wind deflection (Nilsson et al. 2015) in the low-activity plasma environment. At a comet-Sun distance of 1.2 AU in July 2015, the Rosetta magnetometer RPC-MAG has detected several signatures of a diamagnetic cavity. The aim of this paper is to provide a first description of the longest duration diamagnetic cavity event and its properties and discuss possible explanations of its unusual features.

2. Observation

2.1. Instrumentation

All magnetic field data presented here were recorded by the Rosetta Plasma Consortium MAGnetometer (RPC-MAG), a fluxgate magnetometer with a resolution of 39 pT and a range of ±16 384 nT (Glassmeier et al. 2007b). RPC-MAG consists of two separate sensors mounted on a boom of 1.5 m length, one inboard (IB) and one outboard (OB), with a separation of 15 cm. During the interval in question MAG was running in burst mode, meaning an OB sampling frequency of 20 Hz and an IB sampling frequency of 1 Hz. Because of the small separation of the spacecraft main infrastructure and the magnetometers, the magnetic field measurements are polluted by currents from the spacecraft subsystems. First, the influence of the reaction wheels is profound, but they can easily be filtered out in burst mode because their signature is well known (Glassmeier et al. 2007b). Second, the offset of the magnetic field has an error of ∼5 nT in each component that is due to unknown magnetic field sources on the spacecraft as determined from measurements earlier in the mission. Fortunately, the measurements in the cavity can be used to calibrate the data, as it is known from theory that the field inside the cavity must be approximately zero (Biermann et al. 1967).

Unless otherwise indicated, all data are presented in the body-centered solar equatorial frame (CSEQ), where the x-axis points toward the Sun, the z-axis is the component of the solar north pole that is orthogonal to the x-axis, and the y-axis completes the right-handed coordinate system. In July 2015, the Rosetta spacecraft was orbiting the comet in the terminator plane, that is, along the day-night line, with a 90° angle with respect to the Sun-comet line. On July 26, 2015, Rosetta was located 170 km from the nucleus in the negative y and z quadrant. During the 80-min interval presented here, the spacecraft moved 3 km, which is negligible compared to the dimensions of the plasma region discussed here.

For supplemental information, data from the Rosetta Orbiter Spectrometer for Ion and Neutral Analysis (ROSINA) were used to provide a preliminary estimate of the neutral gas density and gas production rate. Information on outbursts was extracted from OSIRIS images. For further information concerning the ROSINA instrument see Balsiger et al. (2007) and for the OSIRIS camera see Keller et al. (2007).

To estimate the solar wind parameters during this time, we use the model developed by Tao et al. (2005) that is available through the Automated Multi Dataset Analysis (AMDA, `amda.cdpp.eu`) archiving system. In this model, OMNI data are used to extract input parameters which are the basis for a one-dimensional, spherically symmetric magnetohydrodynamic (MHD) solar wind propagation model.

2.2. Data

Figure 1 shows the magnetic field components and the field magnitude on July 26, 2015, corrected for the spacecraft bias field of 6.5 nT by subtracting the mean value of the remaining field in the cavity from each component. The diamagnetic cavity is clearly visible from 15:16 to 15:41 as a constant very low magnetic field with almost no wave activity. This lack of fluctuations is remarkable as it is the first time that RPC-MAG has registered no waves at all, which again confirms that this is a diamagnetic cavity. As there is no magnetic field in this region, there can be no magnetic fluctuations. This is the longest interval of cavity measurements up till now, with a duration of ∼25 min. It is also preceded by three short dips (14:46, 14:54, 15:00) that might indicate cavity boundary crossings, but the interval is too short to conclusively prove the presence of a cavity through the lack of wave activity, therefore we focus our studies on the long event.

The average field before the cavity is (−21.4, 0.7, −0.9) nT and afterward (28.5, 2.5, −3.7) nT, but the surrounding area is characterized by structures with very high amplitude that are quasi-periodic and asymmetric. RPC-MAG has been observing these kinds of structures intermittently since June 2015 and continues to do so as of October 2015. We discuss these features in a later publication. The structures have a peak-to-peak amplitude of 30−50 nT with a period of 120−170 s. In this interval they are detected mainly in the B_x component, except for two cases where the y- and z-component also fluctuated heavily. This highly variable field makes it difficult to pinpoint exactly when the spacecraft enters the transition zone around the cavity; the blue shaded areas indicate our estimate of this region. Both crossings were determined on the outside by the fact that the slope of the magnetic field changes at that point in all components. The crossings are 110 s and 50 s long.

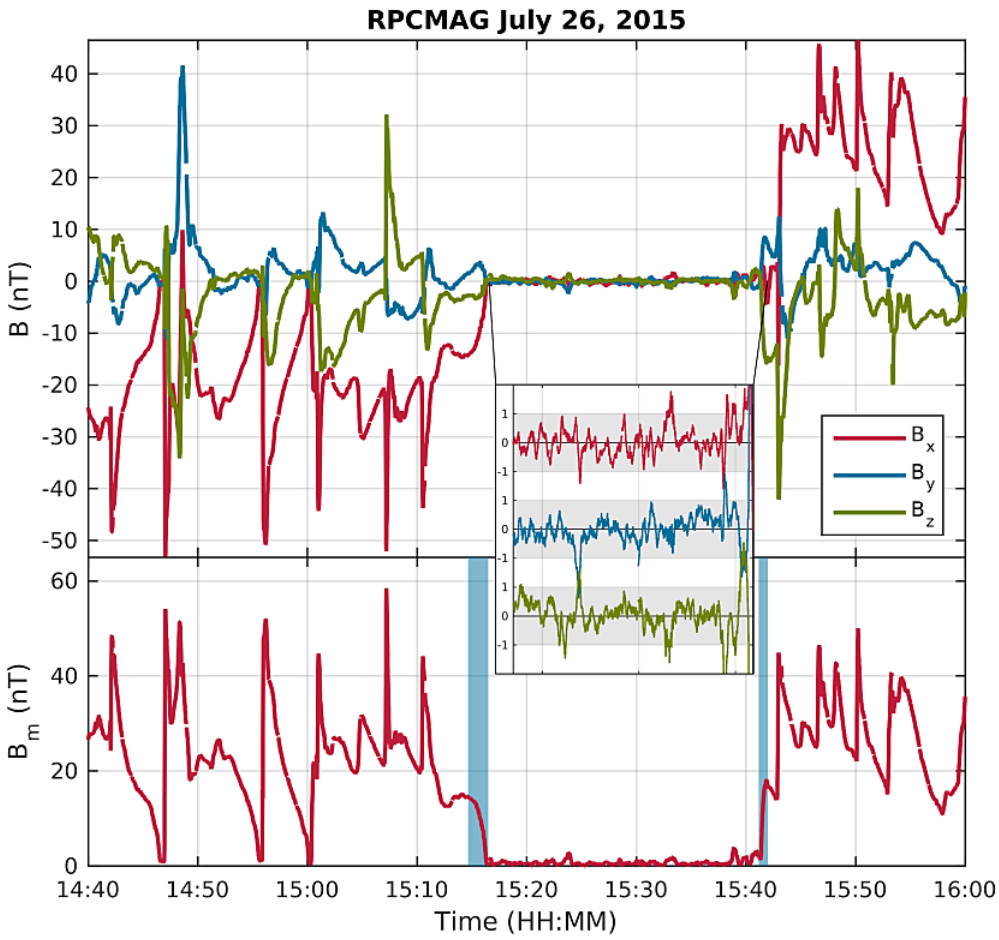

Fig. 1. Magnetic field data on July 26, 2015 from 14:40:00 UT to 16:00:00 UT. The *top panel* shows the three vector components, which have been corrected by subtracting a constant offset determined by the remaining magnetic field data in the cavity. The magnetic field magnitude shown in the *bottom panel* has been calculated from the corrected data. The cavity is visible between 15:16:00 UT and 15:41:00 UT, and the shaded areas mark the transition regions. The inset shows a more detailed picture of the three magnetic field components in the diamagnetic cavity.

There were asymmetries between the outbound and inbound diamagnetic cavity traversals. The outbound crossing is a factor of 2.2 shorter than the inbound one. In addition to the faster transition on the outbound leg, there are other notable differences between the two crossings. The transition region is preceded on the outbound path by three smaller quasi-periodic increases starting at 15:38 that are not observed on the inbound leg. During the outbound pass it is notable that B_x is a factor of ∼2 smaller than the other two components, before a sudden increase directly after this again makes it the primary component.

A further prominent feature of this cavity crossing is the reversal of the magnetic field in x-direction. As seen in Fig. 1, the x-component of the magnetic field is negative (pointing away from the Sun) before the cavity encounter and positive (pointing to the Sun) afterward.

There are two small magnetic anomalies in the cavity at 15:24 and at 15:33. During the first one, the y- and z-components both reach about 2 nT, whereas the x-component drops from 1 nT to −1 nT, which gives a maximum field strength of 3 nT. The second anomaly only has a maximum field strength of 2 nT because only the x-component and y-component contribute.

Table 1 shows the results of a minimum variance analysis (e.g. Sonnerup & Cahill 1967) conducted on the ionopause transition, and Fig. 2 displays the magnetic field and boundary normal configuration. The ionopause crossings used for the analysis are 110 s and 50 s long. For both intervals the ratio of the eigenvalues is sufficiently high to treat the minimum variance direction as indicative of the boundary normal. During both the inbound and the outbound pass, the boundary normal is quasi-perpendicular to the magnetic field, with the main component of the boundary normal in z-direction for the former and in y-direction for the latter.

3. Interpretation of the observations

First, we address the fact that the cavity detected here is significantly farther away from the comet than steady-state simulations (e.g. Koenders et al. 2015) suggest. A possible trigger for the outward motion of the cavity could be a gas and/or dust density increase, which should be detectable by OSIRIS (see Fig. 3). The middle panel approximately coincides with the time when Rosetta entered the cavity, and both the first and second

A&A 588, A24 (2016)

Table 1. Results of a minimum variance analysis of the cavity boundary crossings.

Interval	Duration (s)	n	θ_{Bn}	λ_1:λ_2:λ_3	Position (km)
15:14:40–15:16:30	110	(−0.13, 0.53, 0.84)	84°	1:11:268	(−0.1, −99.1, −138.5)
15:41:10–15:42:00	50	(−0.29, 0.82, 0.5)	106°	1:166:1889	(−0.1, −98.3, −139.0)

Notes. θ_{Bn} was calculated using average magnetic field values outside the cavity; the angle between the in- and outbound normal is 27°.

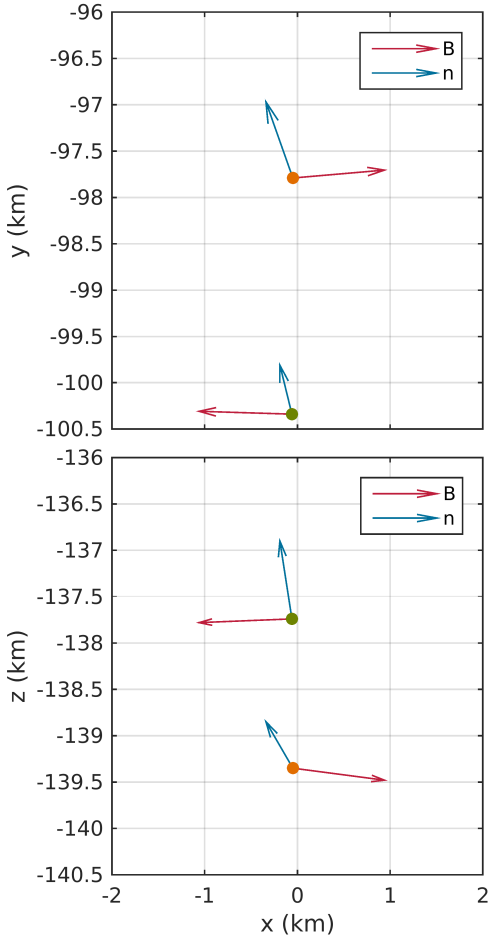

Fig. 2. Normal vector of the ionopause (blue) and averaged magnetic field (red) in the $x - y$ plane (*top*) and the $x - z$ plane (*bottom*) in CSEQ coordinates. The green point marks the inbound crossing, the orange point the outbound crossing. We note that the normal vector only indicates the direction and not the orientation of the boundary normal.

image show similar levels of activity, without any remarkable enhancements. The third image is provided for reference, indicating that the activity has slightly increased about an hour after Rosetta leaves the cavity, but this is within the typical range of diurnal variations. This leads us to conclude that the gas production rate is most likely stable during the interval in question. Another possibility is a generally elevated gas production rate and thereby a higher neutral gas density. According to Cravens (1987), the cavity boundary distance is proportional to $Q^{\frac{1}{4}}$ for a steady-state solution with isotropic outgassing. If we assume this to be true and use a reference value of 25 km for the stand-off distance at a gas production rate of $Q = 5 \times 10^{27}\,\mathrm{s}^{-1}$ (Koenders et al. 2015), the gas production rate that is required to push out the cavity to a distance of 170 km can be estimated. To do this, the position of Rosetta during the measurements needs to be considered as well, as the spacecraft was at a 90° angle from the subsolar point and the cavity does extend farther at these positions. Previously, the cavity has been approximated by fitting a paraboloid to the measurements (e.g. Neubauer 1987, 1988), which implies that the ionopause is farther from the comet at the terminator. Simulations suggest that the cavity boundary distance increases by a factor of 1.5 at these latitudes. With this in mind, the gas production rate for a steady state should be about $3 \times 10^{28}\,\mathrm{s}^{-1}$ to achieve the extended cavity we report here.

Second, the gas production rate can also be estimated from the ROSINA neutral gas densities using the Haser model (Haser 1957):

$$Q = 4\pi u_{\mathrm{ng}}\, r^2 n_{\mathrm{ng}}\, \exp\left(\frac{\nu r}{u_{\mathrm{ng}}}\right), \tag{2}$$

where the exponential term can be neglected for the cometocentric distance in question here, because the ionization constant ν is about $10^{-7}\,\mathrm{s}^{-1}$. A simple estimate for water with a neutral gas velocity of $u_{\mathrm{ng}} = 600$ m/s and values for July 26, 2015, when the neutral gas density n_{ng} was $2 \times 10^7\,\mathrm{cm}^{-3}$ and the distance r to the nucleus was 170 km, gives $Q = 4 \times 10^{27}\,\mathrm{s}^{-1}$. This is one order of magnitude smaller than the estimate above from the cavity crossing at that time. For events at a greater distance, this discrepancy stays roughly the same. It is important to note that this estimate does not take into account coma composition or inhomogeneous outgassing as measured by ROSINA over the course of the mission (Hässig et al. 2015) and therefore provides only a guideline for the outgassing rate. However, it is clear that during the time of the cavity detections, the outgassing rate has to be higher than predicted values. From this first estimate it is unlikely that a change in neutral gas density alone is responsible for the high boundary distance. The right-hand side of Eq. (1) also includes the neutral gas velocity, the ion mass, and the ionization rate. If any of these quantities is higher and not constant, as assumed here, the cavity would also expand.

So far only the right-hand side of Eq. (1) has been investigated, but the left-hand side is also worth studying. The expansion of the cavity may also be triggered by a low magnetic pressure in the incoming solar wind. An estimate of the impinging tangential solar wind magnetic field (Tao et al. 2005) was used to calculate the magnetic pressure in the solar wind around the time of the cavity event. The result together with the magnetic pressure calculated from RPC-MAG data is displayed in Fig. 4. The solar wind dynamic pressure is not shown because it remains unchanged during the interval. The solar wind magnetic pressure as estimated using the Tao et al. (2005) model is significantly lower because Rosetta is situated in the pile-up region, where the solar wind field has been enhanced already. But the solar wind also shows a significant decrease in magnetic pressure around the time when the cavity is observed. The delay time between

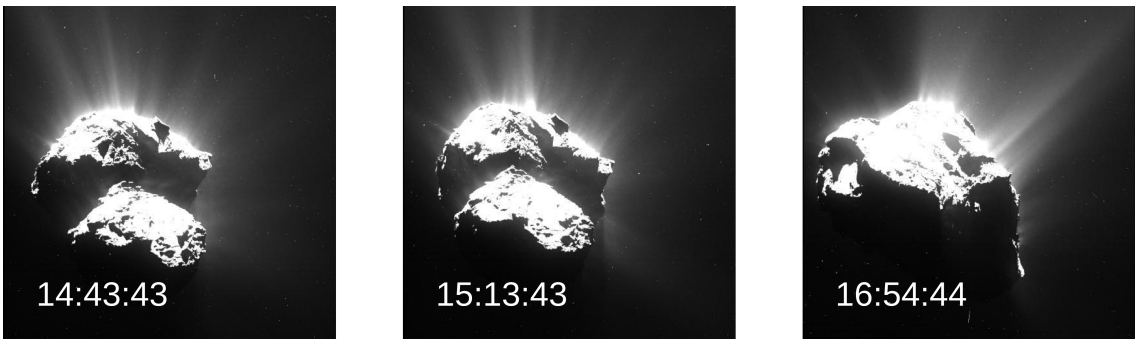

Fig. 3. OSIRIS UV filter images around the time of the cavity detection. The times (UTC) are indicated and all three images were scaled in the same way to visualize the dust coma and make them directly comparable.

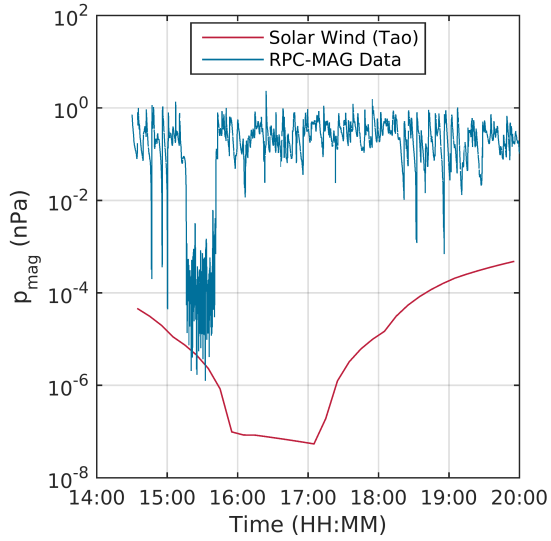

Fig. 4. Solar wind magnetic pressure obtained using the Tao et al. (2005) model and magnetic pressure as measured by RPC-MAG. The low-pressure region in the solar wind lasts from ~16:00 to ~17:00. We note that to predict the solar wind magnetic field at the comet we used a simple one dimensional MHD model that has large uncertainties.

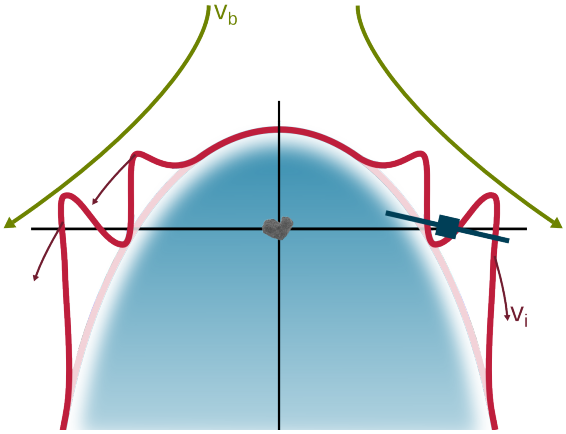

Fig. 5. Sketch of the magnetic field configuration in the frame where the ionopause (red) does not move. The lighter red line indicates the undisturbed cavity boundary. Rosetta's position is indicated in dark blue and the field free region is shaded in blue. v_i indicates the velocity of the instabilities and v_b the velocity of the ion bulk flow (green arrows).

the estimated solar wind magnetic pressure and the pressure observed by RPC-MAG may be caused by model uncertainties. For a constant radial solar wind magnetic field with constant solar wind dynamic pressure, the maximum magnetic field in the pile-up region is lower when the magnetic pressure decreases. This implies that the force created by the magnetic pressure acting on the ion-neutral friction force also decreases. This might explain the outward motion of the cavity. If, by chance, the interplanetary magnetic field reverses in direction during exactly this interval, it would also explain the magnetic field reversal during the crossing.

There are two other possible explanations for this situation: either there is an anomalously high density region that is causing the field to loop around, or instabilities propagate along the cavity boundary. We first examine the former possibility. To balance the magnetic pressure, the neutral density needs to be about 10^9 cm^{-3}, which is three orders of magnitude higher than the ROSINA estimate. We therefore discard this possibility.

The second option is an instability as investigated by Ershkovich & Mendis (1986) and Ershkovich & Flammer (1988). They found that a Kelvin-Helmholtz instability can develop for a sufficiently high velocity shear at the ionopause. The existence of these instabilities was also investigated in MHD (Rubin et al. 2012) and hybrid (Koenders et al. 2015) simulations of the plasma environment of 67P. The former found that these types of instabilities can be triggered by asymmetric outgassing. The latter even confirmed the existence of Kelvin-Helmholtz instabilities for homogeneous outgassing conditions. In both simulations "pockets" free of magnetic field propagate downstream and significantly alter the magnetic field structure. In the most extreme case this causes a field configuration similar to the one measured by Rosetta during this event; this is illustrated in Fig. 5. The instabilities that are triggered, for example, by a low solar wind magnetic field or an anomalously high gas density, propagate tailward along the cavity boundary and move over Rosetta's position. This way, the magnetic field changes direction, depending on whether it is located between two arms of the instability or entirely outside of the cavity including the unstable region.

We estimate the lowest bulk flow velocity v_b that is required by the Kelvin-Helmholtz instability criterion. As detailed in Ershkovich & Mendis (1986), it is possible to solve the Maxwell and MHD equations including the ion-neutral friction and gravity contributions for a dispersion relation that describes both the Rayleigh-Taylor and Kelvin-Helmholtz instability. Then the imaginary part of the dispersion relation (Ershkovich & Mendis 1986, Eq. (27)) can be used to determine the lowest flow velocity necessary to sustain the instabilities. For comet 67P, the gravity terms contribute little, therefore the Rayleigh-Taylor instability may be neglected. Under the assumption that $v_b \parallel B$, both orthogonal to the boundary normal and that the plasma number density and ionization coefficient do not change over the ionopause, the remaining instability criterion reduces to

$$v_b > \sqrt{2} v_A = \sqrt{2 \frac{B^2}{\mu_0 \rho}} \quad (3)$$

with ρ the plasma density at the ionopause and μ_0 the vacuum permittivity. For a rough estimate we assume that the number density of water ions is around 6000 cm^{-3} as measured by RPC, and that the magnetic field is 20 nT, resulting in $v_b > 2\,km\,s^{-1}$. As the bulk flow mainly constitutes the accelerated cometary ions in this region, it is possible to reach these velocities around a comet. However, this estimate is based on the assumption that the instability is triggered at the point where Rosetta is measuring. If the instability is triggered elsewhere and then convected downstream, the necessary velocity is determined by the parameters at the point of origin.

A moving instability might also explain the asymmetry of the in- and outbound ionopause. The apparently shorter transition time might indicate boundaries moving with differing velocities as seen in Koenders et al. (2015). The velocities v_i may even be calculated if we assume a constant thickness of the transition region. Neubauer (1988) found that the ionopause at 1P/Halley is approximately 25 km thick, and both Rubin et al. (2012) and Koenders et al. (2015) have reported similar thicknesses. With the transition times given in Table 1, we calculate velocities of 227 m/s for the inbound ionopause and 500 m/s for the outbound ionopause. This estimate neglects the spacecraft motion because it is slower than 1m/s during the crossings. Compared to characteristic velocities in the coma, for instance the neutral gas velocity, this is in the same order of magnitude, but slightly lower. Neubauer (1987) also speculated that the ionopause at Halley might have "ripples", which could be interpreted as a precursor to an instability. They were found by comparing the boundary normal of the inbound and outbound crossings. However, it should be noted that at Halley, the boundary normals were on opposite sides of the cometosphere and thus not directly comparable to this case. But the boundary normals here are always approximately perpendicular to the field, which matches our model quite well.

It remains to examine the field configuration in the cavity. So far we are unable to explain the two small anomalies at 15:24 and 15:33, but we can exclude the possibility that they are caused by spacecraft disturbances because the inboard magnetometer measures exactly the same amplitude of the anomalies. The field variation before Rosetta leaves the cavity is most likely caused by the instability of the boundary itself. Ershkovich & Flammer (1988) have speculated that at 21P/Giacobini-Zinner, the growing instability can break down the boundary and allow the magnetic field to "seep" into the cavity.

4. Conclusions

We reported the first detection of a diamagnetic cavity at comet 67P/Churyumov-Gerasimenko. Although the cavity was detected significantly farther away from the nucleus than predicted by simulations the very low field and lack of wave activity make it easily recognizable as a field-free region. A reversal of the magnetic field direction during the crossing led us to conclude that one possibility to explain the anomalously large cavity is the presence of instabilities propagating along the cavity boundary with a velocity of 230–500 m/s, with an underlying expansion of the entire cavity due to higher gas densities. This assumption can also explain the difference in time for the two ionopause crossings and the ripples preceding the outbound crossing. Other possible explanations are a low and/or rotating solar wind magnetic field or an anomalous neutral gas and ion background. It remains to be seen which of these explanations is most likely by investigating further cavity measurements.

Acknowledgements. The RPC-MAG and ROSINA data will be made available through the PSA archive of ESA and the PDS archive of NASA. Rosetta is a European Space Agency (ESA) mission with contributions from its member states and the National Aeronautics and Space Administration (NASA). The work on RPC-MAG was financially supported by the German Ministerium für Wirtschaft und Energie and the Deutsches Zentrum für Luft- und Raumfahrt under contract 50QP 1401. The work on ROSINA was funded by the federal state of Bern, the Swiss National Science Foundation, and the ESA PRODEX program. Portions of this research were performed at the Jet Propulsion Laboratory, California Institute of Technology, under contract with NASA. We are indebted to the whole of the Rosetta Mission Team, SGS, and RMOC for their outstanding efforts in making this mission possible. We acknowledge the staff of CDDP and IC for the use of AMDA and the RPC Quicklook database (provided by a collaboration between the Centre de Données de la Physique des Plasmas, supported by CNRS, CNES, Observatoire de Paris and Université Paul Sabatier, Toulouse and Imperial College London, supported by the UK Science and Technology Facilities Council).

References

Auster, H.-U., Apathy, I., Berghofer, G., et al. 2015, Science, 349, 015102
Balsiger, H., Altwegg, K., Bochsler, P., et al. 2007, Space Sci. Rev., 128, 745
Biermann, L., Brosowski, B., & Schmidt, H. U. 1967, Sol. Phys., 1, 254
Cravens, T. E. 1987, Adv. Space Res., 7, 147
Ershkovich, A. I., & Flammer, K. R. 1988, ApJ, 328, 967
Ershkovich, A. I., & Mendis, D. A. 1986, ApJ, 302, 849
Glassmeier, K.-H., Boehnhardt, H., Koschny, D., Kührt, E., & Richter, I. 2007a, Space Sci. Rev., 128, 1
Glassmeier, K.-H., Richter, I., Diedrich, A., et al. 2007b, Space Sci. Rev., 128, 649
Haser, L. 1957, Bull. Soc. Roy. Sci. Liège, 43, 740
Hässig, M., Altwegg, K., Balsiger, H., et al. 2015, Science, 347, 276
Ip, W.-H., & Axford, W. I. 1987, Nature, 325, 418
Keller, H. U., Barbieri, C., Lamy, P., et al. 2007, Space Sci. Rev., 128, 433
Koenders, C., Glassmeier, K.-H., Richter, I., Motschmann, U., & Rubin, M. 2013, Planet. Space Sci., 87, 85
Koenders, C., Glassmeier, K.-H., Richter, I., Ranocha, H., & Motschmann, U. 2015, Planet. Space Sci., 105, 101
Neubauer, F. M. 1987, A&A, 187, 73
Neubauer, F. M. 1988, J. Geophys. Res., 93, 7272
Neubauer, F. M., Glassmeier, K. H., Pohl, M., et al. 1986, Nature, 321, 352
Nilsson, H., Stenberg Wieser, G., Behar, E., et al. 2015, Science, 347, 0571
Richter, I., Koenders, C., Auster, H.-U., et al. 2015, Annales Geophysicae, 33, 1031
Rubin, M., Hansen, K. C., Combi, M. R., et al. 2012, J. Geophys. Res., 117, 6227
Sonnerup, B. U. O., & Cahill, Jr., L. J. 1967, J. Geophys. Res., 72, 171
Szegö, K., Glassmeier, K.-H., Bingham, R., et al. 2000, Space Sci. Rev., 94, 429
Tao, C., Kataoka, R., Fukunishi, H., Takahashi, Y., & Yokoyama, T. 2005, J. Geophys. Res., 110, 11208

A.2. Paper II: Structure and evolution of the diamagnetic cavity

Authors: C. Goetz, C. Koenders, K. C. Hansen, J. Burch, C. Carr, A. Eriksson, D. Frühauff, C. Güttler, P. Henri, H. Nilsson, I. Richter, M. Rubin, H. Sierks, B. Tsurutani, M. Volwerk, K.-H. Glassmeier

Bibliographic Information: Monthly Notices of the Royal Astronomical Society, 462, S459–S467, doi:10.1093/mnras/stw3148

Year: 2016

Citations: 28 (The SAO/NASA Astrophysics Data System, December 2018)

Monthly Notices of the ROYAL ASTRONOMICAL SOCIETY

MNRAS **462,** S459–S467 (2016) doi:10.1093/mnras/stw3148
Advance Access publication 2016 December 7

Structure and evolution of the diamagnetic cavity at comet 67P/Churyumov–Gerasimenko

C. Goetz,[1⋆] C. Koenders,[1] K. C. Hansen,[2] J. Burch,[3] C. Carr,[4] A. Eriksson,[5] D. Frühauff,[1] C. Güttler,[6] P. Henri,[7] H. Nilsson,[8] I. Richter,[1] M. Rubin,[9] H. Sierks,[6] B. Tsurutani,[10] M. Volwerk[11] and K. H. Glassmeier[1,6]

[1]*Institut für Geophysik und extraterrestrische Physik, TU Braunschweig, Mendelssohnstr. 3, D-38106 Braunschweig, Germany*
[2]*Department of Atmospheric, Oceanic and Space Sciences, University of Michigan, 2455 Hayward Street, Ann Arbor, MI 48109, USA*
[3]*Southwest Research Institute, PO Drawer 28510, San Antonio, TX 78228-0510, USA*
[4]*Space and Atmospheric Physics Group, Imperial College London, Exhibition Road, London SW7 2AZ, UK*
[5]*Swedish Institute of Space Physics, Angström Laboratory, Lägerhyddsvägen 1, SE-75105 Uppsala, Sweden*
[6]*Max-Planck-Institut für Sonnensystemforschung, Justus-von-Liebig-Weg 3, D-37077 Göttingen, Germany*
[7]*Laboratoire de Physique et Chimie de l'Environnement et de l'Espace, UMR 7328 CNRS, Université d'Orléans, F-45100 Orléans, France*
[8]*Swedish Institute of Space Physics, PO Box 812, SE-981 28 Kiruna, Sweden*
[9]*Physikalisches Institut, University of Bern, Sidlerstrasse 5, CH-3012 Bern, Switzerland*
[10]*Jet Propulsion Laboratory, California Institute of Technology, 4800 Oak Grove Drive, Pasadena, CA 91109, USA*
[11]*Institut für Weltraumforschung, Österreichische Akademie der Wissenschaften, Schmiedlstr. 6, A-8042 Graz, Austria*

Accepted 2016 December 1. Received 2016 November 25; in original form 2016 June 29

ABSTRACT

The long duration of the *Rosetta* mission allows us to study the evolution of the diamagnetic cavity at comet 67P/Churyumov–Gerasimenko in detail. From 2015 April to 2016 February 665 intervals could be identified where *Rosetta* was located in a zero-magnetic-field region. We study the temporal and spatial distribution of this cavity and its boundary and conclude that the cavity properties depend on the long-term trend of the outgassing rate, but do not respond to transient events at the spacecraft location, such as outbursts or high neutral densities. Using an empirical model of the outgassing rate, we find a functional relationship between the outgassing rate and the distance of the cavity to the nucleus. There is also no indication that this unexpectedly large distance is related to unusual solar wind conditions. Because the deduced shape of the cavity boundary is roughly elliptical on small scales and the distances of the boundary from the nucleus are much larger than expected we conclude that the events observed by *Rosetta* are due to a moving instability of the cavity boundary itself.

Key words: magnetic fields – plasmas – methods: data analysis – comets: individual: 67P.

1 INTRODUCTION

The detection of a diamagnetic cavity at comet 67P/Churyumov–Gerasimenko (67P) in 2015 July by the magnetometer measurements onboard *Rosetta* (Goetz et al. 2016) was the second time a spacecraft has been able to conduct measurements in such a region. The first detection was by the *Giotto* magnetometer experiment at comet 1P/Halley in 1986 (Neubauer et al. 1986; Neubauer 1988). Although *Giotto* was able to confirm the existence of a cavity at an active comet, due to its single pass through the coma, it was not able to study its evolution. A diamagnetic cavity has also been observed by the Active Magnetospheric Particle Tracer Explorers (AMPTE) artificial comet mission (Haerendel et al. 1986; Luehr, Kloecker & Acuna 1988). Here, barium and lithium were released from a spacecraft and the reaction of the resulting plasma was monitored by another spacecraft downstream. This was the first time a diamagnetic cavity was created by adding a neutral cloud to a charged fluid. The artificial cavity created in this way represents an example for local cavities as opposed to the global cavity at 1P/Halley. With *Rosetta* we now have the opportunity to study the evolution of the diamagnetic cavity in a cometary environment, while following the comet through perihelion. This allows one to describe its shape, dynamics and long-term evolution.

The diamagnetic cavity is the innermost part of the interaction region of the solar wind with a comet. Using a purely hydrodynamical approach, Biermann, Brosowski & Schmidt (1967) showed that the deceleration of the solar wind due to the incorporation of cometary ions, the so-called mass loading (Tsurutani & Smith 1986; Szegö et al. 2000), would lead to the inward flow stopping somewhere close to the nucleus. Since the comet nucleus itself is not magnetized (Auster et al. 2015), the only source of a magnetic field at the

⋆ E-mail: c.goetz@tu-bs.de

© 2016 The Authors
Published by Oxford University Press on behalf of the Royal Astronomical Society

comet is the interplanetary magnetic field (IMF) carried by the solar wind. This implies that with the inability of most solar wind particles to penetrate the inner cometary regions, the magnetic field is also excluded, and forms a magnetic field-free region, the *diamagnetic cavity* (Haerendel 1987). After the 1P/Halley flyby, Cravens (1987) and Ip & Axford (1987) found that there is a pressure balance between the ion–neutral friction force inside the cavity and the magnetic field outside:

$$-\frac{\partial}{\partial r}\left(\frac{B^2}{2\mu_0}\right) = n_i m_i k_{in} n_n (u_i - u_n), \quad (1)$$

where B is the magnetic field; n_i, m_i and u_i are the number density, mass and velocity of the cometary ions, respectively. k_{in} is the ion–neutral friction coefficient which we set to 1.7×10^{-9} cm^3 s^{-1} (Gombosi et al. 1996). The neutral gas density and velocity are n_n and u_n, respectively. In most cases the ion velocity at the boundary may be neglected as the ions should come to a stop at the boundary. The neutral gas density depends on the outgassing rate Q that gives the number of molecules that leave the nucleus per second and is different for each species. The water outgassing rate of 67P at perihelion (1.24 AU) is roughly 2.5×10^{28} s^{-1} and decreases to 8×10^{26} s^{-1} at 2 AU (Hansen 2016). The exact distance of the boundary from the comet may be calculated if the exact radial profiles of the magnetic field and density are known, but may only be estimated if values at the boundary are given.

Simulations by Koenders et al. (2015) and Rubin et al. (2012) for comet 67P have shown that in steady-state cases the cavity boundary is indeed characterized by this pressure balance. They find that the distance to the nucleus is about 50–100 km depending on the phase angle, the angle between the Sun-comet line and the spacecraft comet line. Four-fluid simulations presented in Huang et al. (2016) show that with an asymmetric outgassing profile the cavity extends to 100 km.

Goetz et al. (2016) reported that the extension of the cavity was much larger than theoretically expected, based on the analysis of magnetic field data during one cavity detection on 2015 July 26. The authors ruled out that an anomalously high neutral gas or dust background was responsible for the extension and showed that the measured outgassing rate combined with a simple model was not high enough either. Instead the authors speculated that the detection of the cavity was due to an instability propagating along the boundary, which increased the distance of the cavity boundary from the nucleus. The particle signatures, especially the electron distribution inside the diamagnetic cavity at 67P was studied by Nemeth et al. (2016) to reveal that there are significant dropouts of electrons in the 100 and 200 eV range.

In this work we investigate 665 detections of the diamagnetic cavity at 67P over the range of 8 months starting late 2015 April at a comet–Sun distance of 1.8 AU and ending 2016 February at a distance of 2.4 AU. We try to extract a general shape of the cavity and aim at a deeper understanding of the dynamics of the cavity boundary.

2 DATA AND METHODS

2.1 Instrumentation

The *Rosetta* spacecraft carries two three-axis fluxgate magnetometers as part of the Rosetta Plasma Consortium (RPC-MAG) with a measurement range of ±16 384 nT and a resolution of 31 pT. The magnetometers have a sampling frequency of 20 vectors s^{-1} (burst mode), which may be downsampled onboard to 1 vector s^{-1} (normal mode) to save data volume (Glassmeier et al. 2007). Although there are two magnetometers mounted on the 1.5 m boom, only the outboard magnetometer is used in this study. The greater distance of the latter from the main spacecraft infrastructure reduces the influence of disturbances related to the spacecraft. The most influential source of magnetic fields on the spacecraft itself are the reaction wheels, but their signature is easily detectable in dynamic spectra in the frequency band of 2–10 Hz. As this publication is concerned only with low frequency phenomena, a low-pass filter with a cut-off of 2 Hz was applied to the high-resolution data, eliminating essentially all effects of the reaction wheels.

Determining the correct offset of a magnetometer in the Solar system is usually a very intricate process, especially if the spacecraft is not spinning, as it is the case with *Rosetta*. The magnetometers on board are influenced by magnetic fields produced on the spacecraft and by a temperature-dependent measurement characteristic. Because of that, the data delivered by the automatic calibration may be influenced by an unknown offset. This is visible in the measurements made in the diamagnetic cavity: even though the magnetic field should be zero in all components, the remaining spacecraft-generated field may reach up to 25 nT. However, during the comet's active phase the magnetic field usually varies on the order of 20 nT min^{-1}, whereas the cavity is still characterized by an absence of turbulence, so it remains easy to detect. Therefore the measurements in the field-free region may be used to construct a new temperature model, spanning from 155 to 210 K, which reduces the remaining field magnitude to below ∼5 nT. This new temperature model may be used any time the magnetometer is in the given temperature range. It should also be noted that the temperature model can be constructed using only a subset of events and predicts the offset for the other events reasonably well. This is another indicator that the field in the diamagnetic cavity region is of the same value for all events. To enable correct analysis, the remaining field in the cavity is removed by taking the individual interval and subtracting the mean of each component. With these data reduction methods, the remaining field in the cavity is reduced to <1 nT. The data calibrated in this way are used for this study.

There are some auxiliary data sets necessary to examine the evolution of the cavity. We use density data from the RPC Mutual Impedance Probe (RPC-MIP; Trotignon et al. 2007) and electron temperature estimates from the RPC Langmuir Probe (RPC-LAP; Eriksson et al. 2007) as well as neutral gas densities from the Rosetta Orbiter Spectrometer for Ion and Neutral Analysis (ROSINA; Balsiger et al. 2007), especially the Comet Pressure Sensor (ROSINA-COPS). To give references with respect to the larger environment around the nucleus we use data from Optical, Spectroscopic, and Infrared Remote Imaging System (OSIRIS; Keller et al. 2007). To gain insight into the solar wind conditions at the comet, we use the simple model developed by Tao et al. (2005) that is available on the Automated Multi-Dataset Analysis (AMDA, amda.cdpp.eu) portal. This model uses OMNI data and a 1D propagation model to extrapolate the solar wind conditions at *Rosetta*. The data are given in the body-centred solar equatorial frame (CSEQ). In this system, the x-axis points towards the Sun and the z-axis is along the part of the solar north pole that is orthogonal to the x-axis. The right-handed coordinate system is completed by the y-axis with the comet at the origin.

During the time period investigated in this study, the trajectory of *Rosetta* was mostly in the terminator plane, meaning *Rosetta* was in a circular orbit along the day–night plane. This configuration is interrupted by a close fly-by in 2015 February and a sudden increase

in distance after a 'safe mode' event in 2015 April. About 1 month after perihelion, the distance was again increased to accommodate a dayside excursion, before going back to a terminator scheme late 2015 October. We have analysed data from 2015 January to 2016 March. No cavity crossings were detected before or after this interval.

2.2 Data analysis procedure

To study the cavity and its boundary we need to be able to identify the intervals of interest. These are clearly distinguishable by sudden decreases in the magnetic field succeeded by an interval where the field is constant and significantly less disturbed than in the surrounding region. We use two methods to find these intervals, one is by hand, and the other is a multistep algorithm. As an example we use data resampled to 1 s. First we apply a low-pass filter with a cut-off frequency of $f_{co} = 100$ mHz. Second we determine all intervals in the data where all magnetic field components are below 10 nT, the numerical derivative is below 0.2 nT s^{-1} and the 10 s-averaged numerical derivative is below 0.1 nT s^{-1}. After choosing only intervals that are longer than 20 s the field in the cavity is compared to the background field in the hour before and after the cavity. Any interval where the background field is not four times higher than the cavity field is discarded. To assure that the cavity can be detected at all times, these values need to be adjusted on a monthly basis due to the changing field characteristics. Obviously this method is heavily dependent on the parameters and even with well-chosen input parameters may not detect some events that are clearly distinguishable by eye. Therefore we chose not to use the automated method to find the intervals instead falling back on the manually selected data set.

For a second level analysis, the temporal extent of the boundary region needs to be determined to allow the study of cavity shape and evolution. This is complicated due to the highly variable magnetic fields in the inner coma, which makes it difficult to distinguish the variations from the boundary proper. This may be seen in the top panel of Fig. 1. We have applied a simple algorithm to determine the cavity boundary. First, we find the most significant (highest field) component of the magnetic field in the 5 min before the cavity. The signal in that component is then low-pass filtered with a cut-off of 0.8 Hz to remove high frequency variations. Then the last peak in the signal before the field decreases to zero is determined. This is assumed to be the end of the boundary region for the inbound pass. The outbound pass is determined in the same fashion.

With the above information, it is also possible to find the vector that is the normal of the boundary plane of the transition region using a minimum variance analysis (MVA; see Sonnerup & Cahill 1967). The method uses the three magnetic field components and computes the direction in which the variance of the field is minimal. This direction then indicates the normal to a plane boundary in the plasma. One advantage of this method is that only the magnetic field vector on both sides of the boundary is needed, however, it only provides the direction of the normal vector and not the orientation, i.e. the normal gives the orthogonal to the boundary surface, but does not tell whether it is moving outward or inward.

As the aim of this paper is to determine the similarities and differences between the crossings of the diamagnetic cavity, a superposed epoch analysis (SEA; see Chree 1913) provides information on the uniformity of the different events by calculating an average cavity crossing. As the length of the event varies widely, we scale the signatures in time to an arbitrary time, with the point of entry and exit into/out of the field-free region fixed. With this scaling, the general structure of the magnetic field is preserved, however information on the timing is lost.

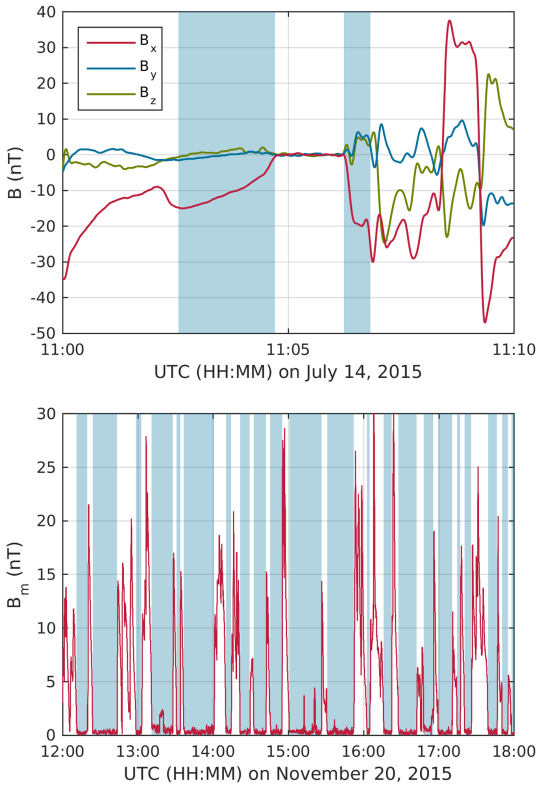

Figure 1. Two examples of RPC-MAG measurements around the cavity. The top panel shows a single event on 2015 July 14 with the boundary area marked in blue. This event is 1 min and 32 s long and is characteristic for many single events. The measurements shown in the bottom panel were made on 2015 November 20 and show several cavity crossings in quick succession interspersed with high magnetic field magnitude intervals. The zero-field regions are marked in blue. There are several days where this clustering can be observed.

3 INTERPRETATION

3.1 Magnetic field features

A total of 665 intervals when RPC-MAG registered the low field magnitudes combined with a lack of turbulence were determined, including estimates of the length of the transition regions. The individual intervals are listed in the Appendix. In total, *Rosetta* spent an accumulated time of 42 h in the cavity. The events are sorted into two groups: single events and clusters. Fig. 1 shows an example of the two groups. In the top panel the magnetic field components for a 10-min interval on 2015 July 14 are shown. First the field is almost entirely in x-direction, but then all components drop to zero. This marks the entry into the diamagnetic cavity. Afterwards the magnitude increases again and now the field direction is fluctuating. In the bottom panel only the magnetic field magnitude is shown. The cavity intervals here are tens of minutes long and are interspersed with shorter intervals with non-zero field. *Rosetta* enters the

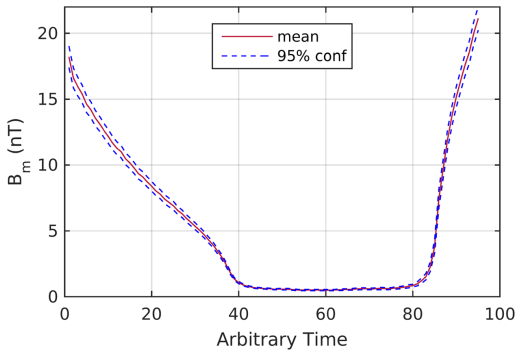

Figure 2. SEA of the magnetic field magnitude for all events (red) including the 95 per cent confidence interval in dashed blue lines.

cavity approximately every 55 min, but there is no stable frequency discernible for this interval. In general single events occur isolated from other cavities and may be as long as ∼30 min, they are always found in regions where the magnetic field is fluctuating heavily. Cluster events are defined as intervals where there are many cavity crossings right after each other. The magnetic field may increase between two events, but it typically does not reach the background field strength. In these intervals the field outside the cavity is generally also fluctuating without any apparent structure. So far the most prominent clusters were detected on 2015 July 30 and on 2015 November 19–21. Although they do occur every few minutes, there is no discernible frequency in the occurrence of clustered cavities.

The SEA of all events is shown in Fig. 2. Any features that may be seen in this analysis will be common features of most cavity crossings. First the magnetic field decreases from 20 to 5 nT, then the decrease steepens until the field is close to zero. In the cavity the field remains zero until a slight upward trend leads into the transition region where the magnetic field again increases to 20 nT. It is notable that the confidence interval of the mean cavity is very small, indicating that all cavity crossings are remarkably similar.

There are some other features that are common to most events. Because of *Rosetta* being mostly above the day–night line of the comet, the magnetic field draping (Alfvén 1957) results in B_x being the dominant component in most cases. The dominant component also changes sign in 1/3 of all cases, as was also observed for a single case by Goetz et al. (2016). As indicated by the SEA the inbound pass (cavity expanding) is almost always longer by a factor of ∼3 than the outbound pass (cavity contracting). The mean duration of the inbound pass, the zero-field region and the outbound pass is 160 s : 230 s : 50 s. Although they do vary quite dramatically from 10 s : 8 s : 6 s to 17 min : 40 min : 24 min.

There is no correlation between low solar wind dynamic pressure/magnetic pressure and the cavity events. Although sometimes they coincide with low solar wind pressures, there are also events where a cavity is measurable and the solar wind dynamic pressure and magnetic pressure are elevated compared to normal levels. Consequently, low solar wind pressures cannot account for the large distance of the cavity boundary to the nucleus. A reversal in the solar wind magnetic field at the exact time that *Rosetta* is in the cavity could possibly account for the change in sign that is observed for some events. However from the observed common occurrence of the changes in magnetic field sign, we rule out the solar wind source of this feature. It should also be noted that solar wind data at the comet is not available and propagation models using Earth-based

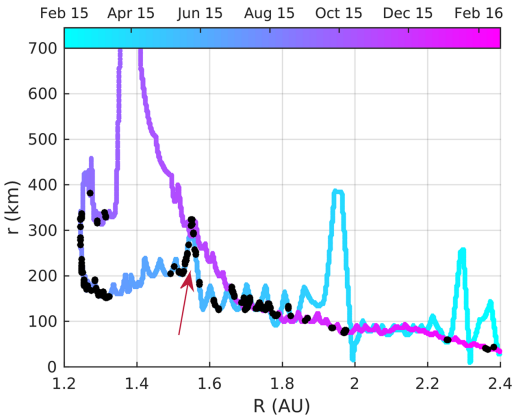

Figure 3. Rosetta's distance from the comet as a function of the distance of the comet to the Sun. The Colour scale indicates the time and the black dots mark the times that *Rosetta* is situated in the diamagnetic cavity. The arrow points to an unusual feature in mid to late May, where the extension of the cavity is unusually large.

data are very limited in capability for most of the mission due to large angular distances between Earth and 67P.

3.2 Dynamical features

Fig. 3 shows *Rosetta*'s position and the comet's position as well as the intervals when *Rosetta* was located in the cavity. First of all, the size of the cavity increases with the comet's approach to the Sun, then after perihelion it increases further. This is due to a delay in the temporal development of the gas production rate, which was still increasing for 2–3 weeks after closest approach. The highest recorded extension of the cavity was on 2015 September 3 at 380 km. Afterwards *Rosetta* increased its distance to the comet significantly and no cavities were detected until mid-November when 67P was at a distance of 1.65 AU from the Sun. Then, the cavity distances are approximately the same as they were on the comet's inbound trajectory, although they are detectable at lower altitudes than before.

There is also an unusual feature (marked by an arrow) in late May, when the cavity distance seems to increase by a factor of 1.5–2 above its usual value. This feature is not related to any obvious change in the plasma environment of the comet, the solar wind or the outgassing rate. Also, no indication of significantly elevated neutral gas densities was observed. It is also not related to the position of the spacecraft with respect to the comet or the Sun. However, this phenomenon coincides with the spring equinox at 67P. At this time the outgassing profile shifts from peaking in the Northern hemisphere to the Southern hemisphere (Hansen 2016). This shift may relate to the cavity boundary distance, however the exact mechanism needs to be studied in more detail.

To search for a relationship of the gas production rate Q with the distance of the cavity r_c from the nucleus, we use the H_2O gas production rate model by Hansen (2016). This model depends on the comet's distance from the Sun R and gives two dependences, one before perihelion, one after:

$$Q = 1.32 \times 10^{28}\, R^{-4.62} \quad \text{for } t \leq t_{\rm ph}, \tag{2}$$

$$Q = 8.72 \times 10^{28}\, R^{-5.71} \quad \text{for } t > t_{\rm ph}, \tag{3}$$

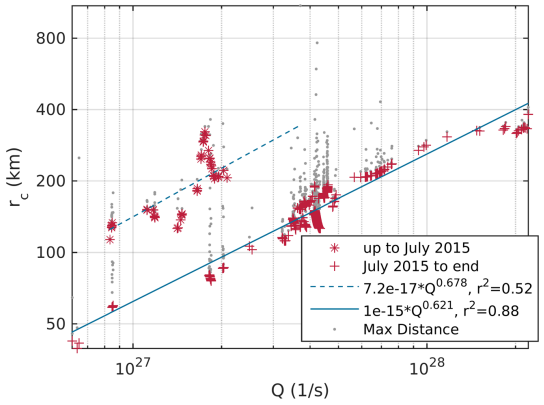

Figure 4. Cavity boundary distance over the empirical gas production rate. The events are clearly grouped: stars indicate the event took place before 2015 July, crosses indicate events from 2015 July to 2016 February. The blue lines show the corresponding linear fit and the fit parameters are given in the legend. The grey dots give an estimate of the maximum extension of the cavity while *Rosetta* is located in this region and cannot observe the boundary.

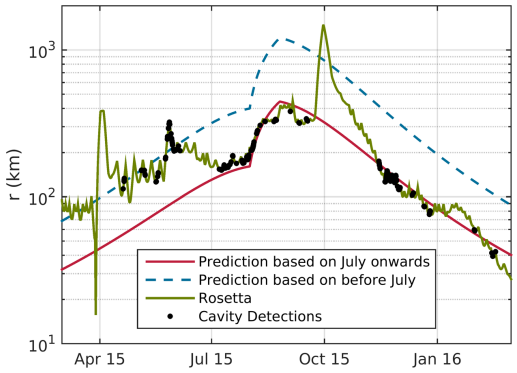

Figure 5. Prediction of cavity distance based on the relationship between gas production rate and distance. The red line corresponds to equation (5) and the blue dashed line to equation (4). *Rosetta*'s trajectory is shown in green and the actual detections of the cavity are indicated by black points. The time interval shown here is truncated from March 15 to March 16, because the cavity has only been detected in that time interval.

where t_{ph} is the time of perihelion passage (2015 August 13) and R is measured in astronomical units. As this model displays a step at perihelion, we apply a smoothing average of 50 points to the model to smooth out the step.

Fig. 4 shows the cavity detection distances as a function of the gas production rate. There are clearly two different populations: one before 2015 July 1 and one after. This is in accordance with the anomaly around equinox. Because of these populations we choose to fit these events separately. The prediction of the cavity distance r_c (km) to the comet is

$$r_c = 7.2 \times 10^{-17}\, Q^{0.678} \quad \text{for } t < 2015\,\text{July}, \tag{4}$$

$$r_c = 1.0 \times 10^{-15}\, Q^{0.621} \quad \text{for } t \geq 2015\,\text{July}. \tag{5}$$

The r^2 values for these fits are 0.52 and 0.88, respectively. The exponent is also very close to an analytical value given by Cravens (1987), who derived a dependence of the contact surface on the production rate to be $Q^{0.75}\,\text{cm}^{-1}$. However we would not expect the above relationships to match the analytical expression exactly as the magnetic field and electron density radial profile they use is not the same as the one we observe with *Rosetta*.

Additionally the analytical model also shows that the distance depends on the magnetic field as $r_c \propto 1/B$, where B is the maximum magnetic field strength in the pile-up region. This relationship is difficult to investigate as the field in the pile-up region is highly variable as described previously. If we assume that the average magnetic field in the pile-up region is the mean field in the hour before the cavity event, we can recreate Fig. 4 and find that the exponent for R in equation (5) is 0.8. However the estimate of the field is heavily skewed towards zero for multiple crossings which skews the entire population. Therefore this estimate can only provide a reference. However, the exponent also matches the analytical model quite well.

It should be noted that the distance we use here is only exact in the moment the cavity boundary moves over *Rosetta*. During the times that *Rosetta* is in the cavity it may expand further. This can be estimated using the velocity estimates as explained below and the duration of zero field measurements. The result is indicated in grey in Fig. 4. This may partially fill the gap between the populations, however it should be noted that this estimate is based on many assumptions. For example, we assume that the expansion speed of the cavity is constant, which is unlikely. Therefore, we do not incorporate these points into our fit.

Additionally the spread of the measurements of r_c at a certain gas production rate may be due to an unstable boundary. This would mean that the fit we have presented here does not indicate the actual global cavity distance, but is instead the cavity distance as an overlap of the global cavity and possible instabilities/anomalies.

In a second step the above fit may be used to predict the cavity distance for the whole interval from 2015 March to 2016 March. Fig. 5 shows the predictions for the cavity distance and *Rosetta*'s trajectory along with the actual detections of a cavity. Clearly the prediction based on the cavity events from April–June is not correct at other times, if it were, *Rosetta* would be in the diamagnetic cavity for almost the entire mission. In contrast, the red curve seems to fit well. During the close flyby in 2015 March, the cavity does not seem to be formed yet (Koenders 2016, this issue), otherwise it should have been detected using either prediction. This should also be the case for late February, where *Rosetta* went sufficiently close to the nucleus to be able to detect a cavity. Because this was not the case, we infer that the cavity was no longer present at that time.

The gas production rate used here is only valid for H_2O, so it stands to reason that the discrepancy between the two fits may be caused by significant contributions of other species. Except for water the most abundant species is CO_2. Fougere et al. (2016) present calculations for the ratio between the CO_2 gas production rate and the H_2O gas production rate for 2015 May 6, which is in the time interval that shows elevated distances for the cavity. They find that the ratio is 0.04–0.05, meaning water is still by far the dominating species. A composition of 5 per cent CO_2 and 95 per cent H_2O would result in a 5 per cent higher ion–neutral drag. This is insignificant compared to what would be needed to push out the cavity to where it is measured.

Additionally it should be noted that with the new model for the gas production rate the peak value increased to $Q_{max} = 4 \times 10^{28}$ which is significantly higher than what was assumed in

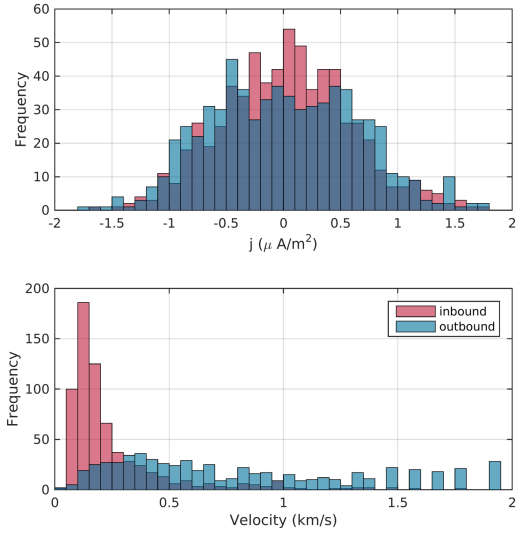

Figure 6. Histogram of the calculated current in the boundary region (top) and the velocity of the boundary (bottom) for the inbound and outbound pass separately. For both calculations the boundary is assumed to be 25 km in width.

simulations and models up until now. For example the gas production rate in the simulations by Koenders et al. (2015) is assumed to be $Q_{\max} = 5 \times 10^{27}$, which in Fig. 4 corresponds to a diamagnetic cavity distance from data of 180 km. This is still significantly larger than the predicted 50 km, however the difference is only a factor of ∼3.6 instead of a factor of ∼7.6.

So far there has been no correlation between outbursts as seen by OSIRIS and the detection of a cavity. This assessment is based on the major outburst listed by Vincent et al. (2016) and a visual inspection of one time interval with many cavities as well as dense OSIRIS imaging cadence, aiming to correlate cavity times also fainter transient events.

If we assume a cavity boundary thickness of $L \approx 25$ km as calculated for 1P/Halley by Neubauer (1988), and for 67P in simulations by Rubin et al. (2012) and Koenders et al. (2015), it is possible to calculate the current density at the boundary:

$$\mu_0 |j| = |\nabla \times B| \approx \frac{|B|}{L}, \tag{6}$$

where L is the characteristic length scale. The results vary widely for the crossings (Fig. 6, top panel). The values for the current density are of the order of 1 μA m^{-2}, which is close to the current density determined from AMPTE magnetic field measurements for the boundary of the artificial cavity (Luehr et al. 1988). As the current depends on the peak magnetic field only and not on the duration, the inbound and outbound crossings follow the same general profile. This is not the case for the velocity of the boundary (Fig. 6, bottom panel), which was estimated using the transition time and a transition region thickness corresponding to L. Because of the very short transition time on the outbound pass, the velocity is highly variable and large in this case, especially when compared to the lower velocity and smaller spread of the inbound pass. The mean velocities and standard deviations are 260 (270) m s^{-1} inbound and 950 (710) m s^{-1} outbound.

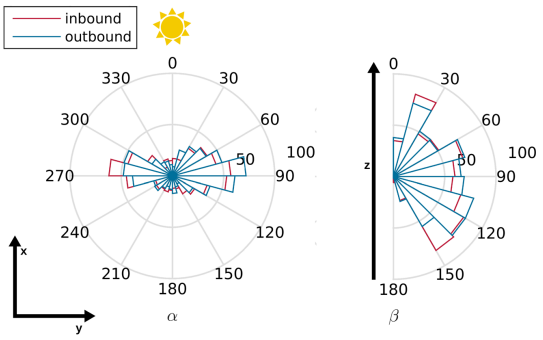

Figure 7. Minimum variance direction angle histogram in the x–y and x–$y_\perp$ plane (CSEQ). The Sun is indicated in yellow. This histogram does not take into account the position of the nucleus and is centred at *Rosetta*.

3.3 Shape of the diamagnetic cavity

The shape of the cavity may be inferred from the normal to the cavity boundary. However it should be noted that the cavity is probably not stable and will vary greatly over the time interval from 2015 April to 2016 February. Nonetheless the distribution of the normal vector is used to infer the cavity shape. This approach has the advantage of being entirely independent of the actual position of the spacecraft around the comet and therefore should exclude the influence of the gas production rate. Fig. 7 shows the histogram of the angle α and β of the normal vectors, which are the angles in the x–y plane and the angle to the positive z-axis, respectively. The vectors were determined by the MVA for the inbound and outbound transitions. The distribution of α is heavily skewed towards 90°. The second peak at 270° belongs to the same group, as the MVA does not yield the orientation of the vector and therefore there are two possible angles in the x–y plane for each individual case. There is no significant difference between inbound and outbound, which indicates that the boundary moving over *Rosetta* does not change direction and therefore is most probably the same one on the inbound and outbound pass.

The angle β behaves differently, in the 15°–150° range there is an almost uniform distribution for both inbound and outbound normal vectors. There are significant deviations from this uniform distribution only at 0° and 180°, meaning there are no normal vectors along the direction of the z-axis. Neither α nor β depend on the position of the spacecraft, meaning there is no correlation between the angles and the spacecraft phase angle, clock angle or distance to the comet.

To discuss this distribution and implications on the shape of the cavity, we first assume that the cavity is roughly ellipsoidal or paraboloidal, as it was done in previous studies at comet 1P/Halley and as shown as case 1 in Fig. 8. Then almost all normal vectors should lie in the y–z plane as *Rosetta* is in a terminator orbit ($x = 0$ km) for most of the time. This case only matches our results if there are small disturbances on top of the global shape as suggested by Neubauer (1987). Then the angle α has a similar distribution as the one we present here. Furthermore, the distribution of β should be dependent on the location of *Rosetta* and approximately be the same for all values between 0° and 180°. This is not observable here. The correlation coefficient between β and the polar angle of *Rosetta's* position is 0.02, meaning there is no correlation. This shows that a strictly ellipsoidal or paraboloidal global cavity surrounding the nucleus as shown as case 1 in Fig. 8 is not supported by the data.

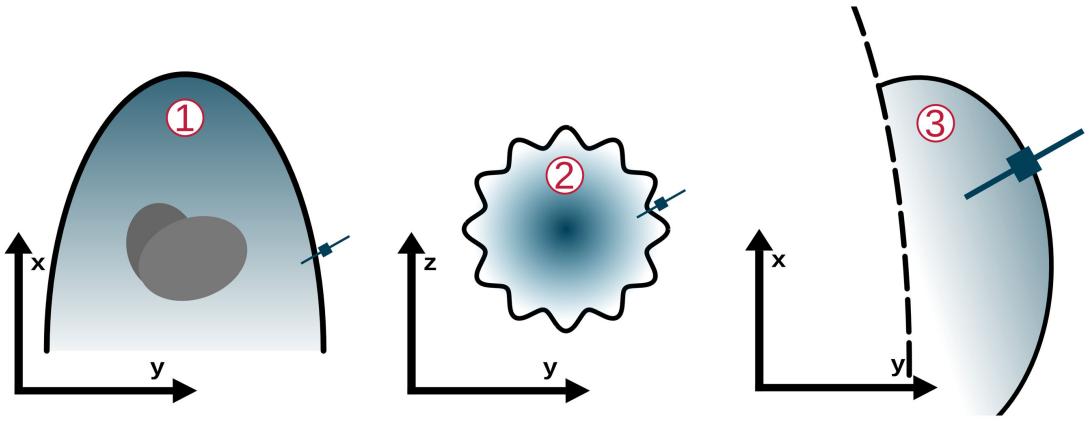

Figure 8. Schematic of the three discussed possibilities for the shape of the cavity. Case 1 and 3 are in the x–y plane and case 2 is a cross-section for $x = 0$ in the y–z plane. In the sketch for case 3 a possibly connected global cavity is alluded to by black dashed lines.

We therefore conclude that the cavity that is observed at 67P is not the global, stable cavity that was crossed at 1P/Halley.

If we still assume that the cavity observed here is a global structure we must consider another case. In this case the global cavity is extended by longitudinally fluted surface undulations as illustrated as case 2 in Fig. 8. In this case it is difficult to differentiate this model from others, as the direction of the angle β should follow a normal distribution. However one fact makes this case unlikely: if these ripples are distributed on an underlying ellipsoid shape then the angle α should change significantly when *Rosetta* is located in front ($x > 0$ km) of the comet. This is not the case with the data. This means that at least a uniformly distributed longitudinal oscillation on a global cavity is unlikely.

Based on our previous study we assume that the cavity boundary crossing are due to *Rosetta* passing strong undulations of the cavity boundary. These undulations cause pockets of plasma into which are moving over *Rosetta* causing it to enter and leave the field-free region on short time-scales. To derive an approximate description of these pockets we tried several different structures. For example, we assumed a longitudinally sinusoidal shape of the undulations and determined the resulting distributions of the boundary normal vectors. No suitable fit was found. Next, we assumed half-circle undulations. Such undulations did not agree with the measured distributions for α and β either. The best match was derived for an ellipsoidal-like structure, that is small ellipsoids attached to the global cavity boundary as sketched in Fig. 8, case 3. We therefore fitted an ellipse to the normal vectors. Because the normal fitting method would require the position of the normal vectors, which we cannot use as it varies with the outgassing rate, we adopted a slightly different approach. First a reference ellipse with its semimajor axis parallel to the x-axis and using a certain ellipticity is constructed. Then, an angle distribution of the normal vector is calculated and compared with the distribution from the data. The final result is the ellipse where the distributions have the highest correlation coefficient. The distributions are shown in Fig. 9. In this case the ellipse has an eccentricity of $e = 0.87 \pm 0.2$ with correlation coefficients greater than 0.85. This means that the semimajor axes have a ratio of about 1: 2. Varying the orientation of the semimajor axis does not result in a better fit. It should also be noted that fitting only one half of the ellipse does not change the results as the MVA does not give the direction of the normal. This study takes into account all 665

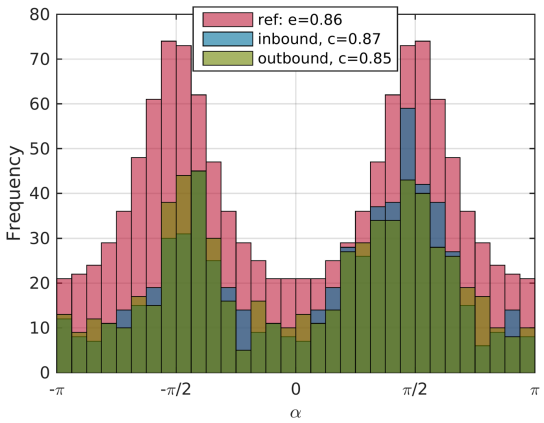

Figure 9. Angle distribution for the angle α for the inbound (blue) and the outbound (green) pass compared to the corresponding angle distribution of the reference ellipse that has the highest correlation with the measured angle distribution (red).

events, if we divide the events into summer (before 2015 October) and winter (after 2015 October) and perform a similar analysis, the ellipse is a better fit for the former interval than it is for the latter. This may indicate that the cavity boundary is more unstable then, which may be related to the lower outgassing rate during that time.

This means the instability deforms the boundary to form roughly elliptically shaped field-free pockets that may extend far from the global cavity as shown in Goetz et al. (2016). In this case, the shape that was calculated here is just the shape of the surface wave and not the shape of the cavity itself. With this model it is also possible to estimate the wavelength of the undulation. From the elliptical fit we know that the semimajor axes have a ratio of 1: 2. Therefore the wavelength should be two times the radial extension of the fitted ellipse. As described in the next section the curvature radius (which is equal to the semiminor axis) is around tens of kilometres. Thus the wavelength should be in the low hundreds of kilometres.

When fitting the ellipse we also cannot rule out that the field-free region is indeed ellipsoidal in shape and not connected to

a larger structure at all. There are two possible mechanisms to explain an isolated cavity: first of all, these pockets may actually be caused by the spacecraft itself. In this case the neutral gas and ion densities in this spacecraft cavity should be elevated far above normal levels. This may be due to spacecraft rotations that cause sublimation (Schläppi et al. 2010) or due to thruster firings. But data from ROSINA show no elevated neutral gas density, RPC does not measure elevated ion counts and there is no correlation with thruster firings. We therefore rule out this possibility.

Second, these pockets could be 'minicavities' caused by passing boulders. As seen by OSIRIS these boulders are of sizes up to 50 m on the surface (Pajola et al. 2015) and 0.8 m detached from the surface (Fulle et al. 2016) and have an outgassing rate of their own. If such a boulder produces enough neutral gas, this may be able to push out the magnetic field in a small region around the boulder. However, as before, we would then expect a significant neutral gas density increase in the cavity, which is not the case. To affirm this supposition we can estimate the size of a cavity produced by a point source with the same outgassing rate as a spherical boulder with a diameter of 10 m. The outgassing rate of the boulder is estimated by scaling it with the surface area. If we assume an outgassing rate of $10^{28}\,\mathrm{s}^{-1}$ for the nucleus, which has a surface area of $\sim 40\,\mathrm{km}^2$, the outgassing rate of the boulder (area of $\sim 300\,\mathrm{m}^2$) is about $8 \times 10^{22}\,\mathrm{s}^{-1}$. The radial profile of the neutral gas close to the source is (Haser 1957)

$$n_\mathrm{n} = \frac{Q}{4\pi u_\mathrm{n} r^2}, \tag{7}$$

and with equation (1) we get

$$r_\mathrm{c}^2 = \frac{n_\mathrm{i} m_\mathrm{i} k_\mathrm{in} Q \mu_0 L}{2\pi B^2}. \tag{8}$$

In this expression the radial derivative has been substituted by a characteristic length scale L that depends on the thickness of the transition region. If we assume water ions with a density of $1000\,\mathrm{cm}^{-3}$ and a magnetic field of 20 nT, which are average values at perihelion, the only unknown is the characteristic length scale. If L is set to a high value of 10 m, the radius of the cavity is 5 m. This is smaller than the diameter of the boulder, but even considering this as a height above the surface *Rosetta* would have to pass within metres of such an object for the cavity to be detected. This has not been observed during the entire mission and boulders with a diameter of 10 m have not been observed so far at comet 67P. In contrast to that the cavity was detected in numerous instances. It is highly unlikely that boulders would pass close to the spacecraft that frequently and be missed by the remote sensing instruments. We therefore conclude that boulders ejected from the comet are not the source of the field-free region that RPC-MAG detected.

4 CONCLUSION

We have analysed RPC-MAG data to find all indications of diamagnetic cavity detections over the entire *Rosetta* mission. The resulting 665 events have been analysed to determine the properties of the cavity and its boundary. There are two distinct groups of cavity events, single and clustered, that seem to be randomly distributed, but there is no discernible frequency in the clustered events, and there is no explanation as to why the cavity is present more often on certain days. The distance of the cavity boundary to the nucleus depends on long-term trends in the outgassing rate but is not related to the rotation rate or short time variations like outbursts. We find that for events after spring equinox the distance r_c is related to the outgassing rate as $r_\mathrm{c} \propto Q^{0.6}$. All boundary crossings show remarkably similar magnetic field features, they are embedded in a magnetically highly variable region, when the magnetic field decreases slowly to zero and then increases, on average, five times faster than the decrease. In 1/3 of all cases the magnetic field changes sign during the cavity. There is no evidence that the cavity is only detected when the solar wind pressure is low.

A MVA reveals that the cavity boundary may roughly be described by an ellipse in the x–y plane, however it is found that this ellipse is not centred on the comet, as the boundary normal distribution does not match a global cavity especially in the perpendicular plane. The boundary velocity was estimated to be of the order of $1\,\mathrm{km\,s}^{-1}$ and the current density is about $1\,\mu\mathrm{A\,m}^{-2}$.

All evidence points to the fact that the cavity observed at 67P is not entirely the global structure as seen at 1P/Halley but small pockets of zero magnetic field. Two explanations, a 'minicavity' due to a passing boulder and a spacecraft produced cavity, has been ruled out. However, the instabilities that were proposed by Goetz et al. (2016) fit the data. In this case we would neither expect the pressures to be equal at the boundary nor the normal vector to be dependent on the measurement.

Based on these discussions, the formation of instabilities at the cavity boundary and a higher than expected outgassing rate is the most likely explanation for the unusual behaviour of the diamagnetic cavity at 67P.

ACKNOWLEDGEMENTS

The RPC-MAG and ROSINA data will be made available through the PSA archive of ESA and the PDS archive of NASA. *Rosetta* is a European Space Agency (ESA) mission with contributions from its member states and the National Aeronautics and Space Administration (NASA). The work on RPC-MAG was financially supported by the German Ministerium für Wirtschaft und Energie and the Deutsches Zentrum für Luft- und Raumfahrt under contract 50QP 1401. The work on ROSINA was funded by the federal state of Bern, the Swiss National Science Foundation and the ESA PRODEX program. Work at LPC2E/CNRS was supported by CNES and by ANR under the financial agreement ANR-15-CE31-0009-01. Portions of this research were performed at the Jet Propulsion Laboratory, California Institute of Technology, under contract with NASA. We are indebted to the whole of the *Rosetta* Mission Team, SGS and RMOC for their outstanding efforts in making this mission possible. We acknowledge the staff of CDDP and IC for the use of AMDA and the RPC Quicklook data base (provided by a collaboration between the Centre de Données de la Physique des Plasmas, supported by CNRS, CNES, Observatoire de Paris and Université Paul Sabatier, Toulouse and Imperial College London, supported by the UK Science and Technology Facilities Council).

REFERENCES

Alfvén H., 1957, Tellus, 9, 92
Auster H.-U. et al., 2015, Science, 349, 015102
Balsiger H. et al., 2007, Space Sci. Rev., 128, 745
Biermann L., Brosowski B., Schmidt H. U., 1967, Sol. Phys., 1, 254
Chree C., 1913, Philos. Trans. R. Soc. Lond. Seri. A, 212, 75
Cravens T. E., 1987, Adv. Space Res., 7, 147
Eriksson A. I. et al., 2007, Space Sci. Rev., 128, 729
Fougere N. et al., 2016, A&A, 588, A134
Fulle M. et al., 2016, ApJ, 821, 19
Glassmeier K.-H. et al., 2007, Space Sci. Rev., 128, 649

Goetz C. et al., 2016, A&A, 588, A24
Gombosi T. I., De Zeeuw D. L., Häberli R. M., Powell K. G., 1996, J. Geophys. Res., 101, 15233
Haerendel G., 1987, Geophys. Res. Lett., 14, 673
Haerendel G., Paschmann G., Baumjohann W., Carlson C. W., 1986, Nature, 320, 720
Hansen K. C., 2016, MNRAS, 00, 00
Haser L., 1957, Bull. Soc. R. Sci. Liege, 43, 740
Huang Z. et al., 2016, J. Geophys. Res. (Space Phys.), 121, 4247
Ip W.-H., Axford W. I., 1987, Nature, 325, 418
Keller H. U. et al., 2007, Space Sci. Rev., 128, 433
Koenders C., 2016, MNRAS, 462, S235
Koenders C., Glassmeier K.-H., Richter I., Ranocha H., Motschmann U., 2015, Planet. Space Sci., 105, 101
Luehr H., Kloecker N., Acuna M. H., 1988, Adv. Space Res., 8, 11
Nemeth Z. et al., 2016, MNRAS, 462, S415
Neubauer F. M., 1987, A&A, 187, 73
Neubauer F. M., 1988, J. Geophys. Res., 93, 7272
Neubauer F. M. et al., 1986, Nature, 321, 352
Pajola M. et al., 2015, A&A, 583, A37
Rubin M., Hansen K. C., Combi M. R., Daldorff L. K. S., Gombosi T. I., Tenishev V. M., 2012, J. Geophys. Res. (Space Phys.), 117, 6227
Schläppi B. et al., 2010, J. Geophys. Res. (Space Phys.), 115, A12313
Sonnerup B. U. O., Cahill L. J., Jr, 1967, J. Geophys. Res., 72, 171
Szegö K. et al., 2000, Space Sci. Rev., 94, 429
Tao C., Kataoka R., Fukunishi H., Takahashi Y., Yokoyama T., 2005, J. Geophys. Res. (Space Phys.), 110, 11208
Trotignon J. G. et al., 2007, Space Sci. Rev., 128, 713
Tsurutani B. T., Smith E. J., 1986, Geophys. Res. Lett., 13, 263
Vincent J.-B. et al., 2016, MNRAS, 462, S184

SUPPORTING INFORMATION

Supplementary data are available at *MNRAS* online.

cavity_times.txt

Please note: Oxford University Press is not responsible for the content or functionality of any supporting materials supplied by the authors. Any queries (other than missing material) should be directed to the corresponding author for the article.

This paper has been typeset from a TEX/LATEX file prepared by the author.

A.3. Paper III: Evolution of the magnetic field at comet 67P/Churyumov–Gerasimenko

Authors: C. Goetz, M. Volwerk, I. Richter, K.-H. Glassmeier C. Goetz, B. T. Tsurutani, P. Henri, M. Volwerk, E. Behar, N. J. T. Edberg, A. Eriksson, R. Goldstein, P. Mokashi, H. Nilsson, I. Richter, A. Wellbrock, K.-H. Glassmeier

Bibliographic Information: Monthly Notices of the Royal Astronomical Society, 469, S268–S275, doi:10.1093/mnras/stx1570

Year: 2017

Citations: 7 (The SAO/NASA Astrophysics Data System, December 2018)

Monthly Notices of the ROYAL ASTRONOMICAL SOCIETY

MNRAS **469,** S268–S275 (2017) doi:10.1093/mnras/stx1570
Advance Access publication 2017 June 22

Evolution of the magnetic field at comet 67P/Churyumov–Gerasimenko

Charlotte Goetz,[1⋆] Martin Volwerk,[2] Ingo Richter[1] and Karl-Heinz Glassmeier[1,3]

[1] *Institut für Geophysik und extraterrestrische Physik, Technische Universtität Braunschweig, Mendelssohnstr. 3, D-38106 Braunschweig, Germany*
[2] *Space Research Institute, Austrian Academy of Sciences, Schmiedlstrasse 6, Graz A-8042, Austria*
[3] *Max-Planck-Institut für Sonnensystemforschung, Justus-von-Liebig-Weg 3, D-37077 Göttingen, Germany*

Accepted 2017 June 20. Received 2017 June 20; in original form 2017 March 29

ABSTRACT

The magnetic field at a comet is significantly influenced by the solar wind on one side and the outgassing rate on the other. There are no simple spatial models for the magnetic field direction, neither at a comet with low outgassing rates ($\sim 10^{25}$ s^{-1}) where ion gyroradius effects are non-negligible, nor at high outgassing rates ($\sim 10^{27}$ s^{-1}) where plasma boundaries form. However, the long duration of the European Space Agency *Rosetta* mission has made it possible to track the evolution of the magnetic field while comet 67P/Churyumov–Gerasimenko approaches the Sun. Herein we present a simple model that fits the data quite well, depending on input parameters. The study also includes the influence of the comet's gas production rate and the solar wind conditions, which both have complex effects on the magnetic field, but are clearly recognizable. The evolution of the magnetic field direction related to draping is more complex than previously suggested. Classical draping only exists at the comet for high outgassing rates, for lower rates, the magnetic field roughly follows the Parker angle. It is shown that the interaction of the solar wind with the comet can be roughly divided into three main classes.

Key words: magnetic fields – plasmas – methods: data analysis – comets: individual: 67P.

1 INTRODUCTION

The magnetic field at comets was first described by Alfvén (1957), who postulated that due to the non-magnetized nucleus (Auster et al. 2015), all magnetic fields measured at a comet had to be of solar wind origin. At the comet, the outgassing neutrals (mostly water) are ionized via photoionization and incorporated in the solar wind flow, which is then slowed down according to the conservation of mass and momentum in the fluid equations. Because the magnetic field is, in a first order scheme, frozen into the flow, this results in a significant strengthening and deformation (draping) of the magnetic field close to the cometary nucleus.

For simplicity, the number of molecules leaving the cometary nucleus is described by the global water outgassing rate, which increases as the comet-Sun distance decreases. As insolation increases so does the ionization rate and close to the Sun the number density of cometary neutrals is higher by about a factor of 1000 than at distances $R > 3$ AU (Hansen et al. 2016). After being photoionized these particles have significantly lower speeds than the solar wind protons and need to be accelerated. For a review of these different ion pick-up processes and particle distributions see Coates & Jones (2009). There have been several attempts to describe the changes of the solar wind magnetic field as it approaches the comet (Biermann, Brosowski & Schmidt 1967; Galeev, Cravens & Gombosi 1985; Flammer & Mendis 1991), however all of them treat the magnetic field as frozen into the flow and are only valid in one dimension. Therefore, different simulations have expanded on this to also provide a more sophisticated 3D approach (e.g. Rubin et al. 2012; Koenders et al. 2013, 2015; Huang et al. 2016, and references therein). They found that for different comet-Sun distances, and therefore different activity levels, the interaction between the comet and the solar wind is significantly different.

In general, for high enough gas production rates the solar wind flow is decelerated until a critical mass is reached, at which point a weak bow shock is formed. After further deceleration and mass loading, the flow is balanced by the outflowing neutrals, and a field-free diamagnetic cavity forms close to the nucleus. Away from the stagnation streamline, the deceleration is less pronounced as deflection of the flow and thereby a deformation of the magnetic field is more pronounced. In turn, the magnetic field pile-up is lower than directly in front of the comet (Cravens 1987).

As this mass loading is heavily dependent on the number of neutrals in the comet's atmosphere, the magnetic field strength is also influenced by the outgassing. In general, high outgassing rates are associated with higher field strengths because of higher mass loading (Richter et al. 2011), although the distance of the measurement location to the nucleus also plays a role.

For low gas production rates the deceleration of the flow is not sufficient to deform the magnetic field and the coma does not prove

⋆ E-mail: c.goetz@tu-bs.de

© 2017 The Authors
Published by Oxford University Press on behalf of the Royal Astronomical Society

to be a significant obstacle to the solar wind flow. However, plasma waves may be observed even at low mass loading (Richter et al. 2015; Glassmeier 2017).

Several comets have been visited before, however all measurements of the magnetic field were made during fast fly-bys, thus limiting the investigations to one single outgassing rate for each comet. Although findings were very different, the increased magnetic field strength compared to the undisturbed solar wind is a common feature amongst all observations. It was also found at comet 1P/Halley that the draped magnetic field exhibited an onion-like structure, caused by different interplanetary magnetic field directions (Riedler et al. 1986).

The European Space Agency *Rosetta* mission (Glassmeier et al. 2007a) accompanied comet 67P/Churyumov–Gerasimenko (67P) along its trajectory in the Solar system and therefore was able to explore the evolution of the outgassing rate far from the Sun as well as at perihelion (1.24 AU). The outgassing profile is spatially and temporally variable, with the active regions on the nucleus producing more gas and dust than the inactive regions (Fougere et al. 2016). The rotation of the nucleus also leads to a modulation of the outgassing profile. These changes are at least partially visible in the magnetic field as well, for example, the diamagnetic cavity expands as the gas production rate increases (Goetz et al. 2016a). Therefore, the *Rosetta* mission affords the first opportunity to study the magnetic field at a comet over a large time interval as well as a variety of gas production rates.

Here we present the magnetic field measurements made by the magnetometer onboard *Rosetta* over the entire mission from 3.6 AU to perihelion and back to 3.8 AU. As has been reported before, the plasma environment and magnetic field change significantly over the mission, with different wave modes, draping of the magnetic field and the formation of boundaries (Goetz et al. 2016a,b; Koenders et al. 2016; Mandt et al. 2016; Richter et al. 2016; Volwerk et al. 2016). The aim of this publication is to provide context for further studies and present long-term features in the magnetic field evolution over the entire *Rosetta* mission.

2 INSTRUMENTS AND DATA

The measurements we present here were made by the *Rosetta* Plasma Consortium magnetometer (RPC–MAG; Glassmeier et al. 2007b) onboard the *Rosetta* spacecraft. There are two magnetometers located on a 1.5 m-boom, one at the end outboard (OB) and one 15 cm closer to the spacecraft inboard (IB). A boom was necessary to decrease the influence of spacecraft generated disturbance fields. The magnetometers are mainly operating in two modes: in burst mode, the sampling rate for the magnetic field vector is 20 Hz (1 Hz) for OB (IB); whereas in normal mode, the sampling rate is 1 Hz (1/32 Hz), respectively. The resolution of both sensors is 31 pT with a range of $\pm$16384 nT.

Due to poor time resolution and data contamination in the IB sensor only data from the OB sensor is used in this study. As this study aims at the long-term evolution, only 1 Hz data is used. This resampled data comes in two formats: first, in normal mode, the high-resolution data is filtered and resampled on the spacecraft and then transmitted; secondly, in burst mode, the high-resolution data is transmitted and then resampled, using a filter with cutoff at 0.4 Hz to prevent aliasing effects. By resampling to 1 Hz, we also avoid the influence of the spacecraft reaction wheels on the magnetic field, as it is always at frequencies larger than 1 Hz (Glassmeier et al. 2007b).

As mentioned in Goetz et al. (2016a), the magnetic field measured by the magnetometer has a temperature dependent offset and is operating in a magnetically polluted environment, which makes accurately determining the magnetic field strength difficult. However with the help of the diamagnetic cavity crossings from 2015 April to 2016 February a new temperature dependent model for the magnetic field could be constructed. This model is only applicable for sensor temperatures between 155 K and 210 K, which approximately covers the time interval from 2015 April to 2016 April. Because the temperature model significantly improves the measurements, it is used when available. If not, the measurements are only ground calibrated as described in Glassmeier et al. (2007a). In 2014, the magnetometer could be calibrated with the help of the Rosetta magnetometer and plasma monitor (ROMAP) onboard the lander *Philae*, but there is as of yet no offset corrected data for the last months of the mission.

For model calculations, it is important to know the distribution of the neutral gas at the comet. The simplest model was published by Haser (1957), where the neutral gas density follows a r^{-2} profile with an additional exponential attenuation due to ionization losses. Typically, these losses are negligible (e.g. Koenders et al. 2013). Recently, Hansen et al. (2016) published an empirical model using various *Rosetta* data and models to reconstruct the neutral density at the comet from 2014 to 2016. This model gives a very detailed neutral density profile that also takes into account illumination conditions and shape of the nucleus. However, because it is not known in which direction the interplanetary magnetic field (IMF) is oriented, any latitudinal or longitudinal variations of the neutral gas profile cannot be immediately linked to structures in the magnetic field. Therefore we have opted to use the simple spherically symmetric r^{-2} profile as suggested by Haser (1957).

The model by Hansen et al. (2016) also gives an empirically determined gas production rate for the time from 2014 August to fall equinox on 2016 March 21.

The magnetic field in the coma is significantly affected by solar wind parameters (density, velocity and magnetic field), however no solar wind monitor is available at the comet. Therefore we use either a Parker type solar wind (Parker 1958) with average solar wind conditions at Earth as an input, or a more sophisticated propagation model (Tao et al. 2005). This magnetohydrodynamic (MHD) model is based on a 1D solar wind propagation model to calculate the solar wind conditions at the comet from Earth based input. Although it is only a crude model, it still gives a more realistic picture of the solar wind dynamics at the comet.

All measurements are given in the body-centred solar equatorial frame (CSEQ), a coordinate system with the comet body at its origin and the x-axis pointing towards the Sun. The z-axis points along the part of the solar north pole that is orthogonal to the x-axis and the y-axis completes the right-handed coordinate system (Acton 1996).

3 MODEL

To interpret the magnetic field data during the entire mission, we use a simple 1D MHD model. At this point there is no need for a more sophisticated approach, as the uncertainties in magnetic field magnitude and direction as well as the unknown solar wind properties make a more detailed analysis impossible.

In this model the solar wind flow is assumed to be only along the x-axis (u_x) and the magnetic field points only along the y-axis (B_y, Parker angle: 90°). The spacecraft is assumed to be located on the x-axis, meaning that the radial spacecraft distance r is the same as the sub-solar distance x.

For the unshocked solar wind flow, we use the 1D MHD model for mass loading suggested by Biermann et al. (1967) and Flammer & Mendis (1991). In essence, this model solves the continuity, momentum and energy equations for a 1D plasma flow with a mass source term. This model has the advantage of providing an analytical expression for the flow velocity

$$u_x(x) = \frac{1}{2(f+1)\left(M(x)+\rho_\infty u_\infty\right)}\left[(f+2)\rho_\infty u_\infty^2 \pm \sqrt{(f+2)\rho_\infty^2 u_\infty^4 - 4(f+1)\left(M(x)+\rho_\infty u_\infty\right)\rho_\infty u_\infty^3}\right], \quad (1)$$

where the mass source is described by

$$M(x) = \int_\infty^x \frac{m_c Q}{4\pi u_{cn}\tau x'^2}\mathrm{d}x'. \quad (2)$$

Here ρ_∞ is the density and u_∞ the velocity of the solar wind, f is the number of degrees of freedom of the ions, which is set to be $f = 3$ as suggested by Koenders et al. (2013). Q is the outgassing rate and m_c is the mass of the cometary ions (18 a.m.u.), u_{cn} denotes the velocity of the outflowing cometary neutrals and $\tau = 10^6$ s is the collision time. The mass source is assumed to be radially symmetric with a r^{-2} decrease in density as suggested by Haser (1957).

As we are interested in the magnetic field strength at a certain distance to the comet, the induction equation is used to estimate the magnetic field for stationary conditions

$$B_y(x) = \frac{u_{x\infty}B_{y\infty}}{u_x(x)} \quad (3)$$

with $B_{y\infty}$ as the magnetic field strength in the undisturbed solar wind. This model adequately describes the solar wind flow and bow shock position in simulations (Koenders et al. 2013), but it breaks down behind the bow shock, where a different approach needs to be used. According to Galeev et al. (1985) the shocked flow may then be described by

$$u_x(x) = u_{BS}\left[1 - \frac{R_L}{x}\left(1 - \frac{r}{R_{BS}}\right)\right]^4 \quad (4)$$

with the characteristic spatial scale of mass loading

$$R_L = \frac{Qm_c}{4\pi u_{cn}\tau\,\rho_{BS}\,u_{BS}}, \quad (5)$$

R_{BS} the bow shock position and u_{BS} the velocity at the bow shock. The magnetic field may then be calculated using the induction equation (3). However as stated in the original publication of the model, it gives a very steep decrease in velocity close to R_L. Alternatively, the model may be modified to include plasma cooling through charge exchange. Then the velocity profile becomes

$$u_x(x) = u_{BS}\sqrt{\left(\frac{\rho(x)}{\rho_{BS}}\right)^{-8/3}(1-\alpha)+\alpha} \quad (6)$$

with

$$\rho(x) = \rho_{BS}\frac{3}{\alpha^{1/2}}\left[\frac{R_L}{x}\left(1-\frac{x}{R_{BS}}\right)+\frac{\alpha^{1/2}}{3}\right], \quad (7)$$

where $\alpha = 0.078$ is the cooling rate, as estimated based on typical solar wind conditions by Galeev et al. (1985) and ρ_{BS} is the density at the bow shock. These values may be extracted from the model for the unshocked solar wind [equations (1)–(2)], where the bow shock is indicated by the velocity becoming complex. It seems reasonable to include this mechanism as it was shown that charge exchange plays an important role in the neutral coma of 67P (Nilsson et al. 2015). Fig. 1 shows the difference between the models including and excluding charge exchange. The parameters are approximately what is expected for 67P at perihelion. It is clear that the magnetic field becomes unphysically large at R_L. Therefore we use equations (1)–(3) and (5)–(7) to model the magnetic field.

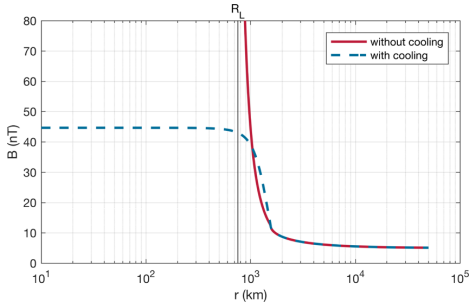

Figure 1. Radial magnetic field profile for the two models. The input parameters were $Q = 10^{27}\,\mathrm{s}^{-1}$, $B_{sw} = 5$ nT, $n_{sw} = 5\,\mathrm{cm}^{-3}$ and $v_{sw} = 400$ km s^{-1}, where the solar wind parameters are those at Earth and a simple Parker model was assumed to propagate them to the comet. The two lines show the model with and without charge exchange cooling and R_L is indicated by a black line.

Obviously this is merely an estimate with several limitations:

(i) The assumption is that the magnetic field in the solar wind is always perpendicular to the flow direction. This will not be the case during perihelion, because the Parker angle θ_p should be closer to 50°.

(ii) An MHD model is assumed, although the ion gyroradius is of the order of the size of the interaction region.

(iii) The model is only valid on the comet-Sun line, however *Rosetta* is mostly located at the terminator, which is 90° from the comet-Sun line. Additionally, we expect the magnetic field to be draped around the nucleus (Alfvén 1957). This means that at the terminator the magnetic field should be mostly in the x-direction, which is not included in the model.

Regardless of these limitations, the model still provides a reference point for comparison with observations and is easier to interpret than more complex numerical models.

As a first test, we use the model to predict the magnetic field strength that *Giotto* should have measured in the pile-up region at comet 1P/Halley. With input parameters of $Q = 8 \times 10^{29}\,\mathrm{s}^{-1}$, a comet-Sun distance of 0.89 AU, and solar wind parameters at Earth of $B_{sw} = 6$ nT, $n_{sw} = 7\,\mathrm{cm}^{-3}$ and $v_{sw} = 430\,\mathrm{kms}^{-1}$, the maximum magnetic field in the pile-up region is 68 nT. This fits very well with the observations, which determined a maximum measured field of 65 nT (Richter et al. 2011).

4 RESULTS

4.1 General structure of the magnetic field

Fig. 2 shows the magnetic field measurements as well as auxiliary data during the entire perihelion passage. The magnetic field magnitude shown here was calculated from hourly averages of the three field components. These averages were then also used to calculate the sliding 4 day average that is used to compare to the model output. The magnetic field variance σ_B was calculated for 10 min

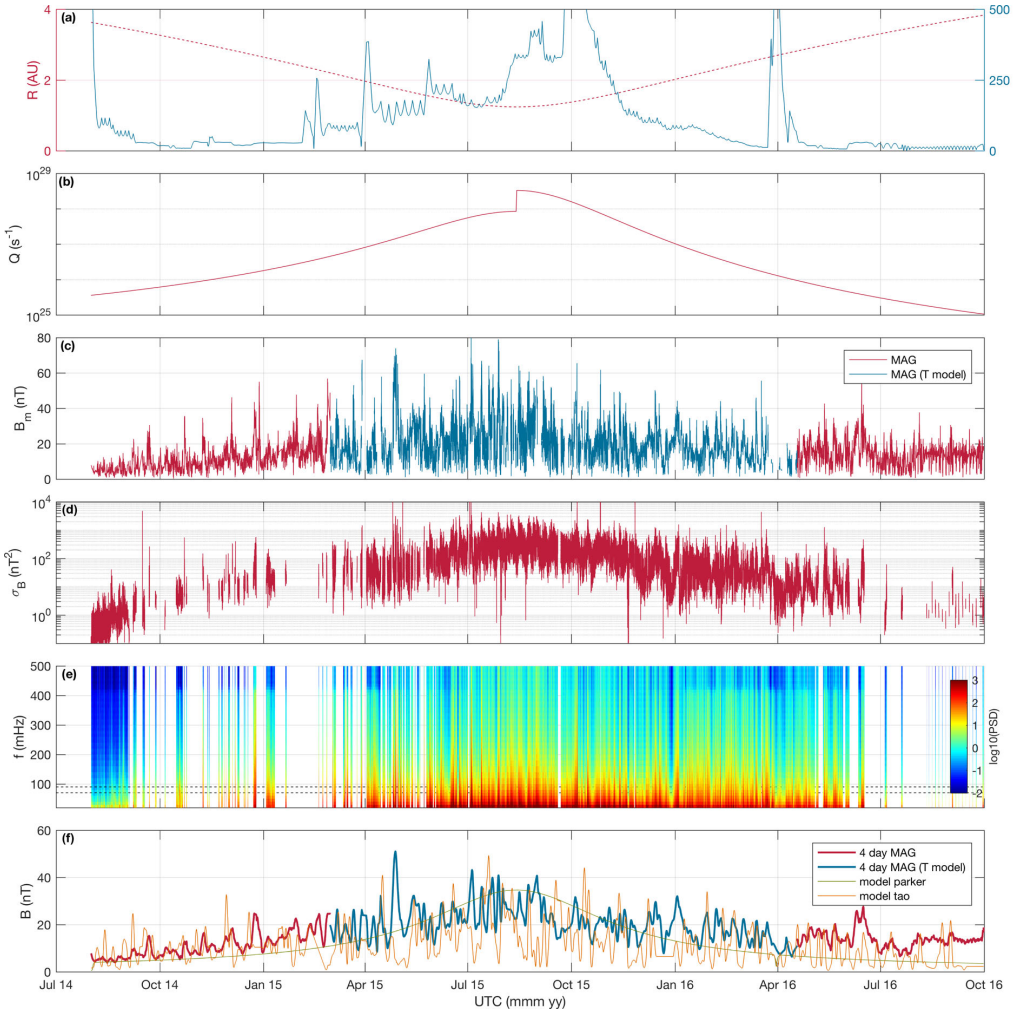

Figure 2. From top to bottom: panel (a) shows the comet-Sun distance (red dashed) and the comet-spacecraft distance (blue). Panel (b) shows the empirical outgassing rate from (Hansen et al. 2016), the values after autumn equinox (2016 March 21) have been extrapolated from the model. Panel (c) and (d) show the magnetic field magnitude and trace of the covariance matrix of the magnetic field, respectively. In panel (e) the trace of the magnetic field spectra is shown. The frequencies along which the power spectral density was extracted are marked by dashed lines. These spectra (and the magnetic field variance) were calculated for 10 min intervals, where a hanning window was used to calculate the spectra. Panel (f) displays the magnetic field magnitude compared to the model outcome.

intervals. These intervals were also the basis for the power spectra, which were calculated using Welch's method with six sub-intervals and an overlap of 50 s.

The spacecraft-comet distance [panel (a)] is highly variable during the mission, but at high gas production rates the distance is generally higher than at low gas production rates. Not shown is the spacecraft longitude in the comet reference frame, because it is mostly close to the $y = 0$ plane, i.e. at the day-night line of the comet.

The gas production rate [panel (b)] is highest (3.3×10^{28} s^{-1}) around perihelion, which, due to higher mass loading, results in a significant enhancement in magnetic field strength closer to the Sun. However, even at low gas production rates, the magnetic field strength may reach above 40 nT for short intervals (e.g. in December 2014). Generally the magnetic field is fluctuating heavily on timescales of a few hours.

There is no immediately obvious correlation between the magnetic field [panel (c)] and the comet-spacecraft distance, however at the beginning of 2016 April, a decrease in magnetic field matches an increase in distance. This was the only instance when *Rosetta* was able to explore the plasma tail at a distance of up to 1000 km. In 2015 October, the spacecraft was located furthest from the comet, in an attempt to detect the cometary bow shock, which was predicted to be around 1500 km (Koenders et al. 2015). However, the data shows no indication of a bow shock, indeed there is no significant decrease in magnetic field with radial distance.

The exact magnetic field magnitude varies significantly. In general, the variance of the magnetic field [panel (d)] seems to increase as the magnitude increases, in fact the increase is about a factor of ∼1000 from 3.6 to 1.24 AU. Although the magnetic field magnitude and variance both increase at a similar rate, a closer examination shows that σ_B/B is highly variable.

The dynamic spectrum [panel (e)] shows a similar behaviour towards perihelion the power spectral density increases significantly in all frequency bands. There are also some instances where short events show up in the spectra as sharp increases in power spectral density (e.g. 2016 January 1). But there is no sign of the ion-cyclotron frequency which should be detectable at frequencies of 10 − 300 mHz depending on the magnetic field. This was unexpected as measurements at 1P/Halley showed clear signatures. However, the interaction region at 67P is much smaller than at Halley due to lower outgassing rate and the instability producing these waves may not have time to develop (Richter et al. 2015).

It is worth noting that σ_B is approximately the same for similar heliocentric distances, whereas B_m is significantly higher for the outbound leg of the comet's trajectory (e.g. 2016 August). This could be related to the lower comet-spacecraft distances at the end of the mission, where r is lower than 20 km, whereas at similar heliocentric distances at the beginning of the mission $r > 30$ km at all times. Alternatively, this could be related to the unknown magnetometer offsets and spacecraft disturbances in late 2016. To untangle the influence of the radial distance we use the model. This gives values at the spacecraft location and its output therefore takes into account the radial distance at which the magnetic field was measured.

First we use constant solar wind conditions of $B_{sw} = 6$ nT, $n_{sw} = 7\,\mathrm{cm}^{-3}$ and $v_{sw} = 430\,\mathrm{kms}^{-1}$ at Earth as input parameters. With this, the model gives a good prediction of the magnetic field. As the gas production rate increases, so does the modelled magnetic field [panel (f)]. However, after 2016 April the model is significantly lower than the measurements. This is unexpected as the model matches quite well at similar gas production rates and distances in 2014. It is also worth noting that due to constant, but heliocentric distance dependent, solar wind conditions, the model output is very smooth and the changes in spacecraft-comet distance are only marginally affecting the model output. This seems to match observations well, as the magnetic field stayed approximately constant from a radial distance of 300 to 1500 km during the bow shock excursion in 2015 October (Edberg et al. 2016).

The main difference between the model and the measured field is the variability in the magnetic field strength on time-scales of a few hours to days. Therefore, in a second run, we use real solar wind conditions at Earth that have been propagated to the location of the comet using the Tao et al. (2005) model. This new model shows significant changes in the magnetic field strength, depending on solar wind conditions. At the beginning of the mission, the field, on average, seems to be well described by the model, although there are still short time discrepancies between model and measurements. Although the correlation coefficient between the entire measured field and the model is low (0.41), there are intervals where the model and observations fit reasonably well.

4.2 Influence of solar and cometary rotation

As shown in Edberg et al. (2015), the plasma at the comet is significantly affected by the rotation of the comet. Due to its unusual shape, the cometary neutral density has two maxima per rotation period, the enhancement may be by a factor of ∼6 (Edberg et al. 2015). Due to photoionization, the ion and electron densities mostly follow the neutral density, but the magnetic field does not (Volwerk et al. 2016). This may be because the long-term variation in magnetic field strength and direction are overshadowed by large amplitude high-frequency variations caused by the solar wind or plasma waves and instabilities.

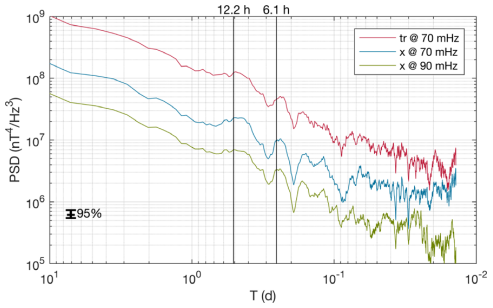

Figure 3. Power spectral density of the energy content in different frequency bands. The input time series for the red line has been extracted from the dynamic spectrum in Fig. 2 at frequencies given in the legend. The band width of the frequency bin is 10 mHz. It covers the entire mission and the spectra were calculated using Welch's method with a window of 14 d and an overlap of 10 d. For the blue and green line only the dynamic spectrum for the magnetic field x-component was used. The black vertical lines indicate the average cometary rotation period and half a rotation period, respectively.

On time-scales of a few days, there is no correlation between the magnetic field strength or variance and the neutral density. However, the dynamic spectrum in Fig. 2 shows a semiperiodic enhancement in frequency bands above 50 mHz. It stands to prove that this is due to the cometary rotation and associated periodicity in the neutral density. To examine the frequency content, we extracted the power spectral density at a certain frequency [70 and 90 mHz, see panel (e) in Fig. 2] where the periodicity seemed to be visible best, for every time interval for which a spectrum was calculated. Thus a time series of the power spectral density in that frequency band is generated which may then be Fourier transformed to gain access to the frequency contents. The result of this for the trace spectral density and the spectral density of the x-component of the magnetic field is shown in Fig. 3. There is a slight peak at the average cometary rotation period of 12.2 h, but there is a much more pronounced peak at about half the average rotation period. Both peaks are broad and slightly below the actual rotation period. This might be due to the shifts in the active region between the northern and southern summer (Hansen et al. 2016) or due to the spacecraft motion. The occurrence of these higher harmonics of the comet's rotation frequency may also be caused by the asymmetric shape of 67P thus leading to a convoluted activity spectrum. Hässig et al. (2015) have also found that during the northern summer, the dominant frequency is not the rotation period itself, but around half of it, because the nucleus' active region is illuminated twice on a comet day. This matches our observations. There are several other significant frequencies that are visible in all components, most notably one at 2 h, however these could not be identified with any physical processes as of yet. For frequencies below ∼1 h the spectra for all three components differ significantly, which indicates that this is where plasma waves dominate over the neutral background contribution. It should also be noted that the cometary rotation period is best visible in the x-, i.e. the antisunward component of the magnetic field. This might be

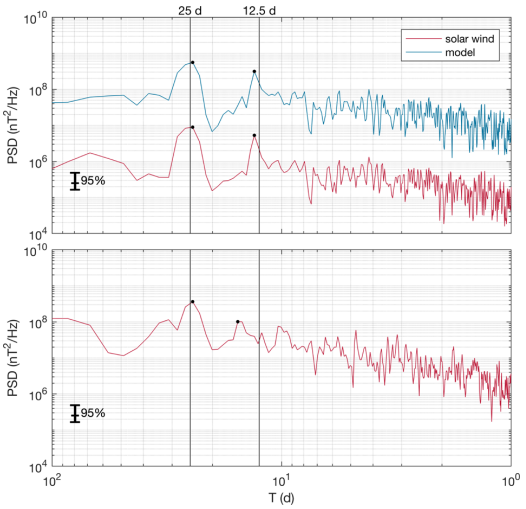

Figure 4. Power spectral densities of the magnetic field x-component over the entire mission. The top panel shows the solar wind data and the magnetic field model. The bottom panel shows the power spectral density of the B_x component measured by RPC–MAG. Black lines indicate the solar rotation period and half a solar rotation period. The black dots mark the most significant peaks in the spectra which were calculated using Welch's method with a window of 340 d and an overlap of 300 d.

due to the fact that the x-component is the dominant one for most of the mission and especially at perihelion.

As shown in the previous section, the magnetic field at the comet is significantly affected by the strength of the IMF. Therefore it stands to reason that periodicities in the solar wind parameters will also be reflected in the magnetic field in the coma of 67P. The most prominent of these would be the solar rotation and its harmonics (Forsyth & Marsch 1999).

To check that this periodicity is indeed present in the solar wind magnetic field, we have calculated the power spectral density of the Tao model solar wind magnetic field. To test that this periodicity should also be visible in the coma, the output of our model for the magnetic field was also used to calculate a power spectral density. Lastly, we take the magnetic field x-component and also find the power spectral density. The result is shown in Fig. 4.

In the first panel the solar rotation is clearly visible in the spectra, as well as half a rotation period. The peak in the spectra is slightly below 25 d, which may be caused either by the comets motion through the Solar system or the non-zero inclination of the comet's orbit.

The second panel of Fig. 4 shows the spectra calculated from magnetic field measurements in the coma. The two most prominent maxima are close to the maxima in the solar wind measurement. The actual peaks are located at 24.4 and 15.5 d, the first one then almost exactly corresponds to the solar wind spectra, although the lower one does not.

There are several possible explanations for this discrepancy. First, the peak at 15.5 d is only barely significant and there is another signature at 13.5 d that is obscured. Therefore the rotation period may be a false detection. On the other hand, *Rosetta* was on a circular trajectory around the comet for weeks during the mission. These trajectories had periods from 10 to 20 d. Although a clear correlation between the spacecraft location and magnetic field could not be found, it is entirely possible that there is a tenuous connection between the two parameters that could influence the spectra shown here.

4.3 Draping

To study the draping structures at the comet, it is opportune to calculate the cone χ and clock ξ angles

$$\tan\chi = \frac{B_x}{\sqrt{B_y^2 + B_z^2}} \tag{8}$$

$$\tan\xi = \frac{B_y}{B_z}, \tag{9}$$

where the magnetic field is given in CSEQ coordinates. In this reference frame, vectors along the x-axis will have $\chi = 90^\circ$, vectors along the y-axis will have $\chi = 0^\circ$ and $\xi = 0^\circ$, whereas vectors along the z-axis will have $\chi = 0^\circ$ and $\xi = 90^\circ$. The cone and clock angle measured over time vary significantly, as they are influenced by short-time-scale plasma oscillations. However, here the interest is on the long-term evolution of possible magnetic field draping, therefore we opted to generate histograms of the cone and clock angle for longer intervals. For this purpose, the cone and clock angles were calculated from the time series shown in Fig. 2, panel (c), i.e. one angle every hour.

The resulting angles were then binned and Fig. 5 shows the evolution of the cone and clock angle of the magnetic field in six time intervals covering the entire mission. There is a significant change in the distributions of cone and clock angle over time, related to the amount of mass loading in the coma.

For low gas production rates [$Q < 10^{26}$ s^{-1}, panel (a)] the cone angle is sharply focused around what should be the Parker cone angle at that time ($10^\circ - 20^\circ$). The clock angle is approximately equally distributed over the entire interval. There is a dearth of cone angles at $\pm 90^\circ$, which is due to the definition of the cone angle. For it to be close to those values both the y- and z-component need to be zero at the same time, which is almost never the case.

For intermediate gas production rates [panel (b)] the distribution barely changes. There is a slight shift to higher cone angles indicating that the magnetic field is still following the Parker angle which should decrease with decreasing distance, and therefore the IMF cone angle should increase. There is little change in the clock angle distribution, but for a slight concentration of the counts around 0°. On the first glance this seems contradictory to what was published in Koenders et al. (2016), who found a significant draping structure in the plane orthogonal to the solar wind magnetic field plane. But further study reveals that this draping signature was only found very close to the comet ($r < 50$ km), whereas we have taken all values regardless of distance into account. In consequence this implies that at this intermediate stage, draping only occurs close to the comet, where the neutral and ion densities are highest, but not at large distances.

However for high gas production rates [$Q > 10^{27}$ s^{-1}, panel (c) and (d)] the magnetic field draping is recognizable. Now the cone angle is significantly higher with values between 50° and 80° and the clock angle is also more focused at 180° and 0°. At this point, the Parker cone angle is around 40°, which is smaller than what we measured at the comet. This is the magnetic field draping that is expected for comets with high outgassing rates, although the ideal case of $\chi = 90^\circ$ is not reached (Alfvén 1957). In panel (c) there are two populations visible, however, these are simply the two different directions of the magnetic field. For steady solar wind conditions one would expect these two directions to occur on two different

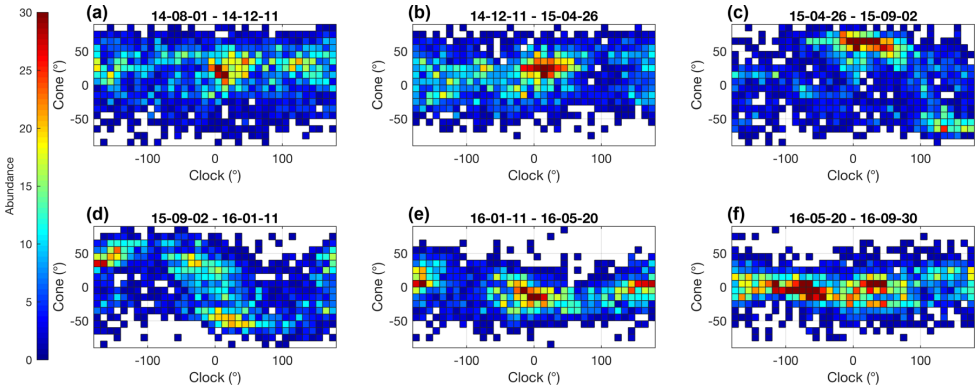

Figure 5. Cone and clock angles for six equally long time periods, spanning the entire mission. Due to large variances, the cone and clock angles (as defined in the text) are shown as a histogram rather than time series. Panel (e) is shown for completeness, but the angles have a large uncertainty due to unknown magnetic field offsets.

sites of the comet, however, as the IMF is constantly changing this is not seen in the data. These data match the simulation results in e.g. Koenders et al. (2015) very well, as they predicted that the magnetic field draping at large distances from the nucleus would not actually reach the ideal values of $\chi = 90^\circ$ as the mass loading far from the nucleus as well as the ion flow speed at those distances inhibit further draping of the field.

In panel (d), there is also a third population with $\chi = 40^\circ$ and $\xi = -30^\circ$, which is of yet unknown origin, however, it should be pointed out that it is not related to the day side excursion where the radial distance of the spacecraft was increased to 1500 km. Instead, we note that the field configuration is rotated compared to panel (c), which may be related to the comet crossing the heliospheric current sheet. Then the third population in the middle could simply signify the slow rotation of the field.

Panel (e) is similar to panel (b) with a second population at clock angles of $\pm 180^\circ$ being the only difference. This can be interpreted as two different directions of the same field line, one being in $+$y-direction and one in $-$y-direction. Panel (f) is shown for completeness' sake but should not be taken at face value as the offset of the data is likely wrong in that interval, resulting in errors in the direction of the magnetic field. In the future, this might be corrected using the offset determination technique presented in Plaschke et al. (2017).

5 CONCLUSIONS

The magnetic field at a comet changes significantly depending on the gas production rate. For low rates the field strength and variance are low, however as outgassing increases so does the magnetic field strength and variance. This increase is modelled with accuracies of around 5 nT, however to account for the large variance in field strength, it is necessary to include realistic solar wind conditions.

The strong influence of the solar wind is also visible in the presence of the solar rotation period in the magnetic field spectrum. This shows a clear peak at the solar rotation rate which is related to the occurrence of corotating interaction region (CIRs) and therefore higher IMF and solar wind dynamic pressure. Additionally the magnetic field is also influenced by the neutral density. Although not visible as a one to one correlation, this is shown by the appearance of the comet rotation rate, which couples to the neutral density, in the magnetic field spectrum. It is important to note that the magnetic field strength is governed by the solar wind, whereas the magnetic field variance and frequency content is governed by the cometary neutral profile.

Depending on the gas production rate, the average magnetic field direction changes. Far from the Sun the magnetic field is not draped and is in the direction of the corresponding Parker angle. This does not change at intermediate outgassing rates and far from the comet, although it has been shown previously that draping exists at intermediate outgassing rates for distances smaller than 50 km. However for high outgassing rates, the magnetic field shows clear signs of draping even far from the comet in the x-y-plane, although the changing solar wind conditions make it impossible to establish a clear draping pattern for the entire plasma environment.

Overall we have shown that the magnetic field at comet 67P is highly variable, which is mostly due to the short time variance of the solar wind and the long term evolution of the gas production rate. This means, that every measurement taken by the magnetometer needs to take into account solar wind and outgassing conditions as well as spacecraft location. The interaction may then be divided into roughly three regimes: low; intermediate and high activity, which have fundamentally different magnetic field signatures.

ACKNOWLEDGEMENTS

The RPC–MAG data will be made available through the PSA archive of ESA and the PDS archive of NASA. *Rosetta* is a European Space Agency (ESA) mission with contributions from its member states and the National Aeronautics and Space Administration (NASA). The work on RPC–MAG was financially supported by the German Ministerium für Wirtschaft und Energie and the Deutsches Zentrum für Luft- und Raumfahrt under contract 50QP 1401. We are indebted to the whole of the *Rosetta* Mission Team, SGS and RMOC for their outstanding efforts in making this mission possible. We acknowledge the staff of CDDP and IC for the use of AMDA and the RPC Quicklook data base (provided by a collaboration between the Centre de Données de la Physique des Plasmas, supported by CNRS, CNES, Observatoire de Paris and Université Paul Sabatier, Toulouse and Imperial College London, supported by the UK Science and Technology Facilities Council).

REFERENCES

Acton C. H., 1996, Planet. Space Sci., 44, 65
Alfvén H., 1957, Tellus, 9, 92
Auster H.-U. et al., 2015, Science, 349, 015102
Biermann L., Brosowski B., Schmidt H. U., 1967, Sol. Phys., 1, 254
Coates A. J., Jones G. H., 2009, Planet. Space Sci., 57, 1175
Cravens T. E., 1987, Adv. Space Res., 7, 147
Edberg N. J. T. et al., 2015, Geophys. Res. Lett., 42, 4263
Edberg N. J. T. et al., 2016, MNRAS, 462, S45
Flammer K. R., Mendis D. A., 1991, Ap&SS, 182, 155
Forsyth R. J., Marsch E., 1999, Space Sci. Rev., 89, 7
Fougere N. et al., 2016, A&A, 588, A134
Galeev A. A., Cravens T. E., Gombosi T. I., 1985, ApJ, 289, 807
Glassmeier K.-H., 2017, Phil. Trans. R. Astron. Soc. A, 375, 20160256
Glassmeier K.-H., Boehnhardt H., Koschny D., Kührt E., Richter I., 2007a, Space Sci. Rev., 128, 1
Glassmeier K.-H. et al., 2007b, Space Sci. Rev., 128, 649
Goetz C. et al., 2016a, MNRAS, 462, S459
Goetz C. et al., 2016b, A&A, 588, A24
Hansen K. C. et al., 2016, MNRAS, 462, S491
Haser L., 1957, Bull. Soc. R. Sci. Liege, 43, 740
Hässig M. et al., 2015, Science, 347, 276
Huang Z. et al., 2016, J. Geophys. Res., 121, 4247
Koenders C., Glassmeier K.-H., Richter I., Motschmann U., Rubin M., 2013, Planet. Space Sci., 87, 85
Koenders C., Glassmeier K.-H., Richter I., Ranocha H., Motschmann U., 2015, Planet. Space Sci., 105, 101
Koenders C., Goetz C., Richter I., Motschmann U., Glassmeier K.-H., 2016, MNRAS, 462, S235
Mandt K. E. et al., 2016, MNRAS, 462, S9
Nilsson H. et al., 2015, Science, 347, aaa0571
Parker E. N., 1958, ApJ, 128, 664
Plaschke F., Goetz C., Volwerk M., Richter I., Fruehauff D., Narita Y., Glassmeier K.-H., 2017, MNRAS, in press
Richter I., Koenders C., Glassmeier K. H., Tsurutani B. T., Goldstein R., 2011, Planet. Space Sci., 59, 691
Richter I. et al., 2015, Ann. Geophys., 33, 1031
Richter I. et al., 2016, Ann. Geophys., 34, 609
Riedler W., Schwingenschuh K., Yeroshenko Y. E., Styashkin V. A., Russell C. T., 1986, Nature, 321, 288
Rubin M., Hansen K. C., Combi M. R., Daldorff L. K. S., Gombosi T. I., Tenishev V. M., 2012, J. Geophys. Res., 117, 6227
Tao C., Kataoka R., Fukunishi H., Takahashi Y., Yokoyama T., 2005, J. Geophys. Res., 110, 11208
Volwerk M. et al., 2016, Ann. Geophys., 34, 1

This paper has been typeset from a TEX/LATEX file prepared by the author.

A.4. Paper IV: Unusually high magnetic fields in the coma of 67P/Churyumov-Gerasimenko during its high-activity phase

Authors: C. Goetz, B. T. Tsurutani, P. Henri, M. Volwerk, E. Behar, N. J. T. Edberg, A. Eriksson, R. Goldstein, P. Mokashi, H. Nilsson, I. Richter, A. Wellbrock, K.-H. Glassmeier

Bibliographic Information: Astronomy & Astrophysics, doi:10.1051/0004-6361/201833544

Year: 2018, accepted

Citations: 0 (The SAO/NASA Astrophysics Data System, December 2018)

Astronomy & Astrophysics manuscript no. 33544-18
December 22, 2018
©ESO 2018

Rosetta mission full comet phase results

Special issue

Unusually high magnetic fields in the coma of 67P/Churyumov–Gerasimenko during its high-activity phase

C. Goetz[1], B. T. Tsurutani[2], P. Henri[3], M. Volwerk[4], E. Behar[5], N. J. T. Edberg[6], A. Eriksson[6], R. Goldstein[7], P. Mokashi[7], H. Nilsson[4], I. Richter[1], A. Wellbrock[8], and K. H. Glassmeier[1]

[1] Institut für Geophysik und extraterrestrische Physik, Technische Universität Braunschweig, Mendelssohnstr. 3, 38106 Braunschweig, Germany
e-mail: c.goetz@tu-bs.de
[2] Jet Propulsion Laboratory, Pasadena, CA, USA
[3] LPC2E, CNRS, Orléans, France
[4] Institut für Weltraumforschung, Österreichische Akademie der Wissenschaften, Schmiedlstr. 6, Graz, Austria
[5] Swedish Institute of Space Physics, PO Box 812, 981 28 Kiruna, Sweden
[6] Swedish Institute of Space Physics, Angström Laboratory, Lägerhyddsvägen 1, Uppsala, Sweden
[7] Southwest Research Institute, PO Drawer 28510, San Antonio, TX 78228-0510, USA
[8] Mullard Space Science Laboratory, UCL Department of Space and Climate Physics, Holmbury St. Mary, Dorking, UK

Received 1 June 2018 / Accepted 3 October 2018

ABSTRACT

Aims. On July 3, 2015, an unprecedented increase in the magnetic field magnitude was measured by the Rosetta spacecraft orbiting comet 67P/Churyumov–Gerasimenko (67P). This increase was accompanied by large variations in magnetic field and ion and electron density and energy. To our knowledge, this unusual event marks the highest magnetic field ever measured in the plasma environment of a comet. Our goal here is to examine possible physical causes for this event, and to explain this reaction of the cometary plasma and magnetic field and its trigger.
Methods. We used observations from the entire Rosetta Plasma Consortium as well as energetic particle measurements from the Standard Radiation Monitor on board Rosetta to characterize the event. To provide context for the solar wind at the comet, observations at Earth were compared with simulations of the solar wind.
Results. We find that the unusual behavior of the plasma around 67P is of solar wind origin and is caused by the impact of an interplanetary coronal mass ejection, combined with a corotating interaction region. This causes the magnetic field to pile up and increase by a factor of six to about 300 nT compared to normal values of the enhanced magnetic field at a comet. This increase is only partially accompanied by an increase in plasma density and energy, indicating that the magnetic field is connected to different regions of the coma.

Key words. comets: individual: 67P/Churyumov–Gerasimenko – plasmas – magnetic fields – methods: data analysis

1. Introduction

The plasma environment at a comet is heavily dependent on the input solar wind conditions far upstream of the coma (Alfvén 1957; Nilsson et al. 2017; Goetz et al. 2017; Glassmeier 2017). The amount of mass-loading, that is, the incorporation of cometary ions in the solar wind flow, depends on solar wind parameters such as density, velocity, and magnetic field. As the comet approaches the Sun, the solar wind dynamic pressure and interplanetary magnetic field (IMF) magnitude increase slowly (Goetz et al. 2017), but so does the neutral outgassing rate of the nucleus as insolation increases. The neutral gas that is expelled from the nucleus is then ionized by processes such as photoionization and electron impact ionization. Therefore, the plasma density is controlled mostly by the intensity of the solar radiation and increases dramatically with decreasing distance between the comet and the Sun. The newly born ions present an obstacle to the solar wind and modify the plasma flow.

As the cometary ions are incorporated into the supersonic solar wind flow, the solar wind is slowed and eventually meets the conditions for the formation of a weak bow shock (Biermann et al. 1967; Koenders et al. 2013). The exact location of the bow shock then depends on the density of cometary ions and therefore on the neutral outgassing rate, as well as on the solar wind ram pressure. Behind the bow shock, the solar wind decelerates further and is deflected around the inner coma, whereas the IMF magnitude increases (pile-up) and the magnetic field starts to drape itself around the comet (Volwerk et al. 2014; Goetz et al. 2017). For sufficiently high gas production rates it may even reach deflections of up to 180°, and finally is entirely expelled from the inner coma (Behar et al. 2017, 2018). At this point, the cometary ions that have been picked up far upstream of the shock take over the main flow of plasma around the comet. At these gas production rates, it is also possible to observe an electron collisionopause (or exobase) in the inner coma (Coates & Jones 2009; Mandt et al. 2016). The innermost region in the plasma environment of the comet is the diamagnetic cavity, an entirely field-free region that is dominated by collisional ions and electrons (Neubauer 1987; Goetz et al. 2016a,b; Madanian et al. 2017; Henri et al. 2017). None of these boundaries is fixed in position, but they move according to gas production rate, as well as solar wind conditions. In particular, transient impulsive events

A&A proofs: manuscript no. 33544-18

in the solar wind of solar origin, such as interplanetary coronal mass ejections (ICMEs) and corotating interaction regions (CIRs), directly affect the cometary plasma properties.

Active regions (ARs) on the Sun are regions of multiple sunspots with complex photospheric and coronal magnetic fields. ARs are known to flare often, many times a day. With each major flare, an ICME is normally released. If the ICME has a speed in the interplanetary medium that is faster than the upstream in situ wave magnetosonic speed, a fast forward shock will form ahead of the ICME. Behind the shock will be a plasma sheath that contains heated and compressed slow solar wind plasma (Tsurutani et al. 1988). This sheath comes from a different solar source than the ICME. The amount of compression of the upstream slow solar wind plasma is directly related to the Mach number of the shock. The compression ratio is a maximum of 4 (Kennel et al. 1985; Tsurutani et al. 2008). When an interplanetary shock and its following sheath impinge upon a compressible object like the Earth's magnetosphere, the high densities lead to magnetospheric compression.

High-speed solar wind streams emanate from coronal hole regions on the Sun. These are open magnetic field regions, and the streams have speeds of 750−800 km s^{-1}. When the high-speed streams interact with low-speed (350−400 km s^{-1}) solar wind, a CIR is formed (Smith & Wolfe 1976). The antisolar side of the CIR is composed of shocked and compressed slow solar wind plasma, and the solar side is composed of shocked and compressed high-speed solar wind plasmas. The two regions are separated by a tangential discontinuity (Pizzo 1985). At distances greater than ∼1.5 AU from the Sun, CIRs are bounded by a forward shock at the antisolar side and by a reverse shock on the solar side. If a CIR that has both a forward and a reverse shock hits the Earth's magnetosphere, the forward shock/sheath will compress the magnetosphere, and as the CIR reverse shock crosses it, the magnetosphere will decompress (Tsurutani et al. 2011).

The impact of CIRs and ICMEs on the cometary plasma environment has previously been investigated in situ only at comet 67P/Churyumov-Gerasimenko (67P) by Edberg et al. (2016a,b), Witasse et al. (2017), and Hajra (2018). They found that CIRs and ICMEs both cause strong compressions of the plasma environment, resulting in higher magnetic fields and plasma densities. These fields and densities were accompanied by an increase in suprathermal electrons that may have been accelerated along the magnetic field lines. It was also found that electron impact ionization increased significantly during the event. For ICMEs it was observed that flux ropes exist in the compressed plasma at 67P. Energetic particle counts are also increased before the impact and culminate in a Forbush decrease (FD; Cane 2000) that begins about two hours before the signatures of the ICME are apparent in the plasma.

The Rosetta orbiter (Glassmeier et al. 2007a) spent two years orbiting comet 67P and continuously collected plasma data. One of the most striking events was an unusually high magnetic field of ∼300 nT, an enhancement of about a factor of 50 compared to normal solar wind conditions and a factor of about six higher than normal for the piled-up magnetic field in the inner coma of 67P. We investigate possible triggers, especially those of solar wind origin. This is fairly difficult as the Rosetta mission did not include a solar wind monitor, which prevents an accurate determination of the upstream parameters. The only source of information are spacecraft near Earth and Mars. In particular, two additional sources for solar wind data were used, the OMNI dataset at Earth (King & Papitashvili 2005), and the MAVEN observations at Mars (Jakosky et al. 2015). To be usable at 67P, the propagation of the plasma through the solar system needs to be modeled accurately.

In this publication we describe the unusual measurements made on July 3, 2015, at comet 67P and search for the physical causes of this increase. Then we relate the significant changes in the plasma to structures in the coma and discuss the influence of the high field on them.

2. Instruments and data

We used all instruments in the Rosetta Plasma Consortium (RPC, Carr et al. 2007) the MAGnetometer (MAG, Glassmeier et al. 2007b), the Mutual Impedance Probe (MIP, Trotignon et al. 2007), the LAngmuir Probe (LAP, Eriksson et al. 2007), the Ion Composition Analyzer (ICA, Nilsson et al. 2007), and the Ion and Electron Sensor (IES, Burch et al. 2007). These instruments together are capable of measuring the magnetic field, electron and ion velocity space distribution functions with mass resolution, as well as plasma densities and temperature of electrons. However, there are a few caveats in using the data, which we briefly describe in the following.

First, the magnetic field, given in cometocentric solar equatorial coordinates (CSEQ), has been calibrated using observations in the diamagnetic cavity, which reduces the spacecraft influence to about 3 nT per field component. In the CSEQ system, the origin is at the nucleus, the x-axis points toward the Sun, the z-axis points out of the ecliptic, and the y-axis completes the right-handed coordinate system. ICA and IES have a limited field of view ($90° \times 360°$) and may miss parts of the particle distribution functions. This is further complicated by the fact that the spacecraft is charged itself. For negative spacecraft potential, as it is observed in this event, slower ions are accelerated by the spacecraft potential and are detected at higher energies. This gives a skewed distribution function. Therefore, we used LAP spacecraft potential measurements to compare to the distribution functions.

MIP was operated in short Debye length (SDL) mode, with transmitters used in phase opposition (push–pull mode) during this event. In this mode, MIP is blind whenever the Debye length is larger than about one meter. For 5 eV electrons, this means that MIP cannot measure plasma densities below 300 cm^{-3}. This lower limit can even increase for warmer electrons.

The lower densities may still be derived by using the LAP current and sweep-derived densities as well as MIP high densities to cross-calibrate and gain access to calibrated and high-time resolution LAP densities, in a way similar to what is described in Heritier et al. (2017). These densities were used here. We note that this cross-calibration assumes an isothermal hypothesis, so that in the presence of an electron temperature increase, as might be expected downstream of a shock, these cross-calibrated derived densities might be underestimated.

Additionally sampling rates vary drastically between instruments. IES has a sampling period of 256 s, ICA 4 s, MAG 0.05 s, and LAP 160 s for density and spacecraft potential and 0.017 s for the current. MIP has sample periods of a few seconds, but they are irregularly spaced, and in this specific case, are characterized by a larger amount of hot electrons. Only a reduced subset of the MIP spectra can be used to retrieve the electron density. ICA was not switched on for some time during the event.

As CIRs and ICMEs are accompanied by an increase in energetic particles, the Standard Radiation Monitor on board Rosetta (SREM, Evans et al. 2008) was used to provide context on these high energies. Rosina-COPS data are contaminated by wheel offloading and slews. Off-nadir pointing during the main event

leads to very low densities, which are easily influenced by electron energies above 12 eV. This makes it impossible to obtain reliable neutral density measurements for this event, therefore we omitted these observations from the analysis.

We used observations made on July 3, 2015. At this time, the spacecraft was 180 km away from the nucleus and orbited at the terminator, and the comet was 1.3 AU away from the Sun, fairly close to perihelion (1.24 AU). According to Hansen et al. (2016), this corresponds to a water-outgassing rate of 5.8×10^{27} s^{-1}. With these conditions, the spacecraft was located in the innermost part of the coma, far downstream of an undetected bow shock.

We used several observations in the solar system to provide context for the solar wind at 67P. STEREO data were not available for the time interval, but SOHO was observing the Earthward side of the Sun. MAVEN was in orbit around Mars and taking full particle distributions (SWIA) and observing the magnetic field (MAG). The solar wind parameters were determined using the method described by Halekas et al. (2017). The OMNI dataset was used to access the solar wind conditions at Earth. In an attempt to tie all observation points together, we used ENLIL simulations that cover the Sun, Earth, 67P, and Mars (Odstrcil 2003).

3. Observations

Figure 1 shows the plasma parameters in the two hours around the onset of the main event. Here, the cone angle ξ and the clock angle χ are defined in the CSEQ system as follows:

$$\tan(\xi) = \frac{B_x}{\sqrt{B_y^2 + B_z^2}} \quad \text{and} \quad \tan(\chi) = \frac{B_z}{B_y}. \tag{1}$$

Thus, a sunward field would have a cone angle of 90° and a northward (along the z-axis) field has a clock angle of 90°. Before the onset, the magnetic field had magnitudes of around 50 nT and exhibited very little fluctuation. The predominant component was the anti-sunward x-component. The plasma density was below the cutoff of MIP, and the electron flux was low. IES barely detected significant ion fluxes, but ICA was able to detect the cometary ion flux. The ions were mostly found to be in the energy range of 20 − 80 eV, but because of the high time resolution mode of ICA at the time, energies above 100 eV were not sampled. IES did not detect any solar wind ions during this interval, but there was significant obstruction (indicated by the white space). LAP probe bias sweeps (not shown) indicate that the electron temperature was around 3−8 eV. This type of plasma is very typical for near-perihelion conditions at comet 67P.

At 21:32:10, the magnetic field magnitude increased by a factor of 2 to approximately 100 nT. The field was still mostly anti-sunward for the next five minutes; the cone and clock angles were unchanged. At the same time, the electron flux and energy were significantly elevated and the electron energy was approximately twice as high, whereas fluxes increased by a factor of five. The ion flux in IES was only slightly elevated, whereas in ICA the ion energies reached the upper energy cutoff and fluxes increased by a factor of 2. The spacecraft potential became slightly more negative, consistent with the increased electron flux.

Five minutes after the initial onset, at 21:37:08, the magnetic field abruptly changed direction to slightly sunward, and the field was below 10 nT for 3 s, the cone and clock angle varied significantly, and the cone angle changed from 90° to 0°. These field fluctuations were accompanied by electron densities of 3000−7000 cm^{-3} and ion flux doubling. This increase was very focused on a population around 100 eV and seemed to match the ICA observations as well, where the cometary ion flux in a range around 80 eV increased by a factor of two. The spacecraft potential decreased further to −16.8 V. This plasma density enhancement ended after several minutes at 21:41:24, when all parameters returned to the previous elevated values.

The next change occured at 22:06:18. The magnetic field suddenly changed direction, and the magnitude increased further to above 200 nT. The magnetic field also fluctuated heavily with $\Delta B/B \approx 1$. These fluctuations were mostly due to clock angle and magnitude changes, as the cone angle remained stable at −90°. The peak field value of ∼300 nT was reached at 22:12:39, which corresponds well to the IES electron flux maximum. This was due to a tenfold increase in flux in the energy band around 10 eV. The electron and ion flux were higher than in the previous quiet time, and the spacecraft potential reached around −13.6 V. Again, this was mostly due to a population of ions of about 100 eV; during the magnetic field peak, there was also an enhancement of about 200 eV. It should be noted that there is a large discrepancy between the density estimates derived from the MIP and LAP sensors, which is most likely due to a variation in electron temperature. Considering the observed change in the MIP lower frequency detection threshold, we are able to derive the factor by which the electron temperature is likely to have increased compared to the low-density region: ∼9. This matches the difference in MIP and LAP densities well: the LAP density peaks are about a factor of ∼3 below the MIP density peaks. As the temperature scales with the square of the density, this also gives a factor of 9. If the temperature in the low-density region was 5 eV, this would result in an electron temperature of 45 eV in the high-density region.

This high-activity region ended at 22:36:00, when the field rotated again and became anti-sunward (cone angle 90°). The high level of fluctuation ceased, and plasma density values returned to below the detection threshold. The ion fluxes also decreased again by a factor of two.

In general, the event can be divided into three regions. Region 0 is the undisturbed coma, with a low field magnitude and variability and a sunward direction. This is accompanied by low ion and electron densities and energies. Region 1 is then characterized by a higher magnitude field that remains stable in the sunward direction and still exhibits low variability. Densities and energies are increased but still low. Region 2 then shows a rotation of the field in the anti-sunward direction and extremely high power in the magnetic field power spectral density (not shown), as well as high particle densities and energies. We have chosen to focus on the shown interval because regions 1 and 2 reoccurred in the next hours, but with diminishing strength that did not add any new features in the plasma environment.

4. Discussion

4.1. Possible triggers

As shown in Goetz et al. (2017), the magnetic field magnitude in the inner coma is determined by the field magnitude and dynamic pressure of the solar wind. Therefore, it is advisable to search solar wind observations for an extreme event that could cause the effects on the cometary plasma described above. Two such events are CIRs and ICMEs. Both have been reported at 67P for other solar wind and outgassing conditions (Edberg et al. 2016a,b; Witasse et al. 2017) to have caused higher magnetic

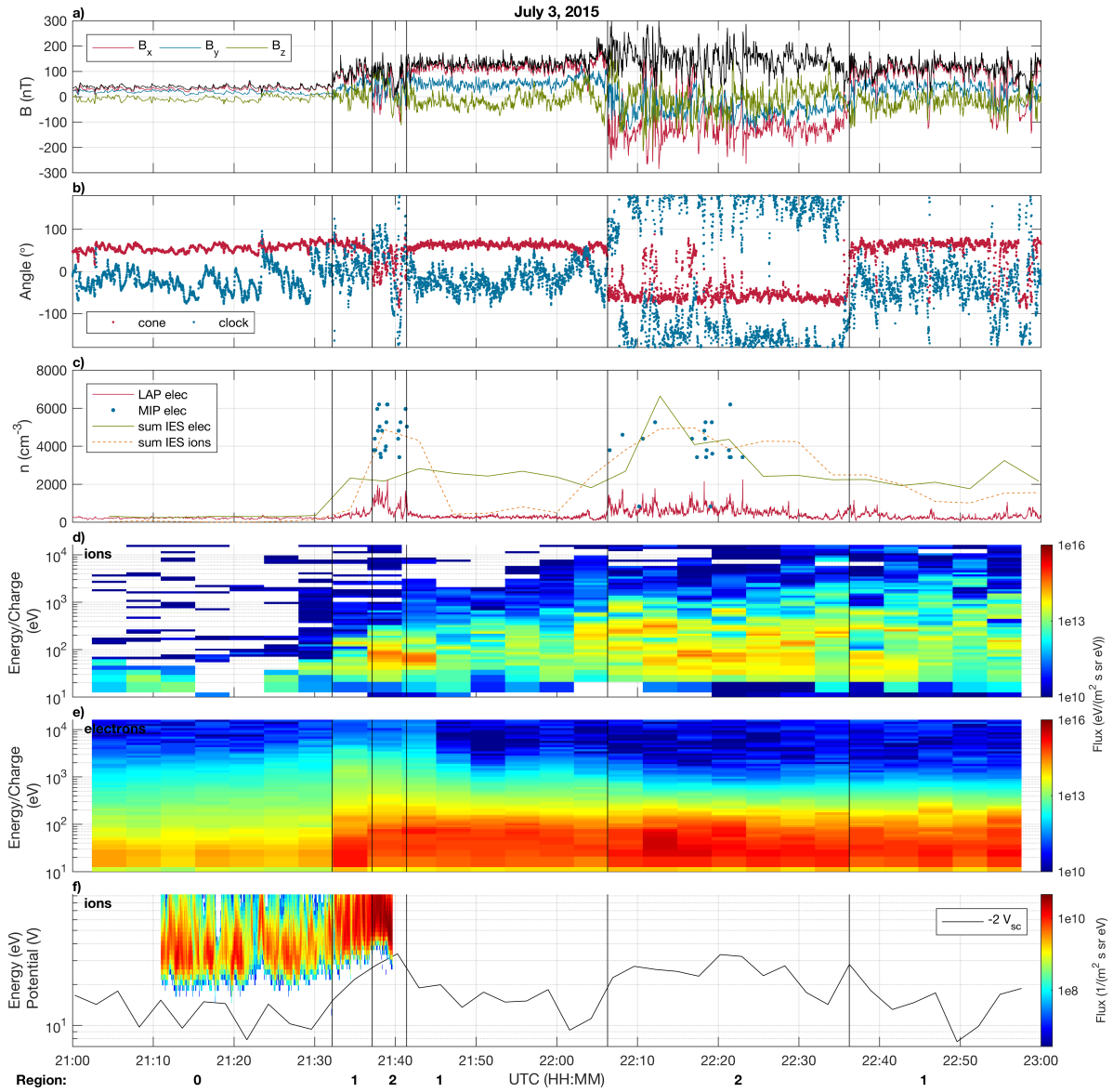

Fig. 1. Plasma parameters as observed by RPC during the main event. *Panel a*: magnetic field components and magnitude (black). *Panel b*: cone and clock angle of the magnetic field. *Panel c*: estimates of the plasma density from different instruments. IES observations are energy-summed flux adjusted to fit the scale. *Panels d and e*: electron and ion flux integrated over the entire field of view of IES. *Panel f*: spacecraft potential (multiplied by −2 for clarity) derived from LAP sweeps and ion energy spectrogram measured by ICA. The vertical lines indicate the boundaries of the three plasma regions (indicated by numbers at the bottom).

field magnitudes, increases in electron density and fluxes over all energies, as well as increases in solar wind and cometary ion fluxes. In at least one case the impact of an ICME was sufficient to move the solar wind ion cavity boundary so close to the nucleus that it was detectable by Rosetta.

We therefore used images taken of the Sun to determine whether there were any ICMEs in the one-week period before the detected impact at the comet. During that time there was only one such event, an ICME on the evening of July 1, 2015, observed by SOHO. A simple calculation shows that to reach the comet in time, the ICME would have to have an average velocity of well above 1000 km s^{-1} on average. Because ICMEs tend to slow down as they propagate into the solar system, we can assume even higher velocities at the Sun. Events with solar wind velocities of 1500 km s^{-1} at 1 AU are very rare, thus it seems unlikely (but not impossible) that this structure reached the comet in time (Tsurutani et al. 2003). To verify whether this ICME reached the comet, we used ENLIL simulations with the cone model[1]. Three

[1] The full heliospheric simulation results may be found at http://ccmc.gsfc.nasa.gov under run number Charlotte_Goetz_062416_SH_1.

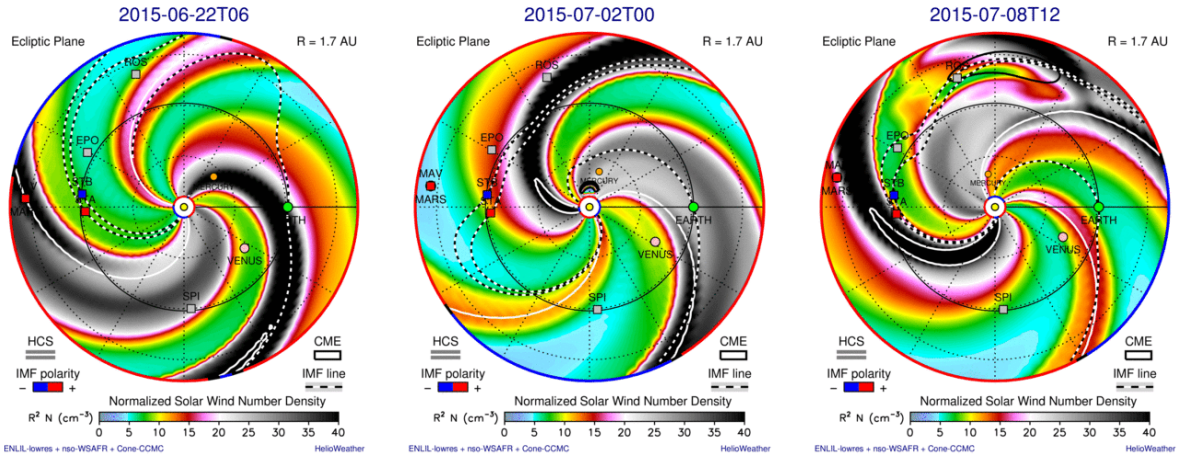

Fig. 2. Three snapshots of the density output of the ENLIL simulation. The position of the comet is marked in gray (labeled "ROS"), and Mars is red, with Maven in orbit (labeled "MAV").

snapshots of the simulation are shown in Fig. 2. The figure shows the plasma density scaled with distance, and it is immediately clear that the ICME, which is visible as a very small disturbance almost reaching Mercury in the middle panel, reaches the comet (right panel) on July 6, which is almost three days after the investigated event. Additionally, the velocity of the ICME was chosen to be very high (1200 km s^{-1}), so that realistically, the ICME would arrive even later. Because of its configuration, it is also questionable if its angular extension was large enough to have a significant impact on the cometary environment at all. However, there are uncertainties in the ENLIL simulations and the observations of the CME footpoint at the Sun, which means that it is not possible to rule out this ICME as the trigger.

A second type of solar wind event that usually has high dynamic pressures is a CIR. The snapshots in Fig. 2 were chosen so that the edge of a high-density CIR was either at Earth (left), 67P (middle), or Mars (right). In the following we try to identify the exact trigger of the July 3 event based on observations at the comet.

Figure 3 shows the magnetic field magnitude, counts from the Rosetta radiation monitor for the time around the investigated event, and the magnetic field and dynamic pressure measured in the solar wind at Earth at the time that the CIR would have to pass Earth to reach 67P on July 3. We also checked MAVEN observations of the solar wind at Mars, but there are several possible high dynamic pressure events that coincide with the predicted arrival time of a CIR at comet 67P, and thus we have opted not to discuss these observations further as they are ambivalent and do not aid in identifying the trigger of the high magnetic field.

First, there is a data gap in the Rosetta measurements when the instrument was shut off as a result of operational constraints. The event was preceded by a smaller magnetic field magnitude increase on June 30, which was associated with a change in cone angle (not shown). The magnetic field direction and amplitude were usually very variable at the comet (Goetz et al. 2017), which was also the case for most of the interval shown here. Conversely, the field magnitude was more stable on July 5 and 6, which also corresponds to steady conditions in the direction of the field. On the evening of July 6, it returned to its usual variable state. Therefore, we constrain the event to the interval from June 30 to July 6 at the comet.

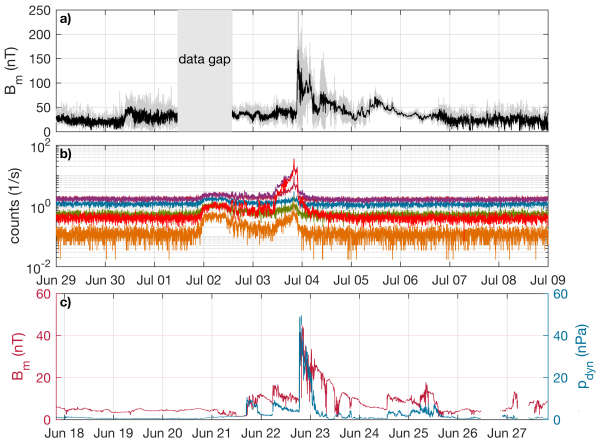

Fig. 3. Ten-day magnetic field magnitude measurements (*panel a*, averaged over 200 s in black) and energetic particle observations (*panel b*) made by Rosetta. *Panel c*: measurements of the solar wind at Earth from the OMNI dataset. The time axis was chosen so that the highest field and dynamic pressure coincide with the high-field event at Rosetta. This is to facilitate comparison of the structures.

An additional point of reference can be the energetic particle measurements that were observed by the Rosetta radiation monitor. This has previously been used to identify ICME impacts by Witasse et al. (2017). We show three energy channels: TC1 has a lower threshold of 27 MeV, and TC3 and S33 have lower thresholds of 12 MeV for protons. For electrons, the thresholds are 2 MeV and 0.8 MeV for TC1 and TC3. S33 is not sensitive to electrons (Evans et al. 2008). The upper threshold is infinity for all channels. As we are only interested in a qualitative evaluation of the measurements, no fluxes were calculated. On the eve of July 1, a first indication of an increased flux was visible. This increase lasted for about half a day before fluxes returned to slightly above normal. Unfortunately, magnetic field measurements are not available for most of that time period, but neither MIP nor LAP measurements changed significantly. On the evening of July 3, the particle counts increased dramatically, reaching their well-defined peak at 20:06:35. This peak is not

associated with any change in the plasma, but the background noise in IES increased. At the time when the discontinuities in the plasma occurred, the energetic particle counts abruptly decreased to slightly above normal, and by 06:00:00 on July 4, the measurements had returned to previous normal levels. These observations are consistent with the results published by Witasse et al. (2017) for a Forbush decrease during an ICME. In addition, the SREM observations are not very typical for a CIR; these are usually accompanied by only marginal increases in energetic particles.

The increase in energetic particles before the actual event then could be related to magnetic connectivity. If the approaching shock front or high-density region were magnetically connected to the comet, high-energy electrons might travel faster along the field lines than the movement of the shock. This would explain the gradual increase before the arrival of the plasma discontinuity. The peak in count rate is usually associated with shock acceleration, but this is not supported by the plasma measurements, as there is no change at that time. All SREM observations indicate that 67P might not have encountered a CIR, but an ICME. This could be associated with a coronal hole that was observed from Earth with the SOHO spacecraft until it rotated out of the field of view in late June. When the rotation of the Sun is accounted for, this coronal hole is approximately in the same section of the heliosphere as 67P, making it a candidate for an ICME propagating toward 67P. However, because STEREO was in conjunction with Earth and unable to send data, observations from that side of the Sun are not available.

Identifying the exact trigger of the plasma disturbance at 67P is essential because no solar wind observations are available at the comet. If this event was triggered by a CIR, the solar wind conditions are much more constrained because there are measurements at Earth and Mars from which the solar wind can be propagated. If it was caused by a singular event like an ICME, observations at other solar system bodies not in the direct path of the ICME cannot be used. All observations indicate that the solar wind event that caused the high magnetic field at the comet was an ICME. That said, Fig. 3a also shows that in addition to the investigated event, no unusual features in the magnetic field at the comet are detected. No other unusually high magnetic field events in the month surrounding the event have been registered, although there should be a CIR passing the comet at least once during that time. The impact of that CIR should then be visible, which is not the case. This leads us to speculate that the event that triggered the reaction of the cometary plasma was the CIR interacting with an ICME. This would explain all observations, plasma, magnetic field and energetic particles, but because there was no solar wind monitor at the comet, this is just conjecture at this point.

4.2. Reaction of the cometary plasma

4.2.1. Simple magnetic field model

Although we were unable to identify the physical cause of the event with certainty, we can estimate the reaction of the plasma environment to a CIR of the configuration that we infer from Earth-based observations. If our previous assumption of a combined CIR and ICME is correct, this should result in an underestimation of the solar wind density, velocity, and magnetic field as compared to a CIR-only case. Therefore, we would expect the reaction of the cometary environment to be stronger than estimated.

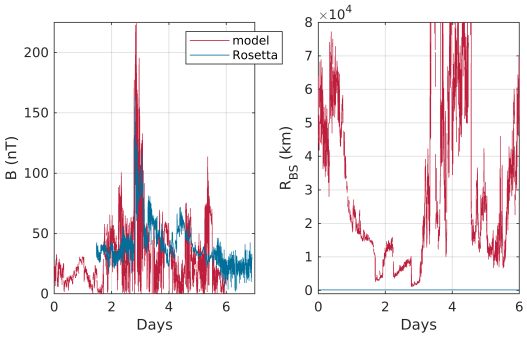

Fig. 4. Modeled magnetic field, bow shock position (red), and measured field and spacecraft position (blue). The input conditions for both models were calculated from OMNI solar wind observations using a Parker model for the propagation to the comet, and a gas production rate of $Q = 5.8 \times 10^{27}\,s^{-1}$. Day 0 corresponds to OMNI data from June 21, 2015. For readability, the magnetic field observations have been averaged over four minutes.

Goetz et al. (2017) presented a simple semi-analytical magnetic field model adapted from Galeev et al. (1985) that used a 1D magnetohydrodynamics (MHD) approach with a spacecraft that is confined to the Sun–comet line. It does not take into account the deflection of solar wind ions or the draping of the field. It was shown that despite the simplicity of the model, the output fit the magnetic field magnitude in the vicinity of the comet for suitable solar wind conditions reasonably well. Here, we use the model to estimate the impact that the high solar wind dynamic pressure has on the field in the inner coma. For this, we ran the model and extracted the magnetic field value at the radial distance of Rosetta, the result of which is shown in the left panel of Fig. 4. The model requires knowledge of the upstream dynamic and magnetic pressure in the solar wind, which is not available. However, as we have concluded in the previous section, the event at the comet may be related to the arrival of a CIR at Earth. Thus, we have chosen to infer the upstream solar wind conditions from the OMNI observations at Earth and propagated them to the comet using a simple Parker model. This approach does not include the influence of an ICME, as it is a transient event and is not observed at Earth, but it is still useful, as it gives us constraints on what the upstream solar wind conditions should be to produce such high magnetic fields at the comet.

The left-hand side of the figure shows that the general structure of the magnetic field in the model matches the observed field reasonably well. The maximum field magnitude in the model is 220 nT, which is still significantly lower than the maximum observed magnitude of ~300 nT (see Fig. 1a). At this point it is not possible to determine whether this is due to model uncertainties or upstream condition uncertainties. The solar wind values that produced the highest fields in the model were 25 nPa for the dynamic pressure and 0.25 nPa for the magnetic pressure. Although the magnetic and dynamic pressure may be higher individually, the importance here lies on the interplay of the two pressures.

4.2.2. Changing boundary positions

Solar wind protons were not detected in IES in this interval. As Rosetta was located in the solar wind-free region (Behar et al. 2017) for high gas production rates, this is not surprising. However, it also indicates that although the dynamic pressure in the

Table 1. Discontinuity parameters.

Time	$\boldsymbol{n}$	$\boldsymbol{B}_u$ (nT)	$\boldsymbol{B}_d$ (nT)	$\lvert\boldsymbol{B}_d\rvert/\lvert\boldsymbol{B}_u\rvert$	$\measuredangle(\boldsymbol{B}_u, \boldsymbol{n})(^\circ)$	$\measuredangle(\boldsymbol{B}_d, \boldsymbol{n})(^\circ)$
21:32:10	(0.24, −0.73, −0.65)	(39, 14, 5)	(74, 22, 5)	1.84	96	92
21:37:08	(0.63, −0.64, 0.43)	(79, 59, 14)	(0, 32, 79)	0.87	79	81
21:41:24	(−0.52, 0.84, −0.16)	(25, 27, 11)	(97, 64, 7)	3.58	90	88
22:06:18	(0.45, −0.69, 0.57)	(135, 64, −32)	(−120, 4, 95)	1.00	91	91
22:36:15	(0.39, −0.75, 0.54)	(−51, −25, −21)	(81, 21, −55)	1.65	102	98

Notes. $\boldsymbol{B}_u$ and $\boldsymbol{B}_d$ give the upstream and downstream magnetic field, i.e., the one-minute average before and after the discontinuity. $\boldsymbol{n}$ is the surface normal of the discontinuity as determined through minimum variance analysis.

solar wind is significantly enhanced, it is not enough to compress the bow shock to reach Rosetta. To ascertain this, we applied a simple mass-loading model to calculate the bow shock position (Biermann et al. 1967), again using the Earth observations as input. The model is a 1D gas dynamic approximation, thus it does not include magnetic fields and kinetic ions. It is therefore limited, and it was shown in Koenders et al. (2013) that it overestimates the bow shock distance compared to more sophisticated hybrid models at lower gas production rates and lower solar wind dynamic pressures. The result is shown on the right-hand side of Fig. 4. Most of the time, the bow shock is located well above 10 000 km, but for very high magnetic fields and thereby high solar wind dynamic pressures, the bow shock is pushed inward. The lowest bow-shock position estimate is still 1000 km, which is still well above the position of Rosetta. This estimate presents a lower boundary as the model does neither include asymmetric outgassing, that is, stronger outgassing on the sunward side of the comet, nor the fact that Rosetta is far from the subsolar point. Both these circumstances will push the bow shock position even farther from the nucleus than predicted (Huang et al. 2016).

According to Henri et al. (2017), the diamagnetic cavity is preferentially detected when the spacecraft is located close to the electron collisionopause, which is the approximate distance to the nucleus at which the electrons become collisional. It is defined as

$$L_e = \frac{Q\sigma_{en}}{4\pi u_n}, \tag{2}$$

with σ_{en} the electron-neutral collision cross-section and u_n and Q the neutral gas velocity and production rate. Close to perihelion, almost all cavity crossings were found to be below 5 L_e. During this unusual event, the neutral gas should not be affected by the higher magnetic fields and ion densities, which means that in the above equation, only σ_{en} is not constant. According to Itikawa & Mason (2005), the cross-section is electron energy dependent and decreases with increasing electron energy. The momentum transfer cross-section generally follows this trend as well, but has a secondary minimum at 2 eV and a secondary maximum at 10 eV. Normally, the electrons inside the diamagnetic cavity tend to be cold (Henri et al. 2017), with energies below 5 eV. It is plausible to assume that during this unusual event, with high densities, high magnetic fields, and high wave activity, that the electrons are heated. If the electrons inside the cavity are heated to below 15 eV, the electron collisionopause should expand as the cross-section increases. However, for electrons above 20 eV, the collisionopause shrinks as the cross-section decreases. With this the cavity boundary might either be moved inward or outward, depending on the electron energy inside the diamagnetic cavity. Unfortunately, it is not possible to distinguish between these two cases as measurements inside the diamagnetic cavity are not available for the studied time interval. The closest detection of the diamagnetic cavity was on July 7, 2015, at a distance of 150 km from the nucleus. At this point, the solar wind conditions had already returned to normal values and measurements are fundamentally different from the extraordinary circumstances studied here.

Another mechanism for the cavity formation was suggested by Cravens (1987), who assumed that the ion-neutral drag counter-balanced the magnetic field. This mechanism was tested by Timar et al. (2017) and found to accurately predict the diamagnetic cavity boundary distance in some cases. In this model, the diamagnetic cavity distance is proportional to $1/B$. Therefore, a fivefold increase in the field as detected here would decrease the boundary distance by a factor of 5. Comparing this to the detection on July 7, this would mean a diamagnetic cavity size of 30 km. This is still significantly larger than the nucleus, and therefore even under the extreme solar wind conditions presented here, the solar wind magnetic field is unlikely to reach the surface of the comet.

4.2.3. Changes in cometary plasma

It is also interesting to note that there is a pronounced increase in the flux of electrons in the energy range of about 60 eV in the highest density region. Previously, this population was studied by Broiles et al. (2015) and Nemeth et al. (2016), the latter of whom found that this particular population vanishes when the spacecraft is inside, or very close to, the diamagnetic cavity. According to the former, this population is suprathermal and of solar wind origin. All of these observations point to the fact that the 60 eV population is most closely associated with the magnetic field. As the magnetic field increases, so does the electron density, and when the field vanishes inside the cavity, so do the electrons. A detailed statistical study of this phenomenon is underway. These results are consistent with what was observed by Edberg et al. (2016a,b), who also suggested that electrons are heated by the interaction with the solar wind and then move along the field lines.

There are five pronounced changes in magnetic field magnitude or direction, shown as vertical black lines in Fig. 1. Unfortunately, the Rankine–Hugoniot jump conditions could not be proven without reliable plasma velocities for any of these discontinuities. However, it is still possible to determine the surface normal, for which we used the average fields in the minute before and after the discontinuities. The times and characteristics of the five events indicated by the vertical black lines are listed in Table 1. The first discontinuity is characterized by a large increase in field and almost no change of direction. This, to a smaller degree, is also the case for the third. The second and fourth discontinuities seem to be best characterized by a rotational discontinuity: the field magnitude does not change significantly, whereas the direction reverses. The fourth

discontinuity is especially remarkable, as the average magnitude does not change at all, whereas the direction reverses almost exactly. It should be pointed out that although the average magnitude does not change, the variability of the field does, giving the highest field shortly after the encounter of the fourth discontinuity. The last discontinuity is then a mixture of both rotational and compressional, but it should be noted that the magnetic field and densities start to slowly decrease even before the discontinuity is encountered. The direction of the normal seems to vary from region to region: the discontinuities bounding region 2 seem to be similar, that is, discontinuity two and three, and four and five are in similar planes. Only the first one is in an entirely different direction.

Goetz et al. (2017) found that the magnetic field variability, especially in a frequency band from 70 to 90 mHz, is an indicator of the neutral gas density and thereby also the ion density. The latter can be verified here as well; the high-density region also shows the highest values of the power spectral density.

It remains to discuss why the first increase in magnetic field at 21:32:10 is not accompanied by an increase in variability. One possibility for this would be that the high-density region is an effect of delayed ionization close to the nucleus. This would mean that the solar wind disturbance travels through the cometosheath to the inner, densest part of the coma and the high-energy electrons contribute significantly to additional electron impact ionization. The newly generated ions then travel outward to eventually reach Rosetta. However, this cannot be the case here, because then we would expect this increase in density to be permanent, which it is not, as region 2 reoccurs at least once.

Unfortunately, the exact amount of additional ionisation cannot be assessed, as neutral gas density observations are lacking for this event. They are fundamental for calculating the electron impact ionization (Vigren & Galand 2013).

A compression region at a CIR streaming interface could be the reason for the delayed increase. This might account for the delay, if the first shock corresponds to the forward wave front and the increase in density to the streaming interface. Thus, it is impossible to determine whether the delay is due to an internal change in the coma, such as increased ionization, or is due to an external trigger like the structure of the CIR.

Edberg et al. (2016a) found flux rope signatures in the magnetic field after the ICME impact and speculated that this might be due to reconnection in the inner coma. Therefore, we also searched for flux rope signatures. After determining the minimum variance direction with a minimum variance analysis (MVA, Sonnerup & Cahill 1967), we searched for a rotation in the magnetic field pointing in the maximum and medium variance direction. Surprisingly, no such structures were found after the high field event. This is unexpected, because the reconnection that was speculated on by Edberg et al. (2016a) should take place in the inner coma, where Rosetta was located during this event. Additionally, we find flux-rope-type structures in large numbers in the undisturbed plasma before and after the impact. Therefore, it seems as if flux-rope structures are a feature of the normal plasma at 67P and are not associated with the impact of an ICME in this case. A more detailed study of this is in preparation.

It is clear from these observations that there are fundamentally three regions in the interaction region around the event. We present two explanations for this: magnetic connectivity, and the structure of the solar wind.

First, the two regions after the shock impact have oppositely directed magnetic fields, meaning that in one instance, the field is mainly in the $+x$ direction and in the other in the $-x$ direction. It stands to reason, then, that the magnetic field is connected to different regions in the inner coma. Along the field line, the plasma can travel more freely, an effect that is often referred to as magnetic connectivity. In this instance, the magnetic field connects the spacecraft to a lower density region first and then to a high-density region. This idea assumes that the magnetic field in the solar wind also has different orientations that are then draped around the nucleus.

Second, the structure could be an intrinsic solar wind structure that propagates into the cometary environment and has higher densities from the start. These are then compressed. The fact that region 2 reoccurs speaks against this idea, as it is not obvious why the solar wind structures should have such a nested configuration. It is certainly not visible in the observations at Earth. Additionally, the plasma seems already to be returning to normal values in the second region 2, which indicates that the solar wind event is already on its trailing edge. Concurrent with Mandt et al. (2016), the high-density region could also be a fixed structure in the plasma environment of the comet that moves back and forth above the spacecraft.

5. Conclusions

We reported on the measurement of the highest magnetic fields ever measured at a comet and the associated plasma structures. In general, the results are consistent with previous findings and may be summarized as follows:

- We find that the high field is caused by unusually high solar wind dynamic and magnetic pressure.
- Based on observations at Earth, Mars, and comet 67P as well as observations of the Sun, we identify a CIR and an ICME as possible triggers, raising the possibility that an interaction of both structures is responsible for the unusually high field.
- A well-distinguished Forbush decrease is associated with the field structures. The highest count in energetic particles is about two hours before the event.
- Three interaction regions are identified: the normal regime before the impact, a high-field regime, and a high-field or high-density regime. It is most likely that these are a result of the magnetic field connecting to different regions of the plasma environment of the comet.
- In the high-density region, the suprathermal electron population increases significantly. This also implies that electron impact ionization is increased, but this could not be proven due to lack of data.
- The simple model produces bow shock distances that are still greater than the cometocentric distance of the spacecraft. This is consistent with the non-observation of solar wind protons in the plasma during this event.

This study adds to previous results by investigating the cometary plasma reaction to high solar wind dynamic pressure events at high gas production rates. All features of the undisturbed plasma at perihelion are enhanced by the unusual solar wind conditions. However, more observations and simulations are needed to clarify the exact nature of the changes.

Acknowledgements. The RPC-MAG data will be made available through the PSA archive of ESA and the PDS archive of NASA. Rosetta is a European Space Agency (ESA) mission with contributions from its member states and the National Aeronautics and Space Administration (NASA). The work on RPC-MAG was financially supported by the German Ministerium für Wirtschaft und Energie and the Deutsches Zentrum für Luft- und Raumfahrt under contract 50QP 1401. We are indebted to the whole of the Rosetta Mission Team, SGS, and RMOC for their outstanding efforts in making this mission possible. We acknowledge the staff of CDDP and IC for the use of AMDA and the RPC

Quicklook database (provided by a collaboration between the Centre de Données de la Physique des Plasmas, supported by CNRS, CNES, Observatoire de Paris and Université Paul Sabatier, Toulouse and Imperial College London, supported by the UK Science and Technology Facilities Council). Portions of this work were performed at the Jet Propulsion Laboratory, California Institute of Technology under contract with NASA. We acknowledge use of NASA/GSFC's Space Physics Data Facility's OMNIWeb (or CDAWeb or ftp) service, and OMNI data. Simulation results have been provided by the Community Coordinated Modeling Center at Goddard Space Flight Center through their public Runs on Request system (http://ccmc.gsfc.nasa.gov). The ENLIL Model was developed by D. Odstrcil at the University of Boulder at Colorado. A.W. acknowledges support from the STFC consolidated grant to UCL-MSSL ST/N000722/1. The authors would like to acknowledge ISSI for the great opportunity it offered for very valuable discussions on this topic as part of the International Team "Plasma Environment of comet 67P after Rosetta".

References

Alfvén, H. 1957, Tellus, 9
Behar, E., Nilsson, H., Alho, M., Goetz, C., & Tsurutani, B. 2017, MNRAS, 469, 396
Behar, E., Tabone, B., Saillenfest, M., et al. 2018, A&A, 620, A35
Biermann, L., Brosowski, B., & Schmidt, H. U. 1967, Sol. Phys., 1, 254
Broiles, T. W., Burch, J. L., Clark, G., et al. 2015, A&A, 583, A21
Burch, J. L., Goldstein, R., Cravens, T. E., et al. 2007, Space Sci. Rev., 128, 697
Cane, H. V. 2000, Space Sci. Rev., 93, 55
Carr, C., Cupido, E., Lee, C. G. Y., et al. 2007, Space Sci. Rev., 128, 629
Coates, A. J., & Jones, G. H. 2009, Planet. Space Sci., 57, 1175
Cravens, T. E. 1987, Adv. Space Res., 7, 147
Edberg, N. J. T., Alho, M., André, M., et al. 2016a, MNRAS, 462, S45
Edberg, N. J. T., Eriksson, A. I., Odelstad, E., et al. 2016b, J. Geophy. Res. (Space Phys.), 121, 949
Eriksson, A. I., Boström, R., Gill, R., et al. 2007, Space Sci. Rev., 128, 729
Evans, H. D. R., Bühler, P., Hajdas, W., et al. 2008, Adv. Space Res., 42, 1527
Galeev, A. A., Cravens, T. E., & Gombosi, T. I. 1985, ApJ, 289, 807
Glassmeier, K.-H., Boehnhardt, H., Koschny, D., Kührt, E., & Richter, I. 2007a, Space Sci. Rev., 128, 1
Glassmeier, K.-H., Richter, I., Diedrich, A., et al. 2007b, Space Sci. Rev., 128, 649
Glassmeier, K.-H. 2017, Philos. Trans. R. Astron. Soc. A, 375, 20160256
Goetz, C., Koenders, C., Hansen, K. C., et al. 2016a, MNRAS, 462, S459
Goetz, C., Koenders, C., Richter, I., et al. 2016b, A&A, 588, A24
Goetz, C., Volwerk, M., Richter, I., & Glassmeier, K.-H. 2017, MNRAS, 469, S268
Hajra, R. 2018, MNRAS, submitted
Halekas, J. S., Ruhunusiri, S., Harada, Y., et al. 2017, J. Geophys. Res. (Space Phys.), 122, 547
Hansen, K. C., Altwegg, K., Berthelier, J.-J., et al. 2016, MNRAS, 462, S491
Henri, P., Vallières, X., Hajra, R., et al. 2017, MNRAS, 469, S372
Heritier, K. L., Henri, P., Vallières, X., et al. 2017, MNRAS, 469, S118
Huang, Z., Tóth, G., Gombosi, T. I., et al. 2016, J. Geophys. Res. (Space Phys.), 121, 4247
Itikawa, Y., & Mason, N. 2005, J. Phys. Chem. Ref. Data, 34, 1
Jakosky, B. M., Lin, R. P., Grebowsky, J. M., et al. 2015, Space Sci. Rev., 195, 3
Kennel, C. F., Edmiston, J. P., & Hada, T. 1985, Geophysical Monograph Series (Washington DC: American Geophysical Union), 34, 1
King, J. H., & Papitashvili, N. E. 2005, J. Geophys. Res. (Space Phys.), 110, A02104
Koenders, C., Glassmeier, K.-H., Richter, I., Motschmann, U., & Rubin, M. 2013, Planet. Space Sci., 87, 85
Madanian, H., Cravens, T. E., Burch, J., et al. 2017, AJ, 153, 30
Mandt, K. E., Eriksson, A., Edberg, N. J. T., et al. 2016, MNRAS, 462, S9
Nemeth, Z., Burch, J., Goetz, C., et al. 2016, MNRAS, 462, S415
Neubauer, F. M. 1987, A&A, 187, 73
Nilsson, H., Lundin, R., Lundin, K., et al. 2007, Space Sci. Rev., 128, 671
Nilsson, H., Wieser, G. S., Behar, E., et al. 2017, MNRAS, 469, S252
Odstrcil, D. 2003, Adv. Space Res., 32, 497
Pizzo, V. J. 1985, Geophysical Monograph Series, (Washington DC: American Geophysical Union) 35, 51
Smith, E. J., & Wolfe, J. H. 1976, Geophys. Res. Lett., 3, 137
Sonnerup, B. U. O., & Cahill, Jr. L. J. 1967, J. Geophys. Res., 72, 171
Timar, A., Nemeth, Z., Szego, K., et al. 2017, MNRAS, 469, S723
Trotignon, J. G., Michau, J. L., Lagoutte, D., et al. 2007, Space Sci. Rev., 128, 713
Tsurutani, B. T., Gonzalez, W. D., Tang, F., Akasofu, S. I., & Smith, E. J. 1988, J. Geophy., Res., 93, 8519
Tsurutani, B. T., Gonzalez, W. D., Lakhina, G. S., & Alex, S. 2003, J. Geophy. Res. (Space Phys.), 108, 1268
Tsurutani, B. T., Echer, E., Guarnieri, F. L., & Kozyra, J. U. 2008, Geophys. Res. Lett., 35
Tsurutani, B. T., Lakhina, G. S., Verkhoglyadova, O. P., et al. 2011, J. Atmos. Sol. Terr. Phys., 73, 5
Vigren, E., & Galand, M. 2013, ApJ, 772, 33
Volwerk, M., Glassmeier, K. H., Delva, M., et al. 2014, Ann. Geophys., 32, 1441
Witasse, O., Sánchez-Cano, B., Mays, M. L., et al. 2017, J. Geophy. Res. (Space Phys.), n/a, 2017JA023884

Acknowledgements

First, I would like to thank my advisor, Karl-Heinz Glaßmeier, for the opportunities he afforded me while supervising my thesis. The intense discussions about science and policy were essential for the success of this work. I would also like to thank him for securing the funding for the many trips I was able to do to present my work at international conferences and meetings with potential cooperation partners. And lastly for giving me the opportunity to expand my work beyond the science into science communication.

I am very grateful to Marina Galand who agreed to be on my PhD committee and had many good questions and suggestions while always being supportive and enthusiastic.

I would also like to thank everyone involved in the Rosetta mission and again congratulate them for the successful completion of such an ambitious and exciting mission. They made trajectory discussions fun and archiving telecons and meetings bearable. A special thanks goes to Matt Taylor who organized not only the meetings but also the evenings afterwards and provided everyone with much needed fun after intense discussions. Thanks goes out to him as well for getting me a spot on the FedCon ESA stand and the end of mission press briefing, those were some of the best experiences of my PhD time.

Then of course thanks goes to every member of the RPC team, who are a wonderful group of people, knowledgeable, kind, and a joy to work with. Thank you to everyone that has invited me to work with them, I have learned a lot from those cooperations. I especially would like to thank Martin Volwerk, Herbert Gunell, Ferdinand Plaschke, Cyril Simon Wedlund, Elias Odelstad, Arnaud Beth, Pierre Henri, Anders Eriksson, Hans Nilsson and Kathy Mandt for fruitful discussions and persistence even when success seemed unreachable. I thank Tomas Karlsson for proof reading my thesis and providing many good suggestions for improvement.

I am grateful that I got the chance to do my PhD at the Institut für Geophysik und extraterrestrische Physik with great colleagues and a beneficial work atmosphere. I would especially like to thank Ingo Richter for bearing my rants about people and life in science in general. A special shoutout also goes to Christoph Koenders who explained cometary science to me and got me through the insanity of the AIKEF code. And lastly, to the Feierabendbierfreitag group: thanks for keeping me halfway sane during my thesis writing time.

Und zu guterletzt möchte ich meinen Freunden und meiner Familie danken. Max und Niklas, die mein ewiges Beschweren ignoriert haben und Jenny, die immer für eine Auszeit zu haben war. Meiner Mutter möchte ich danken, dass ich Star Trek mitschauen durfte, ohne die Inspiration wäre ich niemals dort wo ich heute bin. Und ich danke Udo, der mir meinen ersten Elektronikbaukasten gekauft hat und mich auf die Physikschiene brachte. Danke auch an alle meine Geschwister, die immer für Aufregung gesorgt haben! Oma, Opa, Monika und Franz-Joachim danke ich für die jahrelange Unterstützung und Bestärkung auch wenn ich schwierige Entscheidungen zu treffen hatte.

Image Credits

Front Cover: ESA/Rosetta/NAVCAM, CC BY-SA IGO 3.0 and ESA/ATG medialab, CC BY-SA 2.0
Back Cover: ESA/Rosetta/MPS for OSIRIS Team MPS/UPD/LAM/IAA/SSO/ INTA/UPM/DASP/IDA, CC BY-SA 4.0